



ISSN 2518-7198 (Print)

ISSN 2663-5089 (Online)

BULLETIN

OF THE KARAGANDA UNIVERSITY

PHYSICS

Series

2024 • Volume 29 • Issue 3(115)

ISSN 2663-5089 (Online)
ISSN-L 2518-7198 (Print)
Индексі 74616
Индекс 74616

ҚАРАҒАНДЫ
УНИВЕРСИТЕТІНІҢ
ХАБАРШЫСЫ

ВЕСТНИК
КАРАГАНДИНСКОГО
УНИВЕРСИТЕТА

BULLETIN
OF THE KARAGANDA
UNIVERSITY

ФИЗИКА сериясы

Серия ФИЗИКА

PHYSICS Series

2024

29-том • 3(115)-шығарылым
Том 29 • Выпуск 3(115)
Volume 29 • Issue 3(115)

1996 жылдан бастап шығады
Издается с 1996 года
Founded in 1996

Жылына 4 рет шығады
Выходит 4 раза в год
Published 4 times a year

Қарағанды / Караганда / Karaganda
2024

Бас редакторы

физ.-мат. ғыл. канд., проф. **А.К. Аймуханов**

Жауапты хатшы

PhD д-ры, қауымд. проф. **Д.Ж. Қарабекова**

Редакция алқасы

Н.Х. Ибраев,	физ.-мат. ғыл. д-ры, проф., акад. Е.А. Бөкетов атындағы Қарағанды университеті (Қазақстан);
Т.Ә. Көкөтайтегі,	физ.-мат. ғыл. д-ры, проф., акад. Е.А. Бөкетов атындағы Қарағанды университеті (Қазақстан);
Б.Р. Нүсіпбеков, А.О. Сәулебеков,	техн. ғыл. канд., проф., акад. Е.А. Бөкетов атындағы Қарағанды университеті (Қазақстан); физ.-мат. ғыл. д-ры, проф., М.В. Ломоносов атындағы Мәскеу мемлекеттік университетінің Қазақстан филиалы, Астана (Қазақстан);
Б.Р. Ильясов, А.Д. Погребняк, А.П. Суржиков, И.П. Курытник,	PhD д-ры, қауымд. проф., Astana IT University, Астана (Қазақстан); физ.-мат. ғыл. д-ры, проф., Сумы мемлекеттік университеті (Украина); физ.-мат. ғыл. д-ры, проф., Томск политехникалық университеті (Ресей); техн. ғыл. д-ры, проф., Освенцимдегі В. Пилецкий атындағы Мемлекеттік жоғары кәсіптік мектебі (Польша);
М. Стоев,	PhD д-ры, инженерия д-ры, «Неофит Рильский» Оңтүстік-Батыс университеті, Благоевград (Болгария);
В.Ю. Кучерук, В.А. Кульбачинский,	техн. ғыл. д-ры, проф., Винница ұлттық техникалық университеті (Украина); физ.-мат. ғыл. д-ры, проф., М.В. Ломоносов атындағы Мәскеу мемлекеттік университеті (Ресей);
Bisquert Juan, Chun Li, Д.Т. Валиев,	проф., физика проф., Хайме I университеті, Кастельо-де-ла-Плана (Испания); PhD д-ры, Чанчунь ғылым және технология университеті (Қытай); физ.-мат. ғыл. канд., доц., Томск ұлттық политехникалық зерттеу университеті (Ресей)

Редакцияның мекенжайы: 100024, Қазақстан, Қарағанды қ., Университет к-сі, 28

E-mail: vestnikku@gmail.com; karabekova71@mail.ru

Сайты: physics-vestnik.ksu.kz

Атқарушы редактор

PhD д-ры **Г.Б. Саржанова**

Редакторлары

Ж.Т. Нурмуханова, С.С. Балкеева, И.Н. Муртазина

Компьютерде беттеген

В.В. Бутяйкин

Қарағанды университетінің хабаршысы. «Физика» сериясы. — 2024. — 29-т., 3(115)-шығ. — 100 б. — ISSN-L 2518-7198 (Print). ISSN 2663-5089 (Online).

Меншік иесі: «Академик Е.А. Бөкетов атындағы Қарағанды университеті» КЕАҚ.

Қазақстан Республикасы Ақпарат және қоғамдық даму министрлігімен тіркелген. 30.09.2020 ж. № KZ38VPY00027378 қайта есепке қою туралы куәлігі.

Басуға 17.09.2024 ж. қол қойылды. Пішімі 60×84 1/8. Қағазы офсеттік. Көлемі 12,5 б.т. Таралымы 200 дана. Бағасы келісім бойынша. Тапсырыс № 90.

«Акад. Е.А. Бөкетов ат. Қарағанды ун-ті» КЕАҚ баспасының баспаханасында басылып шықты. 100024, Қазақстан, Қарағанды қ., Университет к-сі, 28. Тел. (7212) 35-63-16. E-mail: izd_kargu@mail.ru

Главный редактор

канд. физ.-мат. наук, проф. **А.К. Аймуханов**

Ответственный секретарь

д-р PhD, ассоц. проф. **Д.Ж. Карабекова**

Редакционная коллегия

Н.Х. Ибраев,	д-р физ.-мат. наук, проф., Карагандинский университет им. акад. Е.А. Букетова (Казахстан);
Т.А. Кокетайтеги,	д-р физ.-мат. наук, проф., Карагандинский университет им. акад. Е.А. Букетова (Казахстан);
Б.Р. Нусупбеков,	канд. техн. наук, проф., Карагандинский университет им. акад. Е.А. Букетова (Казахстан);
А.О. Саулебеков,	д-р физ.-мат. наук, проф., Казахстанский филиал Московского государственного университета им. М.В. Ломоносова, Астана (Казахстан);
Б.Р. Ильясов,	д-р PhD, ассоц. проф., Astana IT University, Астана (Казахстан);
А.Д. Погребняк,	д-р физ.-мат. наук, проф., Сумской государственный университет (Украина);
А.П. Суржиков,	д-р физ.-мат. наук, проф., Томский политехнический университет (Россия);
И.П. Курьтник,	д-р техн. наук, проф., Государственная высшая профессиональная школа им. В. Пилецкого в Освенциме (Польша);
М. Стоев,	д-р PhD, д-р инженерии, Юго-Западный университет «Неофит Рильский», Благоевград (Болгария);
В.Ю. Кучерук,	д-р техн. наук, проф., Винницкий национальный технический университет (Украина);
В.А. Кульбачинский,	д-р физ.-мат. наук, проф., Московский государственный университет им. М.В. Ломоносова (Россия);
Bisquert Juan,	проф., проф. физики, Университет Хайме I, Кастельо-де-ла-Плана (Испания);
Chun Li,	д-р PhD, Чанчуньский университет науки и технологии (Китай);
Д.Т. Валиев,	канд. физ.-мат. наук, доц., Национальный исследовательский Томский политехнический университет (Россия)

Адрес редакции: 100024, Казахстан, г. Караганда, ул. Университетская, 28

E-mail: vestnikku@gmail.com; karabekova71@mail.ru

Сайт: physics-vestnik.ksu.kz

Исполнительный редактор

д-р PhD **Г.Б. Саржанова**

Редакторы

Ж.Т. Нурмуханова, С.С. Балкеева, И.Н. Муртазина

Компьютерная верстка

В.В. Бутяйкин

Вестник Карагандинского университета. Серия «Физика». — 2024. — Т. 29, вып. 3(115). — 100 с. — ISSN-L 2518-7198 (Print). ISSN 2663-5089 (Online).

Собственник: НАО «Карагандинский университет имени академика Е.А. Букетова».

Зарегистрирован Министерством информации и общественного развития Республики Казахстан.

Свидетельство о постановке на переучет № KZ38VPY00027378 от 30.09.2020 г.

Подписано в печать 17.09.2024 г. Формат 60×84 1/8. Бумага офсетная. Объем 12,5 п.л. Тираж 200 экз.

Цена договорная. Заказ № 90.

Отпечатано в типографии издательства НАО «Карагандинский университет им. акад. Е.А. Букетова». 100024, Казахстан, г. Караганда, ул. Университетская, 28. Тел.(7212) 35-63-16. E-mail: izd_kargu@mail.ru

Chief Editor

Professor, Cand. of Phys. and Math. Sci. **A.K. Aimukhanova**

Responsible secretary

Associate Professor, PhD **D.Zh. Karabekova**

Editorial board

N.Kh. Ibrayev,	Prof., Doctor of phys.-math. sciences, Karagandy University of the name of acad. E.A. Buketov (Kazakhstan);
T.A. Koketaitegi,	Prof., Doctor of phys.-math. sciences, Karagandy University of the name of acad. E.A. Buketov (Kazakhstan);
B.R. Nussupbekov,	Prof., Cand. of techn. sciences, Karagandy University of the name of acad. E.A. Buketov (Kazakhstan);
A.O. Saulebekov,	Prof., Doctor of phys.-math. sciences, Kazakhstan branch of Lomonosov Moscow State University, Astana (Kazakhstan);
B.R. Ilyassov,	PhD, Assoc. Prof., Astana IT University (Kazakhstan);
A.D. Pogrebnjak,	Prof., Doctor of phys.-math. sciences, Sumy State University (Ukraine);
A.P. Surzhikov,	Prof., Doctor of phys.-math. sciences, Tomsk Polytechnic University (Russia);
I.P. Kurytnik,	Prof., Doctor of techn. sciences, The State School of Higher Education in Oświęcim (Auschwitz) (Poland);
M. Stoev,	PhD, Doctor of engineering, South-West University “Neofit Rilski”, Blagoevgrad (Bulgaria);
V.Yu. Kucheruk,	Prof., Doctor of techn. sciences, Vinnytsia National Technical University, Vinnitsia (Ukraine);
V.A. Kulbachinskii,	Prof., Doctor of phys.-math. sciences, Lomonosov Moscow State University (Russia);
Bisquert Juan,	Prof. of phys., Prof. (Full), Universitat Jaume I, Castellon de la Plana (Spain);
Chun Li,	PhD, Changchun University of Science and Technology (China);
D.T. Valiev,	Assoc. Prof., Cand. of phys.-math. sciences, National Research Tomsk Polytechnic University (Russia)

Postal address: 28, University Str., 100024, Karaganda, Kazakhstan

E-mail: vestnikku@gmail.com; karabekova71@mail.ru

Web-site: physics-vestnik.ksu.kz

Executive Editor

PhD **G.B. Sarzhanova**

Editors

Zh.T. Nurmukhanova, S.S. Balkeyeva, I.N. Murtazina

Computer layout

V.V. Butyaikin

Bulletin of the Karaganda University. “Physics” Series. — 2024. — Vol. 29, Iss. 3(115). — 100 p. — ISSN-L 2518-7198 (Print). ISSN 2663-5089 (Online).

Proprietary: NLC “Karagandy University of the name of academician E.A. Buketov”.

Registered by the Ministry of Information and Social Development of the Republic of Kazakhstan. Rediscount certificate No. KZ38VPY00027378 dated 30.09.2020.

Signed in print 17.09.2024. Format 60×84 1/8. Offset paper. Volume 12,5 p.sh. Circulation 200 copies. Price upon request. Order № 90.

Printed in the Publishing house of NLC “Karagandy University of the name of acad. E.A. Buketov”.
28, University Str., Karaganda, 100024, Kazakhstan. Tel. (7212) 35-63-16. E-mail: izd_kargu@mail.ru

МАЗМҰНЫ – СОДЕРЖАНИЕ – CONTENTS

КОНДЕНСАЦИЯ ЛАНҒАН КҮЙДІҢ ФИЗИКАСЫ ФИЗИКА КОНДЕНСИРОВАННОГО СОСТОЯНИЯ PHYSICS OF THE CONDENSED MATTER

<i>Koshtybayev T., Aliyeva M.</i> Correlation functions of weakly inhomogeneous plasma.....	6
<i>Beall G.W., Akhmetsadyk D.S., Ilyin A.M., Tulegenova M.A.</i> First-principles study of O ₃ molecule adsorption on pristine, N, Ga-doped and -Ga-N- co-doped graphene	15
<i>Nurakhmetov T.N., Bakhtizin R.Z., Tolekov D.A., Shamieva R.K., Salikhodzha Zh.M., Sadykova B.M., Yusupbekova B.N., Pazyzbek S.A., Bairbaeva G.B., Rakhymzhanov B.M.</i> Formation of a combined electron-hole emission state in the LiRbSO ₄ – Eu phosphor	25
<i>Seisenbayeva G.S., Kambar D.S., Zavgorodniy A.V., Ilyassov B.R.</i> Enhanced charge separation at the interface of Cu ₂ O/CuSCN composite thin films synthesized by electrodeposition technique	34
<i>Mukametkali T.M., Aimukhanov A.K., Zeinidenov A.K.</i> Phthalocyanine and metal phthalocyanine are hole transport buffer layers for perovskite solar cell fabrication	41
<i>Alpysova G.K., Afanasyev D.A., Bakiyeva Zh.K., Lisitsyna L.A., Golkovski M.G., Tussupbekova A.K., Kissabekova A.A., Tuleuov S.D.</i> Optical properties of ZnWO ₄ ceramics obtained by radiation synthesis	51
<i>Uskenbaev D.E., Nogai A.S., Uskenbayev A.D., Nogai E.A., Kudussov A.S., Khamzina B.E.</i> Critical current density of high-temperature superconducting ceramics BSCCO Bi-2223	61

ТЕХНИКАЛЫҚ ФИЗИКА ТЕХНИЧЕСКАЯ ФИЗИКА TECHNICAL PHYSICS

<i>Rakhadilov B.K., Muktanova N., Kakimzhanov D.N., Kowalewski P.</i> Effect of HVOF method spraying parameters on phase composition and mechanical and tribological properties of 86WC-10Co-4Cr coating	71
<i>Buitkenov D.B., Sagdoldina Zh.B., Sulyubayeva L.G., Nabioldina A.B., Raisov N.S.</i> Investigation of mechanical and tribological properties of NiCrAlY/ZrO ₂ -Y ₂ O ₃ coatings obtained by detonation spraying	83

ЖЫЛУФИЗИКАСЫ ЖӘНЕ ТЕОРИЯЛЫҚ ЖЫЛУТЕХНИКАСЫ ТЕПЛОФИЗИКА И ТЕОРЕТИЧЕСКАЯ ТЕПЛОТЕХНИКА THERMOPHYSICS AND THEORETICAL THERMOENGINEERING

<i>Khasenov A.K., Bulkairova G.A., Nussupbekov B.R., Schrager E.R., Karabekova D.Zh., Bolatbekova M.M., Zholdasbek Y.A.</i> Research of heat conductivity of quartz material.....	94
---	----

КОНДЕНСАЦИЯ ЛАНҒАН КҮЙДІҢ ФИЗИКАСЫ ФИЗИКА КОНДЕНСИРОВАННОГО СОСТОЯНИЯ PHYSICS OF THE CONDENSED MATTER

<https://doi.org/10.31489/2024PH3/6-14>
UDC 533.9.01

Received: 18.01.2024
Accepted: 02.04.2024

T. Koshtybayev¹, M. Aliyeva*²

¹*Kazakh National Women's Pedagogical University, Almaty, Kazakhstan;*

²*Abai Kazakh National Pedagogical University, Almaty, Kazakhstan*

**Corresponding author's e-mail: moldir-2008@mail.ru*

Correlation functions of weakly inhomogeneous plasma

Abstract. This article focuses on the kinetic theory of inhomogeneous plasma and explores the interaction between a high-frequency electric field and weakly inhomogeneous plasma. Particularly, it examines the impact of an external variable field on the kinetic and high-frequency properties of the plasma, including kinetic equations, correlation functions, and distribution functions of charged particles. The study derives expressions for the pair (two-particle) correlation function and the corresponding distribution function, taking into account the spatial inhomogeneity of the plasma and electric field, as well as the collisions between charged particles. The results were obtained using the kinetic equation for the spatial-temporal spectral density of fluctuations and the method of successive approximations (separation of slow motions and fast oscillations). The field amplitude is considered a slowly varying function of time and coordinates. The calculations neglect the contribution of the magnetic component of the electromagnetic field, which is applicable to longitudinal electric fields. The results obtained in this article are primarily of theoretical interest, they reveal the picture of the interaction of a weakly inhomogeneous plasma with a high-frequency electric field and can be used in the construction of a kinetic theory of an inhomogeneous plasma located in high-frequency electromagnetic fields. Note that for charged particles of the same sign, the correlation function is negative, and for particles of different signs it is positive. In addition, the correlation function is exponentially small when the distance between the particles is greater than the Debye radius. In all calculations, the contribution of the magnetic component of the electromagnetic field is neglected, which is quite true for the longitudinal electric field.

Keywords: High-frequency properties, inhomogeneous plasma, kinetic equation, variable field, collision integral.

Introduction

The correlation function is a function of time and spatial coordinates that defines the correlation in systems with random processes. The correlation function is a measure of system ordering. It shows how microscopic variables correlate at different moments in time and in different points on average. Sometimes it is required to consider the temporal evolution of microscopic variables. In some cases, it is necessary to consider the temporal evolution of microscopic variables, which is why the spatial correlation function is used. It is important to understand that although in equilibrium some macroscopic variables are not dependent on time, microscopic variables (for example, the particle velocity vector). Therefore, similar correlation functions, essentially macroscopic quantities, may also depend on time. The correlation function is a measure of system ordering. It shows how microscopic variables correlate at different moments in time and in different points on average. The physical meaning of the correlation function of the particle number density is that it shows the probability density of the relative positions of the particles. The correlation is caused by the presence of interactions between particles, leading to short-range order. It is known that isolated charged particles interact with each other according to Coulombs law. However, due to the long-range nature of Coulomb forces, the interaction between two particles in a plasma is influenced by the presence of other charged parti-

cles, i.e. correlation effects (collective interactions between particles) play a significant role in plasma. When describing irreversible processes and constructing the kinetic theory of fluctuations in fully ionized plasma, it is crucial to account for the correlations between particles. This problem is well described, particularly in Klimontovich Yu. L. papers [1] and in the works of other authors [2, 3]. For example, [4, 5] presents the binary (pair) correlation function and the corresponding distribution function of plasma particle coordinates and momenta for a homogeneous and equilibrium plasma, without considering the influence of external fields. Much attention is paid to the effects of external fields on the kinetic properties of plasma in [14–18]. In particular, large-scale fluctuations are considered—fluctuations with correlation times of the order or greater than the free path time and with correlation lengths of the order or greater than the free path length in the presence of a high-frequency electric field. The effect of the interdependence of the motion of individual particles is usually described by introducing correlation functions. Temporal correlation functions play a fundamental role in studying the electrodynamic properties of plasma. Two-particle correlation functions are considered in [19–21], in particular, three functions of paired correlations in a two-component (electrons and ions) plasma are calculated in the second order by the plasma parameter. In [22], a system of equations was obtained for the paired correlation function of phase density fluctuations and the renormalized linear response function, taking into account linear electromagnetic processes that are quadratic in intensity of fluctuations. In [23–25], a kinetic theory of a highly ideal plasma in an external field was constructed. The resulting linearized kinetic equation for the external field and the relations of the theory of linear response allow us to obtain a closed equation for a single-particle distribution function.

Main part. Experimental

Developing a consistent collision theory in plasma encounters significant difficulties associated with the slow decrease of Coulomb forces with increasing distance between interacting particles. At any given time, each charged plasma particle is exposed to a huge number of surrounding particles, and all of these effects shall be somehow taken into account. Instead of a simple two-body problem, we face the challenging problem of many-body interactions. In a strict formulation such a problem is hardly solvable. To make a solution possible, it is necessary to introduce some simplifications. The simplest is the pair collision approximation, in which the plasma particle interactions are reduced to independent and instantaneous interactions of pairs of particles. The effect of interdependence of the motion of individual charged particles is typically described by introducing correlation functions. In this article, expressions for the simultaneous correlation function g_{ab} of particles of components a, b and the two-particle distribution function f_{ab} will be obtained by the method of successive approximations based on the kinetic equation for the space-time spectral density of fluctuations

$$\overline{\delta N_a(\vec{q}, \vec{p}, t) \delta N_b(\vec{q}', \vec{p}', t)}. \quad (1)$$

In this case, let's assume that the plasma is weakly inhomogeneous, i.e. all statistical processes occurring in the six-dimensional phase space of coordinates \vec{q} , \vec{q}' , and momenta, are different, \vec{p} , \vec{p}' and it is subjected to a longitudinally high-frequency and weakly inhomogeneous electric field $\vec{E} = \vec{E}_o(\vec{q}, \varepsilon t) \sin \omega_o t$ (as well as $\vec{B}_o = 0$).

Results and Discussion

To statistically describe processes in plasma under the condition $\varepsilon = \frac{V_T}{\omega_o L} \ll 1$, a closed system of equations for the single-particle distribution functions f_a , f_b and for the functions $\left(\overline{\delta N_a \delta N_b}\right)_Q$, g_{ab} can be used (where $Q = \vec{q}, \vec{q}', \vec{p}, \vec{p}', t$). The higher correlation functions g_{ab} etc. are thus found to be small of order ε^2 . Therefore, to determine g_{ab} , the kinetic equation for function (1) is used, which can be written as [6–10]

$$\hat{A}_o \left(\overline{\delta N_a \delta N_b}\right)_Q = -A_1, \quad (2)$$

where

$$\hat{A}_o = \frac{\partial}{\partial t} + \mathbf{v}_o + \bar{\mathbf{v}} \frac{\partial}{\partial \vec{q}} + \bar{\mathbf{v}}' \frac{\partial}{\partial \vec{q}'} + e_a \bar{\mathbf{E}} \frac{\partial}{\partial \vec{p}} + e_b \bar{\mathbf{E}} \frac{\partial}{\partial \vec{p}'};$$

$$A_1 = e_a n_a \left(\overline{\delta N_b \delta \vec{E}} \right)_\varphi \frac{\partial f_a}{\partial \vec{p}} + e_b n_b \left(\overline{\delta N_a \delta \vec{E}} \right)_\psi \frac{\partial f_b}{\partial \vec{p}'};$$

$$v_o \ll \omega_o; \varphi = \vec{q}, \vec{q}', \vec{p}, \vec{p}', t; \vec{v} = \frac{\vec{p}}{m_a}; \psi = \vec{q}, \vec{p}, t.$$

$m_{a,b}$, $e_{a,b}$, $n_{a,b}$ — and respectively mass, charge and concentration; $\delta \vec{E}$ — electric field fluctuation. It should be noted that equation (2) is written under the condition of weak plasma inhomogeneity. This means that the functions $f_a, f_b, \vec{E}, \left(\overline{\delta N_a \delta N_b} \right)_Q, \left(\overline{\delta N_a \delta \vec{E}} \right)_\psi, \left(\overline{\delta N_b \delta \vec{E}} \right)_\varphi$ vary little over distance of the Debye radius r_d . It is known that in weakly inhomogeneous plasma, correlations at points \vec{q} and \vec{q}' depend on $\vec{r} = \vec{q} - \vec{q}'$ and

$$\vec{r}_o = \frac{\vec{q} + \vec{q}'}{2} = \vec{q} - \frac{\vec{r}}{2}$$

perform a decomposition by $\vec{r} \frac{\partial}{\partial \vec{q}}$. In the first approximation, we get

$$\left(\overline{\delta N_a \delta N_b} \right)_Q = \hat{A}_2 \left(\overline{\delta N_a \delta N_b} \right)_B, \quad (3)$$

where

$$\frac{\vec{r}}{2} \frac{\partial}{\partial \vec{q}} \hat{A}_2 = 1 - \frac{\vec{r}}{2} \frac{\partial}{\partial \vec{q}}; B = \vec{q}, \vec{r}, \vec{p}, \vec{p}', t.$$

Substitute (3) into (2), using the Fourier integral transformation of the following functions:

$$\left(\overline{\delta N_a \delta N_b} \right)_B, \left(\overline{\delta N_a \delta \vec{E}} \right)_{\psi_1}, \left(\overline{\delta N_b \delta \vec{E}} \right)_{\varphi_1}, \frac{\vec{r}}{2} \frac{\partial}{\partial \vec{q}} \left(\overline{\delta N_a \delta N_b} \right)_B.$$

As a result of the calculations, we get [11]:

$$\hat{A}_o \left[1 - \frac{i}{2} \frac{\partial^2}{\partial \vec{k} \partial \vec{q}} \right] \left(\overline{\delta N_a \delta N_b} \right)_{B_o} = -A_3, \quad (4)$$

where

$$\hat{A}_3 = e_a n_a \left(\overline{\delta N_b \delta \vec{E}} \right)_{\varphi_o} \frac{\partial f_a}{\partial \vec{p}} + e_b n_b \left(\overline{\delta N_a \delta \vec{E}} \right)_{\psi_o} \frac{\partial f_b}{\partial \vec{p}'};$$

$$\varphi_1 = \vec{r}, \vec{q}, \vec{p}', t; \psi_1 = \vec{r}, \vec{q}, \vec{p}, t; B_o = \vec{k}, \vec{q}, \vec{p}, \vec{p}', t; \psi_o = \vec{k}, \vec{q}, \vec{p}, t; \varphi_o = \vec{k}, \vec{q}, \vec{p}', t,$$

where \vec{k} is the wave vector, with $\vec{k} \parallel \delta \vec{E}$. We will solve equation (4) by the method of successive approximations for the range of wave numbers $k \gg \frac{1}{L}$, i.e., we represent the general solution of this equation as

$$\left(\overline{\delta N_a \delta N_b} \right)_{B_o} = \left(\overline{\delta N_a \delta N_b} \right)_{B_o}^o + \varepsilon \left(\overline{\delta N_a \delta N_b} \right)_{B_o}^1. \quad (5)$$

From (4) and (5), we obtain the following zero and first approximation equations:

$$\hat{A}_o \left(\overline{\delta N_a \delta N_b} \right)_{B_o}^o = -A_3; \quad (6)$$

$$\hat{A}_o \left(\overline{\delta N_a \delta N_b} \right)_{B_o}^1 = \hat{C}_o \left(\overline{\delta N_a \delta N_b} \right)_{B_o}^o; \quad (7)$$

$$\hat{C}_o = \left(\hat{A}_o \frac{i}{2} \right) \left(\frac{\partial^2}{\partial \vec{k} \partial \vec{q}} \right).$$

Let's make variable transformations:

$$\vec{p} \rightarrow \vec{C}_1; \vec{p}' \rightarrow \vec{C}_2 \quad (8)$$

$$\vec{v} \rightarrow \vec{V}_a = \frac{\vec{P}_a}{m_a}. \quad (9)$$

And instead of spectral and single-particle distribution functions, we introduce the following new functions:

$$f_b(\vec{q}, \vec{C}_2, t); f_a(\vec{q}, \vec{C}_1, t); \left(\overline{\delta N_a \delta \vec{E}} \right)_\rho, \left(\overline{\delta N_b \delta \vec{E}} \right)_R, \left(\overline{\delta N_a \delta N_b} \right)_\eta^{0:1}. \quad (10)$$

Let's remind that in (8) – (10) the following notations were used:

$$\begin{aligned} \vec{C}_1 &= \vec{P}_a + e_a \vec{C}_3 & \vec{C}_2 &= \vec{P}_b + e_b \vec{C}_3 & \vec{C}_3 &= -\frac{\vec{E}_o}{\omega_o} \cos \omega_o t \\ \rho &= \vec{k}, \vec{q}, \vec{C}_1, t & R &= \vec{k}, \vec{q}, \vec{C}_2, t & \eta &= \vec{k}, \vec{q}, \vec{C}_1, \vec{C}_2, t \end{aligned}$$

In order to simplify the further calculations and avoid complicating the introduced functions 10) we will separate the slowly changing parts in each of them, which depend only on the slow variables, by $\vec{q}, \vec{P}_a, \vec{P}_b, t$ averaging over the period of external field $\frac{2\pi}{\omega_o}$, i.e.

$$F(\vec{q}, \vec{P}_a, t), F(\vec{q}, \vec{P}_b, t), \left(\overline{\delta N_b \delta \vec{E}} \right)_H, \left(\overline{\delta N_a \delta \vec{E}} \right)_Y, \left(\overline{\delta N_a \delta N_b} \right)_X^{0:1}.$$

Here

$$H = \vec{k}, \vec{q}, \vec{P}_b, t \quad Y = \vec{k}, \vec{q}, \vec{P}_a, t \quad X = \vec{k}, \vec{q}, \vec{P}_a, \vec{P}_b, t.$$

In this case, equations (6) and (7) are written as

$$\hat{C}_4 \left(\overline{\delta N_a \delta N_b} \right)_X^o = -A_4, \quad (11)$$

$$\hat{C}_4 \left(\overline{\delta N_a \delta N_b} \right)_X^1 = -\frac{i}{2} \hat{C}_4 \hat{C}_5, \quad (12)$$

and the solutions of the initial equation (4), according to (5, 11, 12), can be represented as [12]

$$\left(\overline{\delta N_a \delta N_b} \right)_X = \left(\overline{\delta N_a \delta N_b} \right)_X^o + \varepsilon \left(\overline{\delta N_a \delta N_b} \right)_X^1, \quad (13)$$

where

$$\begin{aligned} \vec{C}_4 &= \frac{\partial}{\partial t} + v_o + (V_a + V_b) \frac{\partial}{\partial t} + e_a \vec{E} \frac{\partial}{\partial \vec{P}_a} + e_b \vec{E} \frac{\partial}{\partial \vec{P}_b}; \\ \hat{C}_5 &= \frac{\partial}{\partial \vec{k}} \left(\frac{\partial}{\partial \vec{q}} \left(\overline{\delta N_a \delta N_b} \right)_X^o \right); \\ A_4 &= e_a n_a \left(\overline{\delta N_b \delta \vec{E}} \right)_H \frac{\partial F_a}{\partial \vec{P}_a} + e_b n_b \left(\overline{\delta N_a \delta \vec{E}} \right)_Y \frac{\partial F_b}{\partial \vec{P}_b}. \end{aligned}$$

In the local equilibrium approximation, the solution of equation (11) is written as

$$\left(\overline{\delta N_a \delta N_b} \right)_X^o = -D_o \int_0^\infty \exp(D_2 - D_1) d\tau F_a F_b, \quad (14)$$

where

$$D_o = \frac{e_a e_b n_a n_b}{k_B T_o} \frac{4\pi r_d}{1 + r_d^2 k^2}; \quad D_1 = i \left(\vec{k} \vec{V}_a - \vec{k} \vec{V}_b - i v_o \right);$$

$$D_2 = -i (A_a - A_b) (\sin \omega_o (t - \tau) - \sin \omega_o t); \quad A_{a,b} = \frac{e_{a,b} \vec{k} \vec{E}_o}{m_{a,b} \omega_o^2}.$$

k_B — Boltzmann constant; T_o — the plasma temperature. We solve equation (12) under the condition

$\varepsilon = \frac{V_T}{\omega_o L} \ll 1$ and in the limit $v_o \rightarrow 0$. Using decomposition

$$\begin{aligned} \exp(-i A_{a,b} \sin \omega_o (t - \tau)) &= \sum_{n=-\infty}^{\infty} I_n(A_{a,b}) \exp(-in \omega_o (t - \tau)); \\ \exp(i A_{a,b} \sin \omega_o t) &= \sum_{n=-\infty}^{\infty} I_n(A_{a,b}) \exp(in \omega_o t) \end{aligned}$$

from (12) we get:

$$\langle (\overline{\delta N_a \delta N_b})_X \rangle^1 = -D_o \sum_{n=-\infty}^{\infty} (D_3 + D_4) = -D_o \sum_{n=-\infty}^{\infty} (\eta_1 + \eta_2 + \eta_3), \quad (15)$$

where the symbol $\langle \rangle$ means averaging over the electric field period \vec{E} ; $I_{n,m}(A_{a,b})$ — Bessel functions of order n and m ;

$$\begin{aligned} \eta_1 &= C_6 \frac{\partial F_a}{\partial \vec{P}_a} F_b \vec{f}_a; & \eta_2 &= C_7 \frac{\partial F_b}{\partial \vec{P}_b} F_a \vec{f}_b; & \eta_3 &= C_8 C_9 \\ C_6 &= 2I_n^2(A_b) I_n(A_a) I_n'(A_a); & C_7 &= 2I_n^2(A_a) I_n(A_b) I_n'(A_b); & C_8 &= \{I_n(A_a) I_n(A_b)\}^2; \\ C_9 &= n_a U_a \frac{\partial^2 F_a}{\partial \vec{P}_a \partial \vec{q}} F_b + n_b U_b \frac{\partial^2 F_b}{\partial \vec{P}_b \partial \vec{q}} F_a, \end{aligned}$$

$\vec{f}_{a,b}$ and $U_{a,b}$ — respectively, Miller forces and high-frequency quasi-potential [13]. Thus, the averaged solution of the initial equation (4), according to (13), follows from expressions (14, 15), i.e.

$$\langle (\overline{\delta N_a \delta N_b})_X \rangle = -D_o \sum_{n=-\infty}^{\infty} (D_3 + D_4), \quad (16)$$

where

$$D_3 = C_8 (C_9 + F_a F_b); \quad D_4 = \eta_1 + \eta_2.$$

Using the integral

$$(2\pi)^{-3} \int_{-\infty}^{\infty} (n_a n_b)^{-1} \langle (\overline{\delta N_a \delta N_b})_X \rangle \exp(i\vec{k}\vec{r}) d\vec{k}, \quad (17)$$

we find the averaged two-particle correlation function $\langle g_{ab}^H(\vec{r}, \vec{q}, \vec{E}_o, \vec{P}_a, \vec{P}_b, t) \rangle$ for weakly inhomogeneous plasma in the presence of an external field \vec{E} , i.e.

$$\langle g_{ab}^H \rangle = -\frac{e_a e_b}{k_B T_o r} \sum_{n=-\infty}^{\infty} (D_3 + D_4) \exp(-rr_d^{-1}), \quad (18)$$

where the index “ H ” means “inhomogeneity” of the plasma and field $\vec{E} = \vec{E}_o(\varepsilon \vec{r}, \varepsilon t) \sin \omega_o t$: the field amplitude \vec{E}_o is a slowly varying function in time t (εt) and coordinates \vec{r} ($\varepsilon \vec{r}$). The parameter ε characterizing the slowness of the amplitude change satisfies the condition $\varepsilon = (V_T / \omega_o L) \ll 1$, here V_T — the thermal velocity of electrons; ω_o — frequency; L — characteristic size of change F_e . It should be noted that expression (18) is obtained under the condition

$$L_{\omega_o} = \frac{e_{a,b} E_o}{m_{a,b} \omega_o^2} < r_d,$$

where $r_d \sim \ell_o < \lambda \sim \frac{1}{k}$. From here, L_{ω_o} — the path length of the more movable plasma particles (a or b) over the period T ; ℓ_o — free path length; λ — wave length. With this approach, we can neglect the dependence of the Bessel function, in expression (17), on the wave vector \vec{k} . From formula (18), it follows that for charged particles of the same sign the correlation function is negative, and for particles of different sign is positive. Moreover, g_{ab} is exponentially small when the distance between particles is larger than r_d , i.e. $r > r_d$. Finally, the averaged two-particle distribution functions of coordinates and momenta is determined by the expression:

$$\langle F_{a,b}^H \rangle = F_a F_b - \frac{e_a e_b n_a n_b}{k_B T_o r} \sum_{n=-\infty}^{\infty} (D_3 + D_4) \exp\left(-\frac{r}{r_d}\right). \quad (19)$$

If there is no external field ($\vec{E} = 0$) and the plasma is homogeneous and in equilibrium, we obtain the well-known expression for the functions and from equations (18, 19), where the index “ O ” denotes “homogeneity”.

Conclusions

Thus, in this article, the problem of the interaction of a high-frequency electric field with a weakly inhomogeneous plasma is investigated. In particular, the influence of an external alternating field on the kinetic and high-frequency properties of plasma, such as kinetic equations, correlation functions and distribution functions of charged particles, is considered. Expressions for the simultaneous two-particle correlation function and the corresponding distribution function have been derived using the method of successive approximations. This method separates slow motions and fast oscillations based on the kinetic equation for the spatial-temporal spectral density of fluctuations. The expressions take into account electron-ion collisions and the influence of a strong inhomogeneous electric field. To obtain these results, the kinetic equation for the space-time spectral density of fluctuations and the method of successive approximations (separation of slow movements and fast oscillations) were used. These results may be of interest to researchers working in the field of kinetic theory of plasma and can be applied to the electrons motion theory in high-frequency fields, fluctuations, nonequilibrium processes, stability of inhomogeneous plasma, and other collective and nonlinear phenomena.

References

- 1 Климонтович Ю.Л. О пространственно-временных корреляционных функциях системы частиц с электромагнитным взаимодействием / Ю.Л. Климонтович // ЖЭТФ. — 1958. — 34. — № 1. — С. 173–185.
- 2 Balescu R. Binary correlations in Ionized Gases / R. Balescu, H. Tayler // Phys. of fluids. — 1961. — 4. — No. 1. — P. 85–93. <https://doi.org/10.1063/1.1706191>
- 3 Balescu R. Approach to Equilibrium of a Quantum Plasma / R. Balescu // Phys. of fluids. — 1961. — 4. — No. 1. — P. 94–99. <https://doi.org/10.1063/1.1706193>
- 4 Haim Y. Pair correlations in a two-component plasma / Y. Haim, Sh. Yaakov // Physics review. — 1978. — 18. — P. 1291–1297. <https://doi.org/10.1103/PhysRevA.18.1291>
- 5 James T. Bartis. Correlation function method for the evaluation of plasma transport coefficients: the shear viscosity coefficient / Bartis James T., Oppenheim Irwin // Physics review. — 1974. — 10. — P. 1263–1271. <https://doi.org/10.1103/PhysRevA.10.1263>
- 6 Bobrov V.B. The kinetic equation for plasma with arbitrary strong interaction in a weak electric field / V.B. Bobrov, S.A. Trigger. // Journal of Physics A. — 1992. — 25. — P. 1–18.
- 7 Силин В.П. Кинетическое уравнение для быстропеременных процессов / В.П. Силин // ЖЭТФ. — 1960. — 38. — № 6. — С. 1771–1777.
- 8 Kosarev I.N. Kinetic theory of plasmas and gases. Interaction of high-intensity laser pulses with plasmas / I.N. Kosarev // Achievements of the physical sciences. — 2006. — 49. — No. 12. — P. 1239–1252. DOI: [10.1070/PU2006v049n12ABEH0006027](https://doi.org/10.1070/PU2006v049n12ABEH0006027)
- 9 Alf H. Oien. Kinetic equation for an electron gas in strong fields and inhomogeneities / Oien Alf H. // Journal of Plasma Physics. — 1979. — 21. — No. 3. — P. 401–420. <https://doi.org/10.1017/S0022377800021978>
- 10 Ландау Л.Д. Кинетическое уравнение в случае кулоновского взаимодействия / Л.Д. Ландау // ЖЭТФ. — 1937. — 7. — С. 203.
- 11 Кондратенко А.В. К кинетике кулоновского торможения быстрых электронов в неоднородной плазме / А.В. Кондратенко // Физика плазмы. — 1996. — 22. — № 3. — С. 251–255.
- 12 Balescu R. Irreversible processes in ionized gases / R. Balescu // Physics of fluid. — 1960. — 3. — P. 52–63. <https://doi.org/10.1063/1.1706002>
- 13 Климонтович Ю.Л. Статистическая теория неравновесных процессов в плазме / Ю.Л. Климонтович. — М.: Изд-во Моск. ун-та, 1964. — 281 с.
- 14 Magee R.M. Direct measurements of the ionization profile in krypton helicon plasmas / R.M. Magee, M.E. Galante, N. Gulbrandsen, D.W. McCarren, E.E. Scime // Physics of Plasmas. — 2012. — 19. — 123506. <https://doi.org/10.1063/1.4772060>
- 15 Charles C. An experimental investigation of alternative propellants for the helicon / C. Charles, R.W. Boswell, R. Laine, P. MacLellan // Journal of Physics D: Applied Physics. — 2008. — 6. — P. 175213. DOI [10.1088/0022-3727/41/17/175213](https://doi.org/10.1088/0022-3727/41/17/175213)
- 16 Lafleur T. Detailed plasma potential measurements in a radio-frequency expanding plasma obtained from various electrostatic probes / T. Lafleur, C. Charles, R.W. Boswell // Physics of Plasmas. — 2009. — 16. — P. 044510. DOI: [10.1063/1.3125314](https://doi.org/10.1063/1.3125314)
- 17 Anisimov I.A. Interaction of a modulated electron beam with an in homogeneous plasma: Two-dimensional electrostatic simulations / I.A. Anisimov, T.E. Litoshenko // Physics of Plasmas. — 2008. — 34. — No. 10. — P. 847–854. <https://doi.org/10.1134/s1063780x0810005x>
- 18 Репин А.Ю. Динамика и взаимодействие с преградой тороидального плазменного сгустка. Ионизационно-динамические характеристики и электромагнитное излучение / А.Ю. Репин, Е.Д. Ступицкий, А.В. Шапранов // Теплофизика высоких температур. — 2004. — 42. — № 4. — С. 523–538. <https://doi.org/10.1023/B:HITE.0000039980.35217.cb>

19 Lafleur T. Ion beam formation in a very low magnetic field expanding helicon discharge / T. Lafleur, R.W. Boswell, C. Charles // *Physics of Plasmas*. — 2010. — 17. — P. 043505. <https://doi.org/10.1063/1.3381093>

20 Shaihitdinov R.Z. The Mechanism of Attraction of Negatively Charged Macroparticles in Dusty Plasma / R.Z. Shaihitdinov // *Low-Temperature Plasma in Functional Coating Processes*. — 2014. — 5. — P. 168–171.

21 Kralkina E.A. Radial inhomogeneity of plasma parameters in a low-pressure inductive RF discharge / E.A. Kralkina, P.A. Neklyudova, V.B. Pavlov, K.V. Vavilin, V.P. Tarakanov // *Moscow University Physics Bulletin*. — 2014. — 1. — P. 79–89. DOI: [10.3103/S0027134914010093](https://doi.org/10.3103/S0027134914010093)

22 Алексеев Б.В. Дисперсионные уравнения плазмы в обобщенной бальмановской кинетической теории / Б.В. Алексеев // *Теплофизика высоких температур*. — 2000. — 38. — № 3. — С. 351–357. <https://doi.org/10.1007/BF02755990>

23 Feygin F.Z. Linear theory of slow drift mirror kinetic instability at finite electron temperature / F.Z. Feygin, Yu. G. Khabazin, V.A. Simonenko, A.A. Kondrat'ev // *Geomagnetism and Aeronomy*. — 2009. — 49. — No. 1. — P. 30–41. DOI: [10.1134/S0016793209010046](https://doi.org/10.1134/S0016793209010046)

24 Krasovsky V.L. Calculation of the electron distribution function in a weakly ionized plasma in an electric field / V.L. Krasovsky // *Doklady Physics*. — 2020. — 65. — No. 4. — P. 136–141. doi:10.1134/s1028335820040072

25 Grishkov V.E. Nonlinear currents generated in plasma by a radiation pulse with a frequency exceeding the electron plasma frequency / V.E. Grishkov, S.A. Uryupin // *Plasma Physics Reports*. — 2016. — 42. — No. 9. — P. 870–875. DOI: [10.1134/S1063780X16090038](https://doi.org/10.1134/S1063780X16090038)

Т. Қоштыбаев, М. Алиева

Әлсіз біртексіз плазманың корреляциялық функциялары

Мақала біртексіз плазманың кинетикалық теориясына арналған. Мұнда жоғары жиілікті электр өрісінің әлсіз біртексіз плазмамен әсерлесуіне қатысты мәселе қарастырылған. Нақтырақ айтар болсақ, сыртқы айнымалы өріс плазманың кинетикалық және жоғары жиілікті қасиеттеріне жататын кинетикалық теңдеуге, корреляциялық функцияға және зарядталған бөлшектердің үлестірім функциясына қаншалықты дәрежеде әсер ете алатындығы зерттелген. Жұптық (екі бөлшектік) корреляциялық функция мен оған сәйкес келетін үлестірім функциясына арналған өрнектер шығарылып, көрсетілді. Бұл өрнектерде плазма мен электр өрісінің кеңістіктік біртексіздіктері және зарядталған бөлшектердің соқтығысулары ескерілген. Сонымен бірге, аталған нәтижелерге қол жеткізу үшін флукуациялардың кеңістікті-уақыттық спектрлік тығыздығына арналған кинетикалық теңдеу мен тізбектестік жуықтаулар (баяу қозғалыстар мен шапшаң тербелістерді бөлу) тәсілі қолданылды. Өрістің амплитудасы координаталар және уақыт бойынша баяу өзгермелі функция деп танылады. Жүргізілген барлық есептеулерде электрмагниттік өрістің магниттік құраушысының әсері ескерілген жоқ және бұл жағдай сыртқы электр өрісінің бойлық қасиетіне сәйкес келеді. Аталған барлық нәтижелер теориялық сипатта болғандықтан оларды жоғары жиілікті электрмагниттік өрістердің әсеріндегі біртексіз плазманың кинетикалық теориясын жасау барысында қолдануға болады. Сонымен бірге, алынған нәтижелер электрондардың жоғары жиілікті өрістердегі қозғалыс теориясында, флукуацияларда, тепе-теңсіздік процестерде және басқа да сызықты емес құбылыстарда қолданыла алады. Корреляциялық функция жүйенің реттілік өлшемі болып табылады және ол микроскоптық айнымалылардың әртүрлі нүктелерде әртүрлі уақыт мезеттерінде қалай корреляцияланатынын көрсетеді. Зарядтары аттас бөлшектер үшін корреляция функциясы теріс, ал зарядтарының таңбалары әртүрлі бөлшектер үшін оң мәнді болады. Сонымен бірге, бөлшектердің арақашықтығы Дебайлық радиустан үлкен болған жағдайда корреляциялық функция экспоненталдық заңдылық бойынша кеми береді.

Кілт сөздер: жоғары жиілікті қасиеттер, біртексіз плазма, кинетикалық теңдеу, айнымалы өріс, соқтығысулар интегралы.

Т. Қоштыбаев, М. Алиева

Корреляционные функции слабо неоднородной плазмы

Статья посвящена кинетической теории неоднородной плазмы. Авторами исследована проблема взаимодействия электрического поля высокой частоты со слабо неоднородной плазмой. В частности рассмотрено влияние внешнего переменного поля на кинетические и высокочастотные свойства плазмы, такие как кинетические уравнения, корреляционные функции и функции распределения заряженных частиц. Получены выражения парной (двухчастичной) корреляционной функции и соответствующей функции распределения, учитывающие пространственную неоднородность плазмы и электрического поля, а также столкновения заряженных частиц. Для получения этих результатов

использовались кинетическое уравнение для пространственно-временной спектральной плотности флуктуаций и метод последовательных приближений (разделение медленных движений и быстрых осцилляций). Амплитуда поля является медленно меняющейся функцией по времени и по координатам. Во всех вычислениях пренебрегается вклад магнитной составляющей электромагнитного поля, что вполне справедливо для продольного электрического поля. Все перечисленные результаты, представляющие, прежде всего, теоретический интерес, могут быть применены при построении кинетической теории неоднородной плазмы, находящейся в электромагнитных полях высокой частоты. Кроме того, эти результаты могут быть использованы в теории движения электронов в высокочастотных полях, флуктуаций, неравновесных процессов, устойчивости неоднородной плазмы и в других коллективно-нелинейных явлениях. Корреляционная функция является мерой упорядоченности системы. Она показывает, как микроскопические переменные коррелируют в различные моменты времени в различных точках в среднем. Заметим, что для заряженных частиц одинакового знака функция корреляции отрицательна, а для частиц разного знака — положительна. Кроме того, корреляционная функция экспоненциально мала, когда расстояние между частицами больше радиуса Дебая.

Ключевые слова: высокочастотные свойства, неоднородная плазма, кинетическое уравнение, переменное поле, интеграл столкновений.

References

- 1 Klimontovich, Yu.L. (1958). O prostranstvenno-vremennykh korrelyatsionnykh funktsiiakh sistemy chastits s elektromagnitnym vzaimodeistviem [On the space-time correlation functions of a particle system with electromagnetic interaction]. *Zhurnal eksperimentalnoi i teoreticheskoi fiziki — Journal of Experimental and Theoretical Physics*, 34(1), 173–185 [in Russian].
- 2 Balescu, R., & Tayler, H. (1961). Binary correlations in Ionised Gases. *Physics of fluids*, 4(1), 85–93. <https://doi.org/10.1063/1.1706191>
- 3 Balescu, R. (1961). Approach to Equilibrium of a Quantum Plasma. *Physics of fluids*, 4(1), 94–99. <https://doi.org/10.1063/1.1706193>
- 4 Yatou, Haim, & Shima, Yaakov (1978). Pair correlations in a two-component plasma. *Physics review*, 18, 1291–1297. <https://doi.org/10.1103/PhysRevA.18.1291>
- 5 Bartis, James T., & Oppenheim Irwin (1974). Correlation function method for the evaluation of plasma transport coefficients: the shear viscosity coefficient. *Physics review*, 10, 1263–1271. <https://doi.org/10.1103/PhysRevA.10.1263>
- 6 Bobrov, V.B., & Trigger, S.A. (1992). The kinetic equation for plasma with arbitrary strong interaction in a weak electric field. *Journal of Physics A*, 25, 1–18.
- 7 Silin, V.P. (1960). Kineticheskoe uravnenie dlia bystroperemennykh protsessov [Kinetic equation for fast-changing processes]. *Zhurnal eksperimentalnoi i teoreticheskoi fiziki — Journal of Experimental and Theoretical Physics*, 38, 6, 1771–1777 [in Russian].
- 8 Kosarev, I.N. (2006). Kinetic theory of plasmas and gases. Interaction of high-intensity laser pulses with plasmas. *Achievements of the physical sciences*, 49(12), 1239–1252. DOI:10.1070/PU2006v049n12ABEH006027
- 9 Oien, Alf. H. (1979). Kinetic equation for an electron gas in strong fields and inhomogeneities. *Journal of Plasma Physics*, 21(3), 401–420. <https://doi.org/10.1017/S0022377800021978>
- 10 Landau, L.D. (1937). Kineticheskoe uravnenie v sluchae kulonovskogo vzaimodeistviia [The kinetic equation in the case of Coulomb interaction]. *Zhurnal eksperimentalnoi i teoreticheskoi fiziki — Journal of Experimental and Theoretical Physics*, 7, 203 [in Russian].
- 11 Kondratenko, A.V. (1996). K kinetike kulonovskogo tormozheniia bystrykh elektronov v neodnorodnoi plazme [On the kinetics of Coulomb braking of fast electrons in an inhomogeneous plasma]. *Fizika plazmy — Plasma Physics*, 22(3), 251–255 [in Russian].
- 12 Balescu, R. (1960). Irreversible processes in ionized gases. *Physics of fluid*, 3, 52–63. <https://doi.org/10.1063/1.1706002>
- 13 Klimontovich, Yu.L. (1964). *Statisticheskaiia teoriia neravnovesnykh protsessov v plazme [Statistical theory of nonequilibrium processes in plasma]*. Moscow: Izdatelstvo Moskovskogo universiteta [in Russian].
- 14 Magee, R.M., Galante, M.E., Gulbrandsen, N., McCarren, D.W., & Scime, E.E. (2012). Direct measurements of the ionization profile in krypton helicon plasmas. *Physics of Plasmas*, 19, 123506. <https://doi.org/10.1063/1.4772060>
- 15 Charles, C., Boswell, R.W., Laine, R., & MacLellan, P. (2008). An experimental investigation of alternative propellants for the helicon. *Journal of Physics D: Applied Physics*, 6, 175213. DOI 10.1088/0022-3727/41/17/175213
- 16 Lafleur, T., Charles, C., & Boswell, R.W. (2009). Detailed plasma potential measurements in a radio-frequency expanding plasma obtained from various electrostatic probes. *Physics of Plasmas*, 16, 044510. DOI: 10.1063/1.3125314
- 17 Anisimov, I.A., & Litoshenko, T.E. (2008). Interaction of a modulated electron beam with an in homogeneous plasma: Two-dimensional electrostatic simulations. *Physics of Plasmas*, 34(10), 847–854. <https://doi.org/10.1134/s1063780x0810005x>
- 18 Repin, A.Yu., Stupicki, E.D., & Shapranov, A.V. (2004). Dinamika i vzaimodeistvie s pregradoi toroidalnogo plazmennogo sgustka. Ionizatsionno-dinamicheskie kharakteristiki i elektromagnitnoe izluchenie [Dynamics and interaction with the barrier of a

toroidal plasma clot. Ionization-dynamic characteristics and electromagnetic radiation]. *Teplofizika vysokikh temperatur — High temperature thermophysics*, 42(4), 523–538. <https://doi.org/10.1023/B:HITE.0000039980.35217.cb> [in Russian].

19 Lafleur, T., Boswell, R.W., & Charles, C. (2010). Ion beam formation in a very low magnetic field expanding helicon discharge. *Physics of Plasmas*, 17, 043505. <https://doi.org/10.1063/1.3381093>

20 Shaihitdinov, R.Z. (2014). The Mechanism of Attraction of Negatively Charged Macroparticles in Dusty Plasma. *Low-Temperature Plasma in Functional Coating Processes*, 5, 168–171.

21 Kralkina, E.A., Neklyudova, P.A., Pavlov, V.B., Vavilin, K.V., & Tarakanov, V.P. (2014). Radial inhomogeneity of plasma parameters in a low-pressure inductive RF discharge. *Moscow University Physics Bulletin*, 1, 79–89. DOI: [10.3103/S0027134914010093](https://doi.org/10.3103/S0027134914010093)

22 Alekseev, B.V. (2000). Dispersionnyye uravneniia plazmy v obobshchennoi boltsmanovskoi kineticheskoi teorii [Plasma dispersion equations in generalized Boltzmann kinetic theory]. *Teplofizika vysokikh temperatur — High temperature thermophysics*, 38(3), 351–357. <https://doi.org/10.1007/BF02755990> [in Russian].

23 Feygin, F.Z., Khabazin, Yu.G., Simonenko, V.A., & Kondrat'ev, A.A. (2009). Linear theory of slow drift mirror kinetic instability at finite electron temperature. *Geomagnetism and Aeronomy*, 49(1), 30–41. DOI: [10.1134/S0016793209010046](https://doi.org/10.1134/S0016793209010046)

24 Krasovsky, V.L. (2020). Calculation of the electron distribution function in a weakly ionized plasma in an electric field. *Doklady Physics*, 65(4), 136–141. doi:10.1134/s1028335820040072

25 Grishkov, V.E., & Uryupin, S.A. (2016). Nonlinear currents generated in plasma by a radiation pulse with a frequency exceeding the electron plasma frequency. *Plasma Physics Reports*, 42(9), 870–875. DOI: [10.1134/S1063780X16090038](https://doi.org/10.1134/S1063780X16090038)

Information about the authors

Koshtybayev, Talgat — Candidate of physical and mathematical sciences, Associate Professor, Department of Physics, Kazakh National Women's Pedagogical University, Almaty, Kazakhstan; e-mail: koshtybayev70@mail.ru; ORCID ID: <https://orcid.org/0009-0004-7344-6801>

Aliyeva, Moldir — Master of sciences, Senior lecturer, Department of Physics, Abai Kazakh National Pedagogical University, Almaty, Kazakhstan; e-mail: moldir-2008@mail.ru; ORCID ID: <https://orcid.org/0000-0003-0440-6211>

G.W. Beall¹, D.S. Akhmetsadyk^{2*}, A.M. Ilyin², M.A. Tulegenova²

¹Materials Science, Engineering, and Commercialization, Texas State University, San Marcos, TX 78666, USA;

²Department of Physics and Technology, Al-Farabi Kazakh National University, Almaty, 050000, Kazakhstan

*Corresponding author's e-mail: d.akhmetsadyk@gmail.com

First-principles study of O₃ molecule adsorption on pristine, N, Ga-doped and -Ga-N- co-doped graphene

Abstract. The adsorption of O₃ molecules (ozone) on graphene, N-doped graphene, Ga-doped graphene, and -Ga-N- co-doped graphene with an emphasis on O₃ detection was examined in this work. The physical characteristics of -Ga-N-co-doped graphene are significantly altered upon O₃ adsorption, which makes it a suitable choice for O₃ detection molecular sensors. The interaction between the O₃ molecule and the adsorbent is explained on the basis of their adsorption energy, adsorption distance and charge transfer. It was found that the adsorption of ozone molecules on the -Ga-N- co-doped graphene was more favorable in energy than that on the pristine one, representing the superior sensing performance of -Ga-N- co-doped system. In our work, we estimated the charge transfer between the O₃ molecule and doped graphene nanostructures based on Mulliken population analysis. The calculated adsorption energy value shows the ozone molecule more firmly adsorbs on the surface of -Ga-N- co-doped graphene nanostructures ($E_{\text{ads}} = -1.74$ eV) than that of pristine graphene ($E_{\text{ads}} = -0.41$ eV), deriving from a stronger covalent bond between the ozone molecule and the -Ga-N- co-doped graphene nanostructures. Our findings thus suggest that -Ga-N- co-doped graphene could be a highly efficient gas sensor device for O₃ detection in the environment.

Keywords: graphene, O₃ adsorption, density functional theory, N-doped graphene, Ga-doped graphene, -Ga-N- co-doped graphene, gas sensor, graphene-based sensors.

Introduction

Environmental pollution is a major concern today due to the increasing number of industrial processes, vehicle exhaust, electronic devices, and human activity, which has led to an urgent need for sensors that are sensitive, responsive, selective, and easy to recover. Sensing gases involving O₃ is crucial for improving home security and keeping the environment healthy, as well as for regulating emissions from vehicles and industries.

Ozone (O₃) is a molecule made up of three oxygen atoms [1], the color is colorless to pale blue. The odor of ozone is pungent and highly flammable. Ozone is found in different layers of the Earth's atmosphere. The majority of ozone resides in the stratosphere. Ozone is a protective layer that shields against harmful ultraviolet radiation hitting the earth. However, the ozone layer we breathe at ground level is dangerous. It forms through chemical reactions between oxides of nitrogen (NO_x) and volatile organic compounds (VOC) in the presence of sunlight [2]. It can have harmful effects on human health, causing respiratory problems. It also has detrimental impacts on vegetation and ecosystems. Therefore, various types of sensors, including graphene-based sensors, are used to measurement of a sensor response to ozone [3, 4].

Graphene-based sensors operate on the principle that the electrical conductivity of graphene can be influenced by the presence of certain gases, including ozone. When ozone molecules come into contact with graphene, they can either donate or accept electrons, leading to changes in the electrical properties of the graphene. This change in conductivity can be measured and correlated with the concentration of ozone in the surrounding environment [5].

Since the graphene discovered by brilliant and curious scientists as Andre Geim and Konstantin Novoselov, the area of two-dimensional (2D) nanomaterials have undergone rapid development, owing to their potential applications in various fields. Applications covered include: electronics [6], optoelectronics [7] and sensors [8], coatings [9], adhesives [10], lubricants [11], energy storage [12] and energy generation [13, 14] composites [15] and plastics [16], membranes [17] and filtration [18], life science [19] and biomedicine [20], construction materials [21], 3D printing/additive manufacturing [22] and much more.

Graphene nanostructures are very sensitive to many surface atoms because their two-dimensional structure means the entire material volume acts as a sensor surface. This makes them sensitive to external environments, such as temperature, electrical signals, chemicals, magnetism and biological agents [23–27]. Besides, to its sensitivity, graphene provides excellent mechanical strength, flexibility, thermal and electrical

conductivity, and compactness. Properties that make graphene attractive for sensor applications: ultra-high charge mobility, transparency, non-toxicity, high-tensile strength, high thermal conductivity, multi-functionality. The technique that graphene devices function as gas sensors is based on how surface adsorbates, which have specific adsorption sites and a chemical structure that makes them either donors or acceptors, change the electrical conductivity of the device [28, 29].

Graphene, graphene oxide (GO) and their related modified nanomaterials exhibit superior performances in the adsorption of environmental pollutants [30]. Despite its remarkable properties, graphene does have some drawbacks, and doping can address these limitations. Pristine graphene lacks a band gap, which can limit its use in certain electronic applications. Doping can be employed to open a band gap and make it more suitable for electronic devices, such as sensors. Also, doped graphene can exhibit enhanced sensitivity in gas sensing applications. Presently, a large number of studies reported on graphene doping to enhance electronic properties, where researchers introduce foreign atoms into the graphene lattice by replacing carbon atoms [31–34]. The toxic gases were often found to have adsorbed more strongly on doped graphene than on pristine graphene, based on the adsorption energies of the gases. This suggests that doped graphene sheets would make effective toxic gas sensors [35]. We choose nitrogen as a representative dopant in graphene depending on the dominant type of nitrogen functional group in which the planar nature of graphene is not disturbed. In comparison to a carbon atom, a nitrogen atom contains one additional electron and is similar in size [36], which is close to that of the carbon atom. Additionally, atoms of nitrogen and carbon can combine to create strong bonds [37]. A more stable structure may emerge in this way. We have also considered gallium (from group IIIA) atom. It is known that replacing a carbon atom in graphene with gallium is a useful way to improve the electronic properties sensing ability [38]. The advantage of choosing gallium as a potential dopant metal is its weak chemical interaction with graphene, which preserves the integrity of the graphene lattice. Multiple heteroatom co-doping has gained popularity recently because it gives an original, synergistically connected electronic structure. In an interesting study conducted by [39] the electronic properties of graphene has been tuned by nitrogen and sulfur co-doping with appropriate doping atom concentration. In another study by X. Yan and co-authors [40] have been investigated multiple transition metal atoms co-doped with graphene in different doping ways to study the effect on SO_2 gas. The results indicate that both Ti-doped as well as Co and Ti co-doped graphene are ideal for SO_2 sensors. Recently, our study [41] have examined that the addition of gallium and nitrogen atoms drastically changes the electronic structure of graphene and may be a good candidate for sensing this toxic gas SO_2 . However, only a few reports about the -Ga-N- co-doping effect on the electronic properties of graphene. Therefore, in this paper, we also suggest to evaluate the adsorption behavior of -Ga-N- co-doped graphene.

It is thought that atomic-level awareness of condensed matter characteristics may be achieved by cutting-edge computer simulations. In the simulation, a real system has been created and its attributes are explored by the simulator. Research using simulations is analogous to experiments in numerous ways. On the other hand, full control over the experimental configurations and detailed access to findings are made possible because of simulations. These advantages make it possible to calculate first-principles material properties in light of the fundamental physics outlined in the Schrödinger equation without free parameters [29].

In materials science, density functional theory (DFT) has become a powerful tool for tackling a variety of issues [42]. DFT is today the most widely used method to study interacting electrons, and its applicability ranges from atoms to solid systems, from nuclei to quantum fluids. In the literature on DFT, the importance of computational approaches for 2D materials research is studied [43]. When it comes to doping graphene, density functional theory calculations play an increasingly important role in predicting and explaining the effects of doping on the electronic and structural properties of graphene-based materials. DFT calculations can be used to determine the binding energies between graphene and dopant atoms. This information is valuable for assessing the strength of the interaction and stability of the doped graphene system. DFT predictions guide experimentalists and researchers in designing and synthesizing doped graphene materials with desired electronic properties. This helps to save time and resources by narrowing down the search for optimal doping strategies.

For literature review, we reviewed different works related to adsorption of ozone molecule. Almost 20 years ago, researchers (2004) reported the feasibility of CNT film as an ozone sensor through first-principles calculations, centred around the interaction of O_3 with carbon nanotubes (CNTs) [44]. Moreover, in another research, ozone (O_3) adsorption on pristine Stone–Wales (SW) defective BC3 graphene-like sheets was investigated using density functional calculations and it was found that O_3 is weakly adsorbed on the pristine sheet [45]. The study of M. Vahdat and co-workers [46] reported about mechanistic insights on functionali-

zation of graphene with ozone. Their calculations highlights that O₃ is extremely attractive to functionalize graphene even at room temperature.

However, as far as we know, Ga-doped graphene and co-doped graphene by gallium and nitrogen atoms have not been reported for adsorption of O₃ molecule. In this work, the adsorption of O₃ molecule on the surface of pristine, N- and Ga- and co-doped by -Ga-N- graphene has been calculated using the state-of-the-art DFT simulation. The charge transfer between them and the density of states of the systems were studied in order to determine their interactions. This study is our starting point for future theoretical and experimental studies. We hope that it would be helpful for the both experimental and theoretical research groups that have been working on the development of graphene based sensors.

Computational details

All calculations have been carried out using spin unrestricted DFT framework as implemented in Dmol³ module [47] to study the interactions between the O₃ molecules and pristine, N-doped graphene, Ga-doped graphene and -Ga-N- co-doped graphene. It is widely recognized that simulations limited to the local density approximation (LDA) underestimate equilibrium distances and overestimate bond energy E_b [48]. Therefore, we used the generalized gradient approximation (GGA) for improving the total energy, atomization energy and energy barrier. The Perdew-Burke-Ernzerhof (PBE) functional within GGA was taken to describe the exchange–correlation interaction [43, 49]. The DFT semi-core pseudopotential (DSPP) for core treatment with double numerical basis set plus polarization (DNP) basis set have been employed [50]. To ensure that the results of the calculations were comparable, identical conditions had been employed for graphene, the nitrogen doped graphene, the gallium doped graphene and also graphene co-doped by gallium and nitrogen system. The energy tolerance, maximum force and displacement convergence were set at 2×10^{-5} Ha, 0.004 Ha/Å and 0.005 Å respectively. The smearing technique was applied to the occupied orbitals with a smearing value of 0.005 Ha (1 Ha = 27.2114 eV). And a real space global cut off radius of 4.5 Å was employed. The Mulliken charge analysis computing procedure is used to find out the charge transfer values between the substrate and adsorbate.

To understand the interaction between the O₃ molecule and four systems, the adsorption energy was calculated by equation

$$E_{ads} = E_{graphene+gas} - E_{graphene} - E_{gas}, \quad (1)$$

where $E_{graphene+gas}$ is the total energy of graphene with adsorbed molecule, $E_{graphene}$ is the total energy of graphene, E_{gas} is the total energy of the molecule.

Results and Discussion

Properties of the Structure: We start first calculating with the geometric structure of O₃ was optimized to their steadiest configuration before studying their adsorption. Figure 1 displays the structure, and the information of bond lengths and angles are shown in Table 1.

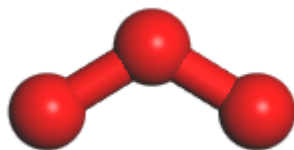


Figure 1. Structures of molecule O₃

Table 1

Structural parameters of structure

Gas molecule	Bond	Length (Å)	Angle (°)
O ₃	O-O	1.27	116.8

Geometry of Pristine Graphene and Doped Graphene: The optimized structure of graphene consists of 50 C atoms. The final configuration is shown in Figure 2. The C–C bond length calculated after optimization is found to be 1.42 Å, which agrees well with previous reports [51, 52].

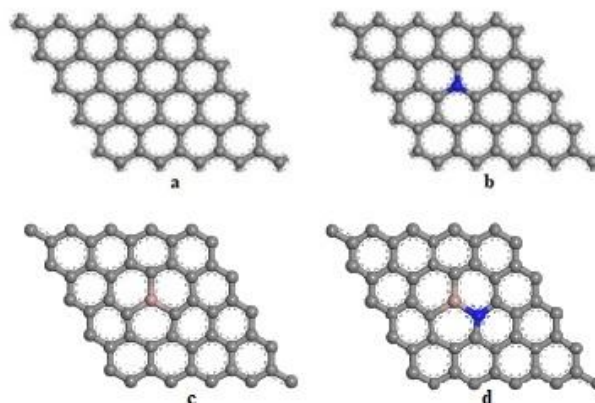


Figure 2. Relaxed geometries of 5×5 supercell of pristine graphene (a), where the carbon atoms are shown in grey and nitrogen-doped graphene (b), where the nitrogen atom is shown in blue; gallium-doped graphene (c), where the gallium atom is shown in pink; graphene co-doped by gallium and nitrogen atoms (d)

Adsorption of O₃ on Pristine Graphene: After that, we investigated the configuration of the O₃ molecule adsorbed on pristine graphene. The optimized structure for the adsorption of the O₃ molecule on pristine is shown in Figure 3. After optimization, the ozone molecule is positioned parallel above the graphene plane. The corresponding geometrical parameters, the adsorption parameters, and the charge transfer of the graphene + gas system are listed in Table 2.

In fact, the O-O distance (=1.27 Å) increases upon adsorption. Meanwhile, it should be noted that the optimized geometry of O₃ molecules on pristine graphene and found physisorption of the molecules due to the inert graphene surface. The results from other authors [46] agree with our results. This indicates that the pristine graphene is insensitive to O₃ molecules.

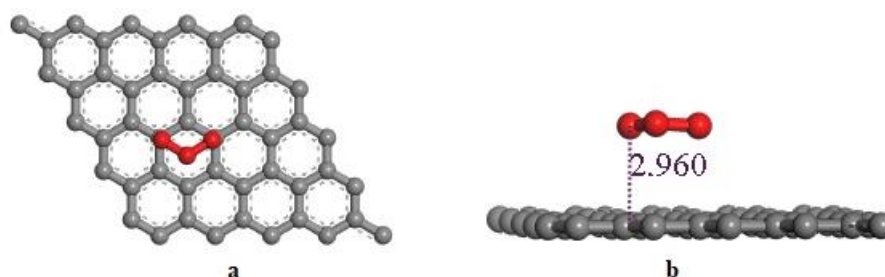


Figure 3. The top view (a) and side view (b) of graphene + O₃ system

Table 2

The detailed parameters of graphene+ gas system

System	Adsorption Distance (Å)	Bond Length (Å)	Bond Angle (°)	E_{ads} (eV)	Q_T (e)
Graphene +O ₃	2.96	1.31 (O ₁ -O ₂) 1.31 (O ₂ -O ₃)	116.8	-0.41	-0.259

Adsorption of O₃ on N-Doped Graphene: The carbon atom of graphene was replaced with the nitrogen atom to find a highly sensitive nanostructure, and the new structure was optimized. The adsorption of the O₃ molecule on N-doped graphene was studied, and the optimized geometry of the N-doped graphene+O₃ system is displayed in Figure 4. After optimization, the ozone molecule is positioned with a tilted \wedge orientation above the graphene plane. The adsorption of the O₃ molecule on N-doped graphene is weak, so the interaction was not affected by the doped nitrogen atom. The ozone molecule is found physisorbed at a distance of 3.07 Å. Surprisingly, the energy adsorption between ozone molecules and nitrogen-doped graphene had a higher value.

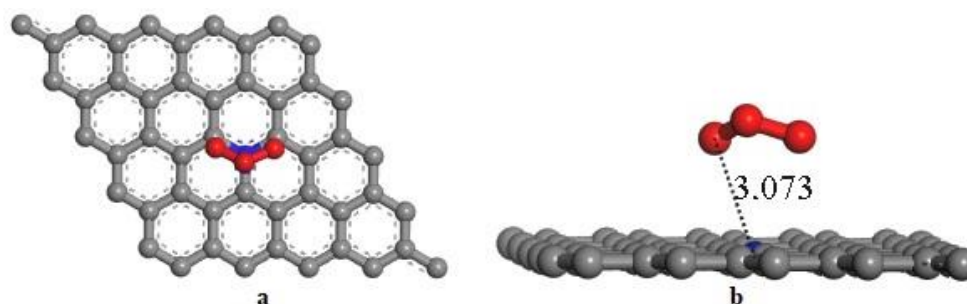
Figure 4. The top view (a) and side view (b) of nitrogen-doped graphene + O₃ system

Table 3

The detailed parameters of nitrogen-doped graphene+ gas system

System	Adsorption Distance (Å)	Bond Length (Å)	Bond Angle (°)	E_{ads} (eV)	Q_T (e)
Nitrogen-doped graphene + O ₃	3.07	1.32 (O ₁ -O ₂) 1.32(O ₂ -O ₃)	116.4	-0.73	-0.404

Adsorption of O₃ on Ga-Doped Graphene: The optimized geometry for the Ga-doped graphene + O₃ system is displayed in Figure 5. In this case, the larger atomic radius of the Ga atom results in a bond length value of 1.86 Å, which is longer than the C–C bond length in pristine graphene. The data conforms properly with the earlier report [53]. The corresponding distance between the O₃ molecule and Ga atom in the Ga-doped graphene is shorter than in the pristine graphene system. Moreover, the adsorption energy of the O₃ molecule in the Ga-doped graphene system is slightly larger than that of the O₃ molecule in the pristine graphene system. Furthermore, to investigate the changes in electronic structures in graphene caused by the physical or chemisorption of O₃ molecules, the net electron transfer (Q_T) from either the pristine or the Ga-doped graphene to the O₃ molecules was by Mulliken analysis, where Q_T is defined as the charge variation caused by the O₃ absorption. The Mulliken atomic charge analysis of the structure shows that charge transfers from doped graphene sheets to O₃ molecules. The electron transfer in the Ga-doped graphene is slightly larger than in the pristine graphene. The results, as shown in Table 4, indicate that graphene doped with gallium atom is much more sensitive to adsorption of molecule. This supports the notion that Ga doping influences the electronic properties of graphene substantially.

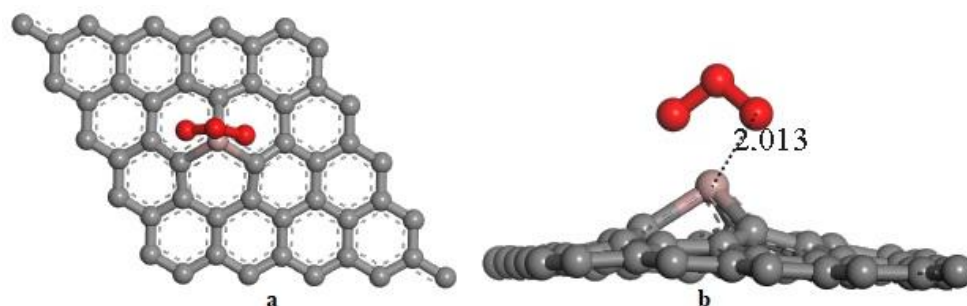
Figure 5. The top view (a) and side view (b) of gallium-doped graphene + O₃ system

Table 4

The detailed parameters of the Ga-doped graphene+ gas system

System	Adsorption Distance (Å)	Bond Length (Å)	Bond Angle (°)	E_{ads} (eV)	Q_T (e)
Ga-doped graphene + O ₃	2.01	1.36 (O ₁ -O ₂) 1.38 (O ₂ -O ₃)	107.5	-0.54	-0.48

Adsorption of O₃ on -Ga-N- co-doped graphene: Three different positions of the O₃ molecule on the -Ga-N- co-doped graphene were taken into consideration to investigate the adsorption behavior of the O₃ molecule and find the most favorable position: the bond-bridge (B-site), the center of the hollow (H-site),

and the center of the top (T-site). The optimized geometries with adsorption distance of all configurations were illustrated in Figure 6. For all configurations, the negative adsorption energies were found which indicate an attractive interaction between the ozone molecule and graphene co-doped by gallium and nitrogen. All adsorption sites of the O_3 molecule are preferred to adsorb with -1.46 eV, -1.74 eV and -1.49 eV at a distance 1.84 Å, 1.95 Å and 1.86 Å from the -Ga-N- co-doped graphene, respectively. The adsorption energies depend on the interaction distance. The adsorption energy is greatly increased with the reduced of interaction distance between the O_3 molecule and -Ga-N- co-doped graphene. This indicates that the adsorption site (H-site) shown in Figure 6 (c-d) is the most stable position with the strongest interaction between the O_3 molecule and graphene co-doped by gallium and nitrogen. The ozone molecule is positioned with a titled Λ orientation above the graphene co-doped by gallium and nitrogen. Based on adsorption energy values in Table 5, the ozone molecule has more interaction with co-doped graphene by gallium and nitrogen atoms.

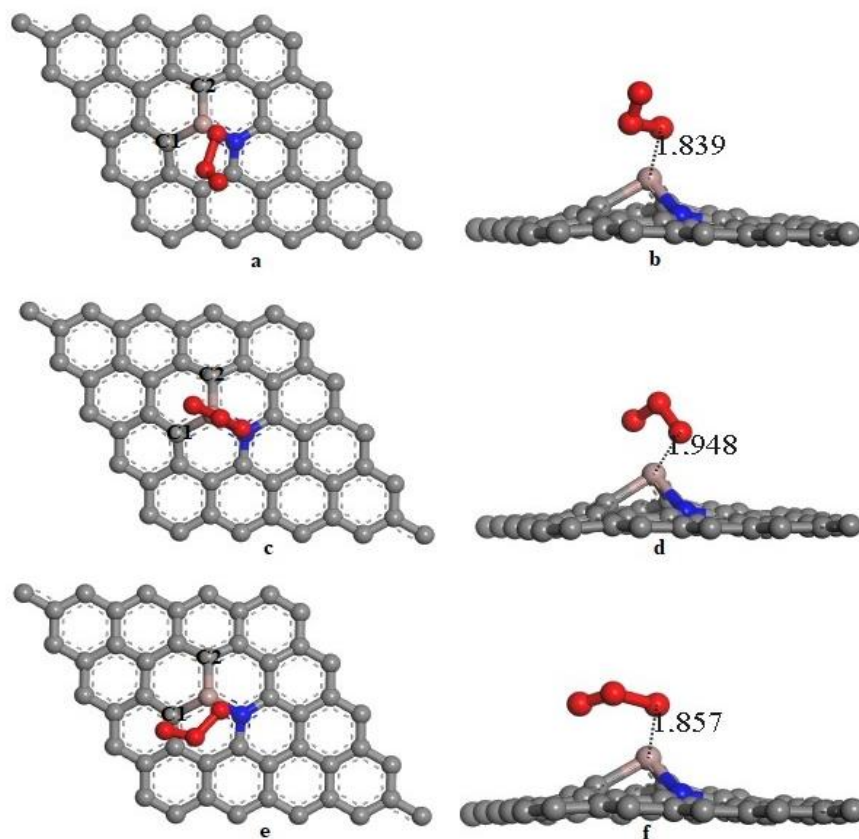


Figure 6. The top view (a) and side view (b) of -Ga-N- co-doped graphene+ O_3 system in the B site; the top view (c) and side view (d) of -Ga-N- co-doped graphene+ O_3 system in the H site; the top view (e) and side view (f) of -Ga-N- co-doped graphene+ O_3 system in the T site.

Table 5

The detailed parameters of the -Ga-N- co-doped graphene + gas system

System	Adsorption Site	Adsorption Distance (Å)	Bond Types (Å)	Bond Length (Å)	Bond Angle (°)	E_{ads} (eV)	Q_T (e)
-Ga-N- co-doped graphene + O_3	B	1.84	1.96 (Ga-N)	1.24 (O_1-O_2) 1.61 (O_2-O_3)	111.6	-1.46	-0.468
	H	1.95	2.03 (Ga-N)	1.36 (O_1-O_2) 1.41 (O_2-O_3)	107.2	-1.74	-0.53
	T	1.86	1.95 (Ga-N)	1.27 (O_1-O_2) 1.56 (O_2-O_3)	113.6	-1.49	-0.504

Before optimization, the bond length between gallium and nitrogen atoms was 1.420 Å. Meanwhile, due to the co-doping of the Ga and N atoms, the stress of the two C atoms around it in the system changed, caus-

ing them to move away from their original positions. For instance, B site: C₁-Ga = 1.892 Å, C₂-Ga = 1.891 Å. We found that the bond length of Ga-N was 1.967 Å, while the angles of C₁-Ga-C₂, C₂-Ga-N, and C₁-Ga-N were 96.8°, 92.3° and 91.8°, respectively. H-site: C₁-Ga = 1.911 Å, C₂-Ga = 1.911 Å. We observed that the bond length of Ga-N was 2.027 Å, while the angles of C₁-Ga-C₂, C₂-Ga-N, and C₁-Ga-N were 99.6°, 88.8° and 88.7°, respectively. T-site: C₁-Ga = 1.885 Å, C₂-Ga = 1.887 Å. In this position, we found that the bond length of Ga-N was 1.956 Å, while the angles of C₁-Ga-C₂, C₂-Ga-N, and C₁-Ga-N were 94.6°, 92.9° and 92.5°, respectively. As seen in Table 5, we found that all initial B, H, and T configurations are almost changed. After optimization, the configurations do not keep their original adsorption site. The results of the adsorption energy indicate that the adsorption on the H site is the most stable configuration, and the stability order is H > T > B.

Summary and Conclusions

In summary, in this work, we conducted a study based on density functional theory (DFT) calculations to investigate of adsorption ozone molecule on pristine, N-, Ga-doped graphene, and -Ga-N- co-doped graphene. The adsorption geometries, adsorption energies, and charge transfer analysis are obtained. The O₃ molecule showed physisorption on pristine graphene with low adsorption energies and little charge transfer, which suggests that the unmodified graphene material. The adsorption of O₃ on the N-doped graphene was slightly stronger, which had an adsorption energy of (−0.73 eV) and little charge transfer. The adsorption energy of O₃ on the Ga-doped graphene (−0.54 eV) was much lower than on N-doped graphene. The N doping improved the interactions between the gas, while the Ga doping had no significant effect on the interactions. In particular, the Ga doping of graphene significantly enhanced the adsorption of ozone molecules relative to pristine graphene. However, -Ga-N- co-doped graphene demonstrates high adsorption energy to ozone molecules (adsorption energy of −1.74 eV) that corresponds to the chemisorption. Thus, -Ga-N- co-doped graphene is of great interest for gas sensing applications since it has stronger interactions with the O₃ molecules than other structures discussed in the paper.

References

- 1 Zhang, J., Wei, Y., & Fang, Z. (2019). Ozone Pollution: A Major Health Hazard Worldwide. *Front. Immunol.*, *10*, 2518, doi:10.3389/fimmu.2019.02518.
- 2 Manisalidis, I., Stavropoulou, E., Stavropoulos, A., & Bezirtzoglou, E. (2020). Environmental and Health Impacts of Air Pollution: A Review. *Front. Public Health*, *8*, 14, doi:10.3389/fpubh.2020.00014.
- 3 Novikov, S., Hämäläinen, J., Walden, J., Iisakka, I., Lebedeva, N., & Satrapinski, A. (2013). Characterization of Epitaxial and CVD Graphene with Double Metal-Graphene Contacts for Gas Sensing. In *Proceedings of the 16th International Congress of Metrology*. EDP Sciences: Paris, France, 13003.
- 4 De Lima, B.S., Komorizono, A.A., Silva, W.A.S., Ndiaye, A.L., Brunet, J., Bernardi, M.I.B., & Mastelaro, V.R. (2021). Ozone Detection in the Ppt-Level with rGO-ZnO Based Sensor. *Sensors and Actuators B: Chemical*, *338*, 129779, doi:10.1016/j.snb.2021.129779.
- 5 Chung, M.G., Kim, D.H., Lee, H.M., Kim, T., Choi, J.H., Seo, D.K., Yoo, J.-B., Hong, S.-H., Kang, T.J., & Kim, Y.H. (2012). Highly Sensitive NO₂ Gas Sensor Based on Ozone Treated Graphene. *Sensors and Actuators B: Chemical*, *166-167*, 172–176, doi:10.1016/j.snb.2012.02.036.
- 6 Šiškins, M., Mullan, C., Son, S.-K., Yin, J., Watanabe, K., Taniguchi, T., Ghazaryan, D., Novoselov, K.S., & Mishchenko, A. (2019). High-Temperature Electronic Devices Enabled by hBN-Encapsulated Graphene. *Applied Physics Letters*, *114*, 123104, doi:10.1063/1.5088587.
- 7 Ubrig, N., Ponomarev, E., Zultak, J., Domaretskiy, D., Zólyomi, V., Terry, D., Howarth, J., Gutiérrez-Lezama, I., Zhukov, A., & Kudrynskiy, Z.R., et al. (2020). Design of van Der Waals Interfaces for Broad-Spectrum Optoelectronics. *Nat. Mater.*, *19*, 299–304, doi:10.1038/s41563-019-0601-3.
- 8 He, P., Brent, J.R., Ding, H., Yang, J., Lewis, D.J., O'Brien, P., & Derby, B. (2018). Fully Printed High Performance Humidity Sensors Based on Two-Dimensional Materials. *Nanoscale*, *10*, 5599–5606, doi:10.1039/C7NR08115D.
- 9 Park, J.B., Kim, Y.-J., Kim, S.-M., Yoo, J.M., Kim, Y., Gorbachev, R., Barbolina, I.I., Kim, S.J., Kang, S., & Yoon, M.-H., et al. (2016). Non-Destructive Electron Microscopy Imaging and Analysis of Biological Samples with Graphene Coating. *2D Mater.*, *3*, 045004, doi:10.1088/2053-1583/3/4/045004.
- 10 Huang, Y., Xia, T., Kinloch, I., & Vallés, C. (2023). Graphene Nanoplatelets/Epoxy Nanocomposites as Conductive Adhesives for out-of-Autoclave in-Situ CFRPs Repair. *Composites Science and Technology*, *237*, 110007, doi:10.1016/j.compscitech.2023.110007.

- 11 Li, X., Zhang, D., Xu, X., & Lee, K.-R. (2020). Tailoring the Nanostructure of Graphene as an Oil-Based Additive: Toward Synergistic Lubrication with an Amorphous Carbon Film. *ACS Appl. Mater. Interfaces*, *12*, 43320–43330, doi:10.1021/acsami.0c12890.
- 12 Sathishkumar, N., Wu, S., & Chen, H. (2019). Boron- and Nitrogen-doped Penta-graphene as a Promising Material for Hydrogen Storage: A Computational Study. *Int J Energy Res*, *43*, 4867–4878, doi:10.1002/er.4639.
- 13 Karmakar, S., Mistari, C.D., Shajahan, A.S., More, M.A., Chakraborty, B., & Behera, D. (2021). Enhancement of Pseudocapacitive Behavior, Cyclic Performance, and Field Emission Characteristics of Reduced Graphene Oxide Reinforced NiGa₂O₄ Nanostructured Electrode: A First Principles Calculation to Correlate with Experimental Observation. *J. Phys. Chem. C*, *125*, 7898–7912, doi:10.1021/acs.jpcc.0c11529.
- 14 Ye, M., Zhang, Z., Zhao, Y., & Qu, L. (2018). Graphene Platforms for Smart Energy Generation and Storage. *Joule*, *2*, 245–268, doi:10.1016/j.joule.2017.11.011.
- 15 Wijerathne, D., Gong, Y., Afroj, S., Karim, N., & Abeykoon, C. (2023). Mechanical and Thermal Properties of Graphene Nanoplatelets-Reinforced Recycled Polycarbonate Composites. *International Journal of Lightweight Materials and Manufacture*, *6*, 117–128, doi:10.1016/j.ijlmm.2022.09.001.
- 16 Chortarea, S., Kuru, O.C., Netkueakul, W., Pelin, M., Keshavan, S., Song, Z., Ma, B., Gomes, J., Abalos, E.V., Lu, L.A.V.D., et al. (2022). Hazard Assessment of Abraded Thermoplastic Composites Reinforced with Reduced Graphene Oxide. *Journal of Hazardous Materials*, *435*, 129053, doi:10.1016/j.jhazmat.2022.129053.
- 17 McNair, R., Cseri, L., Szekely, G., & Dryfe, R. (2020). Asymmetric Membrane Capacitive Deionization Using Anion-Exchange Membranes Based on Quaternized Polymer Blends. *ACS Appl. Polym. Mater.*, *2*, 2946–2956, doi:10.1021/acsapm.0c00432.
- 18 Schmidt, S.J., Dou, W., & Sydlík, S.A. (2023). Regeneratable Graphene-Based Water Filters for Heavy Metal Removal at Home. *ACS EST Water*, *3*, 2179–2185, doi:10.1021/acsestwater.3c00010.
- 19 Peña-Bahamonde, J., Nguyen, H.N., Fanourakis, S.K., & Rodrigues, D.F. (2018). Recent Advances in Graphene-Based Biosensor Technology with Applications in Life Sciences. *J Nanobiotechnol*, *16*, 75, doi:10.1186/s12951-018-0400-z.
- 20 Li, J., Zeng, H., Zeng, Z., Zeng, Y., & Xie, T. (2021). Promising Graphene-Based Nanomaterials and Their Biomedical Applications and Potential Risks: A Comprehensive Review. *ACS Biomater. Sci. Eng.*, *7*, 5363–5396, doi:10.1021/acsbomaterials.1c00875.
- 21 Asim, N., Badiei, M., Samsudin, N.A., Mohammad, M., Razali, H., Soltani, S., & Amin, N. (2022). Application of Graphene-Based Materials in Developing Sustainable Infrastructure: An Overview. *Composites Part B: Engineering*, *245*, 110188, doi:10.1016/j.compositesb.2022.110188.
- 22 Li, Y., Feng, Z., Huang, L., Essa, K., Bilotti, E., Zhang, H., Peijs, T., & Hao, L. (2019). Additive Manufacturing High Performance Graphene-Based Composites: A Review. *Composites Part A: Applied Science and Manufacturing*, *124*, 105483, doi:10.1016/j.compositesa.2019.105483.
- 23 Han, R., Wang, L., Tang, X., Qian, J., Yu, J., Chen, X., & Huang, Y. (2021). Facile Fabrication of rGO/LIG-Based Temperature Sensor with High Sensitivity. *Materials Letters*, *304*, 130637, doi:10.1016/j.matlet.2021.130637.
- 24 Goodrum, R., Weldekidan, H., Li, H., Mohanty, A.K., & Misra, M. (2023). Graphene-Based Nanostructures from Green Processes and Their Applications in Biomedical Sensors. *Advanced Industrial and Engineering Polymer Research*, *S2542504823000179*, doi:10.1016/j.aiepr.2023.03.001.
- 25 Ananda Murthy, H.C., Gebremedhn Kelele, K., Ravikumar, C.R., Nagaswarupa, H.P., Tadesse, A., & Desalegn, T. (2021). Graphene-Supported Nanomaterials as Electrochemical Sensors: A Mini Review. *Results in Chemistry*, *3*, 100131, doi:10.1016/j.rechem.2021.100131.
- 26 Shukla, V. (2020). Observation of Critical Magnetic Behavior in 2D Carbon Based Composites. *Nanoscale Adv.*, *2*, 962–990, doi:10.1039/C9NA00663J.
- 27 Bai, Y., Xu, T., & Zhang, X. (2020). Graphene-Based Biosensors for Detection of Biomarkers. *Micromachines*, *11*, 60, doi:10.3390/mi11010060.
- 28 Demon, S.Z.N., Kamisan, A.I., Abdullah, N., Noor, S.A.M., Khim, O.K., Kasim, N.A.M., Yahya, M.Z.A., Manaf, N.A.A., Azmi, A.F.M., & Halim, N.A. (2020). Graphene-Based Materials in Gas Sensor Applications: A Review. *Sensors and Materials*, *32*, 759, doi:10.18494/SAM.2020.2492.
- 29 Ao, Z., Yang, J., & Li, S. (2011). Applications of Al Modified Graphene on Gas Sensors and Hydrogen Storage. In *Physics and Applications of Graphene — Theory*; Mikhailov, S., Ed.; InTech, ISBN 978-953-307-152-7.
- 30 Kong, Q., Shi, X., Ma, W., Zhang, F., Yu, T., Zhao, F., Zhao, D., & Wei, C. (2021). Strategies to improve the adsorption properties of graphene-based adsorbent towards heavy metal ions and their compound pollutants: A review. *Journal of Hazardous Materials*, *415*, 125690, doi:10.1016/j.jhazmat.2021.125690.
- 31 Yutomo, E.B., Noor, F.A., & Winata, T. (2021). Effect of the Number of Nitrogen Dopants on the Electronic and Magnetic Properties of Graphitic and Pyridinic N-Doped Graphene — a Density-Functional Study. *RSC Adv.*, *11*, 18371–18380, doi:10.1039/D1RA01095F.
- 32 Zhang, J.-N., Ma, L., Zhang, M., Ma, L.-C., & Zhang, J.-M. (2020). First-Principles Study of the Electronic and Optical Properties of Nitrogen and Gold Co-Doped Graphene. *Superlattices and Microstructures*, *139*, 106363, doi:10.1016/j.spmi.2019.106363.
- 33 Xu, Q., Yang, G., Fan, X., & Zheng, W. (2019). Improving the Quantum Capacitance of Graphene-Based Supercapacitors by the Doping and Co-Doping: First-Principles Calculations. *ACS Omega*, *4*, 13209–13217, doi:10.1021/acsomega.9b01359.

- 34 Shih, P.-H., Do, T.-N., Gumbs, G., & Lin, M.-F. (2020). Electronic and Optical Properties of Doped Graphene. *Physica E: Low-dimensional Systems and Nanostructures*, 118, 113894, doi:10.1016/j.physe.2019.113894.
- 35 Cruz-Martínez, H., Rojas-Chávez, H., Montejo-Alvaró, F., Peña-Castañeda, Y.A., Matadamas-Ortiz, P.T., & Medina, D.I. (2021). Recent Developments in Graphene-Based Toxic Gas Sensors: A Theoretical Overview. *Sensors*, 21, 1992, doi:10.3390/s21061992.
- 36 Alam, K.M., Kumar, P., Manuel, A.P., Vahidzadeh, E., Goswami, A., Zeng, S., Wu, W., Mahdi, N., Cui, K., Kobryn, A.E., et al. (2019). CVD Grown Nitrogen Doped Graphene Is an Exceptional Visible-Light Driven Photocatalyst for Surface Catalytic Reactions. *2D Mater.*, 7, 015002, doi:10.1088/2053-1583/ab4554.
- 37 Gaidukevic, J., Aukstakojyte, R., Kozłowski, M., Barkauskas, J., & Pauliukaite, R. (2023). A Simple Preparation of N-Doped Reduced Graphene Oxide as an Electrode Material for the Detection of Hydrogen Peroxide and Glucose. *Electrochimica Acta*, 446, 142113, doi:10.1016/j.electacta.2023.142113.
- 38 Varghese, S.S., Swaminathan, S., Singh, K.K., & Mittal, V. (2016). Ab Initio Study on Gas Sensing Properties of Group III (B, Al and Ga) Doped Graphene. *Computational Condensed Matter*, 9, 40–55, doi:10.1016/j.cocom.2016.09.004.
- 39 Lee, J., Kwon, S., Kwon, S., Cho, M., Kim, K., Han, T., & Lee, S. (2019). Tunable Electronic Properties of Nitrogen and Sulfur Doped Graphene: Density Functional Theory Approach. *Nanomaterials*, 9, 268, doi:10.3390/nano9020268.
- 40 Yan, X., Shen, T., Liu, X., Liu, C., & Gong, A. (2023). Transition Metal (Co, Ti) Decorated Graphene Monolayer and Their Adsorption Properties towards SO₂: First-Principle Calculation. *Solid State Communications*, 369, 115196, doi:10.1016/j.ssc.2023.115196.
- 41 Akhmetsadyk, D., Ilyin, A., Guseinov, N., & Beall, G. (2023). Adsorption of SO₂ Molecule on Pristine, N, Ga-Doped and -Ga-N- Co-Doped Graphene: A DFT Study. *Computation*, 11, 235, doi:10.3390/computation11120235.
- 42 Neugebauer, J., & Hickel, T. (2013). Density Functional Theory in Materials Science. *WIREs Comput Mol Sci*, 3, 438–448, doi:10.1002/wcms.1125.
- 43 Paul, J.T., Singh, A.K., Dong, Z., Zhuang, H., Revard, B.C., Rijal, B., Ashton, M., Linscheid, A., Blonsky, M., Gluhovic, D., et al. (2017). Computational Methods for 2D Materials: Discovery, Property Characterization, and Application Design. *J. Phys.: Condens. Matter*, 29, 473001, doi:10.1088/1361-648X/aa9305.
- 44 Picozzi, S., Santucci, S., Lozzi, L., Cantalini, C., Baratto, C., Sberveglieri, G., Armentano, I., Kenny, J.M., Valentini, L., & Delley, B. (2004). Ozone Adsorption on Carbon Nanotubes: *Ab Initio* Calculations and Experiments. *Journal of Vacuum Science & Technology A: Vacuum, Surfaces, and Films*, 22, 1466–1470, doi:10.1116/1.1705587.
- 45 Peyghan, A.A., & Moradi, M. (2014). DFT Study of Ozone Dissociation on BC₃ Graphene with Stone–Wales Defects. *J Mol Model*, 20, 2071, doi:10.1007/s00894-014-2071-5.
- 46 Vahdat, M.T., Li, S., Huang, S., Bondaz, L., Bonnet, N., Hsu, K.-J., Marzari, N., & Agrawal, K.V. (2023). Mechanistic Insights on Functionalization of Graphene with Ozone. *J. Phys. Chem. C*, 127, 22015–22022, doi:10.1021/acs.jpcc.3c03994.
- 47 Delley, B. (2000). From Molecules to Solids with the DMol3 Approach. *The Journal of Chemical Physics*, 113, 7756–7764, doi:10.1063/1.1316015.
- 48 Pramanik, A., & Kang, H.S. (2011). Density Functional Theory Study of O₂ and NO Adsorption on Heteroatom-Doped Graphenes Including the van Der Waals Interaction. *J. Phys. Chem. C*, 115, 10971–10978, doi:10.1021/jp200783b.
- 49 Perdew, J.P., Burke, K., & Ernzerhof, M. (1996). Generalized Gradient Approximation Made Simple. *Phys. Rev. Lett.*, 77, 3865–3868, doi:10.1103/PhysRevLett.77.3865.
- 50 Delley, B. (2002). Hardness Conserving Semilocal Pseudopotentials. *Phys. Rev. B*, 66, 155125, doi:10.1103/PhysRevB.66.155125.
- 51 Rani, P., & Jindal, V.K. (2013). Designing Band Gap of Graphene by B and N Dopant Atoms. *RSC Adv.*, 3, 802–812, doi:10.1039/C2RA22664B.
- 52 Aasi, A., Aghaei, S., Moore, M., & Panchapakesan, B. (2020). Pt-, Rh-, Ru-, and Cu-Single-Wall Carbon Nanotubes Are Exceptional Candidates for Design of Anti-Viral Surfaces: A Theoretical Study. *IJMS*, 21, 5211, doi:10.3390/ijms21155211.
- 53 Liang, X.-Y., Ding, N., Ng, S.-P., & Wu, C.-M.L. (2017). Adsorption of Gas Molecules on Ga-Doped Graphene and Effect of Applied Electric Field: A DFT Study. *Applied Surface Science*, 411, 11–17, doi:10.1016/j.apsusc.2017.03.178.

Г.У. Билл, Д.С. Ахметсадык, А.М. Ильин, М.А. Тулегенова

Таза графенде, N, Ga және -Ga-N- қоса легирленген графенде O₃ молекуласының адсорбциясының алғашқы принциптерін зерттеу

Мақалада O₃ молекуласының (озон) графенге, азотпен легирленген графенге, галлиймен легирленген графенге және -Ga-N- қоса легирленген графенге адсорбциясы зерттелген. Графенге, азотпен легирленген графенге, галлиймен легирленген графенге және -Ga-N- қоса легирленген графенге O₃ адсорбциясы физикалық қасиеттердің айтарлықтай өзгеруіне әкеледі, бұл оны O₃ молекуласын анықтау мақсатында молекулалық сенсорлар үшін перспективті үміткер етеді. O₃ молекуласы мен адсорбент арасындағы өзара әрекеттесу олардың адсорбциялық энергиясы, адсорбция қашықтығы және зарядтың тасымалдануы негізінде түсіндіріледі. Озон молекуласының -Ga-N- қоса легирленген

графенге адсорбциясы таза графенге қарағанда энергия бойынша қолайлы екені анықталды, бұл -Ga-N- қоса легирленген жүйенің жоғары сенсорлық сипаттамаларын білдіреді. Осы жұмыста Малликен популяциясының талдауына негізделген O_3 молекуласы мен легирленген графен нанокұрылымдары арасындағы зарядты тасымалдау бағаланған. Озон молекуласы мен -Ga-N- графен нанокұрылымдары арасындағы күшті коваленттік байланыстан туындайтын адсорбция энергиясының есептелген мәні таза графенге ($E_{ads} = -1,74$ eV) қарағанда -Ga-N- қоса легирленген графен нанокұрылымдарының ($E_{ads} = -0,41$ eV) бетінде күштірек адсорбцияланатынын көрсетеді. Осылайша, біздің нәтижелеріміз -Ga-N- қоса легирленген графенмен қоршаған ортадағы O_3 анықтау үшін жоғары тиімді газ сенсоры құрылғысы болуы мүмкін екенін көрсетеді.

Кілт сөздер: графен, O_3 адсорбциясы, тығыздықтың функционалдық теориясы, азотпен легирленген графен, галлиймен легирленген графен, -Ga-N- қоса легирленген графен, газ сенсоры, графен негізіндегі газ сенсоры.

Г.У. Билл, Д.С. Ахметсадық, А.М. Ильин, М.А. Тулегенова

Исследование первых принципов адсорбции молекулы O_3 на чистом графене, легированном N, Ga, и -Ga-N- со-легированном графене

В статье исследована адсорбция молекулы O_3 (озона) на графене, легированном графене с азотом, на легированном графене с галлием и -Ga-N- со-легированном графене с акцентом на обнаружение O_3 . Адсорбция O_3 на графене, легированном графене с азотом, на легированном графене с галлием и -Ga-N- со-легированном графене приводит к значительному изменению физических свойств, что делает его перспективным кандидатом для молекулярных датчиков для обнаружения O_3 . Взаимодействие между молекулой O_3 и адсорбентом объясняется на основе их энергии адсорбции, расстояния адсорбции и переноса заряда. Было обнаружено, что адсорбция молекулы озона на -Ga-N- со-легированном графене была более благоприятной по энергии, чем на чистом, что представляет собой превосходные сенсорные характеристики -Ga-N- со-легированной системы. В настоящей работе был оценен перенос заряда между молекулой O_3 и легированными наноструктурами графена на основе анализа популяции Малликена. Рассчитанное значение энергии адсорбции показывает, что молекула озона более прочно адсорбируется на поверхности наноструктур графена, со-легированных -Ga-N- ($E_{ads} = -1,74$ eV), чем на чистом графене ($E_{ads} = -0,41$ eV), вытекая из более сильной ковалентной связи между молекулой озона и -Ga-N- со-легированного графена. Таким образом, наши результаты показывают, что -Ga-N- со-легированный графен может быть высокоэффективным устройством датчика газа для обнаружения O_3 в окружающей среде.

Ключевые слова: графен, адсорбция O_3 , теория функционала плотности, легированный азотом графен, легированный галлием графен, -Ga-N- со-легированный графен, газовый сенсор, сенсоры на основе графена.

Information about the authors

Gary Beall — PhD. Professor (Chemistry and Biochemistry), Texas State University, San Marcos, USA; e-mail: gb11@txstate.edu; <https://orcid.org/0000-0003-3283-1055>

Dinara Akhmetsadyk — PhD student, Al-Farabi Kazakh National University, Al-Farabi Ave., 71, 050040, Almaty, Kazakhstan; e-mail: d.akhmetsadyk@gmail.com; <https://orcid.org/0000-0003-2138-3314>

Arkady Ilyin — Professor, Dr. phys.-math. science, Al-Farabi Kazakh National University, Al-Farabi Ave., 71, 050040, Almaty, Kazakhstan; e-mail: ilyinar@mail.ru

Malika Tulegenova — PhD, Al-Farabi Kazakh National University, Al-Farabi Ave., 71, 050040, Almaty, Kazakhstan; e-mail: malika.tulegenova@bk.ru; <https://orcid.org/0000-0002-6413-4302>

T.N. Nurakhmetov¹, R.Z. Bakhtizin², D.A. Tolekov^{1*}, R.K. Shamieva¹, Zh.M. Salikhodzha¹,
B.M. Sadykova¹, B.N. Yusupbekova¹, S.A. Pazyzbek³, G.B. Bairbaeva¹, B.M. Rakhymzhanov¹

¹L.N. Gumilyov Eurasian National University, Astana, Kazakhstan;

²Bashkir State University, Ufa, Republic of Bashkortostan;

³Zhumabek Akhmetuly Tashenev University, Shymkent, Kazakhstan

*Corresponding author's e-mail: doszhan_ta_93@mail.ru

Formation of a combined electron-hole emission state in the LiRbSO₄ – Eu phosphor

In the irradiated phosphor LiRbSO₄ – Eu, the mechanisms of formation of the induced or combined electron-emitting state at 3.1–2.94 eV were studied using optical and thermal activation spectroscopy methods. It has been shown experimentally that the combined electron-emitting state of the phosphor is formed from the electron states of impurity and intrinsic electron and hole trapping centers of Eu²⁺ – SO₄[–] and SO₄^{3–} – SO₄[–]. Electron and hole trapping centers are created by irradiating the phosphor with photons exceeding the width of the forbidden band of the matrix, where free electrons are created in the conduction band and a hole in the valence band. The trapping center is formed by the capture of free electrons by impurities and anionic complexes according to the reaction $\text{Eu}^{3+} + e^- \rightarrow \text{Eu}^{2+}$, $\text{SO}_4^{2-} + e^- \rightarrow \text{SO}_4^{3-}$. In one process with electron centers, holes in the form of SO₄^{2–} are localized. Thus, impurity and intrinsic Eu²⁺ – SO₄[–] and SO₄^{3–} – SO₄[–] electron-hole trapping centers are formed. Similarly, trapping centers are formed as a result of charge transfer from the excited anion of the SO₄^{2–} complex to the Eu³⁺ impurities and to the neighboring SO₄^{2–} anions according to the reaction (O^{2–} – Eu³⁺) and (O^{2–} – SO₄^{2–}), and localized holes are also formed in one act along with it. Combined electron-emitting states consisting of impurity and intrinsic electron states are excited by photons with energies of ~4.0 eV and ~4.5 eV.

Keywords: electron; hole; recombination emission; intrinsic emission; sulfate; excitation.

Introduction

LiRbSO₄ – Eu phosphors, like other sulfates, can be used in dosimetry, as can CaSO₄ – Dy and CaSO₄ – Eu. In phosphors activated by impurities, the Eu ion in the matrix may exist in different valences. For example, in CaSO₄ – Eu impurities can be in the divalent state Eu²⁺ with an internally centered emission of about 390 nm. If Eu is in the trivalent state of Eu³⁺ in this matrix, emission is observed at 595–610 nm.

The luminescent properties of activated phosphors with an impurity of Eu have been studied for several decades [1–8]. In the works of the authors [9], redox reactions between Eu²⁺ ↔ Eu³⁺ ions in CaSO₄ – Eu were investigated. During thermal annealing up to 975 K and irradiation with gamma rays, based on measurements of photoluminescence, thermoluminescence, and EPR signal, the conversion of Eu²⁺ ions to Eu³⁺, as well as reverse reduction to Eu²⁺, is demonstrated in phosphors.

In the work of the authors [10], a red glow was detected in a single crystal of sodium oxosulfate and yttrium NaY(SO₄)₂·H₂O activated with Eu³⁺ to illuminate emitting displays.

In a review article by the authors [11], the luminescence of Eu³⁺ in various molybdates is considered. It was found that the emission at 615 nm corresponds to the 5D₀–7F₂ transitions in La₂Mo₂O₉ – Eu³⁺ molybdenum.

In the work [12], authors detected red emission at 617 nm, which is excited in La₂Zr₃Mo₂O₉ – Eu³⁺ molybdates by Zr⁴⁺ and Mo⁶⁺ sensitizers at photon energies of 395.5 nm and 465 nm, respectively. These sensitizers are formed as a result of charge transfer from the matrix to the sensitizer ions, such as O^{2–} – Zr⁴⁺ and O^{2–} – Mo⁶⁺.

The mechanisms of formation of electron-hole trapping centers in sulfates of alkaline and alkaline earth metals activated by Mn²⁺, Cu⁺ and Dy³⁺ impurities were studied in the works of the authors [13–21]. It is shown that induced or combined electron-emitting states are formed in sulfates, which are excited in the transparency regions of the matrix at photon energies of approximately 4.0 eV and 4.5 eV.

A brief review of the literature shows that phosphors activated by Eu³⁺ ions emit photons in the red region of the spectrum. These intracenter emissions are mainly excited by sensitizers, which themselves are excited by the intrinsic electronic excitations of the matrix.

In this paper, the nature of the intracenter emission of the Eu^{3+} ion in the LiRbSO_4 matrix will be investigated, as well as the mechanism of formation of an induced or combined electronic emission state, which is formed from the electronic states of its intrinsic and impurity trapping centers when irradiated with photons exceeding the band gap.

Experimental part

The studied samples were synthesized by slow evaporation. To prepare the sample, 1.2 g of LiRbSO_4 powder and 0.3 mol% (0.37 g) Eu_2O_3 were used as starting materials.

Li_2SO_4 and Rb_2SO_4 (SigmaAldrich) were dissolved in double deionized water at a temperature between 35 and 40 °C. After ensuring the solution was transparent, each lanthanide was added and mixed one by one, checking the transparency of the solution. In a separate container, Eu_2O_3 was dissolved in a deionized solution of 40 ml at a temperature of 35–40 °C. Then both solutions were mixed at 35–40 °C within 1 hour. The solution was slowly heated, LiRbSO_4 (Sigma-Aldrich) powder was added and dissolved with stirring.

For luminescent measurements, a LiRbSO_4 sample doped with Eu^{3+} (0.3 mol.%) was obtained by adding Eu_2O_3 (Thermo Scientific, 99.99 %) to the process. $\text{LiRbSO}_4 - \text{Eu}^{3+}$ was prepared by drying the doped sample at 550 °C in air. The finished powders were pressed into tablets with a size of 8–9 mm and a thickness of 1–2 mm. It was found that the optimal concentration of the Eu impurity in the LiRbSO_4 matrix is 0.3 mol.%. The resulting Eu impurity concentration of 0.3 mol.% was found to be optimal for spectroscopic properties in research.

Emission and excitation spectra were obtained using a spectrofluorimeter CM2203 (Belarus). The Solar CM2203 spectrofluorimeter was used to measure the emission spectra in the spectral range of 1.5–6.2 eV.

Chemical analysis (EDX) was carried out on a TESCAN VEGA 3 LMH scanning electron microscope with an Oxford Instruments (UK) microanalyzer system. The resolution was 3 nm at 30 kV (SE), 6 nm at 30 kV (BSE), the magnification ranged from 6× to 300000×, and the screening magnification ranged from 12× to 600000×.

The thermally stimulated luminescence (TSL) method is one of the main experimental methods for studying trapping centers in dielectrics. To obtain TSL curves, the crystal under study is cooled to the boiling point of liquid nitrogen, 77 K. Under these conditions, the crystal is excited for some time by UV emission or X-ray emission. After the excitation stops, the crystal heats up at a constant rate of 0.2 deg/s, and the intensity of thermoluminescent emission is measured depending on the temperature.

Results

The nature of the intracenter emission of the Eu^{3+} impurity and new Raman emissions resulting from the interaction of impurities with the electronic excitations of the matrix were investigated.

The SEM figure (Fig. 1) shows that the powders have different sizes, approximately ranging from 5 to 200 microns (Fig. 1a). According to the results of SEM-EDX, a large number of peaks characteristic of metal ions were registered (Fig. 1b), confirming the presence of Eu content in the LiRbSO_4 powder.

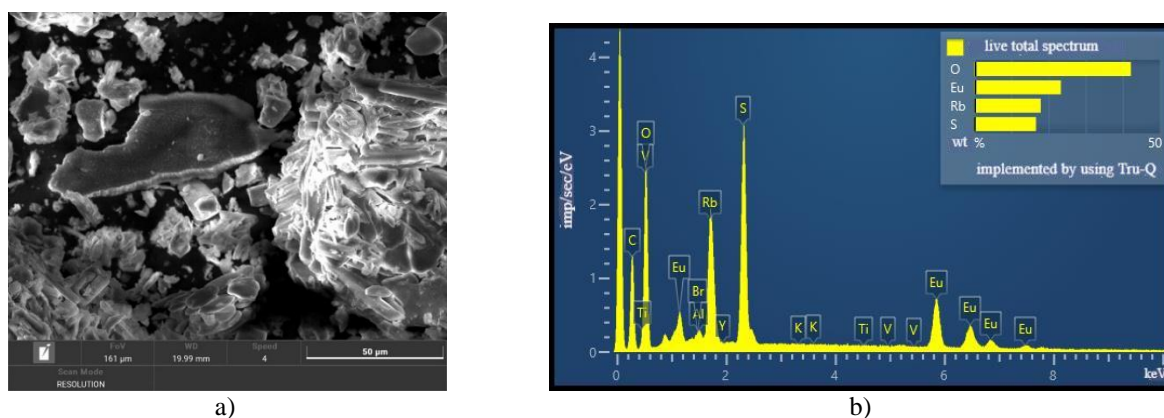


Figure 1. The result of SEM-EDX powder $\text{LiRbSO}_4 - \text{Eu}$

Figure 2 shows the emission spectrum of the $\text{LiRbSO}_4 - \text{Eu}$ phosphor irradiated with photons with an energy of 5.46 eV at 300 K (curve 1). It can be observed from the figure that intracenter emissions of the

Eu^{3+} impurity appear at 2.03 eV, 1.9 eV, 1.8 eV, and 1.7 eV. The same phosphor was irradiated at 80 K (curve 2). Figure 1 shows that at 80 K, in addition to intracenter emission, new radiation bands appear at 3.1 eV, 3.0 eV, 2.9 eV, 2.6 eV, 2.4 eV, 2.3 eV, and 2.2 eV.

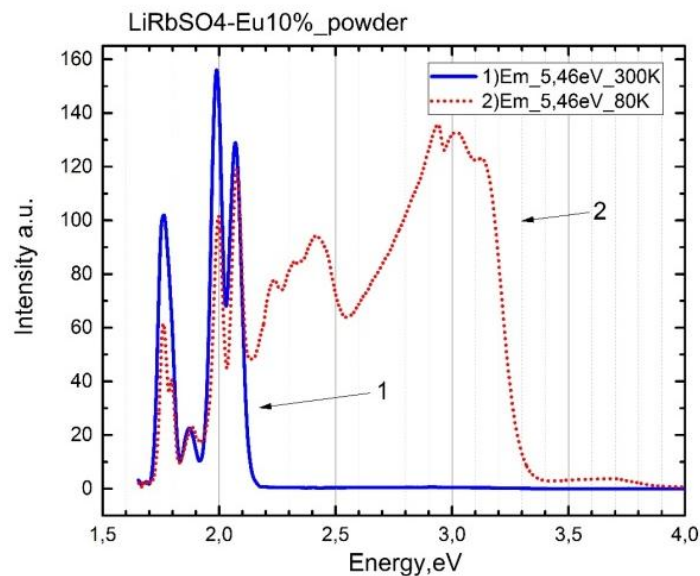


Figure 2. The emission spectrum of the $\text{LiRbSO}_4 - \text{Eu}$ crystal at 300 K and 80 K: when excited by photons: 1) $E = 5.46$ eV; 2) $E = 5.46$ eV

Figure 3 shows the excitation spectrum of new electronic radiative states at 3.1 eV, 3.02 eV, 3.4 eV, 2.94 eV, 2.43 eV, 2.32 eV, and 2.23 eV at 300 K and 80 K. It can be seen from the figure that at 300 K, the excitation bands are not clearly distinguished, and at 80 K, the excitation bands appear for emission of 2.94 eV, 3.02 eV, 3.1 eV, 3.92 eV, 4.43 eV, 5.64 eV, 5.9 eV, and 6.2 eV. From Figure 3 (curves 1–5), it can be seen that the newly formed emission states located in two spectral ranges, 3.1–2.94 eV and 2.43–2.23 eV, are mainly excited in three spectral regions of matrix transparency, 4.43–4.5 eV and 3.9–4.0 eV. Additionally, the same emission states related to trapping centers are created near the fundamental region at 5.64–6.2 eV as a result of charge transfer from anion to impurities or when an electron is captured by impurities or neighboring anions.

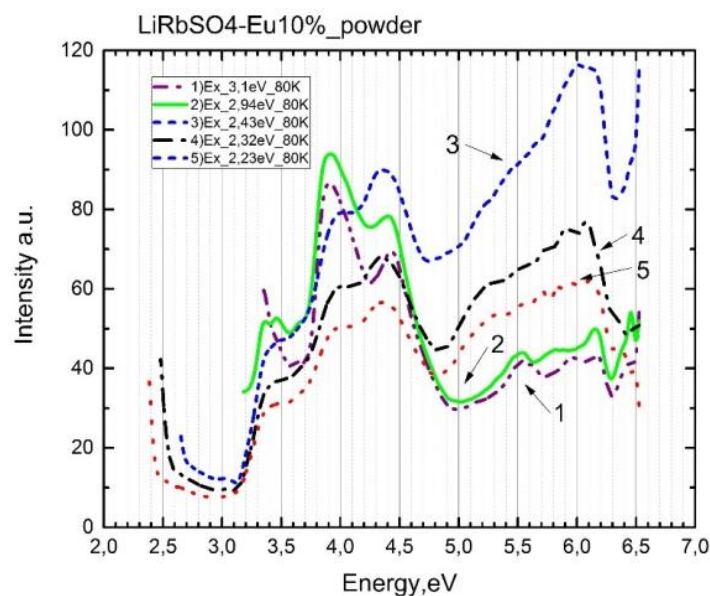


Figure 3. The excitation spectrum of the $\text{LiRbSO}_4 - \text{Eu}$ crystal at 80 K: when excited by photons: 1) $E = 3.1$ eV; 2) $E = 2.94$ eV; 3) $E = 2.43$ eV; 4) $E = 2.32$ eV; 5) $E = 2.23$ eV

Figure 4 shows the excitation spectrum of a pre-irradiated phosphor at 300 K and 80 K for the bands 2.06 eV, 1.9 eV, 1.8 eV, and 1.7 eV of intracenter emission. From Figure 4 (curves 1, 2, 3, 4, and 1', 2', 3', 4'), it can be seen that excitation bands appear corresponding to the emission of Eu^{2+} ions in the $\text{LiRbSO}_4 - \text{Eu}$ phosphor. The emission bands of the Eu^{2+} ion are excited by the emission of the Eu^{3+} ion in the red region of the spectrum.

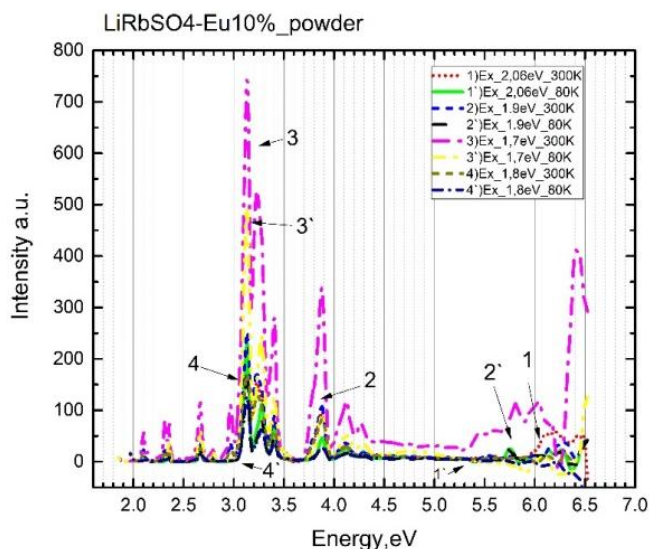


Figure 4. The excitation spectrum of the $\text{LiRbSO}_4 - \text{Eu}$ crystal at 300 K and 80 K: when excited by photons: 1) $E = 2.06$ eV; 1') $E = 2.06$ eV; 2) $E = 1.9$ eV; 2') $E = 1.9$ eV; 3) $E = 1.7$ eV; 3') $E = 1.7$ eV; 4) $E = 1.8$ eV; 4') $E = 1.8$ eV

Figure 5 shows the emission spectra of a pre-irradiated phosphor excited in the transparency region of the matrix by photons with energies of 4.43-4.5 eV and 4.0 eV at 300 K and at 80 K.

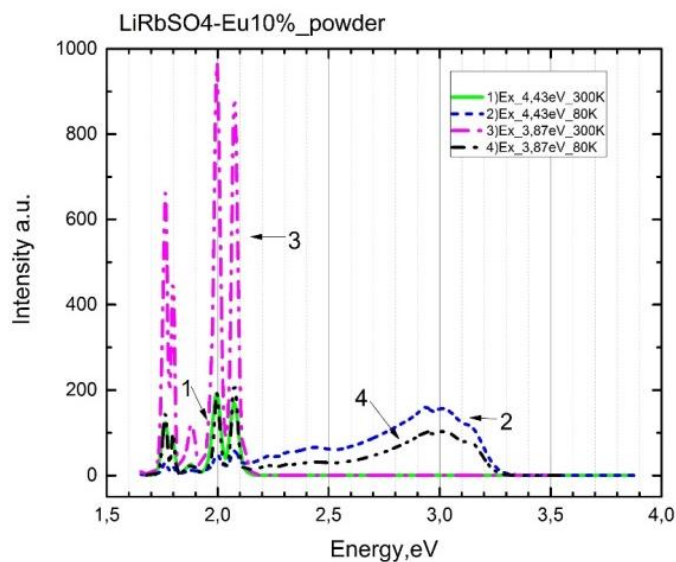


Figure 5. The emission spectrum of the $\text{LiRbSO}_4 - \text{Eu}$ crystal when excited by photons: 1) $E = 4.43$ eV at 300 K; 2) $E = 4.43$ eV at 80 K; 3) $E = 3.87$ eV at 300 K; 4) $E = 3.87$ eV at 80 K

Figure 5 (curves 1, 3) shows that when excited by photons with energies of 4.43-4.5 eV and 3.87-4.0 eV at a temperature of 300 K, intracenter emissions appear at 2.06 eV, 1.9 eV, 1.8 eV and 1.7 eV (curves 1 and 3). At a liquid nitrogen temperature of 80 K (curves 2 and 4), the intensity of the intracenter emission decreases 4-5 times, the positions of the bands are preserved. At 80 K, in addition to the intracenter emission, new radiation bands appear at 3.1 eV, 3.02 eV, 2.44 eV, 2.32 eV and 2.29 eV (curves 2, 4).

The measurement of the intensity of the intracenter and newly created emission radiation bands from the temperature of the matrix is shown in Figure 6.

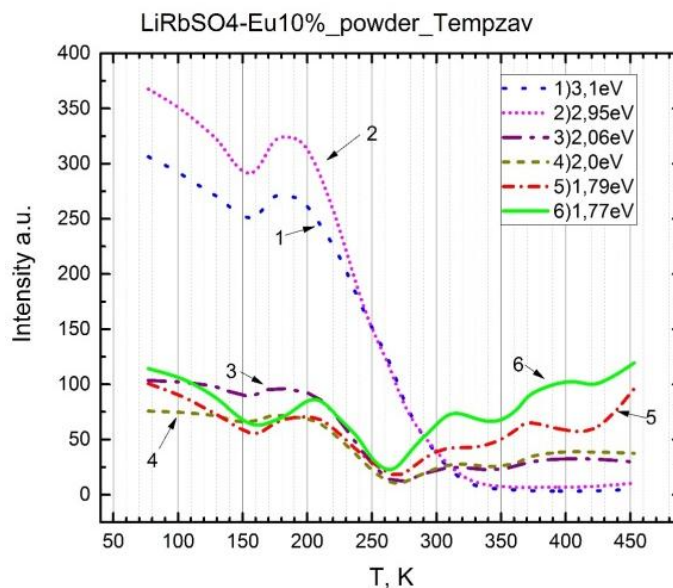


Figure 6. Temperature dependence LiRbSO₄ – Eu luminescence of radiation during excitation: 1) $E = 3.1$ eV; 2) $E = 2.95$ eV; 3) $E = 2.06$ eV; 4) $E = 2.0$ eV; 5) $E = 1.79$ eV; 6) $E = 1.77$ eV

It can be seen from the figure that the intensity of the new emission bands at 3.1 eV and 2.95 eV in the temperature range of 100–150 K gradually decreases and flares up at 150–200 K, then rapidly decreases to a minimum value in the range of 200–350 K (curves 1, 2). The temperature dependence of the change in the intensity of intracenter emission at 2.03 eV, 1.9 eV, 1.8 eV and 1.7 eV looks like this: in the temperature range from 100 K to 250 K, the intensity of all intracenter emission decreases rapidly, with some flare-up in the temperature range of 150–200 K, then in the temperature range of 280–450 K it rapidly increases to the maximum value.

Discussion

The novelty of the work is associated with the appearance of new emission bands when irradiated with photons in the fundamental region of the spectrum at 80 K, where free electron-hole pairs are created or as a result of charge transfer from the excited anionic complex SO_4^{2-} to impurities or to neighboring anions. In the early works of the authors [17], it was known that in irradiated alkali metal sulfates, recombination emission at induced trapping centers occurred in the spectral range of 3.0–3.1 eV, 2.6–2.7 eV, and 2.3–2.4 eV. Figure 5 (curve 2, 4) shows that at 80 K, the intensity of the intracenter emission band at 2.06 eV, 1.9 eV, 1.8 eV, and 1.7 eV decreased and new recombination emission appeared at 2.94–3.1 eV, which are excited at photon energies 3.92–4.0 eV and 4.43–4.5 eV. Low-energy recombination emission at 2.23–2.43 eV is also excited in this spectral region. These recombination emissions are generated in the fundamental spectral range of 5.64 eV, 5.9 eV, and 6.2 eV.

Thus, two groups of new recombination emissions at 2.94–3.1 eV and 2.23–2.43 eV are excited by photons with energies of ~ 4.0 eV and ~ 4.5 eV in the transparency region of the LiRbSO₄ – Eu phosphor. These photon energies at ~ 4.5 eV and ~ 4.0 eV are the absorption and excitation spectra of the electron-hole trapping center formed in the transparency region.

In the next stage, an irradiated phosphor with induced trapping centers was excited with a photon energy equal to the excitation spectrum of the trapping centers at ~ 4.0 eV and ~ 4.5 eV. At the same time, new recombination emissions appear back at 2.94–3.1 eV and 2.23–2.4 eV. The most important thing is that intracenter emissions of the Eu^{3+} impurity appear. These results mean that both emission, recombination, and intracenter radiative decay identically from an induced or combined electron emissivity state. By measuring the temperature dependence of the decay of the induced or combined electronic state, it is shown that the in-

tensity of the recombination emission state at 2.94–3.1 eV in the temperature range from 100 K to 250 K decreases to a minimum value.

The intensity of the intracenter emission of the impurity increases to the maximum value at 2.06 eV, 1.9 eV, 1.8 eV, and 1.7 eV temperature range.

The decay and formation of an induced or recombined electronic emission state can be explained in this way:

During irradiation with photons from 5.64–6.2 eV, electronic trapping centers are created during the localization of free electrons or during charge transfer from the excited anionic complex SO_4^{2-} to impurities Eu^{3+} ($\text{O}^{2-} - \text{Eu}^{3+}$) electronic impurity trapping centers of Eu^{2+} are formed in addition to the holes of SO_4^- localized near the ground state of the Eu^{3+} admixture. Thus, the centers of electronic trapping of impurities $\text{Eu}^{2+} - \text{SO}_4^{2-}$ are created. Similarly, when electrons are trapped or as a result of charge transfer from the excited anion SO_4^{2-} ($\text{O}^{2-} - \text{SO}_4^{2-}$) to neighboring anions, their intrinsic electron trapping centers SO_4^{3-} are formed, complementary to the holes SO_4^- . This is how the correct trapping centers $\text{SO}_4^{3-} - \text{SO}_4^-$ are formed.

Combined or induced electron-emitting states at 2.94–3.1 eV are created from the electronic states Eu^{2+} and SO_4^{3-} under the conduction band with a certain ionization energy to the conduction band.

During heating of a phosphor with induced emission states in the temperature range of 100–250 K, ionization of the electronic trapping centers occurs $\text{Eu}^{2+} \rightarrow \text{Eu}^{3+} + e^-$, $\text{SO}_4^{3-} \rightarrow \text{SO}_4^{2-} + e^-$. The free electron recombines with the hole SO_4^- near the Eu^{3+} admixture; the energy released during recombination excites the impurity in the temperature range 250–450 K, in which we observe a rapid increase in the intensity of red emission from the Eu^{3+} impurity. In this way, energy is transferred from the excited matrix to the impurities.

Conclusions

1. In the irradiated $\text{LiRbSO}_4 - \text{Eu}$ phosphor, new stimulated and combined radiative states were discovered at 3.1–2.94 eV, which are excited at photon energies of ~4.0 eV and ~4.5 eV in the matrix transparency region.

2. The emission states of 3.1–2.94 eV are created when the anion is excited by photons with an energy of 5.64 eV as a result of charge transfer from the SO_4^{2-} ion to the impurities Eu^{3+} and the neighboring ion by the reaction ($\text{O}^{2-} - \text{Eu}^{3+}$) and ($\text{O}^{2-} - \text{SO}_4^{2-}$).

3. Based on the measurement of the excitation spectra of recombination emission of 3.1–2.94 eV and impurity emission of 2.06 eV, 1.8 eV and 1.7 eV, it was shown that they are simultaneously excited at photon energies of ~4.0 eV and ~4.5 eV. These values are the excitation spectrum of a new induced electronic radiative state consisting of intrinsic and impurity electronic states of trapping centers.

References

- 1 Zhou R. et al. Insight into Eu redox and Pr^{3+} 5d emission in K Sr PO_4 by VRBE scheme construction / R. Zhou et al. // Dalton Transactions. — 2018. — Vol. 47. — No. 2. — P. 306–313.
- 2 Kruopyte A. Luminescence and luminescence quenching of efficient $\text{Gd B}_5 \text{O}_9 : \text{Eu}^{3+}$ red phosphors / A. Kruopyte et al. // Journal of Luminescence. — 2017. — Vol. 192. — P. 520–526.
- 3 Laurikenas A. Synthesis and characterization of Tb^{3+} and Eu^{3+} metal-organic frameworks with TFBDC2-linkers / A. Laurikenas et al. // Optical Materials. — 2018. — Vol. 83. — P. 363–369.
- 4 Stanulis A. et al. Temperature-Induced Structural Transformations in Undoped and Eu^{3+} -Doped Ruddlesden–Popper Phases Sr_2SnO_4 and $\text{Sr}_3\text{Sn}_2\text{O}_7$: Relation to the Impedance and Luminescence Behaviors / A. Stanulis et al. // Inorganic Chemistry. — 2019. — Vol. 58. — No. 17. — P. 11410–11419.
- 5 Li Z. et al. Energy transfer and tunable luminescence properties in $\text{Y}_3\text{Al}_2\text{Ga}_3\text{O}_{12} : \text{Tb}^{3+}, \text{Eu}^{3+}$ phosphors / Z. Li et al. // Journal of Alloys and Compounds. — 2019. — Vol. 787. — P. 672–682.
- 6 Laufer S. et al. Yttrium (III) oxomolybdates (VI) as potential host materials for luminescence applications: an investigation of Eu^{3+} -doped $\text{Y}_2[\text{MoO}_4]_3$ and $\text{Y}_2[\text{MoO}_4]_2[\text{Mo}_2\text{O}_7]$ / S. Laufer et al. // New Journal of Chemistry. — 2013. — Vol. 37. — No. 7. — P. 1919–1926.
- 7 Gou J. et al. $\text{Sr}_8\text{ZnSc}(\text{PO}_4)_7 : \text{Eu}^{3+}, \text{Li}^+$ novel red-emitting phosphors: synthesis and photoluminescence properties / J. Gou et al. // Materials Research Bulletin. — 2017. — Vol. 86. — P. 234–240.

- 8 Cho S. LiRE(SO₄)₂ (RE = Y, Gd, Eu): noncentrosymmetric chiral rare-earth sulfates with very large band gaps / S. Cho, K.M. Ok // *Materials Chemistry Frontiers*. — 2023. — Vol. 7. — No. 1. — P. 65–71.
- 9 Nair S.R. et al. Redox reactions, radio-photoluminescence and thermo luminescence in / S.R. Nair et al. // *Journal of Physics: Condensed Matter*. — 1997. — Vol. 9. — No 39. — P. 8307.
- 10 Buyer C. et al. Hydrothermal synthesis, crystal structure, and spectroscopic properties of pure and Eu³⁺-doped NaY[SO₄]₂·H₂O and its anhydrate NaY[SO₄]₂ / C. Buyer et al. // *Crystals*. — 2021. — Vol. 11. — No. 6. — P. 575.
- 11 Baur F. Eu³⁺ activated molybdates—Structure property relations / F. Baur, T. Jüstel // *Optical Materials: X*. — 2019. — Vol. 1. — P. 100015.
- 12 Baur F. New red-emitting phosphor La₂Zr₃(MoO₄)₉:Eu³⁺ and the influence of host absorption on its luminescence efficiency / F. Baur, T. Jüstel // *Australian Journal of Chemistry*. — 2015. — Vol. 68. — No 11. — P. 1727–1734.
- 13 Nurakhmetov T.N. et al. Specific Features of Formation of Electron and Hole Trapping Centers in Irradiated CaSO₄-Mn and BaSO₄-Mn / T.N. Nurakhmetov et al. // *Crystals*. — 2023. — Vol. 13. — No 7. — P. 1054.
- 14 Nurakhmetov T.N. et al. Energy Transfer in the CaSO₄ – Dy Thermoluminescent Dosimeter from the Excited State of the SO₄²⁻ Anionic Complex to the Impurities / T.N. Nurakhmetov et al. // *Crystals*. — 2023. — Vol. 13. — No 11. — P. 1596.
- 15 Nurakhmetov T.N. et al. Electron-hole trapping centers in alkali metal sulfates with Dy³⁺ impurities / T.N. Nurakhmetov et al. // *Eurasian Journal of Physics and Functional Materials*. — 2023. — Vol. 7. — No 2. — P. 115–122.
- 16 Nurakhmetov T.N. et al. Electron-hole trapping centers in Na₂SO₄ with a transition metal impurity Mn / T.N. Nurakhmetov et al. // *Eurasian Journal of Physics and Functional Materials*. — 2023. — Vol. 7. — No 1. — P. 38–44.
- 17 Плеханов В.Г. Исследование спектров отражения и люминесценции сульфата калия при низкой температуре / В.Г. Плеханов, В.С. Осминин // *Оптика и спектроскопия*. — Т. XXXVIII, вып. 1. — С. 120–123. — Л.: Наука, 1975.
- 18 Borodin Y.V. et al. Spectroscopy of nanoscale crystalline structural elements / Y.V. Borodin et al. // *Bulletin of the University of Karaganda-Physics*. — 2020. — Т. 99. — No. 3. — С. 46–53.
- 19 Исмаилов Ж.Т. Влияние легирования оловом, таллием и медью на квантовые подвижности дырок в монокристаллах теллурида сурьмы / Ж.Т. Исмаилов, В.А. Кульбачинский // *Вестн. Караганд. ун-та. Сер. Физика*. — 2020. — Т. 97. — № 1. — С. 26–34.
- 20 Nurakhmetov T.N. et al. Intrinsic emission and electron-hole trapping centers in crystals Li₂SO₄ – Cu / T.N. Nurakhmetov et al. // *Eurasian Journal of Physics and Functional Materials*. — 2021. — Vol. 5. — No 2. — P. 140–147.
- 21 Nurakhmetov T.N. et al. Intrinsic emission and electron-hole trapping centers in irradiated Na₂SO₄ / T.N. Nurakhmetov et al. // *Optik*. — 2021. — Vol. 242. — P. 167081.

Т.Н. Нурахметов, Р.З. Бахтизин, Д.А. Төлеков, Р.К. Шамиева, Ж.М. Салиходжа,
Б.М. Садыкова, Б.Н. Юсупбекова, С.А. Пазылбек, Г.Б. Байрбаева, Б.М. Рахымжанов

LiRbSO₄ – Eu люминофорындағы біріктірілген электронды-кемтік сәулелену күйінің түзілуі

LiRbSO₄–Eu сәулелендірілген люминофорда оптикалық және термоактивациялық спектроскопия әдістерімен 3,1–2,94 эВ индукцияланған немесе біріктірілген электронды сәулелену күйінің пайда болу механизмдері зерттелді. Люминофордың біріктірілген электронды сәулелену күйі қоспа және меншікті электронды және кемтікті қармау орталықтары, электрондық күйінен Eu²⁺–SO₄ және SO₄³⁻–SO₄⁻ түзілетіні эксперименталды түрде көрсетілген. Электронды және кемтікті қармау орталықтары люминофордың тыйым салынған аймақ ені энергиясынан асатын фотондармен сәулелендіру кезінде құрылады, мұнда өткізгіштік зонасында бос электрондар және валенттік аймақта кемтік пайда болады. Қармау орталығы бос электрондарды, қоспалармен және аниондық комплекстер қармалған Eu³⁺ + e⁻ → Eu²⁺, SO₄²⁻ + e⁻ → SO₄³⁻ реакциясы бойынша түзіледі. Бір процесте SO₄²⁻ түріндегі кемтіктер электронды орталықтармен локализацияланады. Осылайша, қоспа және меншікті Eu²⁺–SO₄⁻ және SO₄³⁻–SO₄⁻ электрондық кемтікті қармау орталықтары пайда болады. Осыған ұқсас SO₄²⁻ комплексінің қозған анионынан Eu³⁺ қоспаларға және реакцияға сәйкес көршілес SO₄²⁻ аниондарға зарядтың ауысуы нәтижесінде басып алу орталықтары (O²⁻–Eu³⁺) және (O²⁻–SO₄²⁻), сондай-ақ бір процесінде онымен бірге локализацияланған кемтіктер түзіледі. Қоспалар мен меншікті электрондық күйлерден тұратын біріккен электрон шығаратын күйлер энергиясы, ~4,0 эВ және ~4,5 эВ фотондарымен қоздырылады.

Кілт сөздер: электрон, кемтік, рекомбинациялық сәулелендіру, меншікті радиация, сульфат, козу.

Т.Н. Нурахметов, Р.З. Бахтизин, Д.А. Толеков, Р.К. Шамиева, Ж.М. Салиходжа, Б.М. Садыкова, Б.Н. Юсупбекова, С.А. Пазылбек, Г.Б. Байрбаева, Б.М. Рахымжанов

Образование комбинированного электронно-дырочного излучательного состояния в люминофоре $\text{LiRbSO}_4\text{-Eu}$

В облученном люминофоре $\text{LiRbSO}_4\text{-Eu}$ методами оптической и термоактивационной спектроскопии исследованы механизмы образования индуцированного или комбинированного электронно-излучательного состояния при 3,1–2,94 эВ. Экспериментально показано, что комбинированное электронно-излучательное состояние люминофора формируется из электронных состояний примесных и собственных электронно- и дырочных центров захватов $\text{Eu}^{2+} - \text{SO}_4^-$ и $\text{SO}_4^{3-} - \text{SO}_4^-$. Электронно- и дырочные центры захвата создаются при облучении люминофора фотонами, превышающими ширину запрещенной зоны матрицы, где создаются свободные электроны в зоне проводимости и дырка в валентной зоне. Центр захвата образуется при захвате свободных электронов примесями и анионными комплексами по реакции $\text{Eu}^{3+} + e^- \rightarrow \text{Eu}^{2+}$, $\text{SO}_4^{2-} + e^- \rightarrow \text{SO}_4^{3-}$. В одном акте с электронными центрами локализуются дырки в виде SO_4^{2-} . Таким образом, формируются примесные и собственные $\text{Eu}^{2+} - \text{SO}_4^-$ и $\text{SO}_4^{3-} - \text{SO}_4^-$ электронно-дырочные центры захватов. Аналогично центры захвата образуются в результате переноса заряда от возбужденного аниона комплекса SO_4^{2-} к примесям Eu^{3+} и к соседним анионам SO_4^{2-} по реакции $(\text{O}^{2-} - \text{Eu}^{3+})$ и $(\text{O}^{2-} - \text{SO}_4^{2-})$, также в одном акте вместе с ним формируются локализованные дырки. Комбинированные электронно-излучательные состояния, состоящие из примесных и собственных электронных состояний, возбуждаются фотонами с энергией ~4,0 и ~4,5 эВ.

Ключевые слова: электрон, дырка, рекомбинационное излучение, собственное излучение, сульфат, возбуждение.

References

- Zhou, R. et al. (2018). Insight into Eu redox and Pr^{3+} 5d emission in KSrPO_4 by VRBE scheme construction. *Dalton Transactions*, 47(2), 306–313.
- Kruopyte, A. et al. (2017). Luminescence and luminescence quenching of efficient $\text{GdB}_5\text{O}_9\text{:Eu}^{3+}$ red phosphors. *Journal of Luminescence*, 192, 520–526.
- Laurikenas, A. et al. (2018). Synthesis and characterization of Tb^{3+} and Eu^{3+} metal-organic frameworks with TFBDC2-linkers. *Optical Materials*, 83, 363–369.
- Stanulis, A. et al. (2019). Temperature-Induced Structural Transformations in Undoped and Eu^{3+} -Doped Ruddlesden–Popper Phases Sr_2SnO_4 and $\text{Sr}_3\text{Sn}_2\text{O}_7$: Relation to the Impedance and Luminescence Behaviors. *Inorganic Chemistry*, 58(17), 11410–11419.
- Li, Z. et al. (2019). Energy transfer and tunable luminescence properties in $\text{Y}_3\text{Al}_2\text{Ga}_3\text{O}_{12}\text{:Tb}^{3+}$, Eu^{3+} phosphors. *Journal of Alloys and Compounds*, 787, 672–682.
- Laufer, S. et al. (2013). Yttrium (III) oxomolybdates (VI) as potential host materials for luminescence applications: an investigation of Eu^{3+} -doped $\text{Y}_2[\text{MoO}_4]_3$ and $\text{Y}_2[\text{MoO}_4]_2[\text{Mo}_2\text{O}_7]$. *New Journal of Chemistry*, 37(7), 1919–1926.
- Gou J. et al. (2017). $\text{Sr}_8\text{ZnSc}(\text{PO}_4)_7\text{:Eu}^{3+}$, Li^+ novel red-emitting phosphors: synthesis and photoluminescence properties. *Materials Research Bulletin*, 86, 234–240.
- Cho, S., Ok, K.M. (2023). $\text{LiRE}(\text{SO}_4)_2$ (RE = Y, Gd, Eu): noncentrosymmetric chiral rare-earth sulfates with very large band gaps. *Materials Chemistry Frontiers*, 7(1), 65–71.
- Nair, S.R. et al. (1997). Redox reactions, radio-photoluminescence and thermo luminescence in. *Journal of Physics: Condensed Matter*, 9(39), 8307.
- Buyer, C. et al. (2021). Hydrothermal synthesis, crystal structure, and spectroscopic properties of pure and Eu^{3+} -doped $\text{NaY}[\text{SO}_4]_2 \cdot \text{H}_2\text{O}$ and its anhydrate $\text{NaY}[\text{SO}_4]_2$. *Crystals*, 11(6), 575.
- Baur, F., & Jüstel, T. (2019). Eu^{3+} activated molybdates—Structure property relations. *Optical Materials: X*, 1, 100015.
- Baur, F., & Jüstel, T. (2015). New red-emitting phosphor $\text{La}_2\text{Zr}_3(\text{MoO}_4)_9\text{:Eu}^{3+}$ and the influence of host absorption on its luminescence efficiency. *Australian Journal of Chemistry*, 68(11), 1727–1734.
- Nurakhmetov, T.N. et al. (2023). Specific Features of Formation of Electron and Hole Trapping Centers in Irradiated $\text{CaSO}_4\text{-Mn}$ and $\text{BaSO}_4\text{-Mn}$. *Crystals*, 13(7), 1054.
- Nurakhmetov, T.N. et al. (2023). Energy Transfer in the $\text{CaSO}_4 - \text{Dy}$ Thermoluminescent Dosimeter from the Excited State of the SO_4^{2-} Anionic Complex to the Impurities. *Crystals*, 13(11), 1596.
- Nurakhmetov, T.N. et al. (2023). Electron-hole trapping centers in alkali metal sulfates with Dy^{3+} impurities. *Eurasian Journal of Physics and Functional Materials*, 7(2), 115–122.

- 16 Nurakhmetov, T.N. et al. (2023). Electron-hole trapping centers in Na_2SO_4 with a transition metal impurity Mn. *Eurasian Journal of Physics and Functional Materials*, 7(1), 38–44.
- 17 Plekhanov, V.G., & Osmenin, V.S. (1975). Issledovanie spektrov otrazheniia i liuminesentsii sulfata kaliia pri nizkoi temperature [Investigation of the reflection and luminescence spectra of potassium sulfate at low temperature]. *Optika i spektroskopiia — Optics and spectroscopy*, XXXVIII, 1, 120–123. Leningrad: Nauka [in Russian].
- 18 Borodin, Y.V. et al. (2020). Spectroscopy of nanoscale crystalline structural elements. *Bulletin of the University of Karaganda-Physics*, 99(3), 46–53.
- 19 Ismailov, Zh.T., & Kulbachinskii, V.A. (2020). Vliianie legirovaniia olovom, talliem i mediu na kvantovye podvizhnosti dyrok v monokristallakh tellurida surmy [Influence of doping by tin, thallium and copper on quantum mobility of holes in antimony telluride single crystals]. *Vestnik Karagandinskogo universiteta. Seriya Fizika — Bulletin of the University of Karaganda-Physics*, 97(1), 26–34 [in Russian].
- 20 Nurakhmetov, T.N. et al. (2021). Intrinsic emission and electron-hole trapping centers in crystals $\text{Li}_2\text{SO}_4 - \text{Cu}$. *Eurasian Journal of Physics and Functional Materials*, 5(2), 140–147.
- 21 Nurakhmetov, T.N. et al. (2021). Intrinsic emission and electron-hole trapping centers in irradiated Na_2SO_4 . *Optik*, 242, 167081.

Information about the authors

Nurakhmetov, Turlybek — Doctor of physical and mathematical sciences, professor, L.N. Gumilyov Eurasian National University, Astana, Kazakhstan; e-mail: t.nurakhmetov@yandex.kz; ORCID ID: <https://orcid.org/0000-0002-5914-2324>

Bakhtizin, Rauf — Doctor of physical and mathematical sciences, Professor, Department of Physical Electronics, Bashkir State University, Ufa, Republic of Bashkortostan; e-mail: raouf@bsunet.ru; ORCID ID: <https://orcid.org/0000-0002-2970-3362>

Tolekov, Doszhan — PhD student, Department of Technical Physics, L.N. Gumilyov Eurasian National University, Astana, Kazakhstan; e-mail: doszhan_ta_93@mail.ru; ORCID ID: <https://orcid.org/0000-0002-6528-3879>

Shamieva, Raushan — PhD student, Department of Technical Physics, L.N. Gumilyov Eurasian National University, Astana, Kazakhstan; e-mail: rasha_arman@bk.ru; ORCID ID: <https://orcid.org/0009-0005-3754-0726>

Salikhodzha, Zhusupbek — Associate Professor, PhD; Department of Technical Physics, L.N. Gumilyov Eurasian National University, Astana, Kazakhstan; e-mail: sali.zhm64@yandex.kz; ORCID ID: <https://orcid.org/0000-0002-4862-7553>

Sadykova, Batsai — Senior Lecturer, PhD, Department of Technical Physics, L.N. Gumilyov Eurasian National University, Astana, Kazakhstan; e-mail: batsaiy_s@mail.ru; ORCID ID: <https://orcid.org/0009-0004-3622-0643>

Yusupbekova, Bagila — Senior Lecturer, PhD, Department of Technical Physics, L.N. Gumilyov Eurasian National University, Astana, Kazakhstan; e-mail: bagila7@mail.ru; ORCID ID: <https://orcid.org/0000-0003-0962-5456>

Pazylbek, Sapargali — PhD, Department of Mathematics and Computer Science, Zhumabek Akhmetuly Tashenev University, Shymkent, Kazakhstan; e-mail: sapargali.pa@gmail.com; ORCID ID: <https://orcid.org/0000-0002-2318-9155>

Bairbaeva, Guldari — PhD student, Department of Technical Physics, L.N. Gumilyov Eurasian National University, Astana, Kazakhstan

Rakhymzhanov, Bekzhan — Student; Department of Technical Physics, L.N. Gumilyov Eurasian National University, Astana, Kazakhstan.

G.S. Seisenbayeva, D.S. Kambar, A.V. Zavgorodniy, B.R. Ilyassov*

Astana It University, Mangilik El 55/11, Block C1, 010000 Astana, Kazakhstan
**Corresponding author's e-mail: baurzhan.ilyassov@astanait.edu.kz*

Enhanced charge separation at the interface of Cu₂O/CuSCN composite thin films synthesized by electrodeposition technique

This study focuses on the synthesis and characterization of hole transport layers (HTLs) for solar cells, particularly copper(I) thiocyanate (CuSCN) and cuprous oxide (Cu₂O), synthesized via electrodeposition techniques. CuSCN and Cu₂O offer promising properties for efficient charge transport in photovoltaic devices. The synthesis processes involve precise control of deposition parameters to achieve desired film morphologies and properties. Characterization techniques including scanning electron microscopy (SEM), atomic force microscopy (AFM), and ultraviolet-visible (UV-Vis) spectroscopy provide insights into film morphology and optical properties. Optimization of synthesis parameters for Cu₂O films is explored to enhance their electrical properties. Photoelectric response measurements indicate improved charge separation at the interface of Cu₂O/CuSCN composite films. These findings can contribute to the advancement of solar cell technology. Furthermore, the study extends its exploration to the fabrication of Cu₂O by electrodeposition at different pH levels. SEM and X-ray diffraction (XRD) analyses reveal the impact of deposition parameters on film morphology and crystal structure, providing valuable insights for tailored synthesis approaches. Overall, this comprehensive study not only advances the understanding of HTL materials synthesis and optimization but also provides valuable guidance for the development of high-efficiency and stable solar cell devices.

Keywords: solar cells; hole transport layers; electrodeposition; copper(I) thiocyanate; cuprous oxide; optimal synthesis conditions; photoelectric response, charge transport.

Introduction

Solar energy stands at the forefront of sustainable energy solutions, offering a clean and renewable alternative to conventional fossil fuels. At the heart of solar energy conversion lie solar cells, devices tasked with harnessing sunlight and converting it into electrical energy. The efficiency and effectiveness of these solar cells hinge on the intricate interplay of various materials within their structures. Among these materials, hole transport layers (HTLs) play a crucial role in facilitating the efficient extraction and transportation of positive charge carriers generated during the photovoltaic process [1].

In recent years, significant research efforts have been dedicated to the development and optimization of HTL materials for solar cell applications. Among the promising candidates in this domain are copper(I) thiocyanate (CuSCN) and cuprous oxide (Cu₂O), both of which exhibit favorable properties for efficient charge transport. CuSCN, a well-known semiconductor for photovoltaic applications, boasts suitable optical properties and native p-type conductivity. Meanwhile, Cu₂O, with its p-type semiconducting properties and direct band gap, presents another attractive option for HTL materials [2, 3].

This study focuses on the synthesis and characterization of CuSCN and Cu₂O thin films as HTLs for solar cells, employing electrodeposition techniques for precise control over their properties. Electrodeposition offers advantages in terms of scalability, cost-effectiveness, and the ability to tailor material properties by adjusting deposition parameters. By meticulously controlling deposition conditions, such as precursor solution composition, deposition potential, and temperature, the study aims to optimize the morphological and electrical properties of the synthesized films.

The experimental part of the study delves into detailed synthesis procedures for CuSCN and Cu₂O films, elucidating the intricacies of electrodeposition techniques employed to achieve desired film morphologies and properties. Characterization techniques, including scanning electron microscopy (SEM), four point probe and photoelectric response (PEC) provide valuable insights into the surface morphology, crystal structure and electrical and charge transfer properties of the synthesized films. Furthermore, the study explores variations in synthesis conditions for Cu₂O films, investigating the influence of parameters such as pH on film morphology and electrical properties. Through systematic variation of these parameters, the study aims to elucidate optimal conditions for achieving low resistivity and enhanced charge transport capabilities in Cu₂O films combined with CuSCN films [4].

Methods

To obtain high-quality thin films with minimal impurities, high-purity chemicals purchased from Sigma-Aldrich were utilized. The following high-grade chemicals were employed in this work: Copper(II) sulfate (anhydrous, powder, $\geq 99.99\%$ trace metals basis), Ethylenediaminetetraacetic acid (OmniPur® Grade, $\geq 99.5\%$), Potassium thiocyanate (ReagentPlus®, $\geq 99.0\%$), Diethanolamine (BioUltra, $\geq 99.5\%$ (GC)), Lactic acid (ACS reagent, $\geq 85\%$), and Sodium hydroxide (ACS reagent, $\geq 97.0\%$, pellets). To prepare the aqueous solutions, deionized water with a resistivity of $18.2\text{ M}\Omega\cdot\text{cm}$, purified using a Water Purification System (Drawell Scientific, Smart-Q30UT), was used. The use of these high-grade chemicals helps to minimize impurities in the synthesized thin films, ensuring superior quality.

CuSCN thin films were synthesized by using electrochemical deposition on FTO covered glass substrates. Prior to deposition, FTO substrates were cleaned with ultrasonic in 2% Hellmanex solution (10 min), deionized water (10 min), 2-propanol (10 min), and dried by a nitrogen flow. Then clean substrates were treated by UV irradiation in order to remove any organic residuals. CuSCN-E is prepared by electrodeposition in aqueous solution containing 12 mM CuSO_4 and equivalent amount of EDTA (Ethylenediaminetetraacetic acid) and KSCN (Potassium thiocyanate) whereas CuSCN-D is fabricated in aqueous solution containing 15 mM CuSO_4 , 67.5 mM DEA (Diethanolamine), and 45 mM KSCN . EDTA and DEA were added before adding KSCN to prevent $\text{Cu}(\text{SCN})_2$ precipitate formation. The pH of EDTA-contained precursor solution and DEA-contained precursor solution are 1.6 and 8.2 , respectively. A standard three-electrode configuration was used for electrochemical deposition with Pt counter electrode and Ag/AgCl/sat. KCl reference electrode. All films were prepared using chronoamperometry technique with various duration. The deposition potentials of CuSCN-E and CuSCN-D respectively are -0.3 V and -0.45 V versus reference electrode [5, 6].

The electrochemical deposition of Cu_2O films was carried out in an electrolyte solution consisting of 0.4 M cupric sulfate and 3 M lactic acid. By complexing with lactate ion, the copper is stabilized and the pH can be raised to alkaline values. The pH of the bath solution was adjusted in the range of 10 – 12 by the addition of NaOH. The solution temperature was held constant during deposition by a hot plate with thermostat. Deposition temperature was $30\text{ }^\circ\text{C}$. Films were electrochemically deposited onto ITO (indium tin oxide) substrates, which were placed in solution with a Pt counter electrode and a silver chloride reference electrode (SCE). All potentials are reported versus the SCE reference electrode. Electrochemical deposition was controlled by a potentiostat (CS300, Corrtest Instrument).

The surface morphology of thin films was studied by a scanning electron microscopy (MIRA 3 LMU and Carl Zeiss Crossbeam 540 with GEMINI II). The XRD spectra were probed by Rigaku SmartLab X-ray diffractometer. The surface resistivity was measured by Four-Point Probe Unit (Ossila). PEC was measured by potentiostat (CS300, Corrtest Instrument) and chopped light was supported by Ossila Solar Simulator.

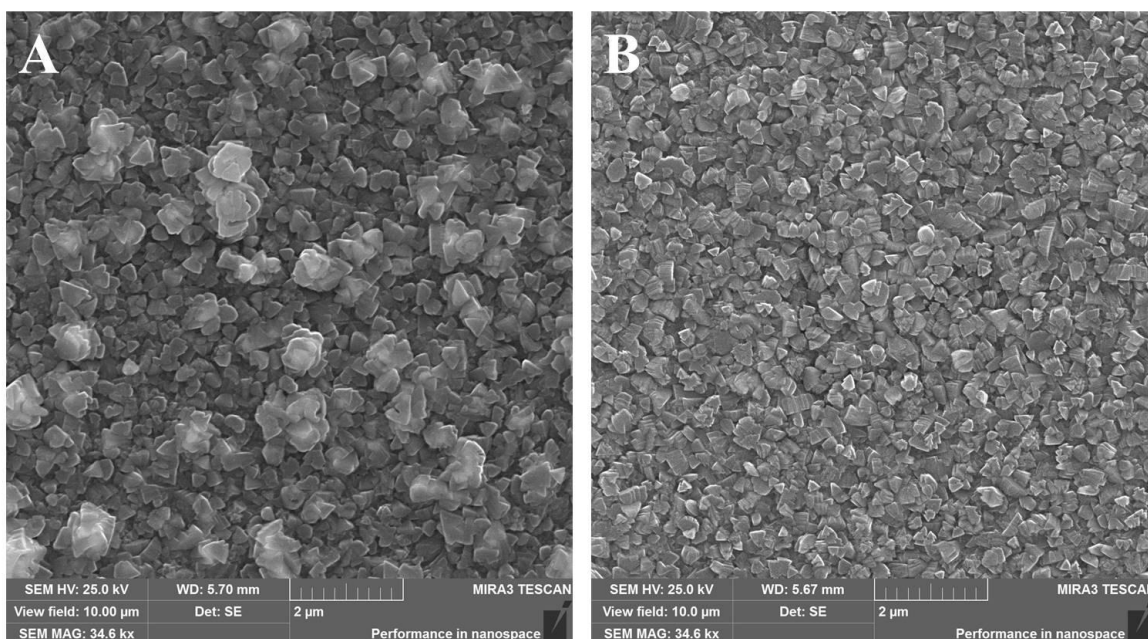
Results and discussion

One of the promising inorganic semiconductors suitable for application in photovoltaics as a hole transport material is copper thiocyanate (CuSCN). CuSCN is a well-known semiconductor for photovoltaic application due to its suitable optical properties and charge transport properties. CuSCN has a high transparency in visible spectrum and have been reported to show native *p*-type conductivity. A benefit of utilizing CuSCN in device applications is that it is non-toxic and its constituents are available in abundance in Earth.

In Figure 1, we present scanning electron microscope (SEM) images depicting the synthesized CuSCN-E and CuSCN-D thin films. Upon examination of these images, a distinct disparity in surface morphology between the two variants becomes evident. Both films exhibit a dense and uniform structure, indicative of a well-controlled synthesis process. However, CuSCN-E demonstrates a notably smoother surface texture, characterized by a relatively even distribution of material across the substrate. The average grain size of the CuSCN-E film, calculated from SEM images, was found to be $2.3\text{ }\mu\text{m}$. In contrast, CuSCN-D film is not uniform and displays clusters or agglomerates of CuSCN nanocrystals, resulting in a rougher appearance. The average size of the grains in CuSCN-D were estimated to be $4.8\text{ }\mu\text{m}$. Despite the surface texture differences, analysis reveals that both types of films possess irregular shapes prevalent in the grain structure of each film. This irregularity suggests inherent complexities in the crystallization process, likely influenced by various synthesis parameters.

The observed smoother surface of the CuSCN-E film holds particular significance in the context of its application as a hole transport layer (HTL) in solar cells. The uniformity and smoothness of this film are de-

sirable traits for facilitating efficient charge transport within the device. In contrast, the presence of agglomerates in the CuSCN-D film may introduce discontinuities or barriers to charge flow, potentially compromising device performance. In furthering our study, CuSCN-E films were used as one of the components for fabricating CuSCN/Cu₂O composite films.



A — CuSCN-D film and B — CuSCN-E film

Figure 1. SEM images of synthesized CuSCN films

Cuprous oxide (Cu₂O) thin films are synthesized by using various techniques, and as a result, the physical and chemical properties are strongly dependent on the synthesis method. Here, we report results of synthesis of Cu₂O by electrodeposition technique (Fig. 2A).

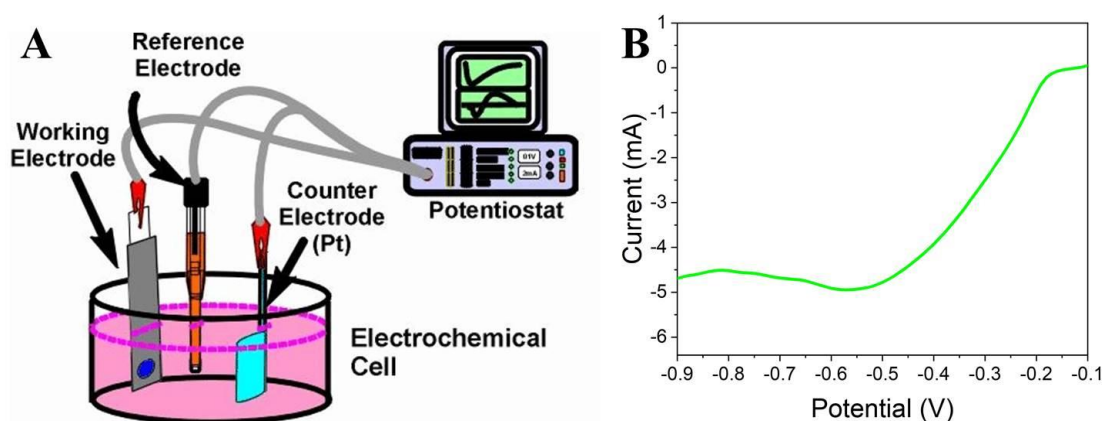


Figure 2. Diagram of the electrodeposition setup (A) and linear sweep voltammetric (LSV) measurement (B). Diagram was adapted from [7]

Electrochemical deposition of films allows precise control of the driving force for the reactions involved in deposition to control the structure and phase composition of the films. The electrochemical deposition of Cu₂O films was carried out in an electrolyte solution consisting of 0.4 M cupric sulfate and 3 M lactic acid. By complexing with lactate ion, the copper is stabilized and the pH can be raised to alkaline values. The pH of the bath solution was adjusted in the range of 10–12 by the addition of NaOH. The solution temperature was held constant during deposition by a hot plate with thermo-regulator. Deposition temperature was 30 °C. Films were electrochemically deposited onto ITO (indium tin oxide) substrates, which were

placed in solution with a Pt counter electrode and a silver chloride reference electrode (SCE). All potentials are reported versus the SCE reference electrode. Electrochemical deposition was controlled by a potentiostat. The diagram of the electrodeposition is illustrated in Figure 2A.

The electrodeposition potential required for a synthesis in the potentiostatic mode is usually unknown. In this situation, linear sweep voltammetric (LSV) measurements assist to identify oxidation-reduction processes potentially undergone by the system of interest and choose an appropriate potential. Figure 2B shows a cathodic scan performed between -0.9 and -1.2 V at a scan rate of $10 \text{ mV} \times \text{s}^{-1}$, at temperature of 30°C and at pH of 11.5. As can be seen from LSV the steady-state currents for the deposition of Cu_2O are in a potential window between -0.35 and -0.55 V. Therefore, electrodeposition of Cu_2O films was performed at working electrode potential of -0.4 V vs SCE.

Synthesis of Cuprous Oxide (Cu_2O) in various modes

In order to study the influence of pH solution on morphology of Cu_2O films the electrodeposition were performed in various pH. The plating bath was a 0.2 M CuSO_4 and 3 M lactic solution in deionized (DI) water with $0.5 \text{ M K}_2\text{HPO}_4$ buffer. pH was adjusted to by adding a controlled amount of 2 M KOH drops. The synthesis was carried out by using potentiostatic mode at 30°C ranging from pH 8 to 12. It should be noted that only the SEM and XRD data of the films deposited at pH 10 and 12 is shown due to there is no any noticeable difference between films deposited at pH 9 and 10 and between pH 11 and 12. In the Figure 3, the morphology and XRD spectra of Cu_2O films electrodeposited at pH 10 and 12 are shown.

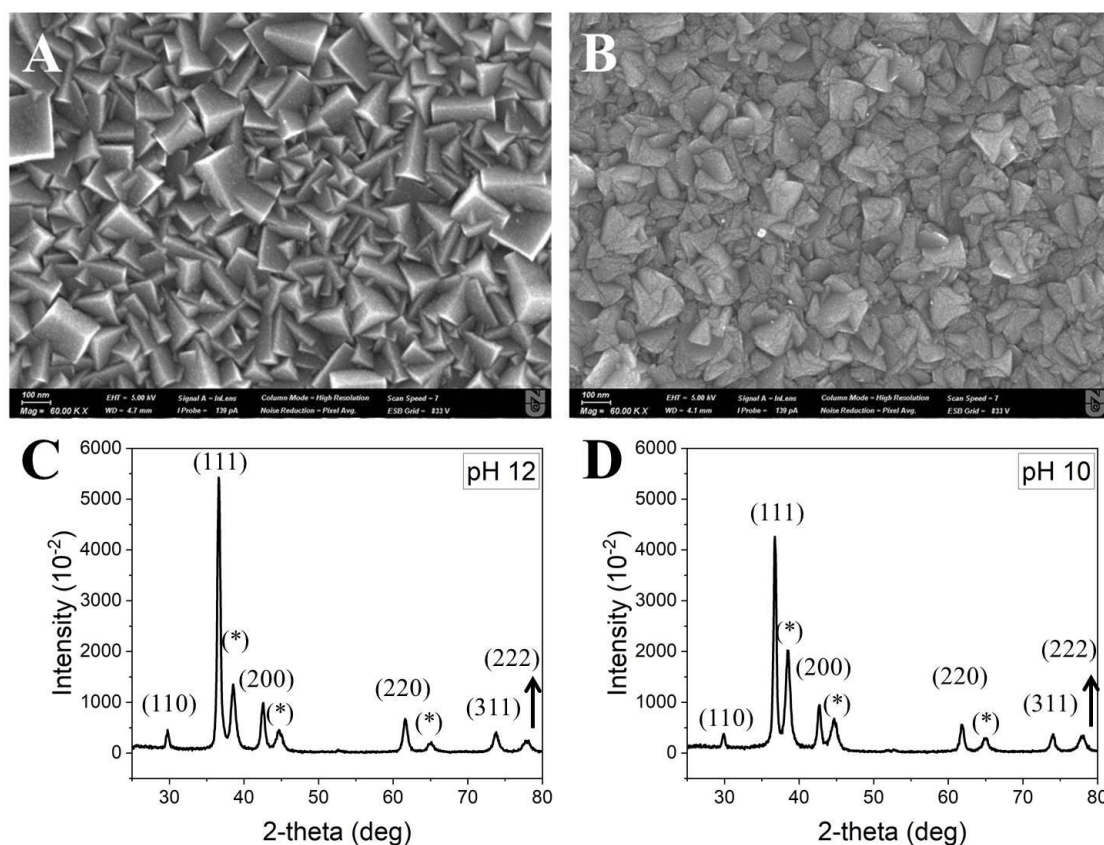


Figure 3. SEM images and XRD spectra of Cu_2O thin films grown by potentiostatic electrochemical deposition at $T = 30^\circ \text{C}$, WE potential -0.4 V and various pH 12 (A, C) and 10 (B, D).

Symbol * represents the signals from the substrate

From the SEM image (Fig. 3A), it is seen that the Cu_2O film electrodeposited at pH 12 consists from grains with cubic morphology and oriented along cubic diagonal. Figure 3C shows XRD pattern of this film. XRD confirmed that film is Cu_2O with cubic structure and there is preferential grain orientation, grains mostly grow along the direction perpendicular to the planes. However, SEM image of Cu_2O films grown pH 10 (Fig. 3B) does not reveal any cubical morphology. The morphology of this film is different from the morphology of the film grown at pH 12. Its grains have more irregular shape and their surfaces are rougher.

XRD confirmed the presence of Cu_2O structure and indicate the preferable grain orientation along [7] direction.

Further we investigated the electrical properties of electrodeposited Cu_2O films. In Figure 4, the resistivity of samples is plotted against the pH of the electrolyte used during fabrication. The graph reveals that the resistivity of the film decreases as the pH increases. For instance, the film prepared at pH 9 has a resistivity of approximately $5 \cdot 10^7 \Omega \cdot \text{cm}$, while the film prepared at pH 13 has a resistivity of about $4 \cdot 10^5 \Omega \cdot \text{cm}$. Therefore, the lowest resistivity is achieved at pH 13.0, which is two orders of magnitude lower than that of the film prepared at pH 9.0.

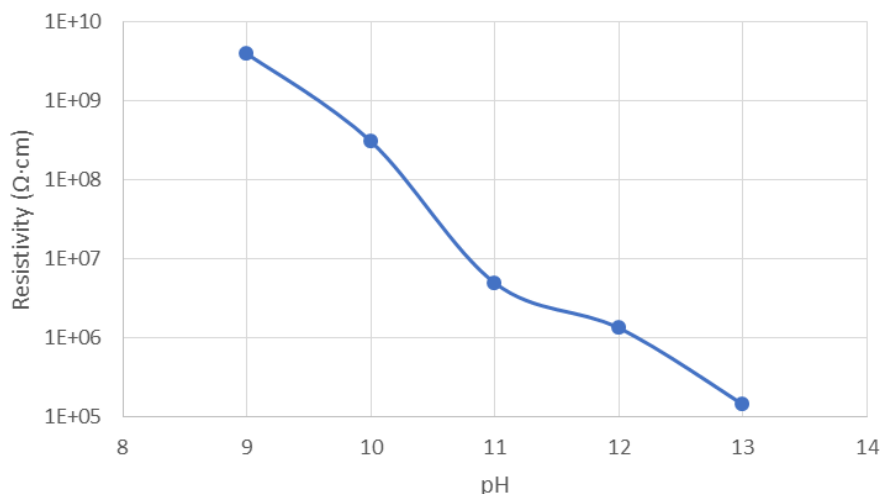


Figure 4. Variation of the resistivity of the films with pH

Finally, we fabricated the composite $\text{Cu}_2\text{O}/\text{CuSCN}$ thin films and studied the efficiency of the charge separation at the $\text{Cu}_2\text{O}/\text{CuSCN}$ interface by a photoelectric responses technique. For it, Cu_2O were deposited on the surface of CuSCN and photoelectric responses (PES) was measured. The Figure 5A represents SEM cross section image of a $\text{Cu}_2\text{O}/\text{CuSCN}$ composite film. The PES responses for bare and $\text{Cu}_2\text{O}/\text{CuSCN}$ composite were measured in order to compare photocurrent response from Cu_2O (Fig. 5B). The PES was measured in a three-electrode configuration. The electrolyte was a 1.0 M Na_2SO_4 solution buffered at pH 4.9 with potassium phosphate (0.1 M). The reference electrode was Ag/AgCl in saturated KCl , and a Pt wire was used as the counter electrode. The photoresponse was measured under chopped irradiation from an Ossila Solar Simulator with a light intensity 100 mW cm^{-2} . The scan rate for the linear sweep voltammetry was 10 mV s^{-1} [8, 9].

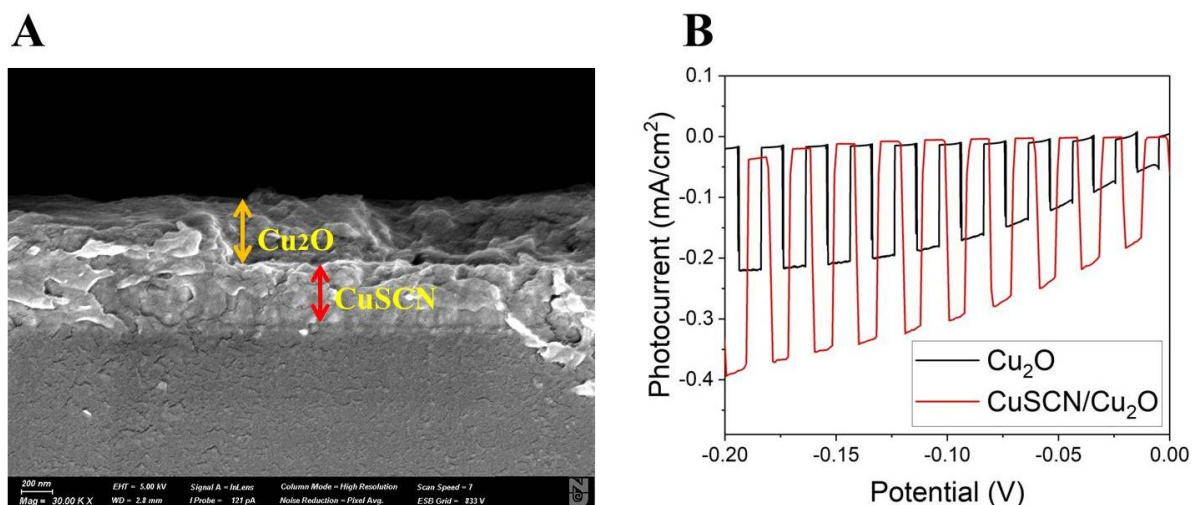


Figure 5. SEM cross-section image $\text{Cu}_2\text{O}/\text{CuSCN}$ thin film (A) and photoelectric responses from a bare Cu_2O and composite $\text{Cu}_2\text{O}/\text{CuSCN}$ films (B)

It seen that Cu₂O/CuSCN HTL has at least two times higher current density in comparison with bare Cu₂O, which indicate on improved charge separation at the Cu₂O/CuSCN. According the work L. Pan et al. a favourable band bending occurs at the CuSCN/Cu₂O interface, which also contributes to the enhanced charge separation, namely, the rapid extraction of holes from Cu₂O [8–10]. In our further study, these fabricated composite Cu₂O/CuSCN thin films will be optimized in order to use as HTL for organic and perovskite solar cells.

Conclusion

In conclusion, this study demonstrates the successful synthesis and characterization of CuSCN and Cu₂O as a potential hole transport layers for solar cells. The electrodeposition techniques utilized allow for precise control over film properties, leading to enhanced charge transport capabilities [11, 12]. Optimization of synthesis parameters, particularly for Cu₂O films, has been investigated to achieve low resistivity, crucial for their application in solar cell devices. Photoelectric response measurements further confirm the effectiveness of Cu₂O/CuSCN composite films in improving charge separation and surface reactivity. These findings provide valuable insights for the development of high-efficiency and stable solar cell devices. Future research may focus on further optimizing synthesis conditions and exploring doping strategies to overcome limitations and advance the practical application of these materials in photovoltaic technology [13–15].

Acknowledgments

The Science Committee of the Republic of Kazakhstan, which is part of the Ministry of Science and Higher Education, provided funding for this research (No. AP19576727).

References

- 1 Linfeng, P., Yuhang, L., Liang, Y., Dan, R., Kevin, S., & Michael, G. (2020). Cu₂O photocathodes with band-tail states assisted hole transport for standalone solar water splitting. *Nature Communications*, 318, <https://doi.org/10.1038/s41467-019-13987-5>
- 2 Tilley, S. (2019). Recent advances and emerging trends in photo-electrochemical solar energy conversion. *Adv. Energy Mater.*, 9, 1802877.
- 3 Paracchino, A., Laporte, V., Sivula, K., Grätzel, M., & Thimsen, E. (2011). Highly active oxide photocathode for photoelectrochemical water reduction. *Nat. Mater.*, 10, 456–461.
- 4 Morales-Guio, C., Tilley, D., Vrubel, H., Grätzel, M., & Hu, X. (2014). Hydrogen evolution from a copper(I) oxide photocathode coated with an amorphous molybdenum sulphide catalyst. *Nat. Commun.*, 5, 1–7.
- 5 Morales-Guio, G. et al. (2015). Photoelectrochemical hydrogen production in alkaline solutions using Cu₂O coated with earth-abundant hydrogen evolution catalysts. *Angew. Chemie — Int. Ed.*, 54, 664–667.
- 6 Tilley, D., Schreier, M., Azevedo, J., Stefiik, M., & Graetzel, M. (2014). Ruthenium oxide hydrogen evolution catalysis on composite cuprous oxide Water splitting photocathodes. *Adv. Funct. Mater.*, 24, 303–311.
- 7 Iuri, B.C.I.L. de Araujo, Vagner, S., & Rafael, G., (2008). Electrical Characterization of Cu/Cu₂O Electrodeposited Contacts. <https://doi.org/10.1149/1.2956056>
- 8 Paracchino, A., Brauer, J., Moser, J., Thimsen, E., & Graetzel, M. (2012). Synthesis and Characterization of High-Photoactivity Electrodeposited Cu₂O Solar Absorber by Photoelectrochemistry and Ultrafast Spectroscopy. *The Journal of Physical Chemistry C*, 116(13), 7341–7350. <https://doi.org/10.1021/jp301176y>
- 9 Wang, H., Xu, X., & Zhang, L. (2017). Interface engineering of highly efficient perovskite solar cells. *Science*, 358(6367), 1192–1197. <https://doi.org/10.1126/science.aao5325>
- 10 Liu, C., Xiao, C., & Cui, W. (2018). Stable perovskite solar cells with efficiency exceeding 24.8 % and 0.3-V voltage loss. *Science*, 360(6396), 1448–1452. <https://doi.org/10.1126/science.aam9361>
- 11 Chen, Y., Wu, T., & Liu, X. (2019). Simultaneous enhancement of efficiency and stability in perovskite solar cells by incorporation of CuSCN nanosheets as hole transport layer. *Nano Energy*, 59, 631–638. <https://doi.org/10.1016/j.nanoen.2019.01.065>
- 12 Li, Z., Shao, Y., & Li, D. (2020). Efficient perovskite solar cells using Cu₂O as hole transport material. *Solar Energy*, 198, 422–428. <https://doi.org/10.1016/j.solener.2020.01.073>
- 13 Park, M., Kim, J., & Jung, H. (2021). Enhanced efficiency and stability of perovskite solar cells with cuprous oxide hole transport layer. *Journal of Power Sources*, 503, 230174. <https://doi.org/10.1016/j.jpowsour.2021.230174>.
- 14 Yang, Y. et al. (2017). Progress in developing metal oxide nanomaterials for photoelectrochemical water splitting. *Adv. Energy Mater.*, 7, 1700555.
- 15 Serikova, T., Bizhanova, G, Hanlin, Hu, & Annie, Ng (2023). Recent Update on Perovskite / Organic Tandem Solar Cells. *Bulletin of the University of Karaganda — Physics.*, 3(111). <https://doi.org/10.31489/2023PH3/6-15>

Г.С. Сейсенбаева, Д.С. Қамбар, А.В. Завгородний, Б.Р. Ильясов

Электр тұндыру әдісімен синтезделген $\text{Cu}_2\text{O}/\text{CuSCN}$ жұқа композиттік пленкалардың интерфейсындағы зарядты бөлуді жақсарту

Бұл зерттеу күн батареялары үшін, атап айтқанда электродепозиция әдістерімен синтезделген мыс (I) тиоцианаты (CuSCN) және мыс оксиді (Cu_2O) үшін кемтіктерді тасымалдау қабаттарын (HTLs) синтездеуге және сипаттауға бағытталған. CuSCN және Cu_2O фотоэлектрлік құрылғыларда зарядты тиімді тасымалдау үшін перспективалы қасиеттерді ұсынады. Синтез процесі қажетті пленканың морфологиялары мен қасиеттеріне қол жеткізу үшін тұндыру параметрлерін дәл бақылауды қамтиды. Сипаттама әдістері, соның ішінде сканерлеуші электронды микроскоп (СЭМ), атомды-күштік микроскоп (АКМ) және ультракүлгін (УК) спектроскопия әдістері пленка морфологиясы мен оптикалық қасиеттері туралы түсінік береді. Cu_2O пленкалары үшін синтез параметрлерін оңтайландыру олардың электрлік қасиеттерін жақсарту үшін зерттелуде. Фотоэлектрлік реакцияны өлшеу $\text{Cu}_2\text{O}/\text{CuSCN}$ композиттік пленкаларының интерфейсында зарядтың бөлінуінің жақсарғанын көрсетеді. Бұл нәтижелер күн батареялары технологиясының дамуына ықпал етуі мүмкін. Сонымен қатар, зерттеу өз зерттеулерін әртүрлі рН деңгейлерінде электродепозициялау арқылы Cu_2O өндіруге дейін кеңейтеді. Сондай-ақ, сканерлеуші электронды микроскоп және рентген құрылымдық талдаулары тұндыру параметрлерінің пленка морфологиясы мен кристалл құрылымына әсерін анықтайды, бұл синтездің жеке тәсілдері туралы құнды түсінік береді. Тұтастай алғанда, бұл жан-жақты зерттеу кемтіктердің тасымалдау қабаттарының материалдарының синтезі мен оңтайландырылуын түсінуді жетілдіріп қана қоймайды, сонымен қатар жоғары тиімді және де тұрақты күн батареялары құрылғыларын жасау бойынша құнды ұсыныстар береді.

Кілт сөздер: күн батареялары, кемтікті тасымалдау қабаты, электр тұндыру, мыс тиоцианаты (I), мыс оксиді, синтездің оңтайлы шарттары, фотоэлектрлік жауап, бөлшектердің тасымалдануы.

Г.С. Сейсенбаева, Д.С. Қамбар, А.В. Завгородний, Б.Р. Ильясов

Улучшенное разделение зарядов на границе раздела тонких композитных пленок $\text{Cu}_2\text{O}/\text{CuSCN}$, синтезированных методом электроосаждения

Это исследование сосредоточено на синтезе и характеристике дырочных транспортных слоев (HTL) для солнечных элементов, в частности тиоцианата меди (I) (CuSCN) и окиси меди (Cu_2O), полученных методами электроосаждения. CuSCN и Cu_2O обладают многообещающими свойствами для эффективного переноса заряда в фотоэлектрических устройствах. Процессы синтеза включают точный контроль параметров осаждения для достижения желаемой морфологии и свойств пленки. Методы определения характеристик, включая сканирующий электронный микроскоп (СЭМ), атомно-силовой микроскоп (АСМ) и ультрафиолетовую (УФ)-спектроскопию, позволяют получить представление о морфологии пленки и оптических свойствах. Изучена возможность оптимизации параметров синтеза пленок Cu_2O для улучшения их электрических свойств. Измерения фотоэлектрического отклика указывают на улучшение разделения зарядов на границе раздела композитных пленок $\text{Cu}_2\text{O}/\text{CuSCN}$. Эти результаты могут способствовать развитию технологии солнечных элементов. Кроме того, в ходе исследования были определены возможности получения Cu_2O методом электроосаждения при различных уровнях рН. СЭМ- и рентгеноструктурный анализы выявляют влияние параметров осаждения на морфологию пленки и кристаллическую структуру, что дает ценную информацию для разработки индивидуальных подходов к синтезу. В целом, это всестороннее исследование не только углубляет понимание синтеза и оптимизации материалов дырочных транспортных слоев, но и дает ценные рекомендации по разработке высокоэффективных и стабильных устройств на солнечных элементах.

Ключевые слова: солнечные элементы, слои переноса дырок, электроосаждение, тиоцианат меди (I), окись меди, оптимальные условия синтеза, фотоэлектрический отклик, перенос частиц.

Information about the authors

Gulsaya Seisenbayeva — Researcher, Astana IT University, Astana, Kazakhstan; ORCID: <https://orcid.org/0009-0003-7004-4498>

Dinara Kambar — Researcher, Astana IT University, Astana, Kazakhstan; ORCID: <https://orcid.org/0000-0003-4742-2000>

Alexey Zavgorodniy — PhD, Astana IT University, Astana, Kazakhstan; ORCID: <https://orcid.org/0000-0002-3024-7237>

Baurzhan Ilyassov — PhD, associate professor, Astana IT University, Astana, Kazakhstan; ORCID: <https://orcid.org/0000-0003-4563-2004>

T.M. Mukametkali, A.K. Aimukhanov, A.K. Zeinidenov*

*Karaganda Buketov University, Scientific Center of nanotechnology and functional nanomaterials,
University str., 28, 100028 Karaganda, Kazakhstan*

**Corresponding author's e-mail: a.k.zeinidenov@gmail.com*

Phthalocyanine and metal phthalocyanine are hole transport buffer layers for perovskite solar cell fabrication

This approach allows you to more accurately evaluate the performance of solar panels and identify any problems or degradation in their operation. The LUMO value of mPc closer to the LUMO value of $\text{CH}_3\text{NH}_3\text{I}_3\text{PbCl}_x$ increased conversion energy and short circuit current density (J_{sc}), which reached a maximum value of 15.97 mA/cm² using the HTL layer of CuPc, and the open circuit voltage (V_{oc}) reached a maximum at 0.97 V. The change in J_{sc} corresponds to the fill factor (FF) change. The filling factor (FF) reached a maximum value of 67.35 % when using the HTL layer of CuPc and a minimum value (FF) of 54.23 % when using the HTL layer of H_2Pc . The lowest series resistance (R_1) and interface resistance (R_3) of 11.2 and 39.9 Ohms, respectively, were shown with the HTL layer of CuPc, Capacitive element CPE1 — 305 pF, Capacitive element CPE2 — 0.95 pF. CPE (Constant Phase Element) is an element used in equivalent circuits to describe the non-ideal dielectric properties of materials. The decrease in CPE1 may indicate a decrease in the heterogeneity of the dielectric properties of the perovskite material after coating with different HTL mPc layers. This may be due to changes in structure or mutual actions between layers as a result of exposure to differences in energy levels.

Keywords: Perovskite solar cells, hole transport layers, metalphthalocyanine, absorption spectra, photovoltaic properties, electrical impedance spectroscopy, ion migration.

Introduction

Phthalocyanine molecules have attracted widespread attention due to their outstanding thermal and chemical stability and other promising properties. This class of molecules is actively studied in various technologically important fields such as magnetism, sensing, and optoelectronics due to the diverse chemical composition and aromatic structure of the molecule. MPc macrocycles (M = Co, Cu, Ni, or Fe) have fourfold symmetry and are typically adsorbed with their molecular plane parallel to the surface on metal surfaces. In addition, MPc is often used as a protective coating for the photoactive perovskite layer, and its high thermal and chemical stability can be extremely beneficial for the operation of perovskite salt solar cells (PSCs) [1–4].

Perovskite solar cells have several advantages, such as high open circuit voltage and high conversion efficiency, due to a wide optical absorption spectrum. A typical perovskite solar cell design includes titanium oxide for electron transfer, a $\text{CH}_3\text{NH}_3\text{PbI}_3$ perovskite crystal as the photoactive layer, and a N'-octakis(4-methoxyphenyl)-9,9'-spirobi[9H-fluorene]-2,2',7 layer. 7'-tetramine (spiro-OMeTAD) for hole transfer. However, to improve the photovoltaic properties and chemical stability, there was a need to develop materials that could replace spiro-OMeTAD as the hole transport layer. In recent years, phthalocyanine complexes have begun to be used as organic semiconductors by modifying their molecular structure, including central metal chemical groups and electronic structures [5–7]. Phthalocyanine plays an important role in improving semiconductivity, charge carrier mobility, recombination-free carrier diffusion, and conversion efficiency.

However, complex synthesis processes and difficulties in purifying Spiro-OMeTAD lead to increased production costs. Moreover, due to the primary structure of Spiro-OMeTAD, all significant conversion efficiencies were achieved by adding dopants and impurities, which further increases the overall cost of the devices and reduces their stability. Due to this, significant efforts have been made to develop more affordable, impurity-free alternatives using simpler syntheses. Various design strategies and various types of impurity-free hole transport materials (HTM) have been developed. Our group first reported the use of cuprophthalocyanine (CuPc) with MoO_3 as a hybrid HTM, achieving an efficiency of 8.12 %.

Metal phthalocyanines (MPcs) offer exciting potential as p-type semiconductor materials for use as hole transport layer (HTL) materials in perovskite solar cells (PSCs). MPcs boast high electrical conductivity, catalytic activity, and exceptional chemical and thermal stability. Furthermore, the alignment of the valence band maximum (VBM) and conduction band minimum (CBM) levels of the MPC with the energy levels of the perovskite and counter electrodes ensures efficient device operation [8, 9]. This strong compatibility be-

tween the MPC and other layers of the perovskite solar cell significantly enhances its performance and stability.

Research has shown that direct contact between perovskite layers and MoO₃ causes an undesirable chemical reaction. P. Schulz and his team investigated the chemical and electronic structure of the MoO₃/MAPbI₃ interface. They discovered that direct contact of perovskite with MoO₃ leads to the reduction of MoO₃ to MoO₂. The alignment of energy levels at the perovskite/MoO₂ interface is not favorable for hole extraction. These findings were confirmed by F. Schulz and his colleagues. They studied the chemical reaction occurring at the boundary of the CH₃NH₃PbCl_xI_{3-x} and MoO₃ layer. Changing the valency of Mo in MoO₃ from Mo⁶⁺ to Mo⁴⁺ led to an increase in the concentration of MoO₂. The oxidation of Pb²⁺ to Pb⁴⁺ or the oxidation of 2I⁻ to I₂ is accompanied by a change in the valence of Mo from Mo⁶⁺ to Mo⁴⁺ [10]. This leads to the formation of regions with a high density of defects at the interface, which become recombination centers and reduce the performance of the perovskite solar cells.

To solve this problem, we applied a metal phthalocyanine (MPC) layer as an HTL interlayer. MPC has excellent charge transfer properties and can effectively act as an HTL. Selection and optimization of HTL layers are challenging tasks in the research and development of perovskite solar cells (PSCs). It is necessary to achieve a balance between electrical conductivity, hole permeability, stability, adhesion to the perovskite layer, and other factors to achieve high efficiency and stability of solar cells [11–14].

In this study, we propose adding an extra layer of phthalocyanine and its metal complexes between the perovskite and the hole-conducting MoO_x layer in order to enhance the efficiency and stability of perovskite solar cells (PSCs). Our plan is to investigate and optimize the composition and structure of phthalocyanine and its metal complexes, as well as various methods for their integration into perovskite material. Additionally, we intend to examine how phthalocyanine nanostructures and their metal complexes affect the efficiency of charge carrier transport in a perovskite solar cell.

Materials and Methods

Sample preparation and deposition process

The fabrication process of the perovskite solar cells (PSCs) involves several steps, including the preparation of substrates, deposition of the electron transport layer (ETL) and perovskite layer, and deposition of the hole transport layer (HTL) and electrode layers.

Substrate Preparation:

Glass substrates coated with a fluorine-doped tin oxide (FTO) layer are cleaned thoroughly using acetone, hot deionized water, and 2-propanol. Subsequently, UV-ozone treatment is performed.

Deposition of Electron Transport Layer (ETL):

A titanium dioxide (TiO₂) sol-gel solution is prepared by mixing titanium VI isopropoxide (TTIP), acetic acid, deionized water, isopropanol, and nitric acid. The solution is spin-coated onto the FTO-coated glass substrates and annealed at 500 °C to obtain a crystalline TiO₂ layer.

Deposition of Perovskite Layer:

A solution containing methylammonium iodide (MAI) and lead chloride (PbCl₂) dissolved in N,N-Dimethylformamide (DMF) solvent is prepared. This perovskite solution is spin-coated onto the TiO₂ surface at various speeds and annealed at 90 °C to form a crystalline perovskite layer.

Deposition of Hole Transport Layer (HTL): Metal phthalocyanine (MPC) is deposited as the HTL on the perovskite surface via thermal evaporation. Subsequently, a layer of molybdenum oxide (MoO_x) is thermally evaporated on top of the MPC layer.

Deposition of Electrode Layers: An anode layer of silver (Ag) is thermally evaporated onto the MoO_x layer to complete the device structure. Throughout the fabrication process, precautions are taken to perform all steps in a glove box filled with nitrogen to minimize exposure to moisture and oxygen, which could degrade the performance of the PSCs.

The structural formulas of MPC, MAI, and PbCl₂, as well as a diagram illustrating the fabrication steps of the perovskite solar cells (PSCs) and the structure of PSCs with energy diagrams of functional layers, are provided in Figure 1 for reference.

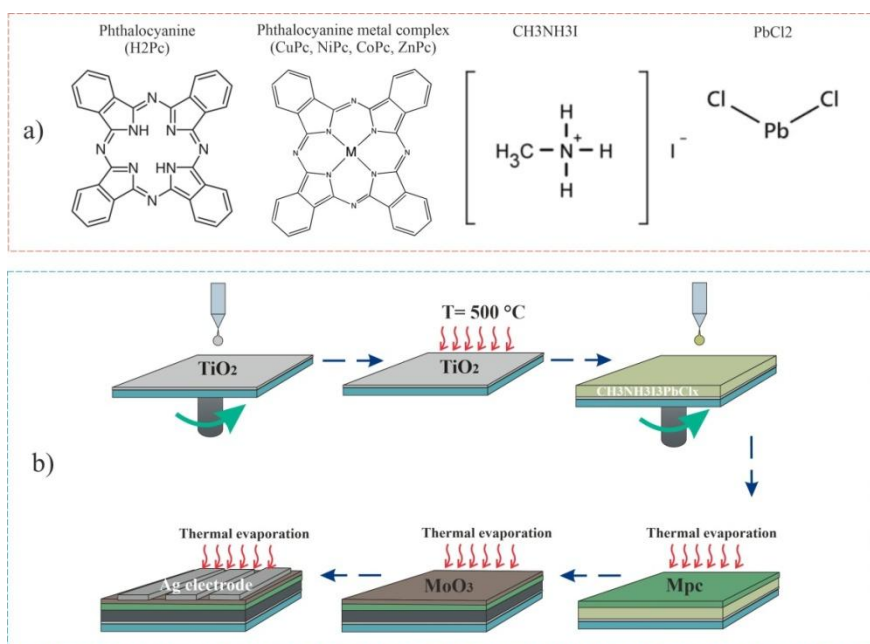


Figure 1. Structural formulas (a), a scheme of perovskite solar cell fabrication steps (b)

Analysis methods

The surface topography and thickness of the samples were probed using a JEOL JSPM-5400 atomic force microscope (AFM). The AFM data were processed using Gwyddion Data-Processing Software, a modular program for SPM (scanning probe microscopy) data visualization and analysis. To measure the local current distribution, an AFM Solver P47 (NT-MDT) was utilized. During current measurements, a voltage was applied to the sample, while the conductive probe covered with a gold film was grounded. The surface topography and root mean square (rms) roughness were measured in the semi-contact mode using an NSC14 probe from Micromash, while the current was measured in the contact mode using a CSC37/Au probe from Micromash.

The absorption spectra of the samples were measured using an AvaSpec-ULS2048CL-EVO spectrometer (Avantes). A combined deuterium-halogen light source AvaLight-DHc (Avantes) with an optical range of 200–2500 nm was employed as the light source. For thermal deposition, the CY-1700x-spc-2 vacuum sputtering unit (Zhengzhou CY Scientific Instruments Co., Ltd) was utilized.

The impedance spectra were measured using a P45X potentiostat-galvanostat with an FRA (frequency response analyzer) module. The current-voltage (I-V) characteristics of solar devices were measured using a PVIV-1A I-V Test Station under light illumination from a Sol3A Class AAA Solar Simulator (Newport).

Results and Discussion

Structural analysis of the prepared films

Figure 2 presents AFM images of the HTL layer's surface composed of various phthalocyanines and MoO₃, created through vacuum thermal deposition. The figure reveals that the HTL layer's surface morphology, when using different metal phthalocyanines and MoO₃, exhibits a granular structure with distinct boundaries. Given that the particle size is roughly equivalent to the film's thickness, it's evident that these films possess a greater number of defects and pores compared to others. For instance, CoPc films with a 250 nm thickness have an average particle size of 230 nm, suggesting a substantial amount of defects and pores. Conversely, CuPc films at 230 nm thickness have an average particle size of 110.9 nm, nearly half the film's thickness, indicating fewer defects and pores. Determining the average particle size in H₂Pc and MoO₃ films is challenging, as such structures' emergence could be attributed to the glass substrate's surface characteristics.

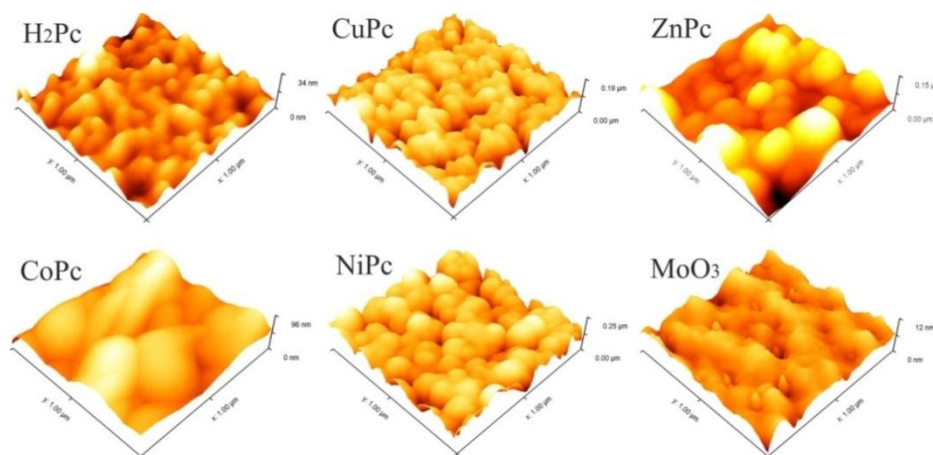


Figure 2. AFM images of hole-transport layers phthalocyanine (a) and molybdenum oxide

Table 1

Phthalocyanine and MoO₃ film roughness and particle size

Sample name	Thickness, nm	R_q , nm	d_{avg} , nm
H ₂ Pc	220	2.75	undetermined
CuPc	230	19.88	110
ZnPc	250	19.5	200
CoPc	250	9.37	230
NiPc	270	27.28	162
MoO ₃	60-70	1.11	undetermined

Optical properties

Figure 3 shows the absorption spectra of metal and nonmetal phthalocyanine nanostructures. The absorption spectra show two very intense bands in the region of 300–400 nm (B-band), which correspond to mixed π - π^* and n - π transitions $a_{2u} \rightarrow 2eg$ and $b_{2u} \rightarrow 2eg$, as well as an absorption band in the region of 550–750 nm (Q-range), which corresponds to the π - π^* transition $a_{1u} \rightarrow 2eg$ [15]. The absorption spectrum of a vacuum-deposited CuPc film (Fig. 3, curve 1) in the Soret region has a maximum at $\lambda=326$ nm, and in the Q-range, two bands are observed with maxima at $\lambda=616$ nm and $\lambda=692$ nm. The characteristic splitting of the absorption of nanostructures in the Q-range into two peaks is associated with Davydov splitting [16].

Understanding the optical absorption spectra of thin films is crucial for revealing the band structure and energy gap of both crystalline and amorphous structures. The substitution of metal ions in phthalocyanine, as well as the type of metal ions, can significantly alter the absorption and the position of the bands in these regions. Phthalocyanine films display distinct absorption spectra in the B-range around 300–350 nm and in the Q-range 550–650 nm, which are influenced by the metal complex [10, 16].

The graph in Figure 3 illustrates the spectral absorption distributions of thin PC films (1–3) within the 300–900 nm wavelength range. Notably, the films exhibited over 75 % transparency in the 400–500 nm and above 750 nm wavelength regions. It is worth mentioning that metal-free phthalocyanine (H₂Pc) and nickel phthalocyanine show a pronounced Q-band absorption region around 599 nm. Conversely, metal phthalocyanine thin films (CuPc and ZnPc) display a red-shift in these regions. Specifically, absorption peaks were observed at 321, 599, and 686 nm for H₂Pc, 321, 602, and 693 nm for CuPc, 330, 602, and 697 nm for ZnPc, 318, 600, and 693 nm for CoPc, and 327, 599, and 681 nm for NiPc.

The Tauc plot [17] was used to calculate the optical band gap of MPc films by plotting the dependence of $(\alpha h\nu)^2$ on photon energy for thin films of H₂Pc, CuPc, ZnPc, CoPc, and NiPc (Fig. 3b). It was found that the bandgap for metal-free thin films was approximately 1.63 eV. Moreover, the corresponding energies for CuPc, ZnPc, CoPc, and NiPc thin films were 1.60, 1.61, 1.65, and 1.67 eV, respectively, indicating a slight difference.

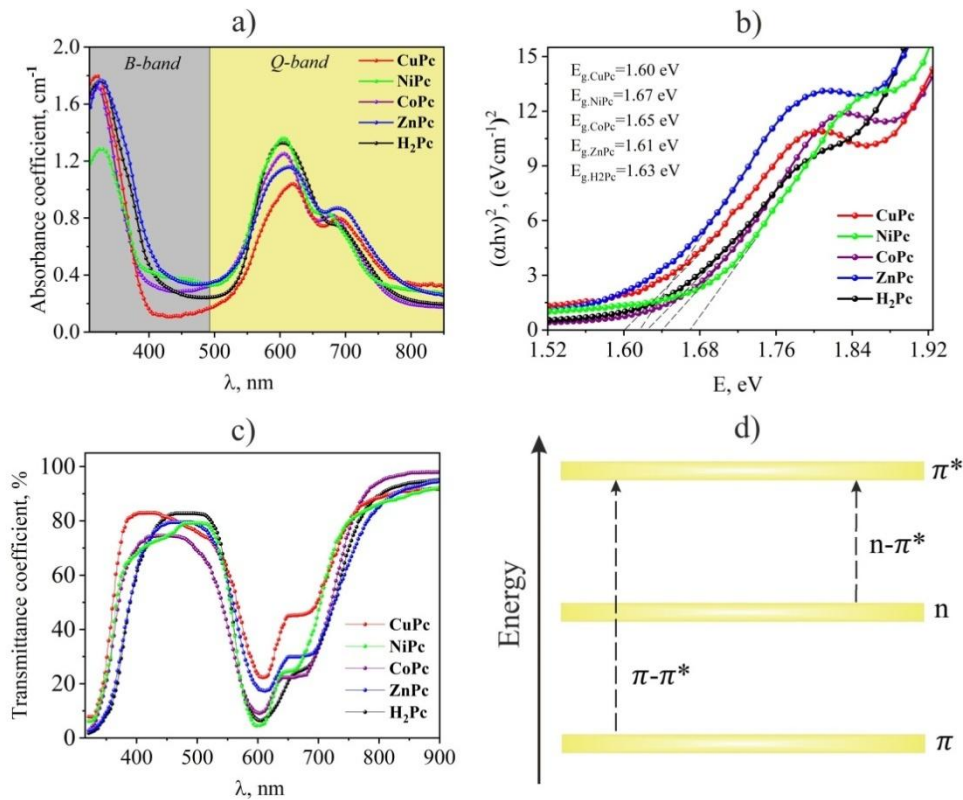


Figure 3. Phthalocyanine films absorbance coefficient (a), optical band gap (b), transmittance coefficient (c) and diagram of electronic transitions (d)

Table 2

Absorbance coefficient, optical bandgap, and transmittance coefficient

Sample name	B-band		Q-band		Band gap, eV	Transmittance (%) in λ=700 nm
	λ max, nm	FWHM, nm	λ max, nm	FWHM, nm		
H ₂ Pc	320.89	103.41	599.33	83.05	1.63	50
			686.49	107.49		
CuPc	321.04	79.21	602.21	85.06	1.60	70
			693.14	115.19		
ZnPc	329.70	90.02	601.70	88.11	1.61	50
			697.18	104.84		
CoPc	317.91	76.03	599.96	87.06	1.65	50
			692.67	73.69		
NiPc	327.23	66.84	598.71	75.92	1.67	70
			680.85	77.51		

Photoelectrical and Electrical Impedance Spectroscopy characterizations

From Figure 4 and Table 3, it can be seen that the lowest LUMO value for CuPc is -5.2 eV, which is closer to the LUMO of the photoactive layer, resulting in improved photovoltaic performance. The device with the HTL CuPc layer showed the highest performance with a power conversion efficiency (PCE) of 10.28 %. At the highest LUMO of -5.1 and -5.0 eV, the photovoltaic performance of PSCs showed lower values compared to devices based on more positive LUMOs.

Decreasing the LUMO value of Pc closer to the LUMO value of $\text{CH}_3\text{NH}_3\text{I}_3\text{PbCl}_x$ increased conversion energy and short circuit current density (J_{sc}), which reached a maximum value of 15.97 mA/cm² using the HTL layer of CuPc, and the open circuit voltage (V_{oc}) reached a maximum at 0.97 V. The change in J_{sc} corresponds to the fill factor (FF) change. The filling factor (FF) reached a maximum value of 67.35 % when using the HTL layer of CuPc and a minimum value (FF) of 54.23 % when using the HTL layer of H₂Pc.

All PSC functional layers, except the different HTL materials, were deposited under the same conditions, so the observed differences in photovoltaic performance are mainly due to the properties of the phthalocyanine HTL and the phthalocyanine/perovskite interface. The differences in the change in fill factor (FF) and hence J_{sc} are largely due to the change in HTL mPc conductivity caused by the change in HTL mPc. J_{sc} is also affected by the mPc/perovskite interface. It is well known that the compatibility of LUMO energy levels for Pc and LUMO for $CH_3NH_3I_3PbCl_x$ reduces its resistivity and increases the conductivity of the film. Therefore, matching the energy levels should lead to an increase in its conductivity, and in the device, this should improve the fill factor (FF) and increase J_{sc} .

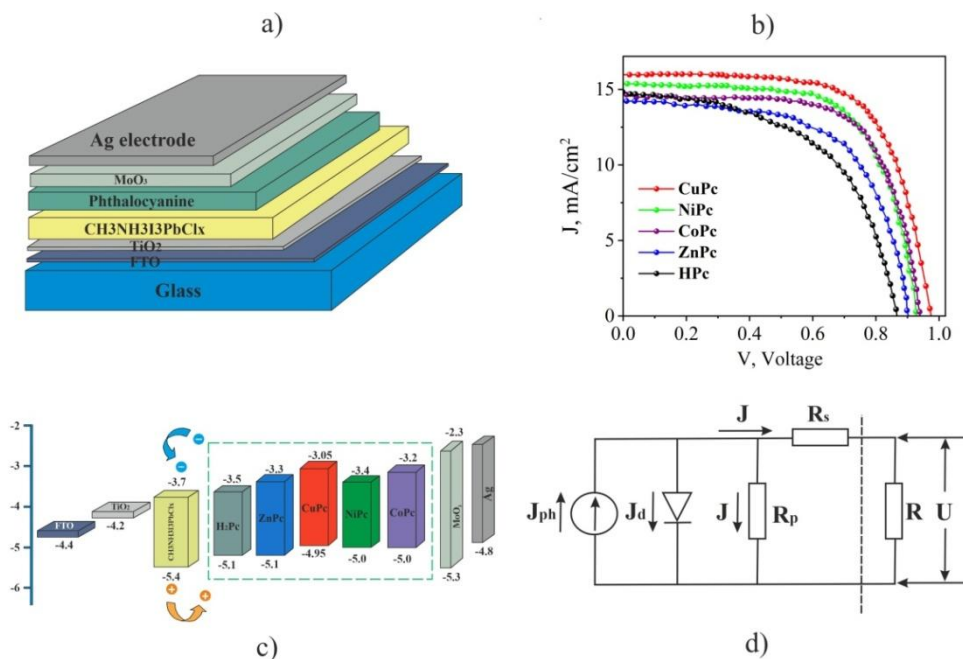


Figure 4. The structure of the device (a), current-voltage characteristics (b), energy diagram (c), and diagram of a single-diode model of the electrical characteristics of IOSC (d)

Table 3

Photovoltaic performance of perovskite solar cells

PSC's HTL	J_{sc} mA/cm ²	V_{oc} V	J_{max} mA/cm ²	V_{max} V	FF %	η %
CuPc	15.97	0.97	13.01	0.79	67.35	10.28
NiPc	15.38	0.94	12.47	0.75	66.39	9.35
CoPc	14.59	0.93	11.98	0.77	65.26	9.22
ZnPc	14.22	0.90	11.16	0.71	61.91	7.92
H ₂ Pc	14.76	0.87	10.88	0.64	54.23	6.96

To gain a detailed understanding of how the mPc HTL layer affects charge carrier transport mechanisms, we conducted impedance spectroscopy on perovskite solar cells. The impedance spectra were analyzed and fitted using the equivalent electrical circuit depicted in Figure 5a.

EIS is a non-destructive electrical characterization technique used to study the bulk and interface electrochemical dynamics of various materials with both electronic and ionic behavior, such as solar cells, various electrochemical electrodes, batteries, and fuel cells. EIS measures the resistive and capacitive behavior of an electrochemical system by applying an alternating current (AC) potential at different frequencies and measuring the AC response through the cell. EIS can be used in combination with light illumination to characterize solar cells under operating conditions. Various physical processes occurring in the device will manifest themselves in EIS responses at different characteristic frequencies.

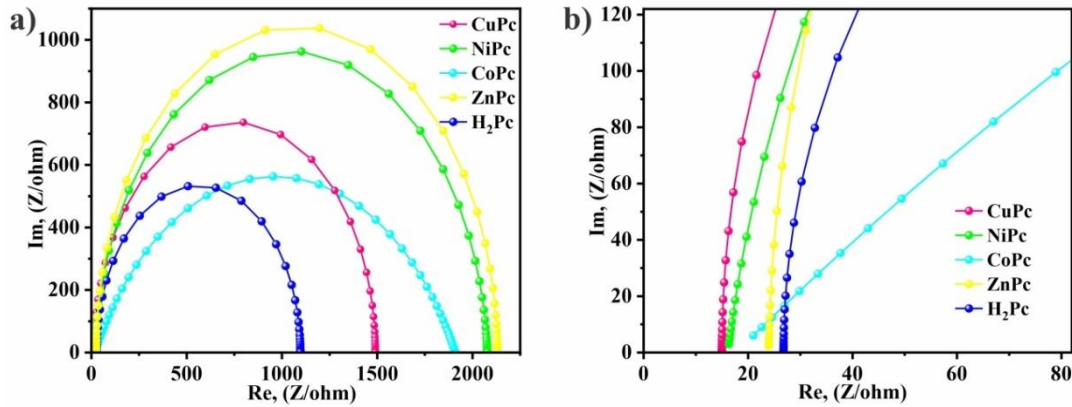


Figure 5. Nyquist impedance curves and equivalent circuit diagrams (insert) (a), and increased high-frequency region curves (b) for perovskite solar cells

To interpret the EIS, the dual time constant equivalent circuit model proposed by Garcia-Belmonte and colleagues [18, 19] is used. The circuit is a combination of a series of external resistance (R_1), including contact resistance, wire resistance, and electrode surface resistance, two non-ideal capacitive elements called constant phase elements (CPE_1 and CPE_2), and two resistive elements (R_2 and R_3). The constant phase element (CPE) impedance is given by:

$$Z_{pce} = \frac{1}{T(j\omega)^p} \quad (1)$$

T is a constant with unit $F \text{ cm}^{-2}$, and P is related to the purity angle. The capacitive element CPE_1 represents a non-ideal geometric capacitance and is related to the dielectric response of the perovskite layer, which dominates the capacitive response in the high-frequency region ($> 1 \text{ kHz}$) of the spectra. The second capacitive element CPE_2 is a low-frequency characteristic ($< 1 \text{ Hz}$) related to the accumulation of surface charge at the solar cell interfaces. The resistance R_2 is related to CPE_1 and is related to the charge transfer resistance of the bulk perovskite. This is also influenced by the low-frequency transport resistance R_3 is associated with many processes such as surface resistance, storage resistance at interfaces, as well as slow processes such as ion diffusion and resistance to trap-mediated charge recombination in the bulk.

So, it is possible to extract the parameters of the equivalent circuit under 8 mW/cm^2 LED illumination (solar simulator) from the provided experiment. These are the parameters:

The lowest series resistance (R_1) and interface resistance (R_3) of 11.2 and 39.9 Ohms, respectively, was shown with the HTL layer of CuPc, Capacitive element CPE_1 — 305 pF, Capacitive element CPE_2 — 0.95 pF. CPE (Constant Phase Element) is an element used in equivalent circuits to describe the non-ideal dielectric properties of materials. The decrease in CPE_1 may indicate a decrease in the inhomogeneity of the dielectric properties of the perovskite material after coating with different HTL mPc layers. This may be due to changes in structure or mutual actions between layers as a result of exposure to differences in energy levels.

These changes could be significant for optimizing the performance of perovskite solar cells and other devices utilizing perovskite materials. This is because the dielectric properties of the material can impact its electrochemical stability, energy conversion efficiency, and other important performance parameters. The increase in CPE_2 may be attributed to the accumulation of ions and electrons at the interfaces as shown in Table 4.

Table 4

The value of charge transport parameters of perovskite solar cells

PSC's HTL	R_1 , Ohm	R_2 , Ohm	R_3 , Ohm	p_1	n_1	p_2	n_2
CuPc	11.2	1478.8	39.9	$3.05 \cdot 10^{-10}$	1	$9.5 \cdot 10^{-13}$	0.03
NiPc	16.1	1642.9	428.6	$1.4 \cdot 10^{-10}$	0.96	$7.4 \cdot 10^{-7}$	0.72
CoPc	24.9	1723.4	339.3	$7.5 \cdot 10^{-11}$	1	$6.7 \cdot 10^{-10}$	0.86
ZnPc	24.0	1909.2	234.5	$7.3 \cdot 10^{-11}$	0.99	$4.9 \cdot 10^{-4}$	0.32
H ₂ Pc	27.47	986.6	110.9	$2.7 \cdot 10^{-10}$	1	$1.3 \cdot 10^{-12}$	0.11

Conclusions

The decrease in CPE_1 may indeed indicate a decrease in the heterogeneity of the dielectric properties of the perovskite material after coating with various layers such as HTL mPc. When coated with different layers, changes can occur in the structure of the perovskite material, as well as interactions between these layers, for example, as a result of differences in energy levels. These changes can affect the dielectric properties of the material, including its heterogeneity. Such analysis helps to understand what processes occur at the interface level and how they affect the electrical characteristics of perovskite solar cells.

The lowest series resistance (R_1) and interface resistance (R_3) of 11.2 and 39.9 Ohms, respectively, was shown with the HTL layer of CuPc, Capacitive element CPE_1 — 305 pF, Capacitive element CPE_2 — 0.95 pF. CPE (Constant Phase Element) is an element used in equivalent circuits to describe the non-ideal dielectric properties of materials. The decrease in CPE_1 may indicate a decrease in the inhomogeneity of the dielectric properties of the perovskite material after coating with different HTL mPc layers. This may be due to changes in structure or mutual actions between layers as a result of exposure to differences in energy levels [10, 20].

Such changes could be important for optimizing the performance of perovskite solar cells and other devices using perovskite materials since the dielectric properties of the material can affect its electrochemical stability, energy conversion efficiency, and other key performance parameters. The increase in CPE_2 may be due to the accumulation of ions and electrons at the interfaces.

Acknowledgments

This research is funded by the Science Committee of the Ministry of Science and Higher Education of the Republic of Kazakhstan (Grant No. AP19576784).

References

- 1 Wu, X. (2023). Realizing 23.9 % Flexible Perovskite Solar Cells via Alleviating the Residual Strain Induced by Delayed Heat Transfer. *ACS Energy Letters*, 8 (9), 3750–3759. [https://doi.org/10.1021/acsenergylett.3c01167](https://doi.org/10.1021/acseenergylett.3c01167)
- 2 Petraki, F., Papaefthimiou, V., & Kennou, S. (2005). A study of the Ni-phthalocyanine/gold interface using x-ray and ultraviolet photoelectron spectroscopies. *J. Phys., Conf. Ser.*, 10, 135. <https://doi.org/10.1088/1742-6596/10/1/033>
- 3 Zhou, Q., Liu, Z.-F., Marks, T.J., & Darancet, P. (2021). Electronic Structure of Metallophthalocyanines, MPc (M = Fe, Co, Ni, Cu, Zn, Mg) and Fluorinated MPc. *The Journal of Physical Chemistry A*, 125(19), 4055–4061. <https://doi.org/10.1021/acs.jpca.0c10766>
- 4 Zavgorodniy, A., Aimukhanov, A., Zeinidenov, A., & Akhatova, Zh. (2019). Study of the effect of an external magnetic field on the photoelectric properties of a copper phthalocyanine film. *Bulletin of the University of Karaganda-Physics*, 2019 (93) 1, 18–25. <https://doi.org/10.31489/2019Ph1/18-25>
- 5 Tağman, İ., Özçeşmeci, M., Gümrükçü, S., & Sorar, İ. (2021). Spectroscopic, electrochemical and optical properties of non-peripherally (2,2-dimethyl-1,3-dioxolan-4-yl)methoxy groups substituted metal-free and metallophthalocyanines, *Journal of Molecular Structure*, 1245, 131045, ISSN 0022-2860. <https://doi.org/10.1016/j.molstruc.2021.131045>
- 6 Park, N.G., Grätzel, M., Miyasaka, T. et al. (2016). Towards stable and commercially available perovskite solar cells. *Nat Energy*, 1, 16152. <https://doi.org/10.1038/nenergy.2016.152>
- 7 Grätzel, M., (2014). The light and shade of perovskite solar cells. *Nature Mater.*, 13, 838–842. <https://doi.org/10.1038/nmat4065>
- 8 Tazhibayev, S.K., Beisembekov, M.K., Rozhkova, X.S., Zhakanova, A.M., Aimukhanov, A.K., Makhabayeva, A.T., & Zeinidenov, A.K. (2023). Impact of the thickness of phthalocyanine films and its metal complexes on optical and electrical properties. *Bulletin of the University of Karaganda-Physics*, 112 (4), 14–22. <https://doi.org/10.31489/2023PH4/14-22>
- 9 Yang J.P., Meissner, M., Yamaguchi, T., Zhang, X.Y., Ueba, T., Cheng, L.W., Ideta, S., Tanaka, K., Zeng, X.H., Ueno, N., & Kera, S. (2018). Band dispersion and hole effective mass of methylammonium lead iodide perovskite, *Solar RRL*, 2. <https://doi.org/10.1002/solr.201800132>
- 10 Schulz, P., Tjepelt, J.O., Christians, J.A., Levine, I., Edri, E., Sanehira, E.M., Hodes, G., Cahen, D., & Kahn, A. (2016). High-Work-Function Molybdenum Oxide Hole Extraction Contacts in Hybrid Organic–Inorganic Perovskite Solar Cells. *ACS Appl. Mater. Interfaces*, 8, 46, 31491–31499. <https://doi.org/10.1021/acsami.6b10898>
- 11 Atsushi Suzuki, Hiroki Okumura, Yasuhiro Yamasaki, & Takeo Oku. Fabrication and characterization of perovskite type solar cells using phthalocyanine complexes. <https://doi.org/10.1016/j.apsusc.2019.05.305>
- 12 Suzuki, A., & Oku, T. (2017). Electronic structures, and optical and magnetic properties of quadruple-decker phthalocyanine, *Magnetochemistry*, 3. <https://doi.org/10.3390/magnetochemistry3020021>.

- 13 Guo, J.J., Bai, Z.C., Meng, X.F., Sun, M.M., Song, J.H., Shen, Z.S., Ma, N., Chen, Z.L., & Zhang, F. (2017). Novel dopant-free metallophthalocyanines based hole transporting materials for perovskite solar cells: the effect of core metal on photovoltaic performance, *Sol. Energy*, 155, 121–129. <https://doi.org/10.1016/j.solener.2017.05.089>.
- 14 Suzuki, A., Ueda, H., Okada, Y., Ohishi, Y., Yamasaki, Y., & Oku, T. (2017). Effects of metal phthalocyanines as hole-transporting layers of perovskite-based solar cells, *Chemical and Materials Engineering* 5, 34–42. <https://doi.org/10.13189/cme.2017.050203>.
- 15 Cao, G., Lia, L., Guana, M., Zhao, J., Li, Y., & Zeng, Y. (2011). Stable organic solar cells employing MoO₃-doped copper phthalocyanine as buffer layer, *Applied Surface Science*, 257, 9382–9385. <https://doi.org/10.1016/j.apsusc.2011.05.120>
- 16 Ghosh, P.N. (1976). Davydov splitting and multipole interactions. *Solid State Communications*, 19, 1. 7, 639-642, ISSN 0038-1098, [https://doi.org/10.1016/0038-1098\(76\)91093-0](https://doi.org/10.1016/0038-1098(76)91093-0).
- 17 Jubu, P.R., Obaseki, O.S., Nathan-Abutu, A., Yam, F.K., Yusof, Y., & Ochang, M.B. (2022). Dispensability of the conventional Tauc's plot for accurate bandgap determination from UV–vis optical diffuse reflectance data. *Results in Optics*, 9, 100273, ISSN 2666-9501. <https://doi.org/10.1016/j.rio.2022.100273>.
- 18 Zarazua, I., Han, G., Boix, P.P., Mhaisalkar, S., Fabregat-Santiago, F., Mora-Seró, I., Bisquert, J., & Garcia-Belmonte, G. (2016). Surface recombination and collection efficiency in perovskite solar cells from impedance analysis *J. Phys. Chem. Lett.*, 7, 5105. <https://doi.org/10.1021/acs.jpcclett.6b02193>
- 19 Zarazúa, I., Sidhik, S., Lopéz-Luke, T., Esparza, D., De la Rosa, E., Reyes-Gomez, J., Mora-Seró, I., & Garcia-Belmonte, G. (2017). Operating Mechanisms of Mesoscopic Perovskite Solar Cells through Impedance Spectroscopy and J-V Modeling. *J. Phys. Chem. Lett.*, 8, 6073. <https://doi.org/10.1021/acs.jpcclett.7b02848>
- 20 Kayumova, A., Savilov, S., Zhanbirbayeva, P., Baltabekov, A., Dzhakupova, M., & Serikov, T. (2023). Effect of TNR/Ag/rGO film area on its photocatalytic activity. *Bulletin of the University of Karaganda-Physics*, 2023(112)4, 6–13. <https://doi.org/10.31489/2023ph4/6-13>

Т.М. Мұқаметқали, А.К. Аймуханов, А.К. Зейниденов

Фталоцианин және металл фталоцианин кемтік тасымалдаушы буферлік қабаттарын перовскит күн батареяларын өндіруге пайдалану

Бұл тәсіл күн батареяларының өнімділігін дәлірек бағалауға және олардың жұмысындағы кез келген проблемаларды немесе деградацияны анықтауға мүмкіндік береді. Фото активті қабат CH₃NH₃I₃PbCl_x LUMO мәніне жақын кемтік тасымалдаушы mPc LUMO мәні түрлендіру энергиясын және қысқа тұйықталу ток тығыздығын (J_{sc}) арттырды, ол CuPc кемтік тасымалдау қабатын пайдаланып 15,97 мА/см² максималды мәнге жетті және ашық тізбек кернеуі (V_{oc}) максимум 0,97 В-қа жетті. J_{sc} өзгерісі толтыру коэффициентінің (FF) өзгеруіне сәйкес келеді. Толтыру коэффициенті (FF) CuPc НТЛ қабатын пайдаланған кезде ең жоғары мәнге 67,35 % және H₂Pc НТЛ қабатын пайдаланған кезде ең төменгі мәнге (FF) 54,23 % жетеді. Ең төменгі сериялық кедергі (R₁) және интерфейс кедергісі (R₃) сәйкесінше 11,2 және 39,9 Ом CuPc НТЛ қабатымен, CPE₁ сыйымдылық элементі — 305 пФ, CPE₂ сыйымдылық элементі — 0,95 пФ көрсетілді. CPE (тұрақты фазалық элемент) — материалдардың идеалды емес диэлектрлік қасиеттерін сипаттау үшін эквивалентті тізбектерде қолданылатын элемент. CPE₁ төмендеуі әртүрлі НТЛ mPc қабаттарымен қапталғаннан кейін перовскит материалының диэлектрлік қасиеттерінің гетерогенділігінің төмендеуін көрсетуі мүмкін. Бұл құрылымның өзгеруіне немесе энергия деңгейлеріндегі айырмашылықтардың әсерінен қабаттар арасындағы өзара әрекеттерге байланысты болуы мүмкін.

Кілт сөздер: перовскитті күн батареялары, өткізгіштік кемтігі бар қабат, металлфталоцианин, жұтылу спектрлері, фотоэлектрлік қасиеттері, импеданс спектроскопиясы, иондардың кезуі.

Т.М. Мұқаметқали, А.К. Аймуханов, А.К. Зейниденов

Перовскитные солнечные элементы с использованием фталоцианина и его металлокомплексов в качестве слоя с дырочной проводимостью

Указанный в работе подход позволяет более точно оценить работу солнечных панелей и выявить любые проблемы или деградацию в их работе. Уменьшение значения LUMO для mPc ближе к значению LUMO для CH₃NH₃I₃PbCl_x привело к увеличению энергии переобразования и плотности тока короткого замыкания (J_{sc}), которая достигла максимального значения в 15,97 мА/см² при использовании НТЛ слоя CuPc, а напряжение холостого хода (V_{oc}) достигло максимума в 0,97 В. Изменение J_{sc} соответствует изменению коэффициента заполнения (FF). Коэффициент заполнения (FF) достиг максимального значения в 67,35 % при применении НТЛ слоя CuPc и минимального значения в 54,23 % при использовании НТЛ слоя H₂Pc. Самое низкое последовательное

сопротивление (R_1) и сопротивление интерфейса (R_3) составили 11,2 и 39,9 Ом соответственно, показав лучший результат при использовании HTL слоя CuPc. Емкостные элементы — CPE_1 -305 пФ и CPE_2 -0,95 пФ. CPE (Constant Phase Element) является элементом, используемым в эквивалентных схемах, для описания неидеальных диэлектрических свойств материалов. Уменьшение CPE_1 может указывать на сокращение неоднородности диэлектрических свойств перовскитного материала после покрытия различными HTL слоями mPc. Это может быть связано с изменениями в структуре или взаимодействием между слоями из-за разницы в энергетических уровнях.

Ключевые слова: перовскитные солнечные элементы, слой с дырочной проводимостью, металлофталониан, спектры поглощения, фотоэлектрические свойства, импедансная спектроскопия, миграция ионов.

Information about the authors

Mukametkali Toktarbek — Master of physics, Doctoral student of the Department of Radiophysics and Electronics, Researcher, Karaganda Buketov University, Scientific Center of Nanotechnology and Functional Nanomaterials, Karaganda, Kazakhstan; e-mail: tmk625@mail.ru; ORCID: 0000-0003-2685-2976

Zeinidenov Assylbek — PhD, Associate professor, Dean of the Physics and Technology Faculty, Head of Scientific Center for Nanotechnology and Functional Nanomaterials, Karaganda Buketov University, Karaganda, Kazakhstan; e-mail: asyl-zeinidenov@mail.ru ORCID: 0000-0001-9780-5072

Aimukhanov Aitbek — Candidate of physical and mathematical sciences, Associate professor, Professor of the Department of Radiophysics and Electronics, Leading Researcher, Karaganda Buketov University, Scientific Center for Nanotechnology and Functional Nanomaterials, Karaganda, Kazakhstan; e-mail: a_k_aitbek@mail.ru ORCID: 0000-0002-4384-5164

G.K. Alpysova¹, D.A. Afanasyev^{1*}, Zh.K. Bakiyeva¹, L.A. Lisitsyna²,
M.G. Golkovski³, A.K. Tussupbekova¹, A.A. Kissabekova⁴, S.D. Tuleuov¹

¹Karaganda Buketov University, Karaganda, Kazakhstan;

²Tomsk State University of Architecture and Building, Tomsk, Russia;

³Budker Institute of Nuclear Physics of the Siberian Branch of the Russian Academy of Sciences, Novosibirsk, Russia;

⁴Pavlodar Pedagogical University named after A. Margulan, Pavlodar, Kazakhstan

*Corresponding author's e-mail: a_d_afanasyev@mail.ru

Optical properties of ZnWO₄ ceramics obtained by radiation synthesis

One of the promising methods for producing ceramics from tungstate metals of the MWO₄ composition is radiation synthesis using powerful electron fluxes. Due to the unique properties of radiation, it was possible to significantly accelerate the synthesis process. It has been demonstrated that ZnWO₄ ceramics can be synthesized by acting on an electron flux with an energy from 1.4 to 2.5 MeV and a high power density of 10–25 kW/cm². In this regard, studies of the optical properties of ceramic samples of zinc tungstate ZnWO₄ obtained by this method were carried out. The morphology of the surface, X-ray diffraction spectra and optical properties of ZnWO₄ ceramics obtained by radiation synthesis were studied. X-ray diffraction measurements and EDX analysis confirmed the formation of zinc tungstate ceramics ZnWO₄ as a result of radiation synthesis. The absorption, luminescence, and luminescence excitation spectra of synthesized samples were measured. Luminescence spectra of a reference single crystal sample were also measured. X-ray diffraction confirmed the formation of zinc tungstate (ZnWO₄) as a result of radiation synthesis. The luminescent spectra of the synthesized sample coincide with the spectra of crystalline ZnWO₄. A comparison of the luminescence spectra of a synthesized ceramic sample and a monocrystalline reference sample measured under different optical excitation conditions shows significant differences in the luminescence spectra of the synthesized sample and the reference sample and indicates possible various defects present in the compared samples.

Keywords: ceramics; luminescence; radiation synthesis; zinc tungstate, X-ray diffraction spectra, EDX analysis, power density, optical properties of ceramics.

Introduction

Most scintillation materials used in ionizing radiation detectors are used in single crystal form. It is known that growing scintillation crystals with high melting point is a labor-intensive and expensive process [1]. One of the promising approaches is the replacement of single crystals by ceramic materials, for example, on the basis of alumina yttrium garnet Y₃Al₅O₁₂ (YAG) with metal tungstate ceramics, the study of which has been carried out for quite a long time [2–5]. Due to their unique scintillation properties, such as isotropy, possibility of giving any shapes [2–7], advantages over monocrystalline materials, optical ceramic materials are promising scintillators and detectors and are characterized by high efficiency, mechanical and thermal stability. In contrast to technologies for the creation of single-crystalline materials, ceramic technology offers the possibility of fabricating highly transparent and large-sized samples at lower synthesis temperatures with homogeneous or controlled gradient distribution of activator ions [8–16], which is its undoubted advantage. Nevertheless, today the technological peculiarities of creating ceramic materials are still the subject of active study.

Metal tungstates of alkaline-earth and transition group metals of the composition MWO₄ (M — Zn, Mg, Ca, Mn, Ca, etc.) with a tungstate structure have long been of practical interest because of their attractive luminescence [17, 18]. ZnWO₄ has been applied as a possible new material for microwave amplification by stimulated emission [19], scintillator [20, 21] and optical hole grating material [22], etc. Recently, new applications of this material have emerged, including large-scale bulk scintillators for high-energy physics [23]. In particular, ZnWO₄ is a wide bandgap semiconductor with a bandgap width close to 4 eV [24] and is a promising material for new generation radiation detectors.

However, there are still many questions that require further study of these materials, so in a number of studies proved the existence of nanodefects confirmed by studies of luminescence LiF:WO₃, MgF₂:WO₃, metal tungstates [25, 26]. In crystals of tungstate luminescence is caused by the existence of their own lattice defects, in crystals of alkaline-earth metal fluorides luminescence is caused by defects introduced with tungsten [27, 28].

Due to the complex of certain properties, luminescent materials are widely used. As a rule, such substances function under conditions of high external loads and therefore they should be resistant to thermal, mechanical, radiation effects. The most promising is the use of ceramic materials, which accumulate the advantages of crystalline and glassy materials. However, the process of synthesizing ceramics from refractory compounds is rather complex, involves many steps, time- and energy- consuming. Many existing technologies for the synthesis of ceramics from refractory materials, focused on a particular type of compounds, are characterized by low reproducibility. There is a need to develop new synthesis methods that are more universal, efficient and controllable. It is possible to significantly accelerate the synthesis of refractory optical materials by stimulating solid-phase reactions in the radiation field. It can be expected that the inclusion of new effects in the synthesis process, reactions between intermediate products of radiolysis, will not only increase their speed, but also open up new possibilities for the creation of composite materials.

One of the promising methods of synthesis of ceramics with metal tungstate of composition MWO_4 is the method of radiation synthesis in the field of powerful electron fluxes. It is supposed to use a powerful flow of high-energy electrons to affect wide-gap refractory materials. In dielectric materials, the main share of radiation (99 %) is spent on the creation of electronic excitations. At high power density (up to 30 kW/cm^2), high electron energies, more than 1 MeV, high ionization density and high concentration of intermediate products of radiolysis are created in the material volume, which leads to the development of effective diffusion processes, solid-phase and gas-phase reactions in the charge of precursor powders. This feature is supposed to be used in the proposed project for the synthesis of promising luminescent materials for LED's, scintillators, dosimeters. The possibility of synthesis is demonstrated on the example of synthesis of scintillation material based on MgF_2 activated by tungsten, YAG:Ce phosphor ceramics [29].

It is necessary to know their optical properties of scintillation materials for using them. Therefore, the work was carried out to study the optical properties of synthesized ceramic samples of zinc tungstate $ZnWO_4$ synthesized by radiation synthesis.

Experimental

Zinc tungstate ceramics ($ZnWO_4$) were used in this work. These samples were obtained by radiation synthesis from WO_3 , ZnO powders at the UNU Stand ELV-6 electron beam accelerator at the G.I. Budker Institute of Nuclear Physics of the Siberian Branch of the Russian Academy of Sciences (G.I. Budker Institute of Nuclear Physics of SB RAS). Electron beams with energies ranging from 1.4 to 2.5 MeV were used. These electron fluxes are sufficient for synthesis of samples with sizes up to 15 cm^3 . More details on the technique of sample synthesis can be found in [29]. The single crystal $ZnWO_4$ was also used as a reference standard.

X-ray diffractograms of the samples were obtained using a Bruker D8 ADVANCE diffractometer equipped with a scintillation detector. Sample identification was performed using a database of powder diffraction files, and indexing was performed using EVA software (Bruker, 2007) and using literature data [30].

The surface structure of tungstates was investigated. The study was carried out on a scanning electron microscope (SEM) Mira 3 (TESCAN). To prepare the material for the study, the samples were fixed on a special conductive tape. Since the investigated samples are dielectrics, the samples were coated with a conductive layer of carbon on a Quorum Q150R ES sputtering machine. The study was carried out at an accelerating voltage of 25 kV. Secondary electrons (SE (secondary electrons) detector) and back scattered electrons (BSE, back scattered electrons) detectors were used. The EDX detector, INCAPentaFET-x3, Oxford Instruments, England, was used for EDX analysis.

Absorption, luminescence and luminescence excitation spectra were measured using an AvaSphere 50-HAL-12V integrating sphere, AvaSpec- ULS2048BCL-EVO spectrometer (Avantes, Netherlands) and AvaLight DH-S deuterium-halogen light source were used to measure absorption spectra. Luminescence and photoluminescence excitation spectra were measured on a SM 2203 Solar spectrofluorimeter. Luminescence spectra were also measured using an AvaSpec-ULS2048BCL-EVO spectrometer with two types of excitation sources UV region of mercury lamp emission obtained with UVS6 filter (ultraviolet glass number six) and 355 nm laser AO-355A-1W.

Results and Discussion

Initially, the surface morphology of the synthesized ceramics was studied (Fig. 1). The sample has a heterogeneous structure and there are microparticles on the surface of the sample of various shapes and sizes. These particles may be the particles from which the ceramics were synthesized.

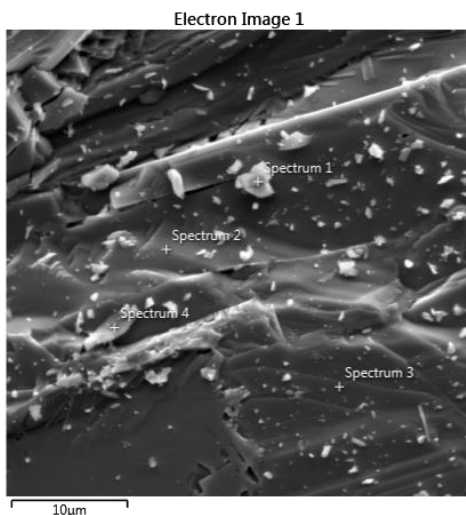


Figure 1. SEM images of the surface of zinc tungstate sample

The EDX spectrum of the sample surface was measured. The EDX spectra confirm the presence of W (1.8, 8.2, 9.5 keV, etc.), Zn (1, 8.5 and 9.5 keV) and O peaks (0.5 keV), Figure 2. The stoichiometric composition of the samples obtained from the measurements is given in Table, where, G — a mass concentration of elements, At — an atomic concentration of elements, σ — a standard deviation of the measured value. The stoichiometric composition was determined from averaged data.

Table

EDX analysis data of zinc tungstate sample

Element	G , %	σ	At , %
Zn	18,3	2,12	13,3
W	57,4	2,58	14,8
O	24,3	3,17	71,9

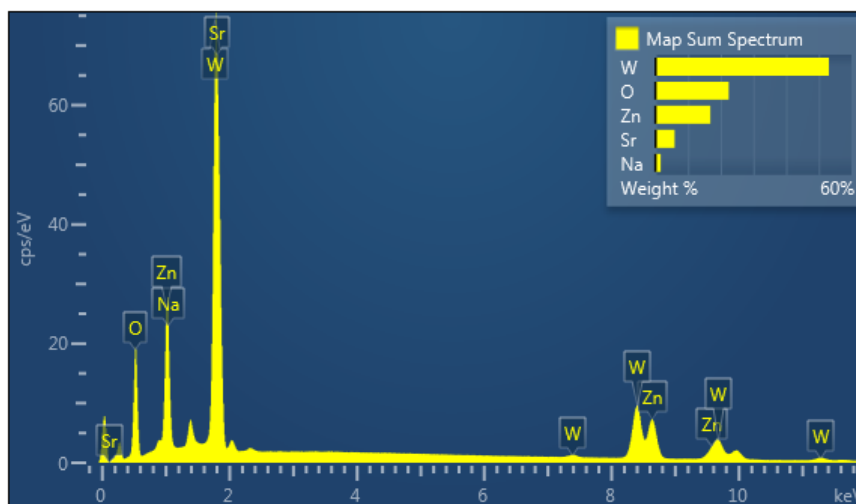


Figure 2. Energy-scattering characteristic X-ray spectra of the sample

According to the atomic concentrations of elements in the sample, the stoichiometric composition of the sample was estimated. It amounted to $ZnW_{1,12}O_{5,43}$. This composition does not significantly differ from the required composition of $ZnWO_4$. The discrepancy can be related both to the accuracy of EDX analysis and possible changes in the composition of ceramics.

The measurement map of the EDX spectra is shown in Figure 3. The elemental composition is shown in Figure 4. Comparison of the data shows that the distribution of tungsten and oxygen is uniform. While zinc

is not evenly distributed on the surface in the microstructure having predominantly green color in Figure 3 zinc content is reduced. In the rest of the map it is distributed quite uniformly. Thus, it can be said that the microstructure with reduced zinc content may be various tungsten oxide compounds WO_2 , WO_3 and possibly intermediate oxides $W_{20}O_{56}$ and $W_{18}O_{49}$ [31].

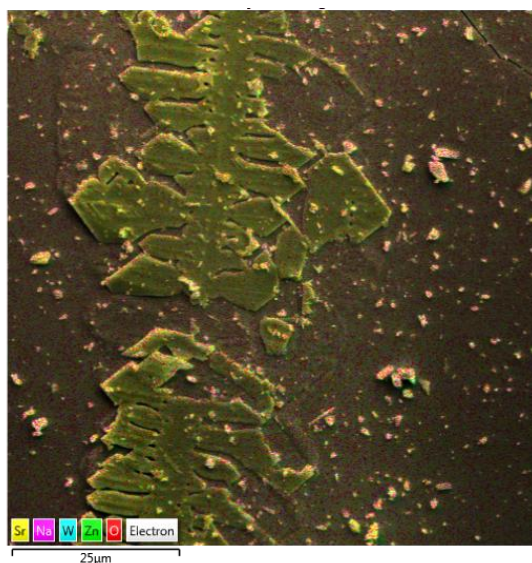


Figure 3. Map of EDX analysis of the sample composition surface

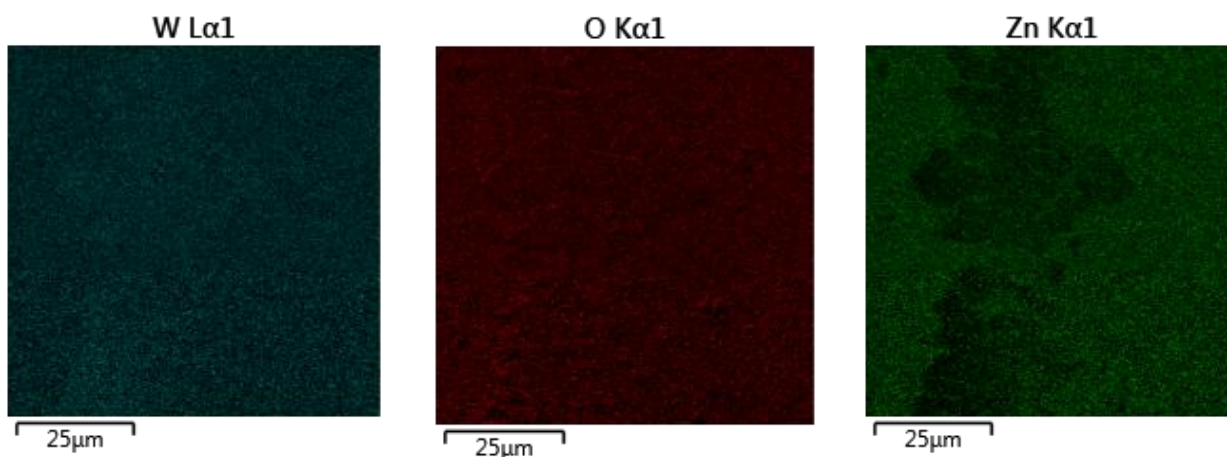


Figure 4. Map of distribution of elements (W, O, Zn) on the surface of the sample

X-ray diffractogram of zinc tungstate $ZnWO_4$ was obtained (Fig. 5).

In Figure 5, all diffraction peaks can be attributed to $ZnWO_4$ using a standard map (JCPDS map No. 73-0554). No peaks from other crystallized phases were observed, which also indicated the formation of $ZnWO_4$ crystals [30].

X-ray diffraction and elemental composition measurements confirmed the formation of zinc tungstate $ZnWO_4$ by radiation synthesis.

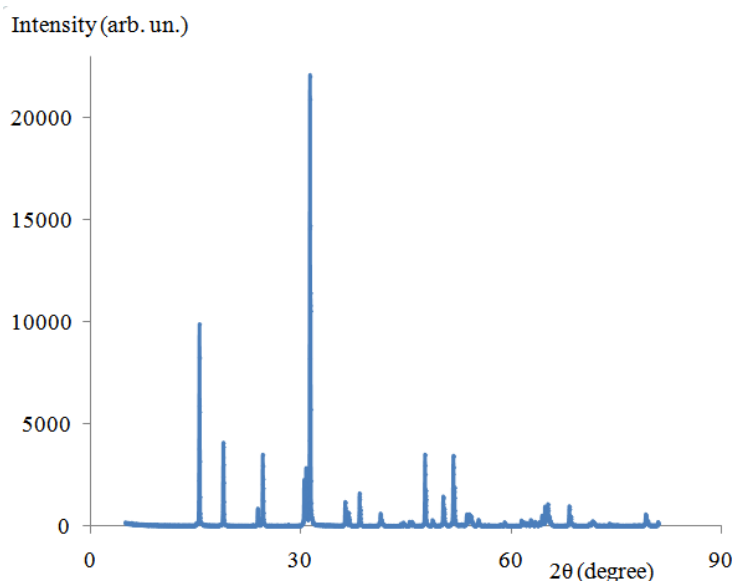


Figure 5. X-ray diffractogram of ZnWO₄

Optical properties of the ceramics were investigated. Absorption spectra were measured for the sample (Fig. 6). Since the samples are opaque absorption spectra cannot be measured by standard methods. Therefore, the measurements were performed using an AvaSphere 50-HAL-12V integrating sphere and an AvaSpec-ULS2048BCL-EVO spectrometer. The AvaLight-DH-S compact combined deuterium-halogen light source was used as a light source.

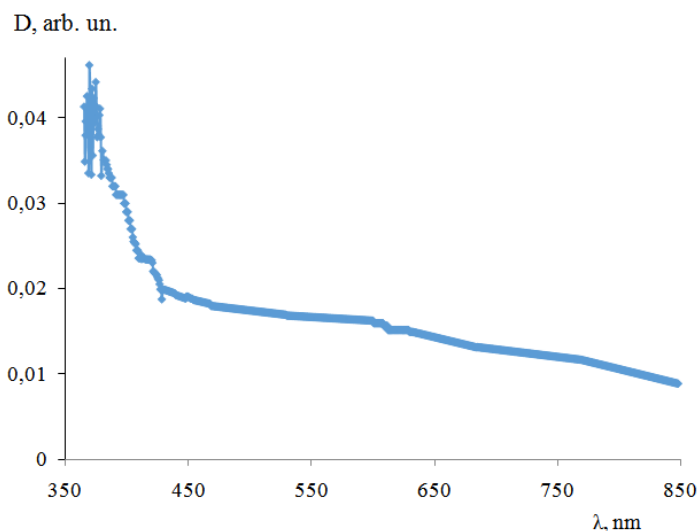


Figure 6. Absorption spectrum of zinc tungstate in the wavelength range from 350 to 1100 nm

Measurement of absorption spectra showed an increase in the optical density of the samples starting from 450 nm to 350 nm. A similar increase in the intensity of the optical density of ZnWO₄ samples was also observed in [32]. It is shown that initially observed growth of optical density of ZnWO₄ crystal from 420 nm to 340 nm is associated with the presence of impurities such as iron and/or chromium [32], further from 340 nm there is an intense growth of optical density of the crystal associated with the fundamental absorption of ZnWO₄ [32, 33].

The absorption spectrum in the range from 200 nm to 350 nm could not be recorded due to the low intensity of the excitation source in this region of the spectrum. For better measurement of absorption spectra in the UV region of the spectrum, a more powerful UV source is needed.

From the absorption spectra, the energy of transitions associated with absorption in the region from 350 to 450 nm was determined. It amounted to 2.25 eV. This value may indicate the possible absorption of de-

fects in synthesized ceramics ZnWO_4 since the width of the forbidden zone of the forbidden zone (E_g), according to literature data is 3.98 eV [33].

Luminescence and luminescence excitation spectra were measured. The luminescence excitation and luminescence spectra are shown in Figures 7 and 8, respectively.

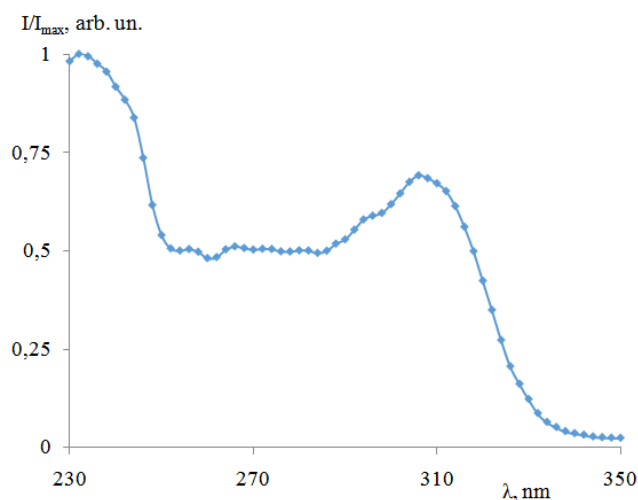


Figure 7. Excitation spectrum of ZnWO_4 luminescence with signal detection in the luminescence maximum at 494 nm

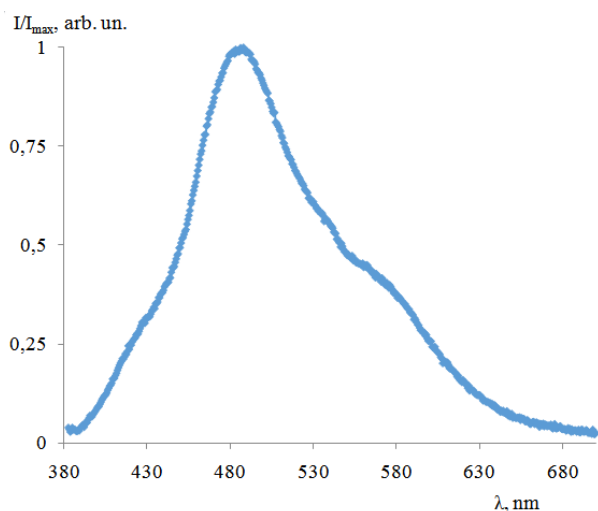


Figure 8. Luminescence spectrum of ZnWO_4 under excitation by a mercury lamp at $\lambda_{\text{max}} = 490$ nm (250–320 nm) (1) and spectrum under excitation by a laser source at 355 nm (2)

In the excitation spectrum, a band in the region from 200 to 260 nm is observed. A band in the region of 300–320 nm with a maximum at 310 nm is also observed.

Luminescence spectra of the samples obtained at excitation in the region of 250–320 nm under excitation by a mercury lamp have the following characteristics: maximum luminescence intensity $\lambda_{\text{max}} = 494$ nm, half-width of the luminescence spectrum $\Delta\lambda_{1/2} = 46$ nm. Luminescence spectra at excitation of samples at 355 nm (AO-355A-1W) shifted to the red region of the spectrum relative to the luminescence spectra of samples excited at 250–320 nm are observed. The maximum luminescence intensity and half-width of the luminescence spectrum were: $\lambda_{\text{max}} = 496$ nm, $\Delta\lambda_{1/2} = 64$ nm. The shift is 2 nm.

The presence of optical density growth in the absorption spectrum from 400 nm to 350 nm with a calculated transition energy of 2.25 eV, as well as the presence of luminescence of the sample when excited by a laser excitation source at 355 nm shows the presence of deep defect levels. Additional information can be obtained by comparing the luminescence spectra of the synthesized ZnWO_4 sample with the reference single-crystal ZnWO_4 sample.

The luminescence spectra of a reference sample of single crystal ZnWO₄ were measured. The spectrum of the reference sample is shown in Figure 9 (a, b).

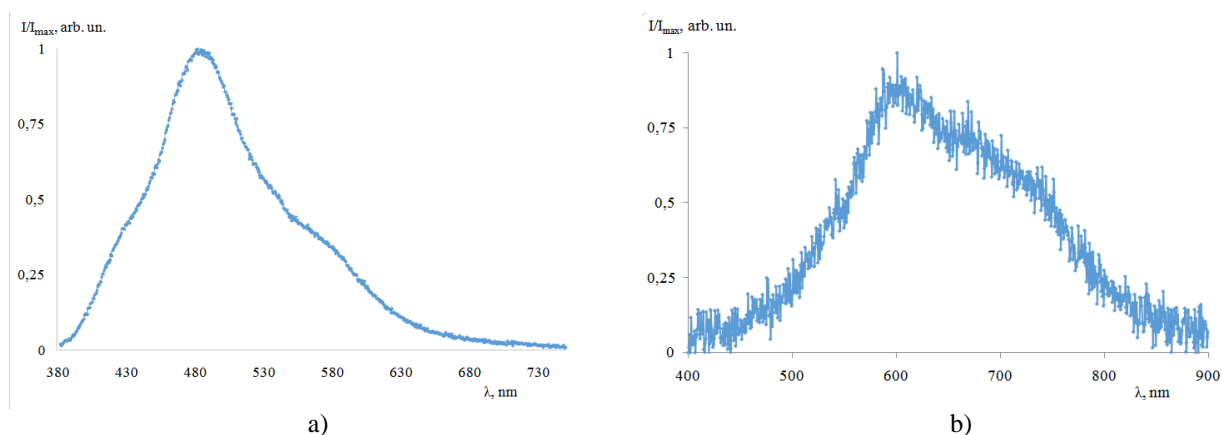


Figure 9. Luminescence spectrum of single crystal ZnWO₄ sample under luminescence excitation by mercury lamp (a) and laser excitation source (b)

In the case of the reference ZnWO₄ sample, the shift of the luminescence intensity maximum is more than 100 nm between the spectrum obtained under excitation by a mercury lamp $\lambda_{\max 1} = 490$ nm (250–320 nm) and the spectrum under excitation at 355 nm $\lambda_{\max 2} = 600$ nm. This is an additional indirect factor indicating high defectivity of ZnWO₄ samples synthesized by the radiation method synthesis. Significant differences in the luminescence spectra of the synthesized sample and the reference sample indicate possible different defects present in the compared samples.

Conclusion

Thus, the surface morphology, EDX analysis, X-ray diffraction spectra and optical properties of ZnWO₄ ceramics obtained by radiation synthesis were studied.

On the surface of synthesized ceramic samples there are microparticles of different shapes and sizes. These particles may be the particles from which the synthesis of ceramics was carried out. The distribution of tungsten and oxygen is uniform on the surface of the sample. Zinc is not uniformly distributed over the surface. It is possible that the areas with reduced zinc content may contain various tungsten oxide compounds.

X-ray diffraction measurements confirmed the formation of zinc tungstate ZnWO₄ by radiation synthesis.

The optical properties of ceramics were investigated. From the absorption spectra the energy value of transitions related to absorption in the region from 350 to 450 nm. It amounted to 2.25 eV. This energy value may indicate a significant presence of defects in the synthesized sample.

The luminescence spectra of the synthesized sample correspond to those of crystalline ZnWO₄. Comparison of luminescence spectra of the synthesized ceramic sample and single-crystal reference sample measured under different conditions of optical excitation indicate significant differences in the luminescence spectra of the synthesized sample and reference sample indicating possible different defects present in the compared samples.

This research was funded by the Science Committee of the Ministry of Science and Higher Education of the Republic of Kazakhstan (Grant No. AP 19579177).

References

- 1 Shi, F. (2012). Ceramic Materials. Progress in Modern Ceramics, 242.
- 2 Lu, B., Li, J.G., Suzuki, T.S., Tanaka, H., Sun, X.D., & Sakka, Y. (2015). Effects of Gd substitution on sintering and optical properties of highly transparent (Y_{0.95-x}Gd_xEu_{0.05})₂O₃. *Ceramics. J. Am. Ceram. Soc.*, 98(8), 2480–2487. DOI: 10.1111/jace.13627

- 3 Karipbaev, Zh., Musakhanov, D., Lisitsyn, V., Golkovskii, M., Lisitsyna, L., Tulegenova, A., Akylbekov, A., Dauletbekova, A., Balabekov, K., Kozlovskii, A., & Usseinov, A. (2019). Synthesis, the study of the structure of YAG and YAGG phosphors in the radiation field. *Bulletin of the University of Karaganda-Physics*, 4(96), 24–29. DOI: <http://dx.doi.org/10.31489/2019Ph4/24-29>
- 4 Deulina, D., Paygin, V., Alishin, T., Stepanov, S., Valiev, D., Dvilis, E., Khasanov, O., & Ilela, A. (2023). Characterization of YAG:Ce ceramics with graphene oxide. *Bulletin of the University of Karaganda-Physics*, 3(111), 151–155. DOI: <https://doi.org/10.31489/2023ph3/151-155>
- 5 Maoqing, C., Zewang, H., Maxim, I., Jiawei, D., Chaoyu, L., Huamin, K., Yun, Sh., Haohong, Ch., Jiayue, X., Yubai, P., & Jiang, L. (2018). Effect of Gd substitution on structure and spectroscopic properties of (Lu, Gd)₂O₃:Eu ceramic scintillator. *Optical Materials*, 76, 323. DOI: <https://doi.org/10.1016/j.optmat.2017.12.053>
- 6 Maoqing, Cao et al. (2017). Fabrication and characterizations of (Lu, Gd)₂O₃: Eu scintillation ceramics. *Ceramics International*, Vol. 43(2), 2165–2169. DOI: <https://doi.org/10.1016/j.ceramint.2016.10.198>
- 7 Seeley, Z.M. et al. (2012). Phase stabilization in transparent Lu₂O₃:Eu ceramics by lattice expansion. *Optical Materials*, 35(1), 74–78. DOI: <https://doi.org/10.1016/j.optmat.2012.07.005>
- 8 Ikesue, A., Aung, Y.L., Taira, T., Kamimura, T., Yoshida, K., & Messing, G.L. (2006). Progress in Ceramic Lasers. *Annu. Rev. Mater. Res.*, 36, 397–429. DOI: <https://doi.org/10.1146/annurev.matsci.36.011205.152926>
- 9 Zych, E., Brecher, C., Wojtowicz, A.J., & Lingertat, H. (1997). Luminescence properties of Ce-activated YAG optical ceramic scintillator materials. *Journal of Luminescence*, 75(3), 193–203. DOI: [https://doi.org/10.1016/S0022-2313\(97\)00103-8](https://doi.org/10.1016/S0022-2313(97)00103-8)
- 10 Solomonov, V.I., Orlov, A.N., Spirina, A.V., Konev, S.F., Cholakh, S.O., & Lukyashin, K.E. (2014). Divalent ytterbium ions in yttrium aluminum garnet and yttrium oxide ceramics. *Optics and Spectroscopy*, 117(6), 908–913. DOI: <http://dx.doi.org/10.1134/S0030400X14110186>
- 11 Osipov, V.V., Ishchenko, A.V., Shitov, V.A., Maksimov, R.N., Lukyashin, K.E., Platonov, V.V., Orlov, A.N., Osipov, S.N., Yagodin, V.V., Viktorov, L.V., & Shulgin, B.V. (2017). Fabrication, optical and scintillation properties of transparent YAG: Ce ceramics. *Optical Materials*, 71, 98–102. DOI: <https://doi.org/10.1016/j.optmat.2016.05.016>
- 12 Bagayev, S.N., Osipov, V.V., Solomonov, V.I., Shitov, V.A., Maksimov, R.N., Lukyashin, K.E., Vatik, S.M., & Vedin, I.A. (2012). Fabrication of Nd³⁺:YAG laser ceramics with various approaches. *Optical Materials*, 34(8), 1482–1487. DOI: <https://doi.org/10.1016/j.optmat.2012.03.004>
- 13 Osipov, V.V., Shitov, V.A., Solomonov, V.I., Lukyashin, K.E., Spirina, A.V., & Maksimov, R.N. (2015). Composite Nd:YAG/Cr⁴⁺:YAG transparent ceramics for thin disk lasers. *Ceramics International*, 41, 13277–13280. DOI: <https://doi.org/10.1016/j.ceramint.2015.07.109>
- 14 Tasoltan, T.B., Basieva, I.T., & Doroshenko, M.E. (2011). Luminescent nanophotonics, fluoride laser ceramics, and crystals. *Phys.–Usp.*, 54, 1262. DOI: 10.3367/UFNe.0181.201112j.1334
- 15 Schauer, P. (2011). Optimization of decay kinetics of YAG:Ce single crystal scintillators for S(T)EM electron detectors. *Nuclear Instruments and Methods in Physics Research*, 269, 2572–2577. DOI: <https://doi.org/10.1016/j.nimb.2011.07.013>
- 16 Maslov, V.A., Fedorov, P.P., Voronov, V.V., Shcherbakov, V.V., Chernova, E.V., & Osiko, V.V. (2012). Fluoride micropowders for laser ceramics. *Inorg. Mater. Appl. Res.*, 3(2), 113. DOI: <http://dx.doi.org/10.1134/S2075113312020128>
- 17 Zhu, Y.C., Lu, J.G., Shao, Y.Y., et al. (1986). Measurements of the scintillation properties of ZnWO₄ crystals. *Nucl. Instrum. Methods A*, 244, 579–581. DOI: [https://doi.org/10.1016/0168-9002\(86\)91089-2](https://doi.org/10.1016/0168-9002(86)91089-2)
- 18 Grabmaier, B.C. (1984). Crystal scintillators. *IEEE Trans. Nucl. Sci.*, 31, 372–376. DOI: <https://doi.org/10.1109/TNS.1984.4333280>
- 19 Uitert, L.G.V., & Preziosi, S. (1962). Zinc Tungstates for Microwave Maser Applications. *Journal Applied Physics*, 33(9), 2908–2909. DOI: <https://doi.org/10.1063/1.1702581>
- 20 Schofield, P.F., Knight, K.S., & Cressey, G. (1996). Neutron Powder Diffraction Study of the Scintillator Material ZnWO₄. *Journal Material Science*, 31(11), 2873–2877. DOI: <https://doi.org/10.1007/BF00355995>
- 21 Krutyak, N., Mikhailin, V.V., Spassky, D., Tupitsyna, I.A., & Dubovik, A.M. (2012). Luminescent properties of MgWO₄ crystals. *IEEE International Conference on Oxide Materials for Electronic Engineering (OMEE)*, 235–236. DOI: 10.1109/OMEE.2012.6464745
- 22 Caprez, P., Meyer, P., Mikhail, P., & Hulliger, J. (1997). New host-lattices for hyperfine optical hole burning: Materials of low nuclear spin moment. *Material Research Bull.*, 32(8), 1045–1054. DOI: [https://doi.org/10.1016/S0025-5408\(97\)00070-6](https://doi.org/10.1016/S0025-5408(97)00070-6)
- 23 Klassen, N., Shmurak, S., Red'kin, B., Ille, B., Lebeau, B., Lecoq, P., & Schneegans, M. (2002). Correlations between Structural and Scintillation Characteristics of Lead and Cadmium Tungstates. *Nuclear Instrument Methods Physics Research A*, 486(1-2), 431–436. DOI: [https://doi.org/10.1016/S0168-9002\(02\)00748-9](https://doi.org/10.1016/S0168-9002(02)00748-9)
- 24 Itoh, M., Fujita, N., & Inabe, Y. (2006). X-Ray Photoelectron Spectroscopy and Electronic Structures of Scheelite- and Wolframite-Type Tungstate Crystals. *Journal Physics Society Japanese*, 75, 084705–084712. DOI: 10.1143/JPSJ.75.084705
- 25 Lisitsyna, L.A., Oleshko, V.I., Putintseva, S.N., & Lisitsyn, V.M. (2008). Pulsed cathodoluminescence of irradiated LiF-O and LiF(U)-O crystals. *Optics and Spectroscopy*, 105(4), 531. DOI: 10.1134/S0030400X0810007X
- 26 Lisitsyna, L.A., Kassymkanova, R.N., Esil'baev, D.B., & Dauletbekova, A.K. (2013). Influence of polyvalent metal ions on formation processes of radiation defects in LiF crystals. *Physics of the Solid State*, 55(5), 11, 2297. DOI: <http://dx.doi.org/10.1134/S1063783413050211>
- 27 Lisitsyn, V.M., Lisitsyna, L.A., Tulegenova, A., Ju, Y., Polissadova, E.F., Lipatov, E., & Vaganov, V. (2019). Nanodefects in YAG:Ce-based phosphor microcrystals. *Crystals*, 9(9), 476. DOI: <http://dx.doi.org/10.3390/cryst9090476>

- 28 Lisitsyn, V.M., Lisitsyna, L.A., & Polissadov, E.F. (2019). Nanodefects in Highly Imperfect Optical Crystals. *Bulletin of the Russian Academy of Sciences Physics*, 83(3), 336–342. DOI: <http://dx.doi.org/10.3103/S1062873819030134>
- 29 Lisitsyn, V.M., Tulegenova, A., Golkovski, M., Polissadova, E.F., Lisitsyna, L.A., Mussakhanov, D., & Alpysova, G.K. (2023). Radiation Synthesis of High-Temperature Wide-Bandgap Ceramics. *Micromachines*, 14(12), 2193. DOI: <https://doi.org/10.3390/mi14122193>
- 30 Guan, B.K., Hu, L.L., Zhang, G.H., et al. (2014). Facile synthesis of ZnWO₄ nanowall arrays on Ni foam for high performance supercapacitors. *RSC Advances*, 4(9), 4212–4217. DOI: <http://dx.doi.org/10.1039/c3ra45866k>
- 31 Weil, M., & Schubert, W.-D. (2013). The Beautiful Colours of Tungsten Oxides. *Tungsten*, 1–12.
- 32 Kraus, H., Mikhailik, V.B., Ramachers, Y., Day, D., Hutton, K.B., & Telfer, J. (2005). Feasibility study of a ZnWO₄ scintillator for exploiting materials signature in cryogenic WIMP dark matter searches. *Physics Letters B*, 610(1-2), 37–44. DOI: <https://doi.org/10.1016/j.physletb.2005.01.095>
- 33 Ruiz-Fuertes, J., López, S., López-Solano, J., Errandonea, D., Segura, A., Lacomba-Perales, R., Munoz, A., Radescu, S., Rodriguez, P., Gospodinov, M.M., & Nagornaya, L.L. (2012). Pressure effects on the electronic and optical properties of AWO₄ wolframites (A = Cd, Mg, Mn, and Zn): The distinctive behavior of multiferroic MnWO₄. *Phys. Rev B*, 86(12), 125202. DOI: <http://dx.doi.org/10.1103/PhysRevB.86.125202>

Г.К. Алпысова, Д.А. Афанасьев, Ж.К. Бакиева, Л.А. Лисицына,
М.Г. Голковский, А.К. Тусупбекова, А.А. Кисабекова, С.Д. Тулеуов

Радиациялық синтез арқылы алынған ZnWO₄ керамикасының оптикалық қасиеттері

MWO₄ құрамындағы вольфрамат металдарынан керамика алудың перспективалы әдістерінің бірі — бұл электрондардың қуатты ағындарын пайдалана отырып, радиациялық синтез әдісі. Сәулеленудің бірегей қасиеттерінің арқасында синтез процесін айтарлықтай жеделдету мүмкін болды. ZnWO₄ керамикасы энергиясы 1,4-тен 2,5 МэВ-ға дейінгі және қуаты 10–25 кВт/см² жоғары тығыздықтағы электрондар ағынына әсер ету жолымен синтезделуі мүмкін екендігі көрсетілді. Осыған байланысты осы әдіспен алынған ZnWO₄ мырыш вольфраматының керамикалық үлгілерінің оптикалық қасиеттеріне зерттеулер жүргізілді. Жұмыста беткі қабаттың морфологиясы, рентген дифракциясының спектрлері және радиациялық синтез әдісімен алынған ZnWO₄ керамиканың оптикалық қасиеттері зерттелді. Рентген дифракциясын өлшеу және EDX талдау радиациялық синтез нәтижесінде ZnWO₄ мырыш вольфраматы керамикасының қалыптасуын растады. Синтезделген үлгілердің сіңіру, люминесценция, люминесценцияны қоздыру спектрлері өлшенді. Сондай-ақ эталондық монокристалдық үлгідегі люминесценция спектрлері өлшенді. Рентген дифракциясы радиациялық синтез нәтижесінде мырыш (ZnWO₄) вольфраматының пайда болуын растады. Синтезделген үлгінің люминесценттік спектрлері кристалды ZnWO₄ спектрлерімен сәйкес келеді. Оптикалық қоздырудың әртүрлі жағдайларында өлшенген синтезделген керамикалық үлгінің және монокристалдық эталондық үлгінің люминесценция спектрлерін салыстыру синтезделген үлгінің және эталондық үлгінің люминесценция спектрлеріндегі елеулі айырмашылықтарды және салыстырылатын үлгілерде болуы мүмкін әртүрлі ақауларды көрсетеді.

Кілт сөздер: керамика, люминесценция, радиациялық синтез, мырыш вольфраматы, рентген дифракциясының спектрлері, EDX-талдау, қуат тығыздығы, керамиканың оптикалық қасиеттері.

Г.К. Алпысова, Д.А. Афанасьев, Ж.К. Бакиева, Л.А. Лисицына,
М.Г. Голковский, А.К. Тусупбекова, А.А. Кисабекова, С.Д. Тулеуов

Оптические свойства ZnWO₄ керамики, полученной методом радиационного синтеза

Один из перспективных методов получения керамики из металлов вольфрамата состава MWO₄ — это радиационный синтез с использованием мощных потоков электронов. Благодаря уникальным свойствам излучения удалось значительно ускорить процесс синтеза. Было продемонстрировано, что керамика ZnWO₄ может быть синтезирована путем воздействия на поток электронов с энергией от 1,4 до 2,5 МэВ и высокой плотностью мощности 10–25 кВт/см². В связи с этим были проведены исследования оптических свойств керамических образцов вольфрамата цинка ZnWO₄, полученных данным методом. В статье были изучены морфология поверхности, спектры рентгеновской дифракции и оптические свойства керамики ZnWO₄ методом радиационного синтеза. Измерения рентгеновской дифракции и EDX анализ подтвердили формирование керамики вольфрамата цинка ZnWO₄ в результате радиационного синтеза. Измерены спектры поглощения, люминесценции, возбуждения лю-

минесценции синтезированных образцов. Также измерены спектры люминесценции эталонного монокристаллического образца. Рентгеновская дифракция подтвердила образование вольфрамата цинка ($ZnWO_4$) в результате радиационного синтеза. Люминесцентные спектры синтезированного образца совпадают со спектрами кристаллического $ZnWO_4$. Сравнение спектров люминесценции синтезированного керамического образца и монокристаллического эталонного образца, измеренные при разных условиях оптического возбуждения, показывает значительные различия в спектрах люминесценции синтезированного образца и эталонного образца и указывает на возможные различные дефекты, имеющиеся в сравниваемых образцах.

Ключевые слова: керамика, люминесценция, радиационный синтез, вольфраMAT цинка, спектры рентгеновской дифракции, EDX-анализ, плотность мощности, оптические свойства керамики.

Information about the authors:

Gulnur Alpysova — PhD, Karaganda Buketov University, University str., 28, Karaganda, Kazakhstan; 100028; e-mail: gulnur-0909@mail.ru; ORCID ID: 0000-0002-7164-2188

Dmitriy Afanasyev — PhD, Karaganda Buketov University, University str., 28, Karaganda, Kazakhstan; 100028; e-mail: a_d_afanasyev@mail.ru; ORCID ID: 0000-0002-0437-5315

Zhanara Bakiyeva — 1st year PhD student, Karaganda Buketov University, University str., 28, Karaganda, Kazakhstan; 100028; e-mail: shonar83@mail.ru ORCID ID: 0009-0005-1949-4535

Liudmila Lisitsyna — PhD, Tomsk State University of Architecture and Building, Solyanaya Sq. 2, Tomsk, Russia.

Mikhail Golkovski — PhD, Senior Researcher, Laboratory of Industrial Electron Accelerators, Budker Institute of Nuclear Physics of Siberian Branch of the Russian Academy of Sciences, Academician Lavrentieva ave., 11, Novosibirsk, Russia, 630090; e-mail: golkovski@mail.ru; ORCID ID: 0000-0003-4399-444X

Ainur Tussupbekova — PhD, Karaganda Buketov University, University str., 28, Karaganda, Kazakhstan; 100028; e-mail: aintus_070482@mail.ru; ORCID ID: 0000-0001-5299-9977.

Assemgul Kissabekova — PhD, Associate Professor, NJSC «Pavlodar Pedagogical University named after A. Margulan», st. Toraigyrova, 58, Pavlodar, Kazakhstan; 140008; e-mail: akisabekova@mail.ru; ORCID ID: 0000-0001-6300-6758

Serik Tuleuov — Student, Karaganda Buketov University, University str., 28, Karaganda, Kazakhstan; e-mail: serik.tu123@gmail.com; ORCID ID: 0009-0002-6009-1672

D.E. Uskenbaev¹, A.S. Nogai¹, A.D. Uskenbayev¹,
E.A. Nogai¹, A.S. Kudussov^{2*}, B.E. Khamzina¹

¹Seifullin University, Astana, Kazakhstan;

²Buketov University, Karaganda, Kazakhstan

*Corresponding author's e-mail: akudusov@mail.ru

Critical current density of high-temperature superconducting ceramics BSCCO Bi-2223

In the paper the results of the study on the synthesis of high-temperature superconducting ceramics of nominal composition $\text{Bi}_{1.6}\text{Pb}_{0.4}\text{Sr}_2\text{Ca}_2\text{Cu}_3\text{O}_y$ by various methods were presented based on amorphous phases using glass-ceramic technology and solid-phase method. For comparison, amorphous phases were obtained in two ways. In the first case, a heating furnace of a special design was developed to obtain an amorphous phase, which provides melting without using a crucible. The heating of the initial samples for melting is carried out due to the combined effect of the convection heat flux and the radiation of heating elements, which consists of the IR region of the spectrum at a melting temperature in the spectral range of 1300–1350 nm. In the second case, melting is carried out under the influence of broadband optical radiation, including UV, visible and IR spectral regions. The production of glassy precursors is carried out by draining the melt onto a quenching device in the form of a propeller made of stainless steel. Studies of the formation rate of the superconducting high-temperature phase Bi-2223 were carried out in the same temperature conditions at 848–850 °C with intermediate grinding every 24 hours and the study of the phase composition by X-ray diffraction method. Studies showed that the glass phase-based method ensures the completeness of the formation of the high-temperature phase Bi-2223 and the rate of its formation is significantly higher than by the solid-phase method (2.5–3 times). Studies of the critical density of the transport current have shown that the current value is $7.05 \times 10^3 \text{ mA/cm}^2$, (measured by the criterion of $1 \mu\text{V/cm}$), which is significantly higher compared to other methods.

Keywords: superconductivity, glass phase, microstructure, ceramics, IR radiation, diffractogram, melt, crystallization.

Introduction

High-temperature superconductors (HTS) are one of the promising materials used in various advanced areas of industry, science and technology. Their field of application covers such diverse areas as energy, electronics and communications, space technology, medicine, metallurgy, instrument engineering and many others. To date, a small group of HTS systems was developed, in which metal cuprates are the basis [1–3]. Among them, the following superconducting compounds are actively used in practice — compounds based on bismuth $(\text{Bi}, \text{Pb})_2\text{Sr}_2\text{CaCu}_2\text{O}_8$ (Bi-2212) and $(\text{Bi}, \text{Pb})_2\text{Sr}_2\text{Ca}_2\text{Cu}_3\text{O}_{10}$ (Bi-2223), as well as yttrium $\text{YBa}_2\text{Cu}_3\text{O}_{7-x}$ (Y123). It is known that the main parameters of HTS materials are critical temperature, critical current and critical magnetic field. The main factors determining the parameters of these HTSPS are: the creation of the necessary phase composition, increased textures, densities, the presence of pinning centers and others, which depend on the methods and technological conditions for their production.

Currently, various methods are used for the synthesis of HTSP — they are widespread: solid-phase synthesis, chemical and cryochemical, as well as various melt methods, etc [4–7]. The results of numerous studies show that obtaining the required critical parameters is not an easy task. A definite solution to the problem of creating HTS materials of a given phase composition with the necessary critical parameters (especially current ones) is the use of a glass-ceramic method. This method has certain advantages over others and allows you to obtain high-density ceramics with the required morphology (texture) and controlled grain size. In [8–11], the authors obtained, using the glass-ceramics method based on amorphous precursors, HTSC samples with increased density (the density value reached closer to the theoretical 99.5 % and higher), as well as with a high crystallite texture (97–98 %) according to direction of the crystal plane [001].

The glass-ceramic method can only be used for compositions having glass-forming properties during melt quenching, which is characteristic of the bismuth system. The method was first developed in the 1990s, but we were unable to evaluate its advantages over the solid-phase method due to the not fully elucidated processes during crystallization from the amorphous state of the phase with high T_c (Bi-2223). The synthesis of bismuth-based HTSP has been carried out by many researchers [12–18]. The analysis of these studies

showed that if the synthesis of the low-temperature superconductor Bi-2212 using glass-ceramic technology is not very difficult, then the synthesis of the high-temperature single-phase Bi-2223 based on glass phase is not an easy task. Traditionally, to obtain glassy precursors, the melting of the initial charge is carried out in a crucible made of corundum or platinum. During melting, there is a violation of the stoichiometric composition, especially significantly in oxygen (oxygen vacancy), as a result, oxygen deficiency negatively affects the kinetics and dynamics, as well as the completeness of the formation of a superconducting high-temperature phase 2223. The generalized results of the work on glass-ceramic technology were discussed in detail in the work of Abe [19], which is also noted about the lack of oxygen. In this case, cations of variable valence are reduced to a low-valent state, especially copper $\text{Cu}^{++} \rightarrow \text{Cu}^+$ [20, 21]. Compensation of oxygen deficiency during thermal annealing during the formation of HTS is difficult, since the rate of oxygen diffusion in dense structures of glassy precursors is very low, therefore long annealing (150–400 hours) is required. In this regard, the use of a method for producing bismuth-containing superconductors based on a glass phase that does not lead to a significant violation of the component composition (especially oxygen) could positively affect the completeness of the formation of the high-temperature superconducting phase Bi-2223, as well as a significant increase in the critical current density and shorten the synthesis time.

In this regard, this paper considers a method for obtaining amorphous precursors without using a crucible and synthesizing high-temperature superconducting ceramics based on them and studying their critical parameters.

The purpose of this work was to study the formation of a superconducting high-temperature phase Bi-2223 and the critical parameters of superconducting ceramics of nominal composition $\text{Bi}_{1.6}\text{Pb}_{0.4}\text{Sr}_2\text{Ca}_2\text{Cu}_3\text{O}_y$ synthesized on the basis of a glass phase using an optical light flux and the study of their critical parameters.

Experimental

For the synthesis of HTSP, reagents of the “extra clean” brand with a content of the main component of at least 99.9 % were used: Bi_2O_3 , PbO_2 , SrCO_3 , CaO and CuO . Before preparing the mixture of components, the reagents were calcined at a temperature of 120 °C for 2 hours.

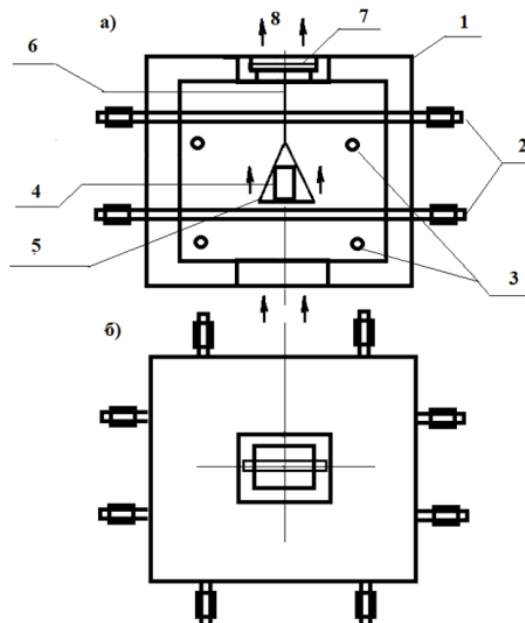
The phase compositions of superconductor samples were determined using Bruker D8ADVANCEECO and XPertPRO X-ray diffractometers (Netherlands). Microstructural and elemental analyses of the samples were carried out on scanning electron microscopes JEOL-6490LA (Japan) with an energy dispersion analyzer system “OXFORD Instruments Analytical Limited” (Great Britain) and JSM-6390LV (Japan) with an integrated energy dispersion X-ray analyzer (EDS) (acc. voltage — 20 kV, probe current — 1.0 nA). The critical temperature and the density of the critical transport current of the sulfur-conducting samples were measured by a four-point probe method using a CryoIndustry REF-1808-ACS cryocamera cooled with helium gas, a LakeShoreModel 340 temperature meter and a microvoltmeter. The density of the critical transport current (J_c) was determined by the criterion of 1 $\mu\text{V}/\text{cm}$. The critical temperature was measured, also by a non-contact method, by studying the temperature dependence of magnetic susceptibility. This method is highly sensitive and can detect traces of HTS phases with higher T_c in superconducting samples.

Results and discussions

The synthesis of HTSP composition $\text{Bi}_{1.6}\text{Pb}_{0.4}\text{Sr}_2\text{Ca}_2\text{Cu}_3\text{O}_y$ was carried out in three ways. Synthesis based on glassy precursors obtained in a specially designed resistive furnace, which provides melting of a mixture of samples in the form of tablets without using a crucible and simultaneous quenching of the melt by gradually draining the melt into a quenching device. The general diagram of the device for producing glassy precursors from a melt is shown in Figure 1.

A platinum substrate was used as a support for the initial samples. The melting of the samples was carried out due to the influence of a thermal convection flow and under the influence of an IR radiant flux in the wavelength range of 1300–1350 nm, which is emitted from heating elements at a temperature of 1200–1250 °C. The distance of the sample from the heating elements is 10–15 mm (the method of melting by resistive heating).

For comparison, there is also a synthesis based on glassy precursors obtained by melting the initial mixture under the influence of a radiant flux (electric arc lamp) and simultaneous quenching of the melt by flowing onto the rotating propeller of the quenching device. The spectral composition of the radiant flux consists of intense continuous radiation from the ultraviolet, visible and infrared regions of the spectrum. In addition, the IR region of the spectrum, along with continuous radiation, contains intense linear radiation in the wavelength range from 800 to 1000 nm (a method of melting by a radiant flux).



a) sectional melting devices: 1 — insulating housing; 2 and 3 — heaters; 4 — initial workpiece; 5 — substrate (platinum) with workpiece; 6 — substrate holder; 7 — ceramic rod for hanging the substrate; 8 — convection air flow; b) top view of the melting device

Figure 1. A device for producing initial glassy precursors by melt quenching

Also, the synthesis of HTSP was carried out according to the traditional solid-phase method by heat treatment of samples in the form of tablets in an isothermal mode at a temperature of 850 °C with intermediate grinding in a planetary mill every 24 hours.

The synthesis of HTSP based on glassy precursors was carried out, subsequently, according to the solid-phase synthesis mode, which is described above according to the scheme: grinding – pressing – thermal annealing.

For the synthesis of HTS ceramics based on glass phase, glassy precursors were previously obtained using the two methods described above. Visually, the precursors did not differ in appearance. Basically, they consisted of plates with a glassy luster (Fig. 2).

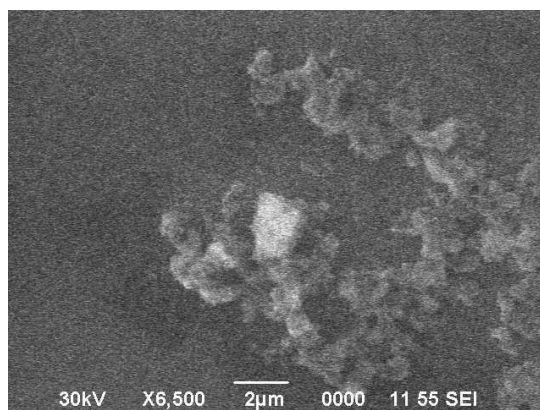
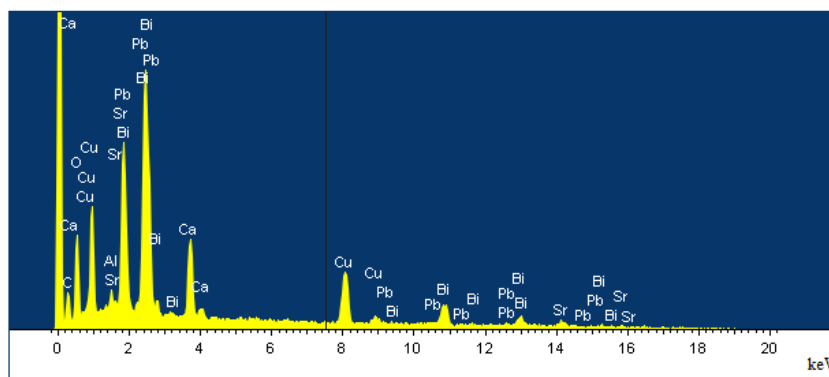
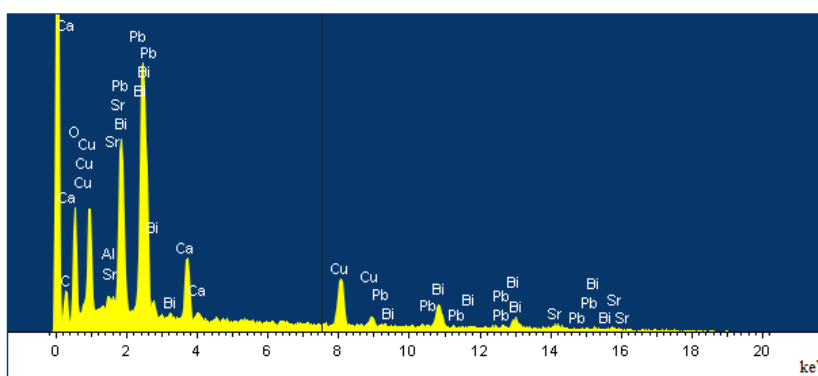


Figure 2. Microstructure of precursors of plates of the composition $\text{Bi}_{1.6}\text{Pb}_{0.4}\text{Sr}_2\text{Ca}_2\text{Cu}_3\text{O}_y$ obtained by quenching the melt by melting by resistive heating without using a crucible

The glassy appearance of the precursors was confirmed by X-ray studies, the absence of peaks on diffractograms. The study of the elemental composition of glassy precursor samples showed a slight deviation from the stoichiometric composition, i.e., a decrease in the content of calcium and lead was observed (Fig. 3, Table).



a)



b)

a — spectrum of a plate obtained in a furnace; b — spectrum of a plate obtained by a radiant flow

Figure 3. Energy-dispersive spectral electron microscopy studies of plate samples obtained by ultra-fast quenching of the melt

Table

Elemental composition of precursors

Name of the samples	O	Ca	Cu	Sr	Pb	Bi	Sum
Melted in the oven, wt. %	22.72	5.25	17.22	16.43	5.15	33.23	100
Fused by a radiant stream, wt. %	24.34	3.96	16.88	16.51	4.08	34.23	100

In the samples obtained by melting with a radiant flux, the deviation is slightly greater. The large decrease in the calcium and lead content in the samples obtained using the radiant flux is apparently related to the increased melt temperature associated with the anisotropic, one-sided effect of the radiant flux. Visually, it can be observed that the surface of the molten sample reaches the boiling point and above. The temperature of the boiling melt (sample surface), as measured by a pyrometer, exceeds 1500–1600 °C. The melting time of the surface of the initial samples under the action of a radiant flux is no more than 5 seconds. As for the melting temperature mode of the initial samples in a device with resistive melting, it can be strictly controlled with a difference of up to 2-3 degrees. At a melting temperature of 1250 °C, the melt begins to drip off in the form of droplets about 10 seconds after loading the initial samples inside the melting device onto a platinum substrate. Therefore, no significant change in the cationic composition was observed. An increase in oxygen content was observed in all precursor plates, since in both methods the melting processes are carried out in an oxidizing atmosphere.

The synthesis of superconducting phases was carried out according to the above technological regime. Previously, the precursors of the plate were annealed at a temperature of 750–800 °C for 10–12 hours for recrystallization. After that, they were crushed in a planetary mill and prepared samples in the form of tablets with a diameter of 15 mm and a thickness of 2.0–2.5 mm by pressing at a pressure of 6000 kgf/cm².

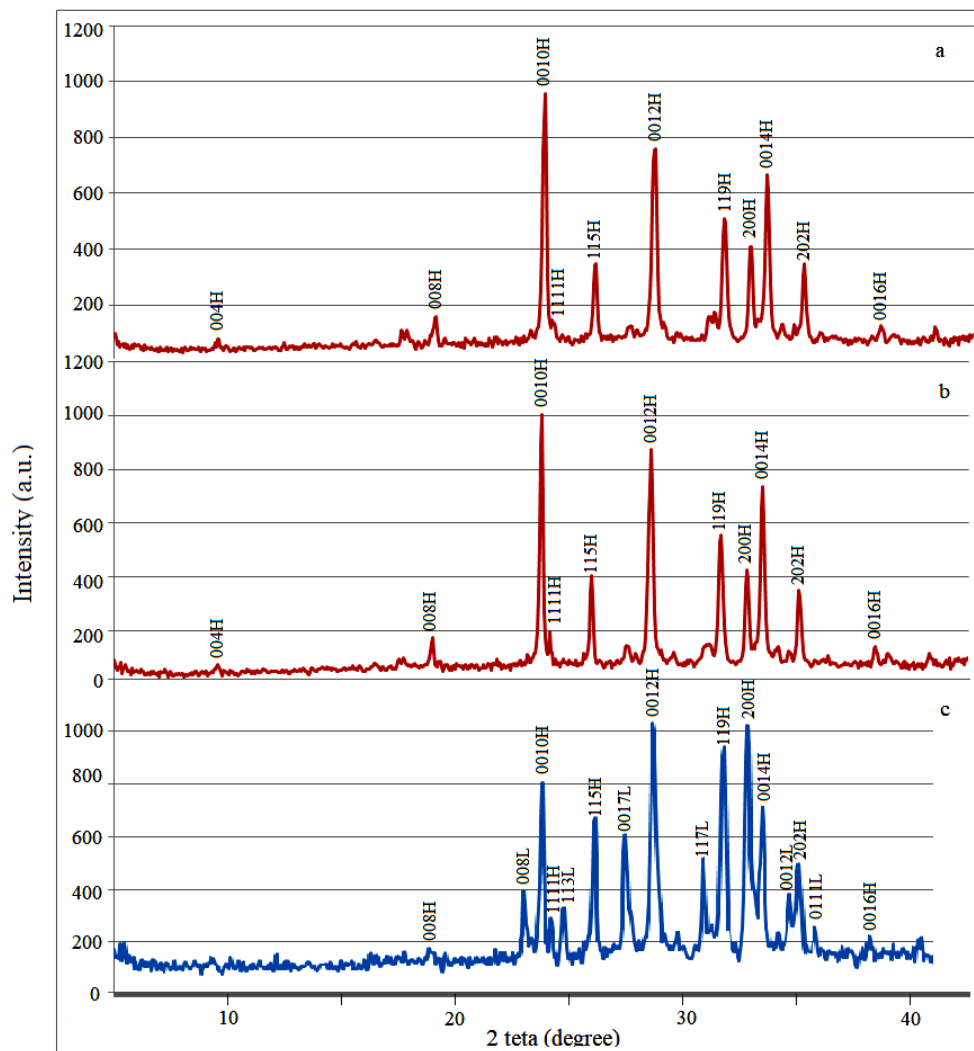
The synthesis of HTSP samples of all three types (using a radiant flux, resistive heating and solid-phase synthesis) was carried out in the same temperature regime and technological conditions. The dynamics of the

formation of the superconducting high-temperature phase Bi-2223 was traced by studying the phase composition of the samples in every 24 hours of heat treatment. Analysis of diffraction patterns revealed the presence of superconducting phases by comparison with data from the international ASTM database. The quantitative assessment of the superconducting high-temperature phase Bi-2223 (K_H) was determined by the ratio of the intensities of X-ray peaks [0010] (H[0010]) and the superconducting low-temperature phase Bi-2212 [008] (L[008]) according to the formula

$$K_H = (H[0010]/(H[0010]+L[008]) \cdot 100 \%$$

After 24 hours of heat treatment, no peaks of the high-temperature phase Bi-2223 were observed in the solid-phase synthesis sample. And after 48 hours of heat treatment, all samples consisted of superconducting phases.

After 48 hours of heat treatment, X-ray reflections of the high-temperature phase Bi-2223 and traces of the low-temperature phase Bi-2212 were observed on the diffractogram of the sample obtained by melting in the furnace. In the samples obtained by the radiant method, the content of the Bi-2212 phase was about 20 %. After 72 hours of heat treatment, only reflexes related to the high-temperature phase of Bi-2223 were present in the samples obtained in the furnace. In the samples obtained by the radiant flux, the complete formation of the high-temperature phase occurred after 96 hours of heat treatment. Whereas in the samples obtained by the solid-phase method, the content of the low-temperature phase was about 25–30 %. Diffractograms of the samples after 96 hours of annealing are shown in Figure 4.



a — melting in a furnace; *b* — radiant melting; *c* — solid-phase method

Figure 4. Diffractograms of HTSP samples of composition $\text{Bi}_{1.6}\text{Pb}_{0.4}\text{Sr}_2\text{Ca}_2\text{Cu}_3\text{O}_y$ after heat treatment at 850 °C, 96 hours

The study of the microstructure showed that the crystallites have a lamellar shape with a plate thickness of up to 350 microns (Fig. 5).

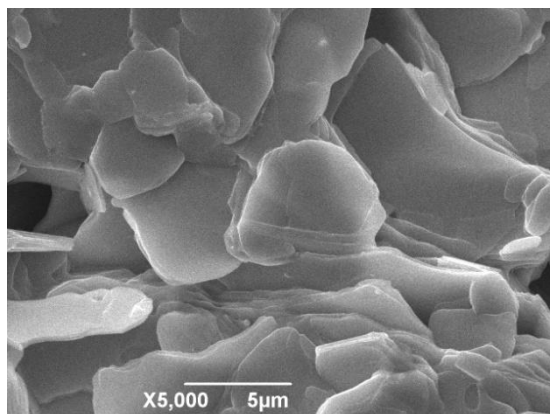
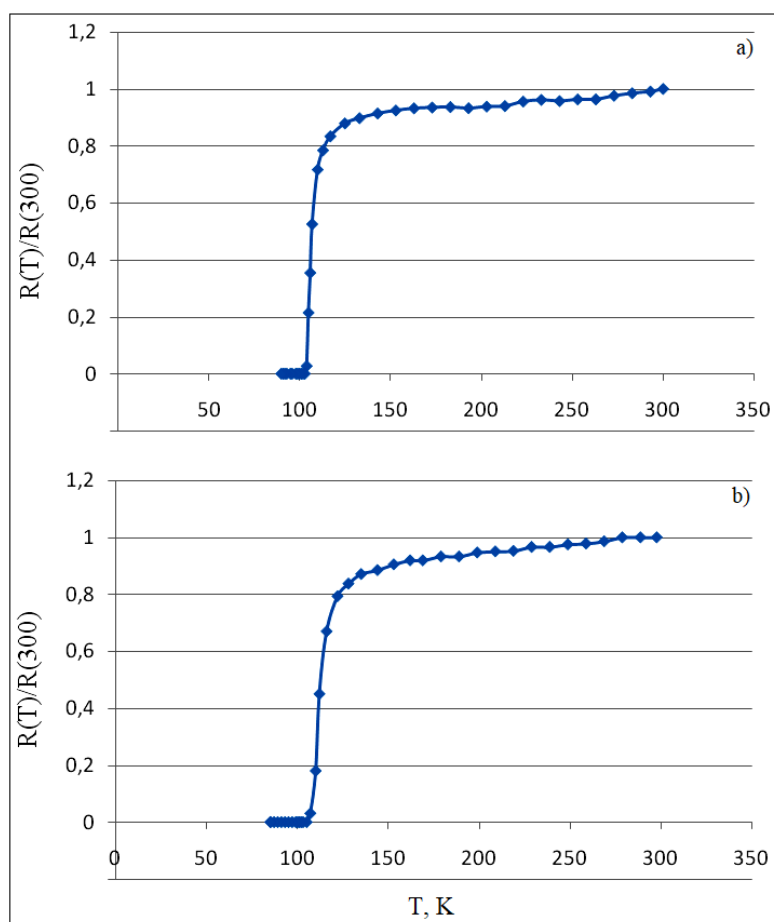


Figure 5. Microstructure of the HTSP sample of the composition $\text{Bi}_{1.6}\text{Pb}_{0.4}\text{Sr}_2\text{Ca}_2\text{Cu}_3\text{O}_y$ obtained on the basis of the glass phase

The study of the critical temperature showed that the temperature of the beginning of the transition to the superconducting state corresponds to 115–117 K. The critical temperature of the T_{zero} corresponds to 103 K and 105 K for samples, respectively, obtained by melting in a furnace and radiant flux (Fig. 6).



a — melting in a furnace; *b* — melting by a radiant stream

Figure 6. Curves of temperature dependence of resistance of HTSP samples of composition $\text{Bi}_{1.6}\text{Pb}_{0.4}\text{Sr}_2\text{Ca}_2\text{Cu}_3\text{O}_y$ obtained on the basis of glass phase

Studies of the critical temperature by the method of measuring the temperature dependence of the magnetic susceptibility of samples obtained by a radiant flux showed that microphases with higher T_c up to 150 K are present in the samples.

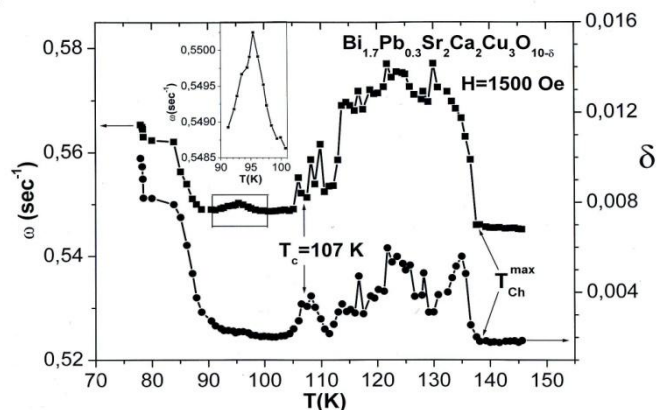


Figure 7. Curves of the temperature dependence of the magnetic susceptibility of the HTSP sample of the composition $\text{Bi}_{1.6}\text{Pb}_{0.4}\text{Sr}_2\text{Ca}_2\text{Cu}_3\text{O}_y$ obtained by a radiant flux

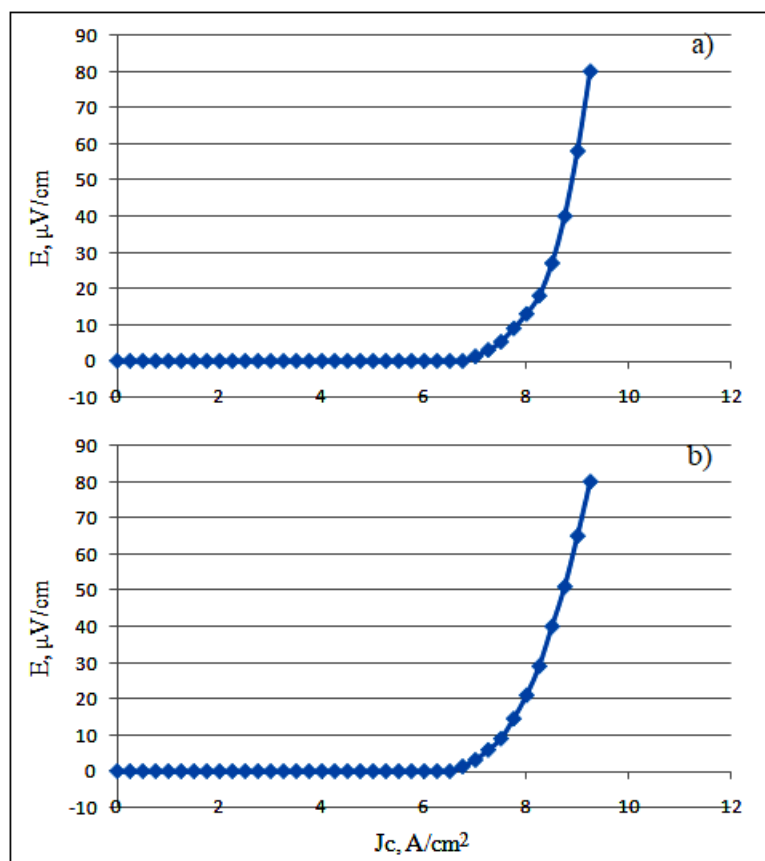


Figure 8. Critical density of the transport current of samples of the composition $\text{Bi}_{1.6}\text{Pb}_{0.4}\text{Sr}_2\text{Ca}_2\text{Cu}_3\text{O}_y$ obtained on the basis of the glass phase

Analysis of the results of a study on the synthesis of HTS ceramics of the composition $\text{Bi}_{1.6}\text{Pb}_{0.4}\text{Sr}_2\text{Ca}_2\text{Cu}_3\text{O}_y$, obtained on the basis of amorphous precursors by quenching the melt during melting in a furnace without using a crucible and using a concentrated radiant flux, as well as by the traditional solid-phase method, show that the formation rate of the superconducting high-temperature phase Bi-2223 differs significantly. The completeness of the formation of the high-temperature phase Bi-2223 and the increased

rate of formation when using the glass phase can be explained by the following: firstly, the homogeneous distribution of the components; secondly, during melting and quenching of the melt, bonds between atoms are formed during the melting process and ultrafast quenching stabilizes the amorphous phase (presence of a short-range order), which has increased internal energy, which ensures increased reactivity; thirdly, melting and quenching of the melt is carried out in an oxidizing atmosphere, precursors contain excessive oxygen content, cations of variable valence (Cu, Bi, Pb) of which are oxidized to a highly valent state; Fourth, it is necessary to take into account the effects of high-density light flux, which can contribute to the formation of defects, changes in the energy state of atoms, etc. During crystallization of the glass phase, depending on the temperature, the formation of the Bi-2212 or Bi-2223 structure occurs due to the ordering of atoms. At temperatures below 840 °C, the Bi-2212 phase stabilizes. At a temperature of 850 °C, the Bi-2223 phase is formed, which means that the temperature range of phase formation is narrow. A slight difference in the rate of formation of the Bi-2223 phase based on the glass phase obtained by various methods can be explained by the fact that the melting temperature in the furnace can be strictly controlled. When melting by a radiant flux, the initial samples are significantly overheated (above the boiling point), which can lead to a violation of the composition due to evaporation. In this case, cations can replace each other. In the synthesis of HTSP based on the glass phase obtained by the above methods, the distribution of components in precursors is more homogeneous.

If we compare the glass-ceramic method, when the melt is obtained in crucibles, then melting occurs under equilibrium conditions and the homogeneity of the components is not ensured due to the difference in the mass of atoms, there is a significant decrease in the oxygen content. This has a negative effect on the rate of formation of the Bi-2223 phase.

As for solid-phase synthesis, the bond between atoms is formed during heat treatment, the distribution of components is heterogeneous, phase formation will occur due to the diffusion of atoms and the formation of a superconducting structure, the processes are relatively slow compared to glass-ceramic methods using the above methods.

Conclusion

Based on amorphous precursors, HTSP ceramics of the composition $\text{Bi}_{1.6}\text{Pb}_{0.4}\text{Sr}_2\text{Ca}_2\text{Cu}_3\text{O}_y$ were synthesized. For comparative analysis, the synthesis of superconducting ceramics was carried out on the basis of glass phases obtained by melt production without using a crucible in a furnace, melting under the influence of broadband optical radiation and synthesis of HTSP by a solid-phase method. Studies of the dynamics of the formation of the Bi-2223 superconducting phase have shown that the rate of its formation is significantly higher than in solid-phase synthesis. The critical temperature of superconductors is 103 K and 105 K for samples obtained in a furnace and water under the action of a radiant flux, respectively. It was also found that the critical density of the transport current is significantly higher than that of superconductors obtained by co-deposition, solid-phase synthesis, etc.

Acknowledgments

The work was carried out under grant AP23490836 with the financial support of the Science Committee of the Ministry of Science and Higher Education of the Republic of Kazakhstan.

References

- 1 Chandehari, M.H., & Brass, S.G. Consecutive Inert and Oxygen Atmosphere Sintering in the Synthesis of $\text{LaBa}_2\text{Cu}_3\text{O}_y$ with $T(R=0)$ Greater Than 90 K. *Journal of Materials Research*, 4 (Sep-Oct 1987), 1111–1115. C.W. Chu, *IEEE Trans. Appl. Supercond.* 7 (1997) 80.
- 2 Wu, M.K., Ashburn, J.R., Torng, C.J., Hor, P.H., Meng, R.L., Gao, L., Huang, Z.J., Wang, Y.Q., & Chu C.W. (1987). Superconductivity at 93 K in a New Mixed-Phase Y-Ba-Cu-O Compound System at Ambient Pressure. *Phys. Rev. Lett.*, 58, 908–910.
- 3 Antipov, E.V., Abakumov, A.M., & Putilin, S.N. (2002). Chemistry and structure of Hg-based superconducting Cu mixed oxides. *Superconductor Science and Technology*, 15(7), R31.
- 4 Khulud Habanjar, F., & El Haj Hassanb, R. (2020). Awad. Physical and dielectric properties of (Bi, Pb)-2223 Superconducting samples added with $\text{BaFe}_{12}\text{O}_{19}$ nanoparticles. *Chemical Physics Letters*, 757(137880).
- 5 Jannah, A.N., & Abdullah, H. (2018). *IOP Conf. Series: Materials Science and Engineering*, 395(012007).

- 6 Uskenbaev, D., Nogai, A.S., Uskenbayev, A., Zhetpisbayev, K., Nogai, E., Dunayev, E., Zhetpisbayeva, A., Nogai, A. (2023). Synthesis and Research of Critical Parameters of Bi-HTSC Ceramics Based on Glass Phase Obtained by IR Heating. *ChemEngineering*, 7, 95–107.
- 7 Uskenbaev, D., Zhetpisbaev, K., Nogai, A., Beissenov, R., Zhetpisbaeva, A., Baigisova, K., Salmenov, E., Nogai, A., & Turuntay, S. (2022). Synthesis of High Temperature Superconducting Ceramics in the Bi(Pb)-Sr-Ca-Cu-O System Based on Amorphous Precursors. *Eastern-European Journal of Enterprise Technologies*, 4/12(118), 29–37.
- 8 Bobylev, I.B., Romanov, E.P., Lyubimov, M.G., Morycheva, V.N., Nasyrov, V.B., & Nikolaeva, F.B. (1991). Preparation of high-density glass ceramics $\text{Bi}_2\text{Sr}_2\text{CaCu}_2\text{O}_8$ with $T_g > 90$ K. *Superconductivity: physics, chemistry, technology*, 4(7), 1335–1343.
- 9 Nadtochiy, Yu.G., Zakharov, S.V., Tishchenko, E.A., Khalilov, G.S., Shaplygin, I.S., & Burtsev, Yu.N. (1993). Kinetic properties of HTSC ceramics of the Bi-Sr-Ca-Cu-O system obtained from the glass phase of composition 2-2-1-2. *Inorg. materials*, 29(12), 1683–1985.
- 10 Gulamova, D.D., & Uskenbaev, D.E. (2006). Effect of substrate composition and crystal structure on the BSCCO texture with the 2223 composition obtained under the action of solar radiation. *Applied Solar Energy*, 42(4), 40–42.
- 11 Khassenov, A.K., Stoev, M., Karabekova, D.Zh., Bulkairova, G.A., & Nurbalayeva, D.A. (2021). Electro-pulse method for obtaining raw materials for subsequent flotation enrichment of ore. *Bulletin of the University of Karaganda–Physics*, 1(101), 57–62.
- 12 Gazda, M., & Winiarski, A. (2005). XPS and XRD studies of early stages of crystallisation process in $(\text{Bi-Pb})_4\text{Sr}_3\text{Ca}_3\text{Cu}_4\text{O}_x$ glass-ceramics. *Physica C*, 432, 35–42.
- 13 Koralaya, H., Cavdar, S., Arslan, A., Ozturk, O., Tolga Tasci, A., & Tugluoglu, N. (2017). Experimental and theoretical approaches for magnetic, superconducting and structural characterization of $\text{Bi}_{1.75}\text{Pb}_{0.25}\text{Sr}_2\text{Ca}_2\text{Cu}_{3-x}\text{Sn}_x\text{O}_{10+y}$ glass ceramics. *Cryogenics*, 88, 17–21.
- 14 Gavdar, S., Koralay, H., & Altindal, S. (2011). Effect of vanadium substitution on the dielectric properties of glass ceramic Bi-2212 superconductor. *J. Low Temp Phys.*, 164, 102–114.
- 15 Koralay, H., Hicyilmaz, O., Cavdar, S., Asikuzun, E., Tasci, A.T., & Ozturk, O. (2014). Effect of Zn content on microstructure and mechanical performance in $\text{Bi}_{1.8}\text{Sr}_2\text{Ca}_2\text{Cu}_{3.2-x}\text{Zn}_x\text{O}_{10+\delta}$ glass ceramic. *J Mater Sci: Mater Electron*, 25, 3116–3126.
- 16 Fruth, V., Tanase, G., Atkinson, I., Pande, C.J., Aldica, G., & Zaharescu, M. (2014). Synthesis and characterization of glass-ceramic superconductors in (Pb, B)-doped Bi-Sr-Ca-Cu-O system. *Revue Roumaine de Chimie*, 59(6-7), 375–383.
- 17 Gulamova, D.D., Chigvinadze, D.G., Akrivos, Zh., & Uskenbaev, D.E. (2012). Obtaining and studying the properties of high-temperature superconductors of homologous series of $\text{Bi}_{1.7}\text{Pb}_{0.3}\text{Sr}_2\text{Ca}_{n-1}\text{Cu}_n\text{O}_y$ ($n = 4-9$) under Influence of Solar Energy. *Applied Solar Energy*, 48(2), 135–139.
- 18 Gulamova, D.D., & Uskenbaev, D.E. (2006). Effect of substrate composition and crystal structure on the BSCCO texture with the 2223 composition obtained under the action of solar radiation. *Applied Solar Energy*, 42(4), 40–42.
- 19 Yoshihiro, Abe (Ed.). (1997). *Superconducting Glass-Ceramics in Bi-Sr-Ca-Cu-O: Fabrication and its Application*. World Scientific Publishing Co. Pte. Ltd. ISBN 981-02-3204-7.
- 20 Won-Hyuk Lee. (1997). Effect of Copper Ions (Cu(I), Cu(II)) on the Properties of Bi-Sr-Ca-Cu-O Glasses and Superconducting Glass-Ceramics // by Yoshihiro Abe. *Superconducting Glass-Ceramics in BiSrCaCuO*. Nogayo, 79–94.
- 21 Komatsu, T., Nakakura, M., Sato, R., Jabri Khaled, J., & Matusita, K. (1996). Thermal stability and hopping conduction in $\text{Bi}_4\text{Sr}_3\text{Ca}_3\text{Cu}_x\text{O}_y$ glasses ($x = 4-9$). *Journal of Non-Crystalline Solids*, 195, 102–112.

Д.Е. Ускенбаев, А.С. Ногай, А.Д. Ускенбаев,
Е.А. Ногай, А.С. Кудусов, Б.Е. Хамзина

BSCCO Bi-2223 жоғары температуралы асқын өткізгіш керамиканың критикалық ток тығыздығы

Жұмыста $\text{Bi}_{1.6}\text{Pb}_{0.4}\text{Sr}_2\text{Ca}_2\text{Cu}_3\text{O}_y$ номиналды құрамындағы жоғары температуралы асқын өткізгіш керамиканы шыны керамикалық технология бойынша аморфты фазалар негізінде және қатты фазалық әдіспен синтездеу бойынша зерттеу нәтижелері келтірілген. Салыстыру үшін аморфты фазаларды алу екі жолмен жүзеге асырылды. Бірінші әдісте, аморфты фазаны алу үшін тигельді пайдаланбай балкуды қамтамасыз ететін арнайы технологиялық жылыту пеші жасалды. Балку үшін бастапқы үлгілерді қыздыру конвекциялық жылу ағынының және 1300–1350 нм спектрлік аймақта балку температуралық режимі кезінде спектрдің ИҚ аймағынан тұратын қыздыру элементтерінің сәулеленуінің бірлескен әсерінен жүзеге асырылады. Екінші әдісте балку спектрдің ультракүлгін, көрінетін және ИҚ аймақтарын қамтитын кең жолақты оптикалық сәулеленудің әсерінен орындалады. Шыны тәрізді прекурсорларды алу тот баспайтын болаттан жасалған винт түріндегі сәндіру құрылғысына балқыманың ағуы арқылы іске асырылады. Bi-2223 асқын өткізгіш жоғары температуралық фазаның түзілу жылдамдығын зерттеу 848–850°C температурада бірдей температуралық режимдерде әр 24 сағат сайын аралық ұнтақтаумен және фазалық құрамын рентгендік дифракциялық әдіспен зерттеумен жүргізілді. Зерттеулер көрсеткендей, шыны фазасына негізделген әдіс жоғары температуралы Bi-2223 фазасының толық қалыптасуын қамтамасыз етеді

және оның түзілу жылдамдығы қатты фазалық әдіске карағанда едәуір жоғары (2,5-3 есе). Критикалық тогының тығыздығын зерттеу көрсеткендей, токтың мөлшері $7,05 \cdot 10^3 \text{ mA/cm}^2$ (1 мкВ/см өлшемімен өлшегенген), бұл басқа әдістермен салыстырғанда айтарлықтай жоғары екендігін білдіреді.

Кілт сөздер: асқын өткізгіштік, шыны фазасы, микроқұрылым, керамика, ИК сәулеленуі, дифрактограмма, балку, кристалдану.

Д.Е. Ускенбаев, А.С. Ногай, А.Д. Ускенбаев,
Е.А. Ногай, А.С. Кудусов, Б.Е. Хамзина

Плотность критического тока высокотемпературной сверхпроводящей керамики BSCCO Bi-2223

В работе приведены результаты исследования по синтезу высокотемпературной сверхпроводящей керамики номинального состава $\text{Bi}_{1.6}\text{Pb}_{0.4}\text{Sr}_2\text{Ca}_2\text{Cu}_3\text{O}_x$, различными способами, на основе аморфных фаз по стеклокерамической технологии и по твердофазному способу. Сравнение получения аморфных фаз осуществлялось двумя способами. В первом случае для получения аморфной фазы разработана нагревательная печь специальной конструкции, которая обеспечивает плавление без использования тигля. Нагрев исходных образцов для плавления осуществлялся за счет совместного влияния конвекционного теплового потока и излучения нагревательных элементов, которые состоят из ИК-области спектра при температурном режиме плавления в спектральной области 1300–1350 нм. Во втором случае плавление реализовывалось под действием широкополосного оптического излучения, включающего УФ-видимый и ИК-области спектра. Получение стеклообразных прекурсоров осуществлялось за счет стекания расплава на устройство закалки в виде пропеллера, изготовленного из нержавеющей стали. Исследования скорости образования сверхпроводящей высокотемпературной фазы Bi-2223 осуществлялись в одинаковых температурных режимах при 848–850 °С с промежуточным измельчением каждые 24 ч и исследованием фазового состава рентгеновским дифракционным методом. Исследования показали, что способ на основе стеклофазы обеспечивает полноту формирования высокотемпературной фазы Bi-2223 и скорость ее образования существенно выше, чем по твердофазному методу (2,5–3 раза). Исследования критической плотности транспортного тока показали, что величина тока (измеренная по критерию 1 мкВ/см) составляет $7,05 \cdot 10^3 \text{ mA/cm}^2$, что значительно превышает показания по сравнению с другими методами.

Ключевые слова: сверхпроводимость, стеклофаза, микроструктура, керамика, ИК излучение, дифрактограмма, расплав, кристаллизация.

Information about the authors

Uskenbaev Daniyar Esankulovich — PhD, Seifullin University, Kabanbay Batyr Avenue, 60/10, Astana, Kazakhstan; 00001; <https://orcid.org/0000-0001-6265-1376>

Nogai Adolf Sergeevich — Doctor of physical and mathematical sciences, Seifullin University, Kabanbay Batyr Avenue, 60/10, Astana, Kazakhstan; 00001; <https://orcid.org/0000-0003-4235-7246>

Khamzina Botakoz Erkenovna — PhD, Seifullin University, Kabanbay Batyr Avenue, 60/10, Astana, Kazakhstan; 00001; e-mail: be_khamzina@mail.ru; ORCID ID: <https://orcid.org/0000-0002-0552-7464>

Kudussov Arystan Satybaldinovich — Candidate of physical and mathematical sciences, Karaganda Buketov University, University str., 28, Karaganda, Kazakhstan; 100028; akudusov@mail.ru; ORCID ID: <https://orcid.org/0009-0006-2821-6446>

Uskenbayev Alicher Daniyarovich — Master of Engineering and Technology, Seifullin University, Kabanbay Batyr Avenue, 60/10, Astana, Kazakhstan; 00001;

Nogai Elianora Adolfovna — Master of Engineering and Technology, Seifullin University, Kabanbay Batyr Avenue, 60/10, Astana, Kazakhstan; 00001 <https://orcid.org/0000-0002-4900-9482>

В.К. Rakhadilov^{1,3}, N. Muktanova^{2,3*}, D.N. Kakimzhanov^{2,3}, P. Kowalewski⁴

¹Sarsen Amanzholov East Kazakhstan University, Ust-Kamenogorsk 070000, Kazakhstan;

²Daulet Serikbaev East Kazakhstan Technical University, Ust-Kamenogorsk 070002, Kazakhstan;

³PlasmaScience LLP, Ust-Kamenogorsk 070010, Kazakhstan;

⁴Wroclaw University of Science and Technology, Wroclaw, Poland

*Corresponding author's e-mail: muktanovan@gmail.com

Effect of HVOF method spraying parameters on phase composition and mechanical and tribological properties of 86WC-10Co-4Cr coating

Valve components used in the petroleum industry are subjected to intense wear during operation, which leads to a sharp decrease in their durability. Usually, the often subjected to the wear process surface of the valves is treated by tungsten carbide cladding to improve its durability. Because of the difficulty in applying tungsten carbide using conventional surfacing techniques, high velocity oxyfuel (HVOF) spraying technology is recommended. In this work, the mechanical, tribological properties and phase composition of 86WC-10Co-4Cr composition coatings obtained by HVOF Termika-3 high-velocity gas-fuel spraying were investigated. Varying the technological parameters of spraying was carried out by changing the spraying distance, which led to differences in the thickness of the coatings. The phase composition, microstructure and distribution of elements were analyzed using X-ray diffraction (XRD), scanning electron microscopy (SEM) methods. The hardness of the samples was measured on a microhardness tester using the Vickers method, the friction coefficient and the wear rate were investigated using a friction and wear tester. It was determined that the surface of the coatings had developed character and high roughness. The results of X-ray phase analysis showed the predominance of hexagonal WC as the major phase, with a small amount of hexagonal tungsten carbide W₂C as the minor phase, and the minor presence of cobalt oxide CoO. It was found that the increased wear resistance and low friction coefficient of 86WC-10Co-4Cr coatings are explained by the high volume fraction of hard and stable WC grains with high resistance to wear.

Keywords: wear resistance, ceramic-metal coatings, high-velocity gas-flame spraying, gate valve, carbides, decarburization, friction coefficient, microstructure.

Introduction

Any significant annual demand of oil and gas production and refining industry for shut-off valves, as well as the high cost of repair and preventive maintenance work determines the need to increase the actual service life of gate valves and the duration of the overhaul period. Gate valves are one of the important elements in the transportation of oil and gas, in the process of production from the well and through a complex network of pipelines, determining safe operating conditions and environmental protection. Gate valves used in the oil industry cause complex problems, one of which is their tightness. The main component affecting the tightness of the gate valve and its good performance is the gate-seat assembly. The durability of the gate assembly is ensured by using high strength, hard materials in all wear processes (adhesion, abrasion, erosion, cavitation and corrosion), especially tungsten carbide sprayed using the high velocity gas flame spraying (HVOF) process [1]. Over the last decade, a significant number of studies have been published on various HVOF gun designs such as JP5000 [2, 3], warm spray [4, 5], DJ2700/2600 [6], Jetkote II [7, 8], CJS [6] and K2 [8]. These studies have mainly focused on obtaining WC-Co-Cg coatings, which are widely used under

high tribological loading conditions for wear protection such as abrasion, contact fatigue, erosion and sliding. An additional advantage of high velocity gas flame spraying is that it can replace electrolytic hard chrome plating (EHC). The EHC process uses toxic chromium compounds, especially hexavalent chromium [Cr(VI)], which is a carcinogen and poses a serious threat to the environment and human health. In addition, the application of EHC on an industrial scale requires high requirements for industrial ventilation, electrolyte disposal and water treatment systems, which increases safety and environmental costs [9–11]. Therefore, the HVOF process is much more efficient than EHC. HVOF high velocity gas flame spraying method is most often used to deposit carbide-based materials, including 86WC-10Co-4Cr, which have high performance characteristics and are the most suitable materials to increase the service life of shut-off valve parts. High wear resistance of gas-thermal WC-Co coatings is provided by the combination of WC as a solid component and cobalt as a plastic binder [12–14]. To improve the corrosion resistance of WC-Co coatings, WC-Co powders are alloyed with chromium, as the Co-Cr matrix provides higher corrosion resistance than WC-Co materials. 86WC-10Co-4Cr coatings have high hardness, low coefficient of friction, and their wear resistance is 3...5 times higher compared to hard chromium [4, 15, 16]. On obtaining a good coating, it also requires tuning the appropriate process parameters. Among the many parameters that strongly influence the quality and properties of the produced coatings is the spraying distance, which is one of the key parameters.

Therefore, the present work describes the mechanical and tribological properties of 86WC-10Co-4Cr coatings obtained at different spraying distances using the HVOF Termika-3 process.

Materials and methods

In the present work, to provide improvement of tribological properties of the “gate-seat” assembly of the valve of pipeline fittings, sintered metal-ceramic powder of tungsten carbide in cobalt-chromium matrix 86WC-10Co-4Cr (JSC “Polema”, Tula, Russia) with particle size 15÷50 microns was used. Samples from high-alloyed, corrosion-resistant steel 30X13 were used as a substrate. Before spraying, the substrate surface was sandblasted under pressure of 0.6 MPa using electrocorundum.

Metallo-ceramic coatings 86WC-10Co-4Cr with different spraying distances were obtained on HVOF Termika-3 (PlasmaScience LLP, Ust-Kamenogorsk). Table shows the parameters of coating spraying, spraying distance values and an example code. The dwell time of all three samples during spraying was 10 s.

T a b l e

Spray coating regimes 86WC-10Co-4Cr

Example code	A1	A2	A3
Spraying distance, mm	200	300	400
Parameter regimes on the gas control panel	Optimal values		
Propane-butane mixture	2.9 Bar		
Oxygen	5 Bar		
Compressed air	3.2 Bar		

The morphology and cross-section of the initial powder are presented in Figure 1 (SEM Phenom XL, Wrocław University of Science and Technology, Wrocław, Poland). The powder particles were sintered according to the manufacturer and their size ranged from 15 to 50 μm . Porosity of coatings was evaluated by SEM images using image analysis software Altami Studio 4.0 of optical microscope Altami MET 5S (Altami LLC, St. Petersburg, Russia). From the figure it can be seen that the powder particles are predominantly spherical in shape (Fig. 1a). This is important from the technological point of view, as it provides a suitable bulkiness of the powder particles during spraying. According to the SEM analysis of the powder cross-sectional image (Fig. 1b), it is found that morphologically the structure consists of two phases with different colors, where, polygonal WC particles have a light color and the metallic phase of cobalt-chromium (matrix) is represented in dark gray color. The tungsten carbide particles are well distributed and embedded in the cobalt-chromium matrix, which is in agreement with many studies in the reported literatures [17–19]. It can also be observed that pores are present, which may facilitate heat distribution and promote better melting or semi-melting of the particles.

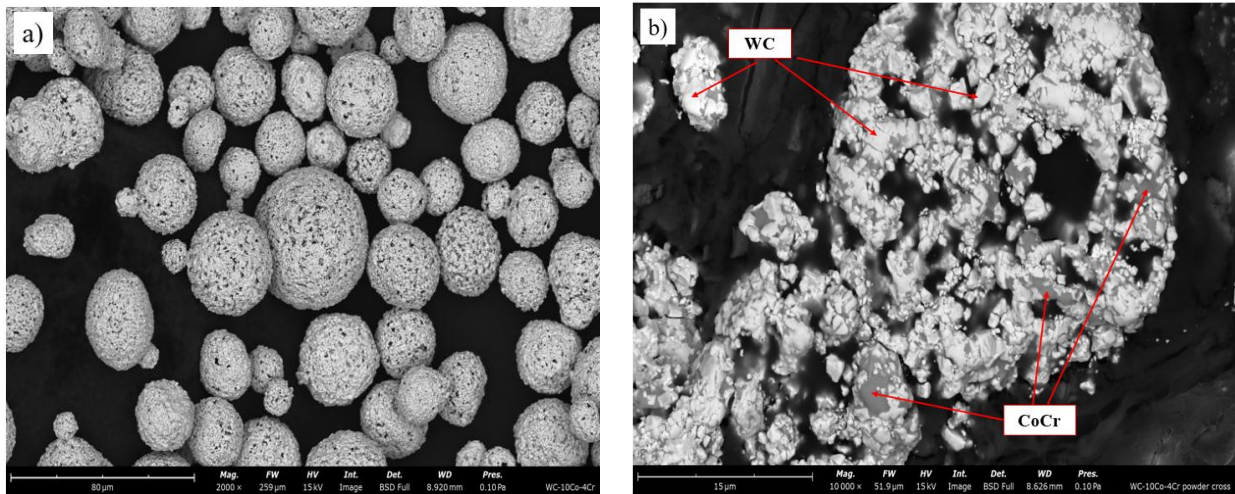


Figure 1. Morphology of the initial (a) and cross section (b) powder agglomerate 86WC-10Co-4Cr

X-ray diffraction analysis (XRD) of the powders and coatings was performed on a Cu-K α -emitting X'PertPRO diffractometer (Philips Corporation, Amsterdam, Netherlands) ($\lambda = 0.154$ nm) operated at a voltage and current of 40 kV and 30 mA, respectively. Measurements were performed over a 2θ range from 10° to 80° , and for the experiments the step width and exposure time were set to 0.05° and 0.5 s for each step. The roughness of the coatings R_a after spraying was determined using a Leica DCM8 3D profilometer (Wroclaw University of Science and Technology, Wroclaw, Poland). The microstructure of the fabricated coatings was analyzed using a Phenom XL scanning electron microscope. For each sample 20–25 images were taken at different magnifications. The microhardness of the samples was measured along the cross section of the coatings (10 measurements for each type of coating) on a microtweedometer MMT-X7B (Wroclaw University of Science and Technology, Wroclaw, Poland) at indenter loads $m = 200$ g and dwell time 10 s. Tribological wear tests were carried out on a friction machine using the standard technique “reciprocating motion” (Wroclaw University of Science and Technology, Wroclaw, Poland), where as a counterbody used SiC ball with a diameter of 3.969 mm and hardness $HV = 2800$ mm was pressed by weights (with a force F_N) to the surface of the sample, at a load of 20 N and linear velocity of 5 mm s $^{-1}$, the length of the wear track 3 mm. The system moving the plate consisted of two bearing bodies moving in the same direction, allowing the friction force to be shared. The actuator was an electric drive consisting of a stepper motor and helical gear. The motion force was transferred from the larger bogie to the smaller bogie using a strain gauge load cell. The system allowed a fixed motion of the steel plate relative to the ball with a defined velocity V_s and displacement S . The force causing the motion F_T was recorded at a frequency of 10 Hz. The kinematic diagram of the friction pair used during the tests is shown in Figure 2.

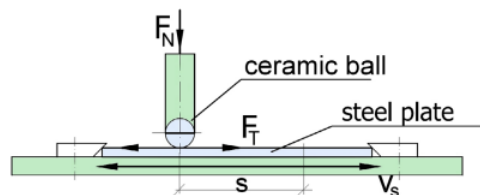


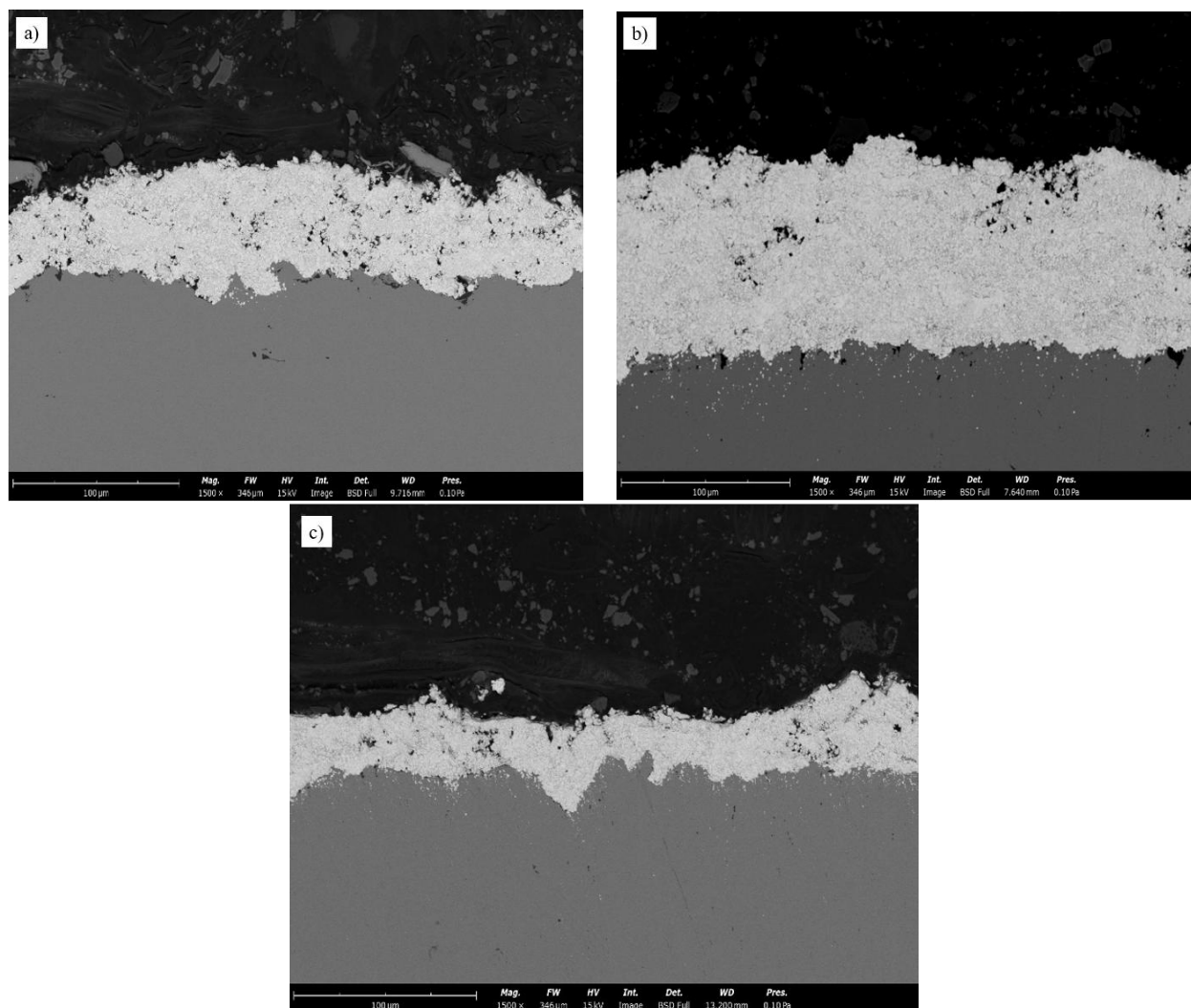
Figure 2. Structural diagram of the system used for friction and wear of coatings in the plate-ball system [20]

At each stage of the series of three measurements, the steel plate (on a moving carriage) performed a series of 500 motion cycles. The motion cycle consisted of two displacements ($V_{s,max} = 5$ mm s $^{-1}$) in both directions. The movement time in each direction was 0.4 s and the load on the friction node was $F_N = 2$ N. The tests were carried out under technically dry friction conditions. The friction coefficient μ was calculated based on the average friction force F_T . The average width of the wear track measured with a LEICA DCM8 microscope (Wroclaw University of Science and Technology, Wroclaw, Poland) after the test was taken as the wear value.

Results and discussion

Figure 3 shows the cross-sectional morphology of the coatings obtained at different spraying distances: A1 — 200 mm, A2 — 300 mm, A3 — 400 mm. All coatings are tightly adhered to the substrate without any cracks and failures and no signs of delamination were observed. The thicknesses of the coatings were $h = 60 \mu\text{m}$, $h = 97 \mu\text{m}$ and $h = 35 \mu\text{m}$ for samples A1, A2 and A3, respectively. According to the variation of the spraying distance, a variety in the thickness of the coatings was observed. In all coatings, the relative porosity did not exceed 1.6 %, but the lowest porosity with a value of 0.5 % was shown by the coating obtained at a spraying distance of 300 mm (Fig. 3b). Hence, the porosity is 1.6 %, 0.5 % and 1.3 % for samples A1, A2 and A3, respectively.

When the spraying distance is increased to 200 mm, the powder particles experience prolonged exposure to heat, which may cause them to overheat and result in the formation of microporous structure in the coating. Further, when the spraying distance is increased up to 300 mm, there is a gradual decrease in the heat effect and more intensive material deposition, which contributes to the formation of a more homogeneous and low-porosity coating. When further increasing the spraying distance up to 400 mm, leads to uneven application of the material, which is probably caused by the non-dissolution of WC in the spraying process and rapid cooling of the particles when reaching the substrate.

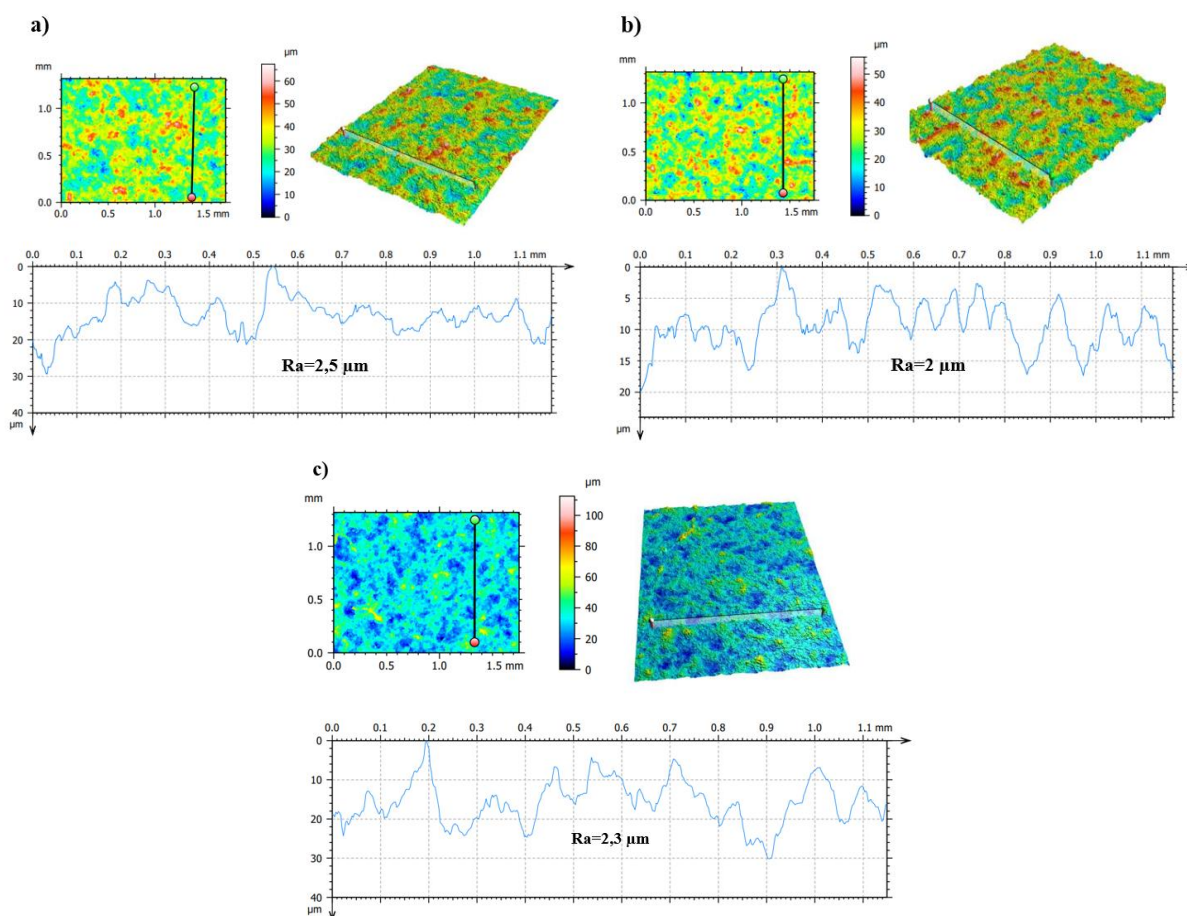


a — 200 mm; *b* — 300 mm; *c* — 400 mm

Figure 3. SEM images of the cross-sectional morphology of 86WC-10Co-4Cr coatings obtained by varying the spraying distance

Figure 4 displays the surface roughness measurements of the coatings obtained using a Leica DCM8 3D profilometer. Images at different depths of the focal plane were acquired and a three-dimensional image and

a plot of the distribution of the arithmetic mean profile deviation over the surface of 86WC-10Co-4Cr coatings were created from these images (Fig. 4). In the analyzed samples there is a slight change in the surface roughness, which is characterized by a regular fine microrelief. The roughness values are 2.5 μm , 2 μm and 2.3 μm for samples A1, A2 and A3, respectively.

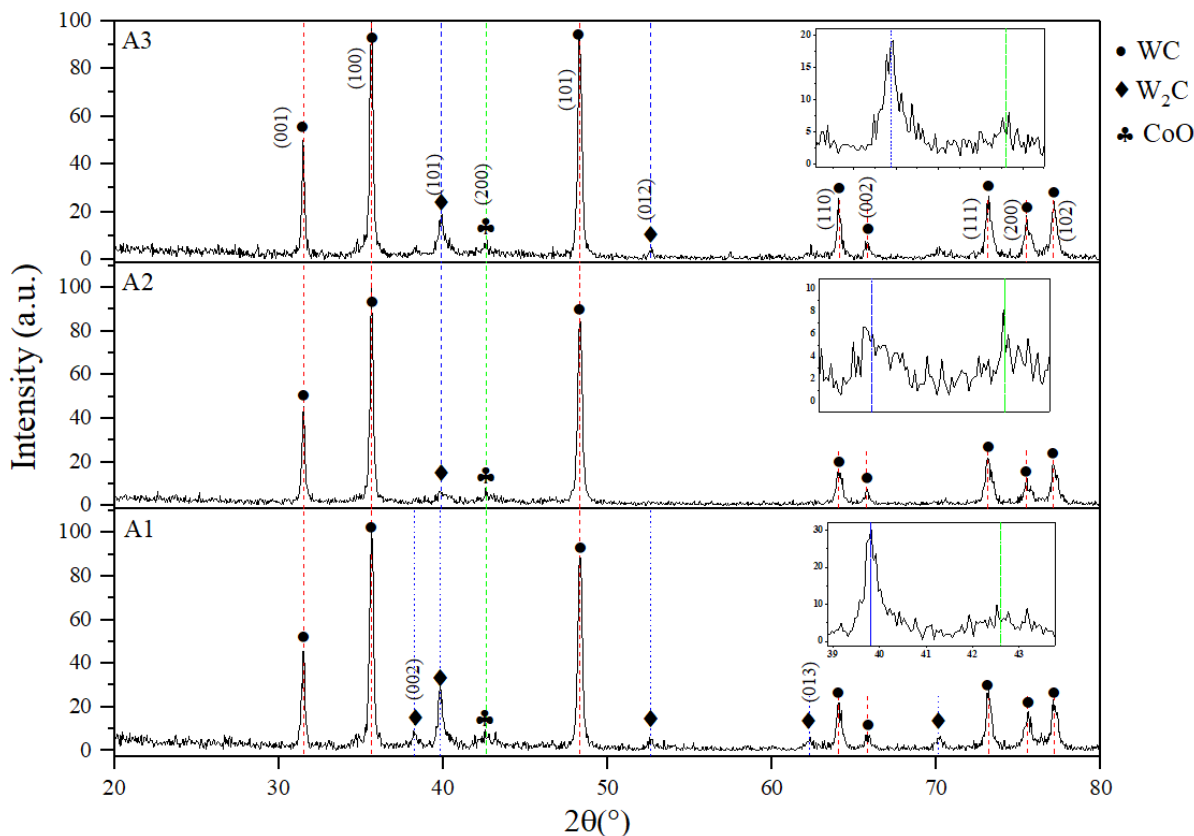


a — A1 — 200 mm; *b* — A2 — 300 mm and *c* — A3 — 400 mm

Figure 4. Topographic images and surface roughnesses of Ra coatings obtained with varying the spraying distance

Figure 5 shows the diffractograms of 86WC-10Co-4Cr based coatings obtained with different spraying distances. The results of XRD analysis showed that the phase composition of the coatings consists of hexagonal higher tungsten carbide WC as the major phase and a relatively small fraction of hexagonal lower tungsten carbide W_2C as the minor phase, and there are also cobalt oxide CoO peaks present, the latter two of which were obtained as a result of thermal decomposition of the powder during spraying, which is in agreement with the author's study [21]. Based on the diagram of state of the W-C double system, it can be assumed that in the temperature range of 2400–2800 $^{\circ}\text{C}$ there is a loss of carbon from the WC phase, which leads to the formation of the brittle phase W_2C [22–24]. At a spraying distance of 200 mm, the particles can have a higher temperature and velocity, which promotes a more intense decomposition of WC to W_2C . This resulted in high intensity of W_2C phase in A1 coating compared to other coatings. At a spraying distance of 300 mm, the particle and surface temperature, may be lower compared to the distance of 200 mm, which resulted in less intensive decomposition of WC to W_2C and hence lower intensity of the W_2C phase in the A2 coating. At a spraying distance of 400 mm, the particle and surface temperatures may not be as high as at closer distances. However, due to the increased residence time of the particles in the flame, they have more time to cool down and interact with the substrate. This may favor a more intense decomposition of WC to W_2C , which in turn may lead to an increase in the intensity of the W_2C phase in the A3 coating, as can be seen in Figure 5. The formation of the CoO oxide phase is explained by the fact that the high-speed gas flame spraying used an oxygen-propane mixture as the oxidizing gas flame medium, which leads to a more

intense interaction between WC and oxygen. As a result, there is a partial loss of carbon, consequently, the excess carbon formed as a result of WC dissolution diffuses into the metal matrix and forms another carbide W_2C and oxide CoO phase. Thus, the appearance of the W_2C phase in the coatings can be attributed to the partial decarburization of WC during the deposition process. This mechanism is well known for coatings containing tungsten carbide, as confirmed by literature sources [25, 26].



A1 — 200 mm; A2 — 300 mm; A3 — 400 mm

Figure 5. Coating diagrams of 86WC-10Co-4Cr at different spraying distances

The results of measurements of average values of microhardness of coatings depending on the regime of spraying are presented in Figure 6. The results agree with the author's studies [27, 28], i.e., the higher the degree of decarburization (transformation of WC into W_2C), the lower the hardness.

These results also correlate with the XRD data (Fig. 5), where partial decarburization is observed in A1 and A3 coatings, while less pronounced decarburization is observed in A2 coating. This is confirmed by the disappearance of the phase in some angles (52.6 and 62.3°), which, in turn, contributed to the hardness of the coating.

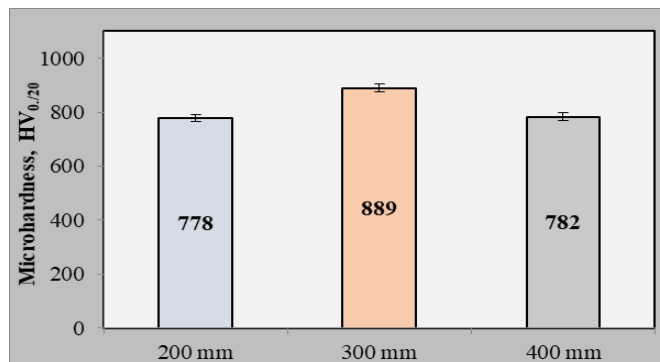


Figure 6. Microhardness of 86WC-10Co-4Cr coatings as a function of spraying distance

Tribological wear tests were performed on a friction machine (Fig. 2) using the standard “reciprocating motion” technique. Figure 7 shows the wear marks observed on the coating surface after the friction machine tests. Also shown is a graph illustrating the dependence of the wear mark width on its depth, which was obtained using a Leica DCM8 3D microscope.

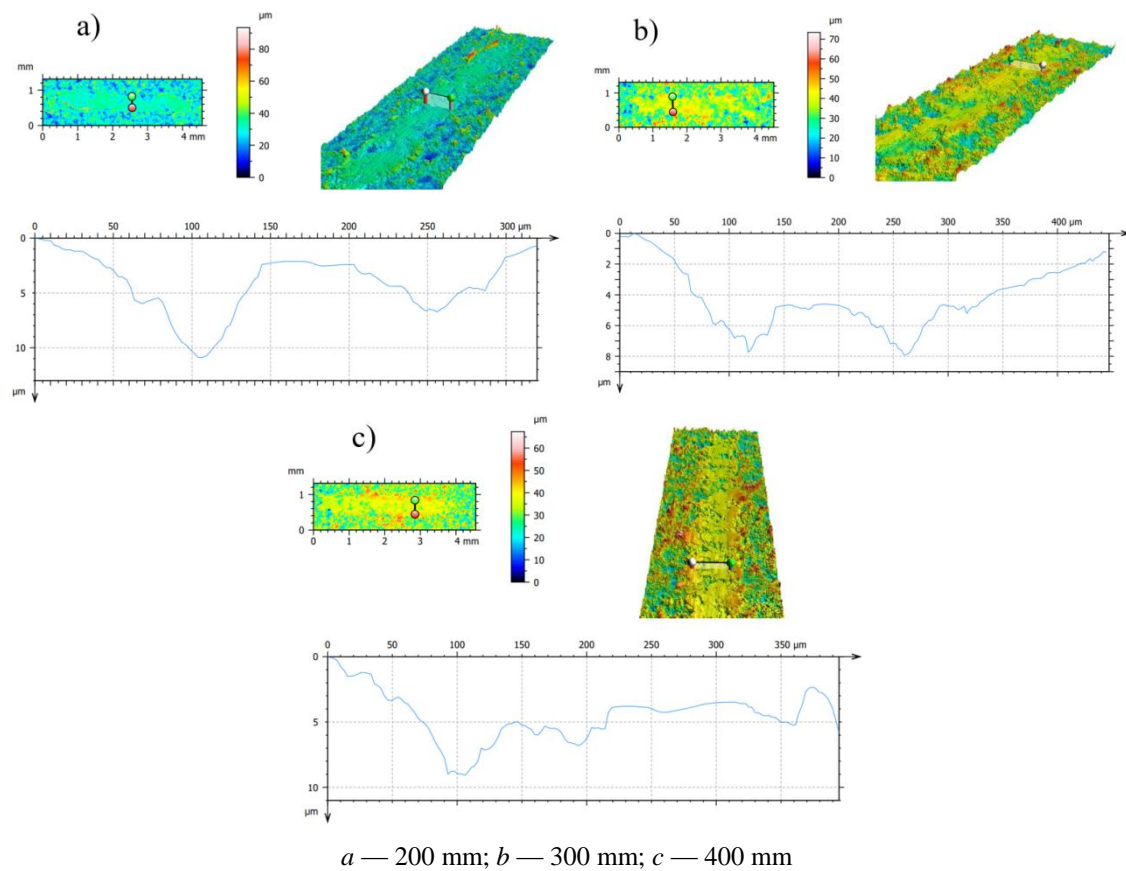


Figure 7. Wear traces observed on the surface of 86WC-10Co-4Cr coating after reciprocating wear test

As shown in Figure 7a, the coating obtained at a spraying distance of 200 mm undergoes wear to a greater depth compared to other coatings (Fig. 7b, c), which show signs of wear to a less significant depth. Figure 8 present graph shows the dependence of the wear volume on the spraying distance.

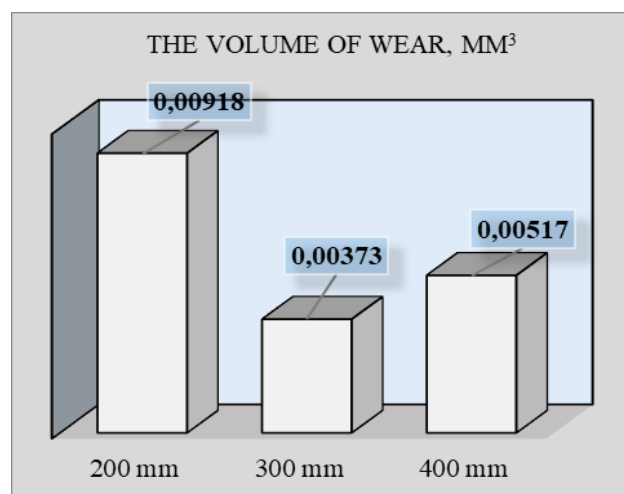


Figure 8. Graph of dependence of wear volume on the spraying distance

It has been established that with the increase of spraying distance the average friction coefficient and wear volume of 86WC-10Co-4Cr metal-ceramic coating change by jumps, taking values $\mu = 0,23369$; $\mu = 0,0562$; $\mu = 0,0566$ and $v = 0,00918 \text{ mm}^3$; $v = 0,00373 \text{ mm}^3$; $v = 0,00517 \text{ mm}^3$ (Fig. 8) for samples A1, A2 and A3. It can be seen from Figure 8 that the maximum wear resistance is characteristic of the coating obtained at a spraying distance of 300 mm, while the minimum is for the sample obtained at a spraying distance of 200 mm. The increase in wear resistance can be explained by the decrease in the content of the lowest carbide phase W_2C , which is in agreement with the results of XRD analysis (Fig. 5 (A2)). The coating obtained at a spraying distance of 300 mm is characterized by a high-volume fraction of hard and stable WC grains with high wear resistance. Thus, the tribological test results show that the A2 coating after high-speed gas-flame spraying has improved wear resistance and low coefficient of friction.

Conclusions

Thus, summarizing the above results, the following main conclusions of this paper can be drawn:

High velocity gas-flame spraying of 86WC-10Co-4Cr powder at different spacing resulted in coatings with dense structure without cracks and fractures, tightly adhering to the base.

The porosity of the coatings did not exceed 1.6 %. The lowest porosity with the index of 0.5 % was the coating obtained at a spraying distance of 300 mm.

X-ray diffraction analysis showed that the phase composition of the metal-ceramic coatings consisted of hexagonal WC, hexagonal W_2C and cubic cobalt oxide (CoO). The average spraying distance (300 mm) resulted in a less intense decomposition of WC to W_2C .

It was found that the maximum microhardness ($889HV_{0.2}$) was observed in A2 coating, which can be attributed to the decrease in the W_2C phase fraction, while the minimum microhardness values were observed in A1 and A3 coatings.

The roughness of the coatings practically does not change with increasing spraying distance: $2.5 \mu\text{m}$, $2 \mu\text{m}$ and $2.3 \mu\text{m}$ for samples A1 — 200 mm, A2 — 300 mm and A3 — 400 mm, respectively.

The maximum wear resistance is observed for the coating obtained at a spraying distance of 300 mm (wear volume 0.00373 mm^3), while the minimum wear resistance is characteristic of the coating obtained at a distance of 200 mm ($v = 0.00918 \text{ mm}^3$).

Acknowledgments

This research is funded by the Committee of Science of the Ministry of Science and Higher Education of the Republic of Kazakhstan (grant No. 14870977).

References

- 1 Ulmanu V. Research Regarding the Hard-facing of Petroleum Gate Valves by Using High Velocity Oxygen Fuel Technology / V. Ulmanu, M. Bădicioiu, M. Căltaru, Gh. Zecheru, Gh. Drăghici, M. Minescu, C. Preda // Cercetări privind durificarea prin pulverizare cu flacăra cu viteză mare a sertarelor robinetelor din industria petrolieră // Journal of the Balkan Tribological Association. — 2010. — Vol. 16. — No. 4. — P. 551-557.
- 2 Altuncu E. Sliding Wear Behaviour of HVOF Sprayed Metal Matrix Carbides / E. Altuncu, F. Ustel, A. Turk, A. Uzun // Proceedings of the International Thermal Spray Conference ITSC 2011. — 2011. — P. 485-488. DOI:10.31399/asm.cp.itsc2011p0463
- 3 Murthy J.K.N. Abrasive Wear Behaviour of WC-CoCr and $Cr_3C_2-20(NiCr)$ Deposited by HVOF and Detonation Spray Processes / J.K.N. Murthy, B. Venkataraman // Surface and Coatings Technology. — 2006. — 200 (8). — 2642-2652. DOI: 10.1016/j.surfcoat.2004.10.136
- 4 Chivavibul P. Development of WC-Co Coatings Deposited by Warm Spray Process / P. Chivavibul, M. Watanabe, S. Kuroda, J. Kawakita, M. Komatsu, Mr. Kazuto Sato, J. Kitamura // Journal of Thermal Spray Technology. — 2008. — 17(5-6). — P. 750-756. DOI: 10.1007/s11666-008-9271-4
- 5 Kissabekova P.A. Theoretical foundations of the construction of the operation of heat flow devices / P.A. Kissabekova, D.Z. Karabekova, A.K. Khassenov, V.Y. Kucheruk, A.S. Kudusov, S.S. Kyzdarbekova // Bulletin of the University of Karaganda — Physics. — 2023. — 109(1). — 80-87.
- 6 Bergonzini E. Wear Behaviour of HVOF-Sprayed Nanostructured WC-Co-Cr Coatings / E. Bergonzini, G. Bolelli, B. Bonferroni, L. Lusvarghi, T. Varis, U. Kanerva, T. Suhonen, J. Oksanen, O. Söderberg, S.P. Hannula // Proceedings of the International Thermal Spray Conference ITSC 2011. — 2011. — 612-618. https://doi.org/10.31399/asm.cp.itsc2011p0590
- 7 Clavette P.P.L. Erosion Resistance of WC-12Co High Velocity Oxy-Fuel Coatings / P.P.L. Clavette, A.J. Nardi, B.L. Laube, J. Shi, R. Ely, L. Centolanza // Proceedings of the International Thermal Spray Conference ITSC 2011. — 2011. — P. 246-251. https://doi.org/10.31399/asm.cp.itsc2011p0224

- 8 Berger L.-M. Microstructure and Properties of HVOF-Sprayed WC-(W, Cr)2C-Ni Coatings. / L.-M. Berger, S. Saaro, T. Naumann, M. Kasparova, F. Zahalka // *Journal of Thermal Spray Technology*. — 2008. — 17(3). — P. 395-403. DOI: [10.1007/s11666-008-9189-x](https://doi.org/10.1007/s11666-008-9189-x)
- 9 Борисов Ю.С. Исследование структуры и свойств газотермических покрытий системы WC-Co-Cr, полученных высокоскоростными методами напыления / Ю.С. Борисов, Е.А. Астахов, А.П. Мурашов, А.П. Грищенко, Н.В. Вигилянская, М.В. Коломыцев // *Автоматическая сварка*. — 2015. — № 10 (746). — С. 26–29.
- 10 Houdkova S. Comparative study of thermally sprayed coatings under different types of wear conditions for hard chromium replacement / S. Houdkova, F. Zahalka, M. Kasparova, L.-M. Berger // *Tribol Lett.* — 2011. — 43. — P. 139-154. DOI: [10.1007/s11249-011-9791-9](https://doi.org/10.1007/s11249-011-9791-9)
- 11 Krelling A.P. HVOF-sprayed coating over AISI 4140 steel for hard chromium replacement / A.P. Krelling, M.M. de Souza, C.E. da Costa, J.C. Giubilei Milan // *Materials Research*. — 2018. — 21(4). DOI: [10.1590/1980-5373-mr-2018-0138](https://doi.org/10.1590/1980-5373-mr-2018-0138)
- 12 Chivavibul P. Development of WC-Co Coatings Deposited by Warm Spray Process / P. Chivavibul, M. Watanabe, S. Kuroda (2008) // *Journal of Thermal Spray Technology*. — 2008. — 17, Issue 5-6. — P. 750–756. DOI: [10.1007/s11666-008-9271-4](https://doi.org/10.1007/s11666-008-9271-4)
- 13 Ma N. Improvement on mechanical properties and wear resistance of HVOF sprayed WC-12Co coatings by optimizing feed-stock structure / N. Ma, L. Guo, Z. Cheng, H. Wu, F. Ye, K. Zhang // *Applied Surface Science*. — 2014. — 320. — P. 364-371. <https://doi.org/10.1016/j.apsusc.2014.09.081>
- 14 Chen H. Structure and wear behaviour of nanostructured and ultrafine HVOF spraying WC-17Co coatings / H. Chen, G.Q. Gou, M.J. Tu, Y. Liu // *Surface Engineering*. — 2009. — 25(7). — 502–506. DOI: [10.1179/026708408X329489](https://doi.org/10.1179/026708408X329489)
- 15 Bobzin K. Investigation and Characterization of HVOF WC-Co-Cr Coatings and Comparison to Galvanic Hard Chrome Coatings / K. Bobzin, N. Kopp, T. Warda, S. Matthias, V. Andrei // *Proceedings paper*. — 2013. — P. 389–394. <https://doi.org/10.31399/asm.cp.itsc2013p0389>
- 16 Ward L.P. The dry sliding wear behavior of HVOF-sprayed WC: Metal composite coatings / L.P. Ward, A. Pilkington // *Journal of Materials Engineering Performance*. — 2014. — 23. — 3266-3278. DOI: [10.1007/s11665-014-1122-5](https://doi.org/10.1007/s11665-014-1122-5)
- 17 Aguero A. HVOF-Deposited WCCoCr as Replacement for Hard Cr in Landing Gear Actuators / A. Aguero, F. Camo'n, J. Garcia de Blas, J.C. del Hoyo, R. Muelas, A. Santaballa, S. Ulargui, and P. Valle's. // *Journal of Thermal Spray Technology*. — 2011. — 20(6). — 1292-1309. DOI: [10.1007/s11666-011-9686-1](https://doi.org/10.1007/s11666-011-9686-1)
- 18 Wang Q. Effect of Cobalt and Chromium Content on Microstructure and Properties of WC-Co-Cr Coatings Prepared by High-Velocity Oxy-Fuel Spraying / Q. Wang, Y. Zhong, H. Li, S. Wang, J. Liu, Y. Wang, C.S. Ramachandran (2023) // *Materials*. — 2023. — 16. — P. 7003. <https://doi.org/10.3390/ma16217003>
- 19 Rakhadilov B. Influence of varying the spraying distance on the structural-phase state and mechanotribological properties of 86WC-10Co-4Cr-based coatings obtained by the HVOF method / B. Rakhadilov, N. Muktanova, D. Kakimzhanov, M. Adilkanova, Sh. Kurbanbekov, S. Abdulina // *Coatings*. — 2024. — 14. — P. 264. <https://doi.org/10.3390/coatings14030264>
- 20 Łęcka K.M. Wear resistance of laser-induced annealing of AISI 316 (EN 1.4401) stainless steel / K.M. Łęcka, A.J. Antończak, P. Kowalewski, M. Trzcinski // *Laser Physics*. — 2018. — 28. DOI [10.1088/1555-6611/aac507](https://doi.org/10.1088/1555-6611/aac507)
- 21 Magnania Marina. WC-CoCr coatings sprayed by high velocity oxygen-fuel (HVOF) flame on AA7050 aluminum alloy: electrochemical behavior in 3.5 % NaCl solution / Marina Magnania, Patricia Hatsue Suegamaa, Abel André Cândido Reccob, Josep Maria Guilemany, Cecilio Sadao Fugivaraa, Assis Vicente Benedettia // *Materials Research*. — 2007. — 10(4). <https://doi.org/10.1590/S1516-14392007000400010>
- 22 Myalska H. Tribological behavior of WC-Co HVOF-sprayed composite coatings modified by nano-sized TiC addition / H. Myalska, L. Lusvarghi, G. Bolelli, P. Sassatelli, G. Moskal G. // *Surface Coatings Technology*. — 2019. — 371. — 401–416. <https://doi.org/10.1016/j.surfcoat.2018.09.017>
- 23 Mateen A. Tribological behavior of HVOF sprayed near-nanostructured and microstructured WC-17wt.%Co coatings / A. Mateen, G.C. Saha, T.I. Khan, F. Khalid // *Surface Coatings Technology*. — 2011. — 206. — 1077–1084. <https://doi.org/10.1016/j.surfcoat.2011.07.075>
- 24 Курлов А.С. Фазовые равновесия в системе W-C и карбиды вольфрама / А.С. Курлов, А.И. Гусев // *Успехи химии*. — 2006. — 75 (7). — С. 687–708.
- 25 Jonda E. Microstructure Investigation of WC-Based Coatings Prepared by HVOF onto AZ31 Substrate / E. Jonda, L. Łatka, A. Tomiczek, M. Godzierz, W. Pakieła, P. Nuckowski // *Materials*. — 2022. — 15. — 40. <https://doi.org/10.3390/ma15010040>
- 26 Masoumi H. Effect of grinding on the residual stress and adhesion strength of HVOF thermally sprayed WC-10Co-4Cr coating / H. Masoumi, S.M. Safavi, M. Salehi, S.M. Nahvi // *Mater. Manuf. Process*. — 2014. — 29. — 1139–1151. <https://doi.org/10.1080/10426914.2014.930893>
- 27 Murugan K. Optimizing HVOF spray process parameters to attain minimum porosity and maximum hardness in WC-10Co-4Cr coatings / K. Murugan, A. Ragupathy, V. Balasubramanian, K. Sridhar // *Surface and Coatings Technology*. — 2014. — 247. — 90–102. [doi:10.1016/j.surfcoat.2014.03.022](https://doi.org/10.1016/j.surfcoat.2014.03.022)
- 28 Lakhdari R. Fe based (W, Ti)C EAS and WC-12Co HVOF sprayed coatings: microstructure, mechanical properties and micro-scale abrasion performance / R. Lakhdari, F. Fernandes, P. V. Antunes, Y. Mebdoua, A. Cavaleiro and M. Legouera // *Materials Research Express*. — 2019. — Vol. 6. — № 9. DOI [10.1088/2053-1591/ab3037](https://doi.org/10.1088/2053-1591/ab3037)

Б.К. Рахадиллов, Н. Мұқтанова, Д.Н. Кәкімжанов, П. Ковалевский

86WC-10Co-4Cr жабынының фазалық құрамы мен механикалық-трибологиялық қасиеттеріне HVOF әдісінің бүрку параметрлерінің әсері

Эксплуатация кезінде мұнай өнеркәсібінде қолданылатын клапандардың компоненттері қатты тозуға ұшырайды, бұл олардың беріктігінің күрт төмендеуіне әкеледі. Әдетте, тозу процесіне жиі ұшырайтын ысырмалардың беті, олардың беріктігін арттыру үшін вольфрам карбидін қолдану арқылы балқытумен өңделеді. Дәстүрлі балқыту технологияларын қолдана отырып, вольфрам карбидін қолдану қиын болғандықтан, жоғары жылдамдықты оттегі-отынымен бүрку (HVOF) технологиясын қолдану ұсынылады. Жұмыста HVOF Termika-3 жоғары жылдамдықты газдық жалынды бүрку әдісімен алынған 86WC-10Co-4Cr жабындарының механикалық-трибологиялық қасиеттері мен фазалық құрамы зерттелді. Бүркудің технологиялық параметрлерінің өзгеруі бүрку қашықтығын өзгерту арқылы жүзеге асырылды, бұл жабындардың қалыңдығының өзгеруіне әкеледі. Элементтердің таралуы, фазалық құрам, микроқұрылым сканерлеуші электрондық микроскоп (СЭМ) және рентгендік дифракция (РД) әдістерін қолдану арқылы талданды. Сынамалардың қаттылығы Виккерс әдісімен микроқаттылық өлшегіште өлшенді, үйкеліс коэффициенті мен тозу дәрежесі үйкеліс пен тозу өлшегішінің көмегімен зерттелді. Жабындардың беті дамыған сипатқа және жоғары кедір-бұдырға ие екендігі анықталды. Рентгендік фазалық талдау нәтижелері алтыбұрышты WC-нің негізгі фаза ретінде басым болуын, алтыбұрышты вольфрам карбиді W_2C -нің екінші фаза ретінде аз болуын, сондай-ақ CoO кобальт оксидінің шамалы болуын көрсетті. 86WC-10Co-4Cr жабындарының тозуға төзімділігінің жоғары болуы және төмен үйкеліс коэффициентіне ие болуы жоғары қатты және тұрақты WC түйіршіктерінің жоғары көлемді үлесімен түсіндірілетіні анықталды.

Кілт сөздер: тозуға төзімділік, металл-керамикалық жабындар, жоғары жылдамдықты газжалынымен бүрку, ысырма, карбидтер, көміртексіздену, үйкеліс коэффициенті, микроқұрылым.

Б.К. Рахадиллов, Н. Муктанова, Д.Н. Какимжанов, П. Ковалевский

Влияние параметров напыления HVOF метода на фазовый состав и механико-трибологические свойства покрытия 86WC-10Co-4Cr

В процессе эксплуатации компоненты клапанов, используемые в нефтяной промышленности, подвергаются интенсивному износу, что приводит к резкому снижению их долговечности. Обычно поверхность затворов, которая часто подвержена процессу износа, обрабатывается наплавкой с применением карбида вольфрама для повышения ее долговечности. В связи с тем, что трудно наносить карбид вольфрама с использованием традиционных технологий наплавки, рекомендуется применять технологию высокоскоростного кислородно-топливного напыления (HVOF). В данной работе исследованы механико-трибологические свойства и фазовый состав покрытий состава 86WC-10Co-4Cr, полученных методом высокоскоростного газопламенного напыления HVOF Termika-3. Варьирование технологических параметров напыления осуществлялось путем изменения расстояния напыления, что привело к различиям в толщине покрытий. Фазовый состав, микроструктура и распределение элементов проанализированы с использованием методов рентгеновской дифракции (РФА), сканирующей электронной микроскопии (СЭМ). Твердость образцов измерялась на микротвердомере по методу Виккерса, коэффициент трения и степень износа исследовались с применением измерителя трения и износа. Определено, что поверхность покрытий обладает развитым характером и высокой шероховатостью. Результаты рентгенофазового анализа показали преобладание гексагонального WC в качестве основной фазы, с небольшим содержанием гексагонального карбида вольфрама W_2C в качестве второстепенной фазы, а также незначительное присутствие оксида кобальта CoO. Установлено, что повышенная износостойкость и низкий коэффициент трения покрытий 86WC-10Co-4Cr объясняются высокой объемной долей твердых и стабильных зерен WC, обладающих высокой стойкостью к износу.

Ключевые слова: износостойкость, металлокерамические покрытия, высокоскоростное газопламенное напыление, задвижка, карбиды, обезуглероживание, коэффициент трения, микроструктура.

References

- 1 Ulmanu, V., Bădicioiu, M., Călțaru, M., Zecheru, Gh., Drăghici, Gh., Minescu, M., & Preda, C. (2010). Research Regarding the Hard-facing of Petroleum Gate Valves by Using High Velocity Oxygen Fuel Technology. *Journal of the Balkan Tribological Association*, 16(4), 551–557 [in Romanian].
- 2 Altuncu, E., Ustel, F., Turk, A., & Uzun, A. (2011). Sliding Wear Behaviour of HVOF Sprayed Metal Matrix Carbides. *Proceedings of the International Thermal Spray Conference ITSC 2011*, 485–488. DOI: 10.31399/asm.cp.itsc2011p0463

- 3 Murthy, J.K.N., & Venkataraman, B. (2006). Abrasive Wear Behaviour of WC-CoCr and Cr₃C₂-20(NiCr) Deposited by HVOF and Detonation Spray Processes. *Surface and Coatings Technology*, 200(8), 2642–2652. DOI: [10.1016/j.surfcoat.2004.10.136](https://doi.org/10.1016/j.surfcoat.2004.10.136)
- 4 Chivavibul, P., Watanabe, M., Kuroda, S., Kawakita, J., Komatsu, M., Kazuto Sato, Mr., & Kitamura, J. (2008). Development of WC-Co Coatings Deposited by Warm Spray Process. *Journal of Thermal Spray Technology*, 17(5-6), 750–756. DOI: [10.1007/s11666-008-9271-4](https://doi.org/10.1007/s11666-008-9271-4)
- 5 Kissabekova, P.A., Karabekova, D.Z., Khassenov, A.K., Kucheruk, V.Y., Kudusov, A.S., & Kyzdarbekova, S.S. (2023). Theoretical foundations of the construction of the operation of heat flow devices. *Bulletin of the University of Karaganda — Physics*, 109(1), 80–87.
- 6 Bergonzini, E., Bolelli, G., Bonferroni, B., Lusvardi, L., Varis, T., Kanerva, U., Suhonen, T., Oksanen, J., Söderberg, O., & Hannula, S.P. (2011). Wear Behaviour of HVOF-Sprayed Nanostructured WC-Co-Cr Coatings. *Proceedings of the International Thermal Spray Conference ITSC 2011*, 612–618. <https://doi.org/10.31399/asm.cp.itsc2011p0590>
- 7 Clavette, P.P.L., Nardi, A.J., Laube, B.L., Shi, J., Ely, R., & Centolanza, L. (2011). Erosion Resistance of WC-12Co High Velocity Oxy-Fuel Coatings. *Proceedings of the International Thermal Spray Conference ITSC 2011*, 246–251. <https://doi.org/10.31399/asm.cp.itsc2011p0224>
- 8 Berger, L.-M., Saaro, S., Naumann, T., Kasparova, M., & Zahalka, F. (2008). Microstructure and Properties of HVOF-Sprayed WC-(W, Cr)₂C-Ni Coatings. *Journal of Thermal Spray Technology*, 17(3), 395–403. DOI: [10.1007/s11666-008-9189-x](https://doi.org/10.1007/s11666-008-9189-x)
- 9 Borisov, Yu.S., Astakhov, Ye.A., Murashov, A.P., Grishchenko, A.P., Vigilyanskaya, N.V., & Kolomytsev, M.V. (2015). Issledovanie struktury i svoystv gazotermicheskikh pokrytii sistemy WC-Co-Cr, poluchennykh vysokoskorostnymi metodami napyleniia [Investigation of structure and properties of gas-thermal coatings of WC-Co-Cr system obtained by high-speed sputtering methods]. *Avtomaticheskaya svarka — Automatic welding*, 10(746), 26–29 [in Russian].
- 10 Houdkova, S., Zahalka, F., Kasparova, M., & Berger, L.-M. (2011). Comparative study of thermally sprayed coatings under different types of wear conditions for hard chromium replacement. *Tribol Lett*, 43, 139–154. DOI: [10.1007/s11249-011-9791-9](https://doi.org/10.1007/s11249-011-9791-9)
- 11 Krelling, A.P., de Souza, M.M., da Costa, C.E., & Giubilei Milan, J.C. (2018). HVOF-sprayed coating over AISI 4140 steel for hard chromium replacement. *Materials Research*, 21(4). DOI: [10.1590/1980-5373-mr-2018-0138](https://doi.org/10.1590/1980-5373-mr-2018-0138)
- 12 Chivavibul, P., Watanabe, M., & Kuroda, S. (2008). Development of WC-Co Coatings Deposited by Warm Spray Process. *Journal of Thermal Spray Technology*, 17, 5-6, 750–756. DOI: [10.1007/s11666-008-9271-4](https://doi.org/10.1007/s11666-008-9271-4)
- 13 Ma, N., Guo, L., Cheng, Z., Wu, H., Ye, F., & Zhang, K. (2014). Improvement on mechanical properties and wear resistance of HVOF sprayed WC-12Co coatings by optimizing feedstock structure. *Applied Surface Science*, 320, 364–371. <https://doi.org/10.1016/j.apsusc.2014.09.081>
- 14 Chen, H., Gou, G.Q., Tu, M.J., & Liu, Y. (2009). Structure and wear behaviour of nanostructured and ultrafine HVOF spraying WC-17Co coatings. *Surface Engineering*, 25(7), 502–506. DOI: [10.1179/026708408X329489](https://doi.org/10.1179/026708408X329489)
- 15 Bobzin, K., Kopp, N., Warda, T., Matthias, S., & Andrei, V. (2013). Investigation and Characterization of HVOF WC-Co-Cr Coatings and Comparison to Galvanic Hard Chrome Coatings. *Proceedings paper*, 389–394. <https://doi.org/10.31399/asm.cp.itsc2013p0389>
- 16 Ward, L.P., & Pilkington, A. (2014). The dry sliding wear behavior of HVOF-sprayed WC: Metal composite coatings. *Journal of Materials Engineering Performance*, 23, 3266–3278. DOI: [10.1007/s11665-014-1122-5](https://doi.org/10.1007/s11665-014-1122-5)
- 17 Aguero, A., Camo'n, F., Garc'a de Blas, J., del Hoyo, J.C., Muelas, R., Santaballa, A., Ulargui, S., & Valle's, P. (2011). HVOF-Deposited WCCoCr as Replacement for Hard Cr in Landing Gear Actuators. *Journal of Thermal Spray Technology*, 20(6), 1292–1309. DOI: [10.1007/s11666-011-9686-1](https://doi.org/10.1007/s11666-011-9686-1)
- 18 Wang, Q., Zhong, Y., Li, H., Wang, S., Liu, J., Wang, Y., & Ramachandran, C.S. (2023). Effect of Cobalt and Chromium Content on Microstructure and Properties of WC-Co-Cr Coatings Prepared by High-Velocity Oxy-Fuel Spraying. *Materials*, 16, 7003. <https://doi.org/10.3390/ma16217003>
- 19 Rakhadilov, B., Muktanova, N., Kakimzhanov, D., Adilkanova, M., Kurbanbekov, Sh., & Abdulina, S. (2024). Influence of varying the spraying distance on the structural-phase state and mechanotribological properties of 86WC-10Co-4Cr-based coatings obtained by the HVOF method. *Coatings*, 14, 264. <https://doi.org/10.3390/coatings14030264>
- 20 Łęcka, K.M., Antończak, A.J., Kowalewski, P., & Trzcinski, M. (2018). Wear resistance of laser-induced annealing of AISI 316 (EN 1.4401) stainless steel. *Laser Physics*, 28. DOI [10.1088/1555-6611/aac507](https://doi.org/10.1088/1555-6611/aac507)
- 21 Marina Magnania, Patricia Hatsue Suegamaa, Abel André Cândido Reccob, Josep Maria Guilemany, Cecilio Sadao Fugivaraa, & Assis Vicente Benedettia (2007). WC-CoCr coatings sprayed by high velocity oxygen-fuel (HVOF) flame on AA7050 aluminum alloy: electrochemical behavior in 3.5 % NaCl solution. *Materials Research*, 10(4). <https://doi.org/10.1590/S1516-14392007000400010>
- 22 Myalska, H., Lusvardi, L., Bolelli, G., Sassatelli, P., & Moskal, G. (2019). Tribological behavior of WC-Co HVOF-sprayed composite coatings modified by nano-sized TiC addition. *Surface Coatings Technology*, 371, 401–416. <https://doi.org/10.1016/j.surfcoat.2018.09.017>
- 23 Mateen, A., Saha, G.C., Khan, T.I., & Khalid, F. (2011). Tribological behavior of HVOF sprayed near-nanostructured and microstructured WC-17wt.%Co coatings. *Surface Coatings Technology*, 206, 1077–1084. <https://doi.org/10.1016/j.surfcoat.2011.07.075>
- 24 Kurlov, A.S., & Gusev, A.I. (2006). Fazovye ravnovesiia v sisteme W-C i karbidy volframa [Phase equilibria in the system W-C and tungsten carbides]. *Uspekhi khimii — Advances in chemistry*, 75(7), 687–708 [in Russian].
- 25 Jonda, E., Łatka, L., Tomiczek, A., Godzierz, M., Pakieła, W., & Nuckowski, P. (2022). Microstructure Investigation of WC-Based Coatings Prepared by HVOF onto AZ31 Substrate. *Materials*, 15, 40. <https://doi.org/10.3390/ma15010040>

26 Masoumi, H., Safavi, S.M., Salehi, M., & Nahvi, S.M. (2014). Effect of grinding on the residual stress and adhesion strength of HVOF thermally sprayed WC-10Co-4Cr coating. *Mater. Manuf. Process*, 29, 1139–1151. <https://doi.org/10.1080/10426914.2014.930893>

27 Murugan, K., Ragupathy, A., Balasubramanian, V., & Sridhar, K. (2014). Optimizing HVOF spray process parameters to attain minimum porosity and maximum hardness in WC-10Co-4Cr coatings. *Surface and Coatings Technology*, 247, 90–102. doi:10.1016/j.surfcoat.2014.03.022

28 Lakhdari, K., Fernandes, F., Antunes, P.V., Mebdoua, Y., Cavaleiro, A., & Legouera, M. (2019). Fe based (W, Ti)C EAS and WC-12Co HVOF sprayed coatings: microstructure, mechanical properties and micro-scale abrasion performance. *Materials Research Express*, 6(9). DOI 10.1088/2053-1591/ab3037

Information about the authors

Rakhadilov Bauyrzhan Korabaevich — PhD, Senior researcher at Plasma Science LLP, Associate Professor, Sarsen Amanzholov East Kazakhstan University, Ust-Kamenogorsk, Kazakhstan; e-mail: rakhadilovb@mail.ru, <https://orcid.org/0000-0001-5990-7123>

Muktanova Nazerke — PhD student of 3d years of study in the specialty “Technical Physics” of Daulet Serikbayev East Kazakhstan Technical University, Researcher at Plasma Science LLP, Ust-Kamenogorsk, Kazakhstan; e-mail: muktanovan@gmail.com, <https://orcid.org/0000-0002-4823-6640>

Kakimzhanov Daur Nurzhanuly — PhD student of 3d years of study in the specialty “Technical Physics” of Daulet Serikbayev East Kazakhstan Technical University, Researcher at Plasma Science LLP, Ust-Kamenogorsk, Kazakhstan; e-mail: daur_97@mail.ru, <https://orcid.org/0000-0001-9453-0456>

Piotr Kowalewski — Doctor of Science, degree: habilitation, Professor, Wroclaw University of Science and Technology, Wroclaw, Poland; e-mail: piotr.kowalewski@pwr.edu.pl, <https://orcid.org/0000-0003-2216-5706>

D.B. Buitkenov, Zh.B. Sagdoldina, L.G. Sulyubayeva, A.B. Nabioldina, N.S. Raisov*

*Scientific Research Center "Surface Engineering and Tribology",
Sarsen Amanzholov East Kazakhstan University, Ust-Kamenogorsk, Kazakhstan
Corresponding author's e-mail: nurmakhanbetraisov@gmail.com

Investigation of mechanical and tribological properties of NiCrAlY/ZrO₂-Y₂O₃ coatings obtained by detonation spraying

In this study, multilayer gradient NiCrAlY/ZrO₂-Y₂O₃ coatings obtained by detonation spraying in 1D (spot sputtering) and 2D (full-surface scanning sputtering) modes were investigated. The structure of coatings was analyzed using scanning electron microscopy and electron dispersion analysis, mechanical properties (hardness, modulus of elasticity) were determined using various techniques. The tribological characteristics of the coatings including abrasion resistance and coefficient of friction were also studied. It was determined that the coatings consist of alternating layers of NiCrAlY and ZrO₂-Y₂O₃, creating a multilayer gradient structure. It was found that the NiCrAlY layers act as a bonding element, providing interlayer adhesion, and the ceramic ZrO₂-Y₂O₃ layer serves as a thermal barrier protecting the substrate from high temperature loads. It was found that the coatings in 2D mode have high microhardness compared to coatings in 1D mode. It was determined that the hardness of coatings smoothly increases from the substrate to the surface layers due to the gradient increase in the content of ceramic materials. It was found that coatings obtained in 2D mode have better wear resistance and lower coefficient of friction compared to coatings in 1D mode, indicating the greater efficiency of coatings in dry friction conditions and their ability to prevent wear of the substrate material.

Keywords: thermal protection coating, gradient coatings, detonation spraying, tribological properties, microhardness.

Introduction

Modern industry faces the need to improve the thermal stability of various machine parts and mechanisms. This is especially relevant for the aviation industry, power engineering, chemical industry and other areas where materials are exposed to high temperatures, aggressive media and intensive mechanical wear. One of the promising methods of improving the performance characteristics of materials is the use of thermal protective coatings (TPC) [1–5]. A thermal protective coating usually consists of a metallic bonding layer and a ceramic top layer of zirconium dioxide stabilized with yttrium oxide (YSZ). YSZ is often used as a top layer for high-temperature applications such as turbine blades in jet engines due to its low thermal conductivity, excellent chemical stability, and high fracture resistance. The metallic bonding coating typically performs two main functions: 1) reduces the thermal mismatch between the YSZ and the substrate, and 2) protects the substrate from oxidation and corrosion. MCrAlY (M = Ni or Ni, Co) is a widely used alloy for these purposes [6, 7].

The main problem with the use of heat protective coatings is the difference in thermal expansion coefficients between the part and coating materials. At significant temperature gradients, this can lead to cracking of the coating and loss of its protective properties [8–11]. The mismatch in thermal expansion coefficients between the bonding layer and the ceramic topcoat can also cause coating failure during thermal cycling [12–15]. The binder layer generally has a higher coefficient of thermal expansion than the ceramic topcoat, resulting in stress accumulation and coating damage. To address this problem, multilayer gradient coatings have been developed to equalize the coefficients of thermal expansion between the layers. Multilayer gradient coatings offer numerous advantages over single materials due to their improved properties. Such coatings reduce thermal stresses by evenly distributing the thermal mismatch between the metal substrate and the ceramic top layer over a large number of layers, which increases the durability of the TPC.

Various methods are used to apply thermal protection coatings, among which the most common are electron beam physical vapor deposition (EB-PVD) and plasma spraying. EB-PVD method allows to create coatings with columnar microstructure, providing high resistance to thermal cycling and improved adhesion [16–18]. Plasma spraying allows the formation of coatings with a lamellar microstructure, which provides good thermal insulation properties and resistance to thermomechanical stresses. Although these methods have been used with great success, they are costly and time-consuming, and coating complexly shaped parts can be difficult or even impossible to achieve [19].

The detonation spraying (DS) method has recently attracted increasing attention due to its high versatility and efficiency in working with various materials. Detonation spraying allows to vary technological parameters and alternate powder feeding, which makes it possible to control the temperature of the powder and the applied coating. This makes it possible to regulate the structural-phase state of the coating material and obtain coatings with specified properties. Advantages of the method include low porosity of the coating, high bond strength with the substrate, minimal thermal effects, which allows avoiding thermal stresses and deformations even in thin-walled complex parts. Due to the low porosity and preservation of the chemical composition of the powder, as well as the possibility of application using two dispensers, the detonation method is promising for obtaining heat protective coatings [9]. In this regard, multilayer gradient coatings by detonation spraying have been developed in this work, and their mechanical and tribological properties have been considered.

The purpose of this work is to investigate the hardness and wear resistance of NiCrAlY/ZrO₂ based gradient detonation coatings.

Materials and methods of research

In this work, 12Kh18N10T stainless steel with dimensions of 20mm was chosen as the substrate. The surfaces of the substrate were sanded with MIRKA brand sandpaper to achieve a smooth and even surface and sandblasted on all sides in a Nordberd NS3 percussion chamber to improve adhesion and relieve surface stresses.

Table 1

Chemical composition of steel grade 12X18H10T

C	Si	Mn	Ni	S	P	Cr	Mo	V	Cu
0.1–0.15	0.17–0.37	0.4–0.7	> 0.3	> 0.025	> 0.03	0.9–1.2	0.25–0.35	0.15–0.3	> 0.2

Metro 233B (YSZ) and PNx20K20Y13 (NiCrAlY) powders were used to obtain gradient coating based on NiCrAlY/ZrO₂-Y₂O₃. The morphology of YSZ and NiCrAlY powders are shown in Figure 1 (a, b), respectively. YSZ powder has a particle size range of 20–45 μm, and the powder particles are spherical in shape. PNx20K20Y13 (NiCrAlY) powder particles have an irregular shape with a particle size of 40 μm.

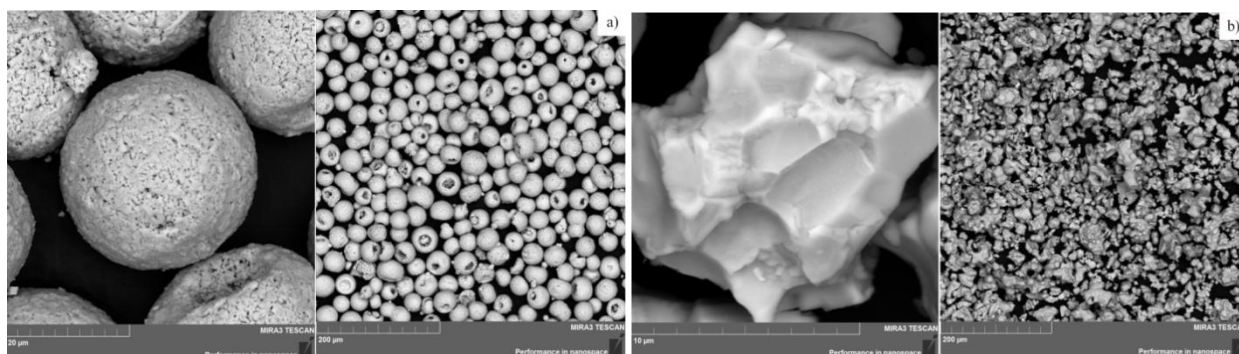


Figure 1. Morphology of powders YSZ (a), NiCrAlY (b)

The chemical composition of the powders is given in Table 2 and 2.1, respectively.

Table 2

Chemical composition of Metco 233B powder (YSZ)

Y ₂ O ₃ SiO ₂ (max)	SiO ₂ (max)	Al ₂ O ₃ (max)	Fe ₂ O ₃ (max)	TiO ₂ (max)	Other oxides (max)	Monoclinic ZrO ₂ (vol.% max)
7.0–9.0	0.5	0.2	0.2	0.2	0.8	<25

Table 2.1

Chemical composition of PNX20K20Yu13 powder (NiCrAlY)

Fe	Cr	Ni	Co	Mo	Al	Other (Y Si Nb C)
<0,3	20	basis	20	–	13	0.01–0.15

The CCDS2000 detonation spraying complex was used to produce gradient coatings. The coatings were applied to the samples using the CCDS2000 (computer-controlled detonation spraying) unit. Figure 1 shows the general view of the CCDS2000 detonation unit.



a — manipulator; *b* — powder dispenser; *c* — spark plug; *d* — dispensing plate

Figure 2. General view of the detonation unit CCDS2000

Gradient coating based on NiCrAlY/ZrO₂-Y₂O₃ were applied to 12Kh18N10T steel specimens using a method developed by us. This method includes abrasive blasting and coatings using PNX20K20Yu13 (NiCrAlY) and Metco 233B (YSZ) powders. The treated surface is infected with a jet of heated powder particles generated in the barrel of the detonation spraying unit. Surface blasting and coating are carried out sequentially in different detonation spraying model using the same NiCrAlY and YSZ powders. The surface blasting mode is selected so that the abrasive particles reach the sprayed surface in a solid state and atomize upon impact. The coating is applied by stepwise changing the detonation sputtering mode to obtain a gradient structure in which NiCrAlY smoothly transitions to YSZ from the substrate to the surface, and the sputtering process includes the following continuous steps:

- first stage — volume of barrel filling with gas mixture of acetylene and oxygen 35 % molar ratio of barrel filling O₂/C₂H₂ is 0.97;
- second stage — volume of barrel filling with gas mixture of acetylene and oxygen is 61 % molar ratio of barrel filling O₂/C₂H₂ is 2.52.

Gradient NiCrAlY/ZrO₂-Y₂O₃ coatings were obtained by detonation sputtering in two modes differing from each other in the number of shots and the form of application on the substrate: spot sputtering (1D), sputtering on the whole surface (2D). The number of shots in each of the modes is presented in Table 3 and Table 4.

Table 3

Number of shots for 1D mode

NiCrAlY	10	6	4	4	2	2	2	2	2	2	2	2	2	2	2	2
YSZ	2	2	2	2	2	2	2	2	2	2	2	2	4	4	6	40

Table 4

Number of shots for 2D mode

NiCrAlY	5	3	2	2	1	1	1	1	1	1	1	1	1	1	1	1
YSZ	1	1	1	1	1	1	1	1	1	1	1	1	2	2	3	20

The volume of barrel filling with burning mixture for the two modes was selected experimentally and is the same for both modes and is presented in Table 5.

Table 5

Volume of filling the detonation barrel with combustible mixture

Coating type	Molar ratio O ₂ /C ₂ H ₂	Volume of barrel filling with gas mixture, %
PNX20K20Yu13 (NiCrAlY)	0.97	35
Metco 233B (YSZ)	2.52	61

The study of surface microstructure and analysis of morphology of cross sections of coatings were carried out using scanning electron microscopy (SEM) on MIRA3 TESCAN equipment and with the help of energy dispersive analyzer INCA ENERGY at E.A. Buketov Karaganda University.

The hardness tester “METOLAB 502” (GOST 6507-1-2007) was used to check microhardness by Vickers method. The indenter used for measurement was a diamond pyramid with an angle between the two faces of 136°. The following mode was chosen to measure hardness by Vickers method: load 0.1 kg, load time 10 sec.

To measure the nanohardness and Young's modulus of the obtained coatings a hardness tester “FISHERSCOPE HM2000 S” was used, the principle of operation of which is based on the Martens method (DIN EN ISO 14577-1). For the hardness test a load of 2N and a dwell time at this load of 5 sec were chosen.

The obtained coatings with mechanical properties (Young's modulus, hardness) were investigated using a NanoScan-4D Compact nanohardness tester (FGBU “TISNSM”, Russia). Nanoindentation of coatings was carried out by Oliver and Farr method using Berkovich indenter at a load of 100 mN (ASTM E2546-07).

Studies of abrasive wear of samples were carried out on a special experimental stand in accordance with GOST 23,208-79, which corresponds to the American standard ASTM C6568 [20]. In the process of these tests, a technique based on the impact of a rotating roller on the flat surface of the specimen was used. Before starting the experiments, the specimens were pre-treated, including degreasing steps using acetone and subsequent drying. Then, a cylindrical rubber roller was pressed against the flat surface of the test specimen with a force of 44 N, and the roller began to rotate at a speed of 1 second per revolution. Abrasive particles (200–250 µm grit electrocorundum) were introduced into the test area at a rate of 41–42 g/min. The specimens were tested for 10 minutes, resulting in a total wear length of 28.8 mm.

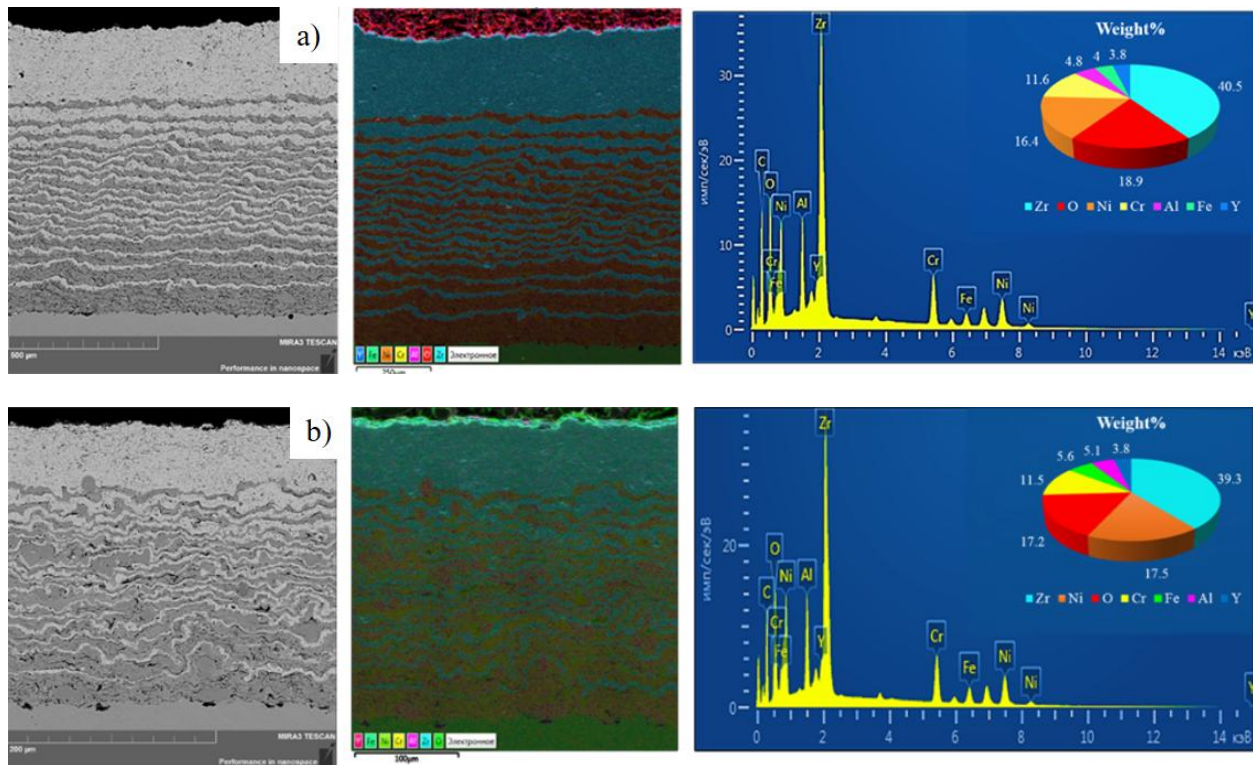
To assess the wear resistance of the tested samples, their wear was compared with the reference sample in accordance with GOST-23,208-79. The mass of samples was measured using analytical scales Gibertini CRYSTAL 100 CE with magnetic compensation. Before each weighing, the samples were cleaned from residual abrasive particles using compressed air. Assessment of material wear was carried out by measuring the change in mass of the samples during the tests in accordance with the requirements of GOST-23,208-79.

The reciprocating friction tests were performed using a TRB³ tribometer from Anton Paar Srl, based in Peseux, Switzerland, using the standard ball-to-disk technique in accordance with ASTM G 133-95 and ASTM G99. A WC ball with a diameter of 6.0 mm was used as a counterbody. A load of 10 N and a full amplitude of motion of 5 mm with a frequency of motion of 7.50 Hz was selected. The length of the friction path was — 300 m. Then with the help of profilometer were measured the area of wear trace and by substituting the obtained values into the formula were calculated the values of wear volume, on the basis of the data obtained with the help of profilometer were created profilograms. Then, using specialized software, the coefficient of wear intensity for the studied coatings was calculated.

Results and Discussion

Scanning electron microscopy (SEM) results showed that the coating consists of alternating layers of NiCrAlY and ZrO₂-Y₂O₃. The ZrO₂-Y₂O₃ layer is located on the surface of the coating and acts as a thermal barrier layer, while the NiCrAlY layer serves as a bonding element between the substrate and the ceramic layer underneath the coating. The coating has a multilayer structure obtained by alternating layers of different materials. Several intermediate layers consisting of PNX20K20Yu13 and YSZ powders are present between the main layers. The electron dispersive spectral (EDS) analysis of the coatings in terms of the content of individual elements for the 1D mode is shown in Figure 3, and for the 2D mode in Figure 3.

The map of element distribution in the NiCrAlY/ZrO₂-Y₂O₃ gradient coating shows how the concentration of elements varies with the depth of the coating. This allows to evaluate the quality and homogeneity of the gradient transition between layers. The results of cross-sectional mapping of the studied samples showed the presence of the main elements of the coatings Zr, O, Ni, Cr, Al, Y and substrate Fe, with no extraneous impurities. The thickness of the layers varied depending on the number of detonation sputtering shots. The coating thickness was $273.72 \pm 1.26 \mu\text{m}$ for sample 1D1 and $963.67 \pm 13.59 \mu\text{m}$ for sample 2D2. Figure 3 also shows a gradual decrease in the NiCrAlY content from the substrate to the coating surface, while the YSZ content gradually increases. The study of the element distribution map confirmed that alternating layers of different materials helps to improve adhesion and reduce the probability of thermal stresses during coating operation. The thermal barrier properties of the coating due to the presence of the ZrO₂-Y₂O₃ layer provide effective protection of the substrate from high temperatures.



a — mode 1D; *b* — mode 2D

Figure 3. Element distribution map in NiCrAlY/ZrO₂-Y₂O₃ gradient coating

The results of hardness measurements by the Martens method on a Fisherscope HM 2000 hardness tester are presented in Table 6.

Table 6

Results of hardness measurements according to the Martens method

Mode 1D			Mode 2D		
№	HM [N/mm ²]	Eit/1-ν ² [GPa]	№	HM [N/mm ²]	Eit/1-ν ² [GPa]
1	3873.2	100.0	1	4658.3	111.1
2	4262.1	121.6	2	3398.4	87.9
3	3466.4	100.4	3	4153.9	109.5
4	4202.4	120.9	4	4733.0	122.0
5	3611.0	89.6	5	4853.3	129.8

The results show that the coated samples obtained using 2D mode have the highest hardness with an average hardness (HM) value of 4359.4 N/mm² and an average modulus of elasticity (Eit/1-ν²) of 112.1 GPa. In turn, the samples obtained using 1D mode have an average Martens hardness value of 3957.9 N/mm² and

a modulus of elasticity of 108.6 GPa. The values for both samples are significantly higher than the hardness of the substrate material, which is 2002.03 N/mm² on the Martens scale. From these values, it can be concluded that these coatings significantly increase the hardness of the specimen. Investigation of the elastic modulus value showed that the original sample has a value of 186.86 GPa. The decrease in the elastic deformation ability of the sample is due to the presence of ZrO₂-Y₂O₃ ceramic layers in the coating.

To determine the hardness of individual layers of the gradient coating, microhardness was investigated by the Vickers method [21]. The arithmetic mean of three measurements in each of the investigated layers was taken as the final values, since due to the design features of the device and the small thickness of the individual layers, the indenter trace was left on the bordering layers. The microindentation results show a clear pattern of increasing hardness values from the substrate to the YSZ surface layer. This trend is observed in both coatings. The hardness increases smoothly with each layer due to the gradient increase in ceramic content in the coating. The results of Vickers microhardness analysis for individual layers are presented in Figure 4. For convenience, cross-sectional images of two samples with indentation traces obtained with an Altamy Met 5C metallographic microscope were presented.

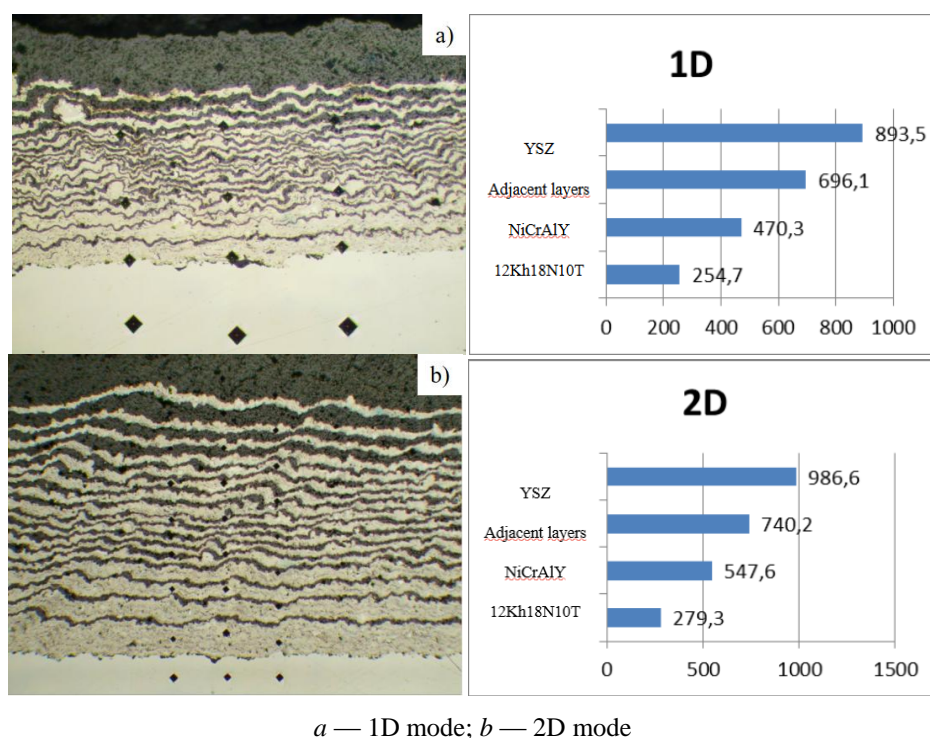
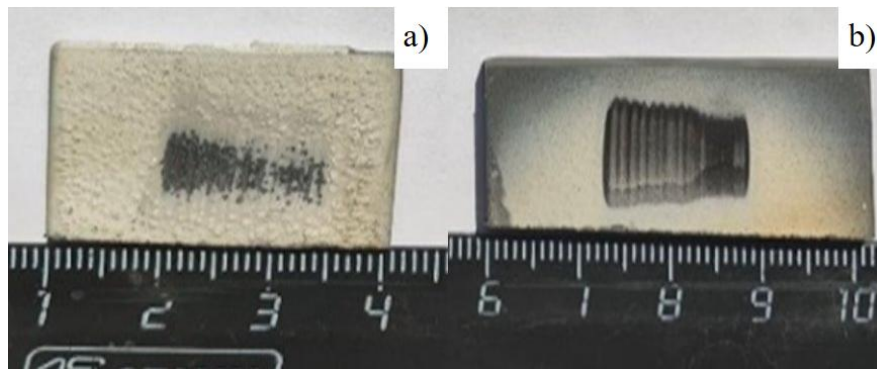


Figure 4. NiCrAlY/ZrO₂-Y₂O₃ gradient coatings in cross section

In addition to hardness determination, to study the protective properties of gradient coatings in two modes, the resistance to wear under dry friction against non-rigidly fixed particles was investigated according to GOST 23.208-79. The results of relative wear resistance were determined. According to the results of wear resistance studies the following values were obtained: the value of relative wear resistance for the 1D mode is 3 times higher than for the 2D mode and amounted to 0.97, while for the coating in the 2D mode this value amounted to 0.30. Figure 5 shows the footprints after WR measurement. The width of the trace for both modes was 1.5 cm. Visually, it can be seen that the abrasion test trace is deeper for mode 1D than for mode 2D, indicating the greater stability of the coating in mode 1D (Fig. 5).



a — 2D mode; *b* — 1D mode

Figure 5. Traces after relative wear resistance measurement

Figure 6 shows the time dependence of the friction coefficient of detonation multilayer gradient coatings. The average value of the friction coefficient of the sample in the first mode is 0.215 ± 0.048 , and no coating failure was observed until the sliding distance reached 400 meters (or 4000 seconds). For the second specimen, the coefficient of friction was 0.584 ± 0.130 . This value is higher than that of the first specimen, which may indicate its less effective thermal protection or sliding wear capability. The roughness and microhardness values can affect the tribological characteristics of the samples [22]. The increase in surface roughness of sample 1D compared to sample 2D leads to a decrease in the actual contact area of the interacting bodies, which also leads to a decrease in the coefficient of friction.

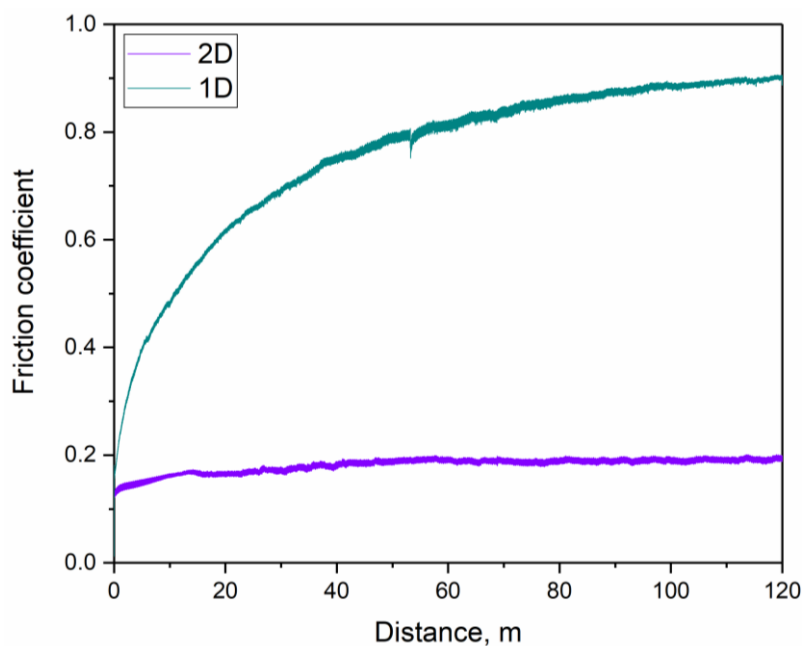
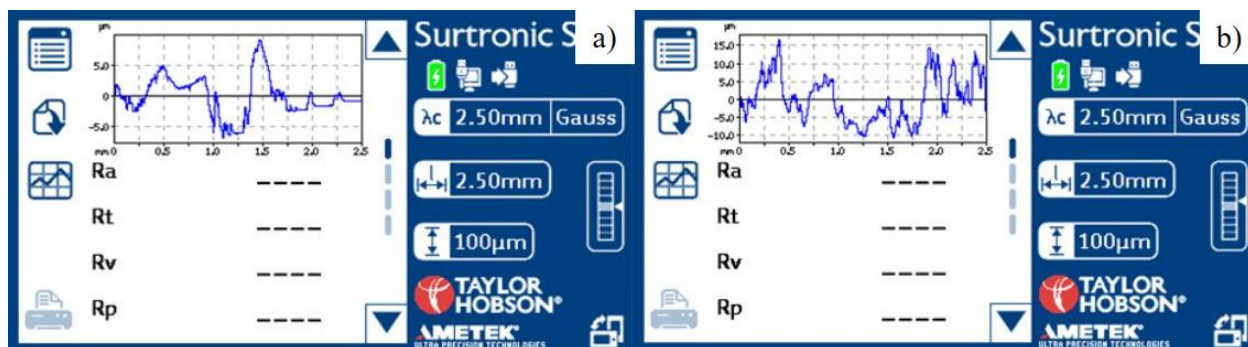


Figure 6. Graph of dependence of friction coefficient on friction path for both regimes

To determine the coefficient of wear intensity, profilograms were obtained on a Surtronic S128 abhvs TAYLOR HOBSON profilometer. According to the measurement results, the roughness for the sample with 1D mode was $4.62 \mu\text{m}$, and for 2D mode — $5.23 \mu\text{m}$. The profilograms are presented in Figure 7. The K_{ii} value for the 1D sample was $5.226\text{E-}005 \text{ [mm}^3\text{/N/m]}$, for the 2D sample the same value was $6.805\text{E-}006 \text{ [mm}^3\text{/N/m]}$. These parameters show the resistance of the obtained coatings to friction wear, as the results show the coating in 1D mode is more resistant to friction and wear.



a — mode 1D; *b* — mode 2D

Figure 7. Profilograms for modes

Conclusion

The following conclusions can be drawn from the studies of gradient multilayer NiCrAlY/ZrO₂-Y₂O₃ coatings obtained by detonation sputtering:

SEM and EDS analysis results confirmed the presence of a clear boundary between NiCrAlY and ZrO₂-Y₂O₃ layers, as well as intermediate layers consisting of PNx20K20Yu13 and YSZ powders. The elemental distribution map showed a homogeneous gradient transition between the layers, which is important for the thermal barrier properties of the coating. Hardness studies by the Martens method and microhardness by the Vickers method showed a significant increase in the hardness of the coated samples compared to the original substrate material. The samples obtained in 2D mode showed higher hardness and elastic modulus compared to those obtained in 1D mode. The results of wear resistance and coefficient of friction tests showed that the coatings obtained in 1D mode had higher wear resistance and lower coefficient of friction compared to those obtained in 2D mode. This indicates a better behavior of the 1D coating under dry friction and abrasion. Measurements of roughness and wear intensity coefficient showed that coatings obtained in 1D mode have lower roughness and higher wear resistance compared to coatings obtained in 2D mode.

In general, the developed NiCrAlY/ZrO₂-Y₂O₃-based gradient coatings exhibit high hardness, good adhesion, excellent thermal barrier properties and high wear resistance. These coatings can be effectively used to protect steel components operating under high temperature and abrasive wear conditions.

Acknowledgments

This research is funded by the Science Committee of the Ministry of Science and Higher Education of the Republic of Kazakhstan (Grant No. AP13068364).

References

- 1 Ермалаев Г.В. Создание и совершенствование технологии плазменного напыления термобарьерных и антиокислительных покрытий и исследование их стойкости в высокоскоростных высокотемпературных газовых потоках / Г.В. Ермалаев, О.Б. Ковалев, В.М. Фомин, С.П. Ващенко, В.И. Кузьмин, А.Н. Шиплюк // Журн. материаловедения. — 2015. — С. 162–163.
- 2 Sukhjinder S. A review on protection of boiler tube steels with thermal spray coatings from hot corrosion / S. Sukhjinder, G. Khushdeep, B. Rakesh // Materials Today Proceedings. — 2022. — Vol. 56. — P. 379–383.
- 3 Kantay K. Influence of detonation-spraying parameters on the phase composition and tribological properties of Al₂O₃ coatings / K. Kantay, B. Rakhadilov, S. Kurbanbekov, D. Yeskermessov // Coatings. — 2021. — Vol. 11. — P. 793.
- 4 Ghadami F. Microstructural characteristics and oxidation behavior of the modified MCrAlX coatings: A critical review / F. Ghadami, S. Ghadami, R. A, Sabour // Vacuum. — 2021. — Vol. 185. — P. 109980.
- 5 Ulianitsky V.Y. Computer-controlled detonation spraying: Flexible control of the coating chemistry and microstructure / V.Y. Ulianitsky, D.V. Dudina, A. Shtertser, I. Smurov // Metals. — 2019. — Vol. 12. — P. 1244.
- 6 Pankov V.P. Investigation of alloys and coatings of turbine blades of gas turbine engines during operation / V.P. Pankov // Strengthening technologies and coatings. — 2016. — Vol. 5(137). — P. 36–40.
- 7 Cao S. Influence of composition and microstructure on the tribological property of SPS sintered MCrAlY alloys at elevated temperatures / S. Cao, S. Ren, J. Zhou, Y. Yu, L. Wang, C. Guo, B. Xin // Journal of Alloys and Compounds. — 2018. — Vol. 740. — P. 790–800.

- 8 Cheng J. High temperature tribological properties of a nickel-alloy-based solid-lubricating composite: Effect of surface tribochemistry, counterpart and mechanical properties / J. Cheng, F. Li, S. Zhu, J. Hao, J. Yang, W. Li, W. Liu // *Wear*. — 2017. — P. 386-387.
- 9 Rakhadilov B. Structure and tribological properties of Ni-Cr-Al based gradient coating prepared by detonation spraying / B. Rakhadilov, M. Maulet, M. Abilov // *Coatings*. — 2021. — Vol. 11. — P. 218.
- 10 Рахадиллов Б.К. Исследование трибологических свойств детонационных покрытий на основе оксида алюминия и карбида вольфрама / Б.К. Рахадиллов, М.Б. Баяндинова, Д.Б. Буйткенов, Д.Н. Кәкімжанов, Л.Г. Журерова, Г.У. Ерболатова // *Вестн. НЯЦ РК*. — 2023. — Вып. 3(95). — С. 168–173.
- 11 Маулет М. Исследование свойств жаростойких покрытий на основе Ni–Cr–Al, полученных методом детонационного напыления / М. Маулет, Б.К. Рахадиллов, Ж.Б. Сағдолдина, Н.С. Райсов // *Междунар. науч.-техн. молод. конф. «Перспективные материалы конструкционного и функционального назначения»*. — Томск, 2023. — С. 311–313.
- 12 Maulet M. Impact of aluminum content upon the microstructure of Ni-Cr-Al gradient coatings. / M. Maulet, W. Wieleba // *Materials of International Practical Internet Conference “Chakkenges of Science”*. — Almaty. — 2023. — P. 233–236.
- 13 Sagdoldina Zh.B. Obtaining functional-gradient Ti-HA coatings by detonation spraying / Zh.B. Sagdoldina, D.R. Baizhan, E.E. Kambarov, K. Torebek / *Bulletin of the University of Karaganda–Physics*. — 2022. — Iss. 3(107). DOI: <https://doi.org/10.31489/2022ph3/43-51>
- 14 Savitha U. Additive laser deposition of compositionally graded NiCrAlY-YSZ multi-materials on IN625-NiCrAlY substrate / U. Savitha, G.J. Reddy, S. Vajinder, A.A. Gokhale, M. Sundararaman // *Materials Characterization*. — 2020. — Vol. 164. — P. 110317.
- 15 Mendelson M.I. Statistically Designed Experiments to Improve Coating Life / M.I. Mendelson // *22nd Annual Conference on Composites, Advanced Ceramics, Materials, and Structures: Ceramic Engineering and Science Proceedings*. — 2008. — Vol. 65. — P. 579–586. DOI: 10.1002/9780470294482.
- 16 Dobbins T.A. HVOF thermal spray deposited Y_2O_3 -stabilized ZrO_2 coatings for thermal barrier applications / T.A. Dobbins, R. Knight, M.J. Mayo // *Therm Spray Tech*. — 2003. — Vol. 12. — P. 214–225.
- 17 Пантелеенко Ф.И. Формирование многофункциональных плазменных покрытий на основе керамических материалов / Ф.И. Пантелеенко, В.А. Оковитый // *БНТУ*. — 2019. — 251 с.
- 18 Девойно О.Г. Плазменные теплозащитные покрытия на основе диоксида циркония с повышенной термостойкостью / О.Г. Девойно, В.В. Оковитый // *Наука и техника*. — 2014. — № 6. — С. 3–10.
- 19 Cabral-Miramontes J.A. Parameter Studies on High-Velocity Oxy-Fuel Spraying of CoNiCrAlY Coatings Used in the Aeronautical Industry / J.A. Cabral-Miramontes // *International Journal of Corrosion*. — 2014. — Vol. 3. — P. 1–8.
- 20 Yeskermessov D. Surface modification of coatings based on Ni-Cr-Al by pulsed plasma treatment / D. Yeskermessov, B. Rakhadilov, L. Zhurerova, A. Apsezhanova, Z. Aringozhina, M. Booth, Y. Tabiyeva // *AIMS Materials Science*. — 2023. — Vol. 10(5). — P. 755–766. DOI: 10.3934/mat.2023042
- 21 Yurov V.M. High entropic coatings FeCrNiTiZrAl and their properties / V.M. Yurov, A.T. Berdibekov, N.A. Belgibekov, K.M. Makhhanov // *Bulletin of the University of Karaganda — Physics*. — 2021. — No. 3(103). DOI: <https://doi.org/10.31489/2021ph3/104-114>
- 22 Kantay N. Research of annealing influence on the hardness of detonation coatings from aluminum oxide / N. Kantay, B.K. Rakhadilov, M. Paszkowski, B. Tuyakbayev, Sh. Kurbanbekov, A. Nabioldina // *Bulletin of the University of Karaganda — Physics*. — 2021. — Vol. 2(102). DOI: <https://doi.org/10.31489/2021ph2/6-13>

Д.Б. Буйткенов, Ж.Б. Сағдолдина, Л.Г. Сулюбаева, А.Б. Нәбиолдина, Н.С. Райсов

Детонациялық бүрку әдісімен алынған NiCrAlY/ZrO₂-Y₂O₃ жабындарының механикалық-трибологиялық қасиеттерін зерттеу

Жұмыста 1D (бір орында нүктелік бүрку) және 2D (сканерлеу арқылы бүкіл бетке бүрку) режимдерінде детонациялық бүрку арқылы алынған NiCrAlY/ZrO₂-Y₂O₃ көп қабатты градиентті жылу қорғайтын жабындары зерттелген. Сканерлеуші электронды микроскопия (СЭМ) мен электронды дисперсиялық талдауды қолдана отырып, жабындардың микроқұрылымына талдау жүргізілді, әртүрлі әдістерді, соның ішінде Викерс әдісі мен Мартенс әдісін қолдана отырып, механикалық қасиеттері (қаттылық, серпімділік модулі) зерттелді. Сондай-ақ, жабындардың трибологиялық сипаттамалары, соның ішінде абразивті тозуға төзімділік және үйкеліс коэффициенті зерттеу жұмыстары жүргізілген. Жабындар NiCrAlY және ZrO₂-Y₂O₃ негізіндегі ауыспалы қабаттарынан тұратыны сондай-ақ, көп қабатты градиент құрылымын жасайтыны белгілі болды. NiCrAlY жабын қабаттары қабат аралық адгезияны қамтамасыз ететін байланыстырушы функцияны орындайтыны белгілі, ал ZrO₂-Y₂O₃ керамикалық қабаты төсенішті жоғары температура жүктемелерінен қорғайтын термиялық тосқауыл ретінде қызмет етеді. 2D режимінде алынған жабындар 1D режиміндегі жабындармен салыстырғанда жоғары микроқаттылық мәнін көрсетті. Керамикалық материалдардың құрамының градиентті ұлғаюына байланысты жабындардың қаттылығы төсеніштен беткі қабаттарға дейін біркелкі өсетіні белгілі болды. 2D режимінде алынған жабындардың тозуға төзімділігі жоғары екені және 1D

режиміндегі жабындармен салыстырғанда үйкеліс коэффициенті төмен екендігі анықталды, бұл зерттеу нәтижелері бойынша құрғақ үйкеліс жағдайында жабындардың үлкен тиімділігін және олардың төсеніш материалының тозуын болдырмау қабілетін көрсетеді.

Кілт сөздер: жылуудан қорғайтын жабындар, градиент жабындары, детонациялық бүрку, трибологиялық қасиеттері, микроқаттылық.

Д.Б. Буйткенов, Ж.Б. Сагдолдина, Л.Г. Сулюбаева, А.Б. Набиолдина, Н.С. Райсов

Исследование механико-трибологических свойств NiCrAlY/ ZrO₂-Y₂O₃ покрытий, полученных методом детонационного напыления

В статье изучены многослойные градиентные NiCrAlY/ZrO₂-Y₂O₃, полученные методом детонационного напыления в режимах 1D (точечное напыление в одном месте) и 2D (напыление на всю поверхность сканированием). Проведен анализ структуры покрытий с использованием сканирующей электронной микроскопии (СЭМ) и электронно-дисперсионного анализа, определены механические свойства (твердость, модуль упругости) с применением различных методик, включая метод Виккерса и метод Мартенса. Также изучены трибологические характеристики покрытий, включая абразивную износостойкость и коэффициент трения. Определено, что покрытия состоят из чередующихся слоев NiCrAlY и ZrO₂-Y₂O₃, создавая многослойную градиентную структуру. Установлено, что слои NiCrAlY выполняют функцию связующего элемента, обеспечивая межслоевую адгезию, а керамический слой ZrO₂-Y₂O₃ служит термобарьером, защищающим подложку от высоких температурных нагрузок. Установлено, что покрытия в режиме 2D обладают высокой микротвердостью по сравнению с покрытиями в режиме 1D. Определено, что твердость покрытий плавно увеличивается от подложки к поверхностным слоям благодаря градиентному увеличению содержания керамических материалов. Установлено, что покрытия, полученные в режиме 2D, обладают лучшей износостойкостью и более низким коэффициентом трения по сравнению с покрытиями в режиме 1D, что указывает на большую эффективность покрытий в условиях сухого трения и их способность предотвращать износ материала подложки.

Ключевые слова: теплозащитное покрытие, градиентные покрытия, детонационное напыление, трибологические свойства, микротвердость.

References

- 1 Ermalaeв, G.V., Kovalev, O.B., Fomin, V.M., Vashchenko, S.P., Kuz'min, V.I., & Shpilyuk, A.N. (2015). Sozdanie i sovershenstvovanie tekhnologii plazmennogo napyleniia termobarernykh i antiokislitelnykh pokrytii i issledovanie ikh stoikosti v vysokoskorostnykh vysokotemperaturnykh gazovykh potokakh [Creation and improvement of the technology of plasma spraying of thermal barrier and antioxidant coatings and the study of their resistance in high-speed high-temperature gas flows]. *Zhurnal materialovedeniia — Journal of Materials Science*, 162–163 [in Russian].
- 2 Sukhjinder, S., Khushdeep, G., & Rakesh, B. (2022). A review on protection of boiler tube steels with thermal spray coatings from hot corrosion. *Materials Today Proceedings*, 56, 379–383.
- 3 Kantay, K., Rakhadilov, B., Kurbanbekov, S., & Yeskermessov D. (2021). Influence of detonation-spraying parameters on the phase composition and tribological properties of Al₂O₃ coatings. *Coatings*, 11, 793.
- 4 Ghadami, F., Ghadami, S., & Sabour Rouh Aghdam, A. (2021). Microstructural characteristics and oxidation behavior of the modified MCrAlX coatings: A critical review. *Vacuum*, 185, 109980.
- 5 Ulianitsky, V.Y., Dudina, D.V., Shtertser, A., & Smurov, I. (2019). Computer-controlled detonation spraying: Flexible control of the coating chemistry and microstructure. *Metals*, 12, 1244.
- 6 Pankov, V.P. (2016). Investigation of alloys and coatings of turbine blades of gas turbine engines during operation. *Strengthening technologies and coatings*, 5(137), 36–40.
- 7 Cao, S., Ren, S., Zhou, J., Yu, Y., Wang, L., Guo, C., & Xin, B. (2018). Influence of composition and microstructure on the tribological property of SPS sintered MCrAlY alloys at elevated temperatures. *Journal of Alloys and Compounds*, 740, 790–800.
- 8 Cheng, J., Li, F., Zhu, S., Hao, J., Yang, J., Li, W., & Liu, W. (2017). High temperature tribological properties of a nickel-alloy-based solid-lubricating composite: Effect of surface tribo-chemistry, counterpart and mechanical properties. *Wear*, 386–387.
- 9 Rakhadilov, B. Maulet, M., & Abilov, M. (2021). Structure and tribological properties of Ni-Cr-Al based gradient coating prepared by detonation spraying. *Coatings*, 11, 218.
- 10 Rakhadilov, B.K., Bayandinova, M.B., Bujtkenov, D.B., Kakimzhanov, D.N., Zhureroва, L.G., & Erbolatova, G.U. (2023). Issledovanie tribologicheskikh svoistv detonatsionnykh pokrytii na osnove oksida aliuminiia i karbida volframa. *Vestnik Natsionalnogo yadernogo tsentra Respubliki Kazakhstan — Bulletin of the National Nuclear Center of the Republic of Kazakhstan*, 3(95), 168–173 [in Russian].

- 11 Maulet, M., Rahadilov, B.K., Sagdoldina, Zh.B., & Rajsov, N.S. (2023). Issledovanie svoystv zharostoikikh pokrytii na osnove Ni–Cr–Al, poluchennykh metodom detonatsionnogo napyleniia [Investigation of the properties of heat-resistant coatings based on Ni–Cr–Al obtained by detonation spraying]. *Mezhdunarodnaia nauchno-tekhnicheskaiia molodezhnaia konferentsiia «Perspektivnye materialy konstruksionnogo i funktsionalnogo naznacheniiia» — International Scientific and Technical Youth Conference “Advanced Materials for Structural and Functional Purposes”*. Tomsk, 311–313 [in Russian].
- 12 Maulet, M., & Wieleba, W. (2023). Impact of aluminum content upon the microstructure of Ni–Cr–Al gradient coatings. *Materials of International Practical Internet Conference “Chakkenges of Science”* (pp. 233–236). Almaty.
- 13 Sagdoldina, Zh.B., Baizhan, D.R., Kambarov, E.E., & Torebek, K. (2022). Obtaining functional-gradient Ti–HA coatings by detonation spraying. *Bulletin of the University of Karaganda–Physics*, 3(107), DOI: <https://doi.org/10.31489/2022ph3/43-51>
- 14 Savitha, U., Reddy, G.J., Vajinder, S., Gokhale, A.A. & Sundararaman M. (2020). Additive laser deposition of compositionally graded NiCrAlY-YSZ multi-materials on IN625-NiCrAlY substrate. *Materials Characterization*, 164, 110317.
- 15 Mendelson, M.I. (2008). Statistically Designed Experiments to Improve Coating Life. 22nd Annual Conference on Composites, Advanced Ceramics, Materials, and Structures: *Ceramic Engineering and Science Proceedings*, 65, 579–586, DOI: 10.1002/9780470294482.
- 16 Dobbins, T.A., Knight, R., & Mayo, M.J. (2003). HVOF thermal spray deposited Y₂O₃-stabilized ZrO₂ coatings for thermal barrier applications. *Therm Spray Tech*, 12, 214–225.
- 17 Panteleenko, F.I., & Okovity, V.A. (2019). Formirovanie mnogofunktsionalnykh plazmennykh pokrytii na osnove keramicheskikh materialov [Formation of Multifunctional Plasma Coatings Based on Ceramic Materials]. *Belorusskii natsionalnyi tekhnicheskii universitet — Belarusian National Technical University*, 251 [in Russian].
- 18 Devoino, O.G., & Okovity, V.V. (2014). Plazmennye teplozashchitnye pokrytiia na osnove dioksida tsirkoniia s povyshennoi termostoikosti [Plasma Heat Protective Coatings Based on Zirconium Dioxide with Increased Heat Resistance]. *Nauka i tekhnika — Science and technology*, 6, 3–10 [in Russian].
- 19 Cabral-Miramontes, J.A. (2014). Parameter Studies on High-Velocity Oxy-Fuel Spraying of CoNiCrAlY Coatings Used in the Aeronautical Industry. *International Journal of Corrosion*, 3, 1–8. <https://doi.org/10.1155/2014/703806>.
- 20 Yeskermessov, D., Rakhadilov, B., Zhureroova, L., Apezhanova, A., Aringozhina, Z., Booth, M., & Tabyieva, Y. (2023). Surface modification of coatings based on Ni–Cr–Al by pulsed plasma treatment. *AIMS Materials Science*, 10(5), 755–766, DOI: 10.3934/mat.2023042.
- 21 Yurov, V.M., Berdibekov, A.T., Belgibekov, N.A., & Makhanov, K.M. (2021). High entropic coatings FeCrNiTiZrAl and their properties. *Bulletin of the University of Karaganda — Physics*, 3(103), DOI: <https://doi.org/10.31489/2021ph3/104-114>
- 22 Kantay, N., Rakhadilov, B.K., Paszkowski, M., Tuyakbayev, B., Kurbanbekov, Sh., & Nabioldina, A. (2021). Research of annealing influence on the hardness of detonation coatings from aluminum oxide. *Bulletin of the University of Karaganda — Physics*, 2(102), DOI: <https://doi.org/10.31489/2021ph2/6-13>

Information about the authors

Dastan, Buitkenov — PhD, Leading Researcher of Scientific Research Center “Surface Engineering and Tribology” at S. Amanzholov East Kazakhstan University, Ust-Kamenogorsk, Kazakhstan; e-mail: buitkenov@gmail.com; ORCID ID: <https://orcid.org/0000-0002-0239-5849>

Zhuldyz, Sagdoldina — PhD, Associate professor, Senior Researcher of Scientific Research Center “Surface Engineering and Tribology” at S. Amanzholov East Kazakhstan University, Ust-Kamenogorsk, Kazakhstan; e-mail: zh.sagdoldina@gmail.com; ORCID ID: <https://orcid.org/0000-0001-6421-2000>

Laila, Sulyubayeva — PhD, Associate professor, Senior Researcher of Scientific Research Center “Surface Engineering and Tribology” at S. Amanzholov East Kazakhstan University, Ust-Kamenogorsk, Kazakhstan; e-mail: lsulyubayeva@gmail.com; ORCID ID: <https://orcid.org/0000-0002-1924-1459>

Aiym, Nabioldina — Junior Researcher of Scientific Research Center “Surface Engineering and Tribology” at S. Amanzholov East Kazakhstan University, Ust-Kamenogorsk, Kazakhstan; e-mail: anabioldina@gmail.com; ORCID ID: <https://orcid.org/0000-0001-5581-2194>

Nurmahanbet, Raisov — Engineer of Scientific Research Center “Surface Engineering and Tribology” at S. Amanzholov East Kazakhstan University, Ust-Kamenogorsk, Kazakhstan; e-mail: 2002raisov@gmail.com; ORCID ID: <https://orcid.org/0009-0007-1698-957X>

ЖЫЛУФИЗИКАСЫ ЖӘНЕ ТЕОРИЯЛЫҚ ЖЫЛУТЕХНИКАСЫ ТЕПЛОФИЗИКА И ТЕОРЕТИЧЕСКАЯ ТЕПЛОТЕХНИКА THERMOPHYSICS AND THEORETICAL THERMOENGINEERING

<https://doi.org/10.31489/2024PH3/94-100>
UDC 536.21; 552.45; 537.528; 537.529

Received: 30.04.2024
Accepted: 18.06.2024

A.K. Khassenov^{*1}, G.A. Bulkaïrova¹, B.R. Nussupbekov¹, E.R. Schragger²,
D.Zh. Karabekova¹, M.M. Bolatbekova¹, Y.A. Zholdasbek¹

¹Karaganda Buketov University, Karaganda, Kazakhstan;

²National Research Tomsk State University, Tomsk, Russia

*Corresponding author's e-mail: ayanbergen@mail.ru

Research of heat conductivity of quartz material

In the article the results of a study of heat conductivity and thermal resistance of quartz-containing materials were presented. The object of the study was a quartz mineral from the Aktas deposit, located in the Ulytau district of the Karaganda region. The initial size was a piece of quartz mineral measuring 5–10 mm, which was disassembled mechanically. To prepare the samples under study, quartz powder 0.2 mm thick, crushed by the electric pulse method, was used. Electropulse technology is one of the methods based on the influence of Yutkin, accompanied by the formation of a specially formed high-voltage pulsed electrical discharge inside a volume of liquid. The pulse discharge frequency of the electrohydropulse installation for grinding the mineral to the required fraction was $f = 3$ Hz, the pulse capacitor capacitance $C = 0.4$ μ F, the pulse discharge voltage $U = 18$ – 37 kV. The samples under study were made in the following dimensions: width 100 mm, length 100 mm, height 25 mm. To evaluate the thermophysical properties of manufactured samples in a stationary mode, the ITP-MG4 “100” installation was used, which determines the heat conductivity and thermal resistance of materials for thermal insulation of industrial equipment and pipelines in accordance with GOST 7076, based on the thermoelectric method, and GOST 30256, based on the thermal probe method. As a result of the study, a graph of the temperature dependence of heat conductivity and thermal resistance of quartz-containing materials was obtained. Based on the results obtained, it was established that the thermophysical parameters of the sample containing quartz are lower compared to the sample consisting of cement.

Keywords: heat conductivity, thermal resistance, quartz powder, electrical pulse, granulometric composition.

Introduction

Currently, there is a large number of building structures that provides the required level of thermal protection of buildings [1]. One of the most important problems in the production of building materials is the reduction of energy costs and material intensity in the production of products and structures. Particular attention is paid to obtaining materials for construction based on local raw materials. One such raw material is quartz [2].

Natural quartz is a crystalline mineral composed of silicon dioxide. It has a number of physical, chemical and optical characteristics and is an important industrial raw material. Due to its high quality and affordable price, it is widely used in various industries such as ceramics, chemistry, metallurgy and electronics. At the same time, quartz powder is also widely used in construction. For the production of many building materials, a sufficient amount of natural components is added to its composition. The quartz mineral ranks 7th in terms of hardness on the Mohs scale. Its hardness and strength have an important role in production. This feature makes it effective for businesses that require high-strength materials. It is added to cement, concrete and other building materials in the construction sector. In this case, quartz powder is used as a filler in the construction industry, combining the volume and strength of the mixture with other materials. Mixtures of these raw materials in large volumes increase the strength of various materials by

about 100 times. Thanks to the quartz powder added to the composition, these materials become durable and elastic, which makes them resistant to abrasion and atmospheric influences.

Fine fractions of quartz powder are used for the production of dry construction mixtures [3]. They are used in concrete restoration, for laying stoves and fireplaces, floor screed equipment, waterproofing structures, as well as for interior and exterior decoration. The high physical and chemical properties of quartz sand find their application in a wide variety of industrial fields. Moreover, its use in a specific industry directly depends on the type of quartz and its physical characteristics [4]. At the same time, quartz powder is widely used to improve the strength, weather resistance, texture and appearance of paints, coatings and sealants.

Kazakhstan is one of the states known for its mineral resources. Owing to the country's vast reserves, it is able to meet the global demand for quartz powder in various industries. Quartz is a multifaceted mineral used in a variety of industries, both industrially and in everyday life. Kazakhstan continues to make a significant contribution to meeting the needs of industries around the world with its quartz powder exporters to the global market. Quartz powder remains an indispensable raw material for strengthening structures in construction or demonstrating its importance in our daily lives and in various fields.

As a versatile material, quartz powder has many properties that make it popular in various industries. The heatphysical properties of materials play an important role in various fields such as engineering, physics, chemistry and technology. Understanding these properties makes it possible to improve heat transfer processes and develop more efficient materials at different temperatures. Heat conductivity is also an important value taken into account when planning thermal insulation work [5]. Selecting the right material is very important; it determines how much thermal energy you will have to expend to heat the finished room.

Experimental methods for determining λ values are based on measuring the amount of heat passing through a test sample of normalized dimensions in a certain time at a given temperature difference [6]. Reduced heat conductivity reduces the rate of heat transfer between the internal and external environments. Thus, the use of the studied materials, especially thermal conductivity measurements, potentially improves the thermal performance of the building envelope. It also helps to reduce energy costs spent on air conditioning over many years of operation of the structure [7].

Analysis of heat transfer through building elements is of great importance in solving construction problems, such as energy efficient design, thermal load of structures, thermal comfort planning [8–10].

The purpose of the work is an experimental research of heat conductivity and thermal resistance of quartz-containing materials.

To achieve this aim, it is necessary to solve the following tasks:

- production of quartz-based samples processed using the electric pulse method;
- investigation of the heat physical properties of quartz-containing materials.

Experimental

The object of the research was the quartz mineral of the Aktas deposit (Fig. 1). Since quartz mineral is used in construction in different sizes, powdered raw materials were obtained using the electric pulse method [11]. This technology is one of the most environmentally efficient methods of crushing natural ores and household waste [12–14]. Since the raw material has large dimensions (70–150 mm) before processing by the electric pulse method, a piece of quartz was mechanically crushed to 5–10 mm so that it could fit into the working cell of the installation (Fig. 2).

The production of quartz powder by the electric pulse method was carried out in the following parameters: frequency of pulse discharges $f = 3$ Hz; pulse capacitor capacity $C = 0.4$ μF ; pulse discharge voltage $U = 18$ – 37 kV [15]. The granulometric composition of quartz powder obtained by the electric pulse method was determined by the sieve method according to GOST 12536-2014 “Methods for laboratory determination of granulometric (grain) and microaggregate composition”.

In construction, quartz powder 0.2 mm in size is used in the manufacture of various products (plaster materials, replacing a certain amount of cement with quartz flour, in the production of concrete and ceramic materials). The resulting powder was passed through standard sieves with a mesh opening diameter of 0.2 mm (Fig. 3).

To assess the heatphysical properties of a granular sample, the ITP-MG4 “100” device was used, which allows determining the heat conductivity and thermal resistance of materials for thermal insulation of industrial equipment and pipelines in stationary mode according to GOST 7076 and by the heating probe method according to GOST 30256, based on the thermoelectric method (Fig. 4).



Figure 1. Piece of quartz from Aktas mine



Figure 2. Pieces of quartz 5–10 mm



Figure 3. Powder size 0.2 mm quartz



Figure 4. Heat conductivity meter ITP-MG4 100

Various samples were prepared to investigate the heat conductivity of quartz-containing samples:

Sample 1 is a mixture of 50 % quartz and 50 % Portland cement of the M400 brand;

Sample 2 is a mixture of 70 % quartz and 30 % Portland cement of the M400 brand.

The samples had a width of 100 mm, a length of 100 mm and a height of 25 mm (Fig. 5). When developing mixtures, the amount of water was the same for each sample: 100 ml.

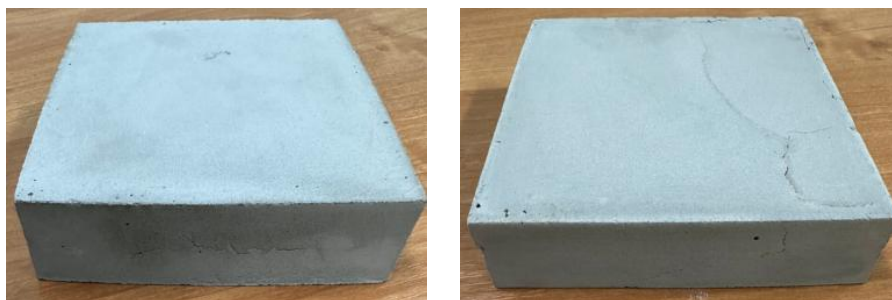


Figure 5. Investigated specimens

To study the thermal conductivity of the samples at a constant temperature of the cooler in the device (15 °C), the temperature of the heater was changed from 25 °C to 45 °C. The graph (Fig. 6 and 7) below shows the temperature dependence of the thermal conductivity and thermal resistance of the samples according to the experimental results. The heatphysical parameters of the studied samples were compared with those of a sample consisting of 100 % cement. 1 — a sample consisting of 100 % cement in the figures; 2 — a sample consisting of 50 % quartz powder; 3 — A sample consisting of 70 % quartz powder.

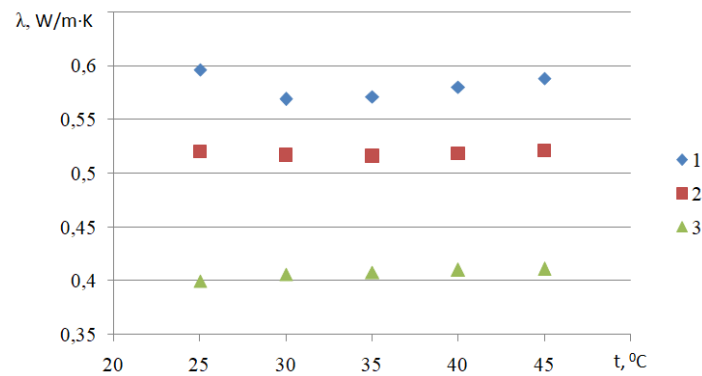


Figure 6. Temperature-dependent change in heat conductivity of samples

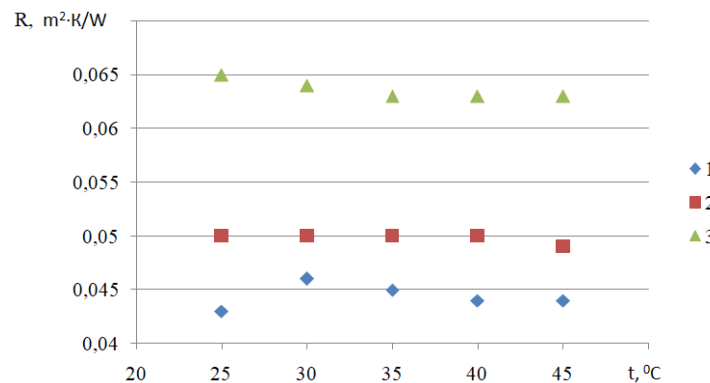


Figure 7. Temperature-dependent change in the thermal resistance of samples

It follows from the experimental data that the thermal conductivity of acid-free Portland cement in the considered temperature ranges was $\lambda = 0.569\text{--}0.596$ W/m·K. The thermal conductivity of the quartz-containing material varied in the following intervals: $\lambda = 0.516\text{--}0.521$ W/m·K for a mixture of Portland cement of the 50 % M400 brand and $\lambda = 0.400\text{--}0.411$ W/m·K for a mixture of Portland cement of the 50 % M400 brand; $\lambda = 0.400\text{--}0.411$ W/m·K. from the data given, it follows that thermal conductivity of cement it has been established that composite samples have low thermal conductivity. These results prove that a certain amount of cement can be replaced with quartz powder [16].

Conclusions

The heat conductivity and thermal resistance of quartz-containing samples were investigated in scientific work. When quartz was added to cement in the range of 50–70 %, construction raw materials with favorable heatphysical parameters were obtained.

It was found that the thermal resistance of a material containing 70 % quartz is higher than the temperature dependence of the thermal resistance of the samples. The thermal resistance of a material is a parameter of the thermal conductivity resistance. The results obtained indicate the effectiveness of using quartz as a heat-insulating material in construction.

From the above fraction, it was found that the addition of quartz powder to the material has a low thermal conductivity. The experimental data can be used in the development of materials containing natural minerals.

This research is funded by the Science Committee of the Ministry of Science and Higher Education of the Republic of Kazakhstan (Grant AP14870607).

References

- 1 Мальцев А.В. Теплопроводность увлажненного материала наружных ограждающих конструкций при промерзании и ее влияние на тепловые потери / А.В. Мальцев, М.Н. Карев // Новый университет. Сер. Технические науки. — 2015. — № 3–4 (37–38). — С. 83–86.

- 2 Митина Н.А. Строительные материалы на основе активированного кварцевого песка / Н.А. Митина, В.И. Верещагин // Изв. Том. политех. ун-та. — 2009. — Т. 314, № 3. — С. 1–4.
- 3 Лотов В.А. Нанодисперсные системы в технологии строительных материалов и изделий / В.А. Лотов // Изв. Том. политех. ун-та. — 2007. — Т. 311, № 3. — С. 84–88.
- 4 Хавкин Л.М. Технология силикатного кирпича / Л.М. Хавкин. — М.: Стройиздат, 1982. — 384 с.
- 5 Исаченко В.П. Теплопередача / В.П. Исаченко, В.А. Осипова, А.С. Сукомел. — М.: Энергия, 1975. — 488 с.
- 6 Баранова А.А. Теплопроводность и термическое сопротивление неавтоклавного пенобетона на основе микрокремнезёма / А.А. Баранова // Изв. вузов. Инвестиции. Строительство. Недвижимость. — 2020. — Т. 10. — № 3. — С. 370–377.
- 7 Толстова Ю.И. Основы строительной теплофизики / Ю.И. Толстова, Р.Н. Шумилов. — Екатеринбург: Изд-во Урал. ун-та, 2014. — 104 с.
- 8 Demirboga R. The effects of expanded perlite aggregate, silica fume and fly ash on the thermal conductivity of lightweight concrete / R. Demirboga, R. Gül // Cement Concr. — 2003. — Res. 33. — P. 723–727.
- 9 Khan M. Factors affecting the thermal properties of concrete and applicability of its prediction models / M. Khan // Building and Environment. — 2002. — Vol. 37. — P. 607–614.
- 10 Kim K. An experimental study on thermal conductivity of concrete / K. Kim, S. Jeon, J. Kim, S. Yang // Cement Concr. — 2003. — Res. 33. — P. 363–371.
- 11 Bulkaïrova G. A research of the effect of an underwater electric explosion on the selectivity of destruction of quartz raw materials / G. Bulkaïrova, B. Nussupbekov, M. Bolatbekova, A. Khassenov, U. Nussupbekov, D. Karabekova // Eastern-European Journal of Enterprise Technologies. — 2023. — 3(12(123)). — P. 30–37.
- 12 Юткин Л.А. Электрогидравлический эффект и его применение в промышленности / Л.А. Юткин. — Л.: Машиностроение, 1986. — 253 с.
- 13 Khassenov A.K. Electro-pulse method for obtaining raw materials for subsequent flotation enrichment of ore / A.K. Khassenov, M. Stoev, D.Zh. Karabekova, G.A. Bulkaïrova, D.A. Nurbalayeva // Bulletin of the University of Karaganda–Physics. — 2021. — Vol. 1. — Iss. 101. — P. 57–62.
- 14 Курец В.И. Электроразрывные технологии обработки и разрушения материалов / В.И. Курец, М.А. Соловьев, А.И. Жучков, А.В. Барская. — Томск: Том. политех. ун-т, 2012. — 272 с.
- 15 Khassenov A.K. Investigation of the influences of pulsed electrical discharges on the grinding of quartz raw materials / A.K. Khassenov, D.Zh. Karabekova, B.R. Nussupbekov, G.A. Bulkaïrova, A.S. Kudussov, G.K. Alpyssova, M.M. Bolatbekova // Bulletin of the University of Karaganda–Physics. — 2023. — Vol. 2. — Iss. 110. — P. 93–99.
- 16 Пустовгар А.П. Исследование возможности частичного замещения портландцемента кварцевой мукой SILVERBOND в составе тампонажных материалов / А.П. Пустовгар, А.Ю. Абрамова, Н.Е. Ерёмкина, С.Р. Ганиев // Строительство нефтяных и газовых скважин на суше и на море. — 2019. — № 8. — С. 27–36.

А.К. Хасенов, Г.А. Булкаïрова, Б.Р. Нусупбеков, Е.Р. Шрагер,
Д.Ж. Карабекова, М.М. Болатбекова, Е.А. Жолдасбек

Кварц құрамды материалдың жылу өткізгіштігін зерттеу

Мақалада кварц құрамды материалдардың жылу өткізгіштігі мен термиялық кедергісін зерттеу нәтижелері келтірілген. Зерттеу нысаны ретінде Ұлытау облысының Ұлытау ауданында орналасқан Ақтас кен орнынан алынған кварц минералы алынды. Бастапқы өлшемі ретінде механикалық әдіпен бөлшектенген 5-10 мм болатын кварц минералының кесегі пайдаланылды. Зерттелетін үлгілерді дайындау үшін электроимпульс әдісімен ұнтақталған 0,2 мм кварц ұнтағы қолданылды. Электроимпульстік технология Юткиннің әсеріне негізделген, сұйық көлемінің ішінде арнайы қалыптасқан жоғары вольтты импульстік электр разрядының пайда болуымен жүретін әдістің бірі. Минералды қажетті фракцияға ұнтақтау үшін электрогидроимпульстік қондырғының импульстік разряд жиілігі $f = 3$ Гц, импульстік конденсатордың сыйымдылығы $C = 0,4$ мкФ, импульстік разрядтардың кернеуі $U = 18–37$ кВ болды. Зерттелетін үлгілер келесі өлшемде дайындалды: ені 100 мм, ұзындығы 100 мм, биіктігі 25 мм. Дайындалған үлгілердің жылу физикалық қасиетін зерттеу үшін стационарлық режимде термоэлектрлік әдіске негізделген МЕМСТ 7076 мемлекеттік стандарттарға сәйкес және жылу зонд әдіске негізделген МЕМСТ 30256 мемлекеттік стандарттарға сәйкес өнеркәсіптік жабдықтар мен құбырларды жылу оқшаулауға арналған материалдардың жылу өткізгіштігін және жылу кедергісін анықтайтын ИТП-МГ4 «100» қондырғысы қолданылды. Зерттеу нәтижесінде кварц құрамды материалдардың жылу өткізгіштігі мен термиялық кедергісінің температураға тәуелділік графигі алынды. Алынған нәтижелер негізінде құрамында кварц бар үлгінің жылу физикалық көрсеткіштерінің цементтен тұратын үлгімен салыстырғанда төмен екендігі анықталды.

Кілт сөздер: жылу өткізгіштік, термиялық кедергі, кварц ұнтағы, электримпульс, гранулометриялық құрам.

А.К. Хасенов, Г.А. Булкайрова, Б.Р. Нусупбеков, Е.Р. Шрагер,
Д.Ж. Карабекова, М.М. Болатбекова, Е.А. Жолдасбек

Исследование теплопроводности кварцевого материала

В статье представлены результаты исследования теплопроводности и термического сопротивления кварцосодержащих образцов. Объект исследования — природный минерал кварцит месторождения Актас, расположенного в Улытауском районе Карагандинской области. В качестве первоначального размера использовался кусок кварцевого минерала размером 5–10 мм, который был измельчен механическим способом. Для изготовления образцов применялся кварцевый песок диаметром 0,2 мм, измельченный электроимпульсным методом. Электроимпульсная технология является одним из методов, основанных на эффекте Юткина, сопровождающегося образованием специально сформированного высоковольтного импульсного электрического разряда в объеме жидкости. Частота импульсного разряда электрогидроимпульсной установки для измельчения минерала до нужной фракции составляла $f = 3$ Гц, емкость импульсного конденсатора $C = 0,4$ мкФ, напряжение импульсных разрядов $U = 18–37$ кВ. Исследуемые образцы были изготовлены в следующих размерах: ширина 100 мм, длина 100 мм, высота 25 мм. Для оценки теплофизических свойств изготовленных образцов в стационарном режиме применена установка ИТП-МГ4 «100», определяющая теплопроводность и тепловое сопротивление материалов для теплоизоляции промышленного оборудования и трубопроводов в соответствии с ГОСТ 7076, основанным на термоэлектрическом методе, и ГОСТ 30256, основанным на тепловом зондовом методе. В результате исследования получен график температурной зависимости теплопроводности и термического сопротивления кварцосодержащих материалов. На основании полученных результатов установлено, что теплофизические показатели образца, содержащего кварц, ниже, по сравнению с образцом, состоящим из цемента.

Ключевые слова: теплопроводность, термическое сопротивление, кварцевый порошок, электроимпульс, гранулометрический состав.

References

- 1 Maltsev, A.V., & Karev, M.N. (2015). Teploprovodnost uvlazhennogo materiala naruzhnykh ograzhdaiushchikh konstruksii pri promerzanii i ee vliianie na teplovye poteri [Thermal conductivity of the moistened material of external enclosing structures during freezing and its effect on heat losses]. *Novyi universitet. Seriya Tekhnicheskie nauki — A new university. Series: Technical sciences*, 3–4 (37-38), 83–86 [in Russian].
- 2 Mitina, N.A., & Vereshchagin, V.I. (2009). Stroitelnye materialy na osnove aktivirovannogo kvartsevogo peska [Building materials based on activated quartz sand]. *Izvestiia Tomskogo politekhnicheskogo universiteta — Proceedings of Tomsk Polytechnic University*, 314(3), 1–4 [in Russian].
- 3 Lotov, V.A. (2007). Nanodispersnye sistemy v tekhnologii stroitelnykh materialov i izdelii [Nanodisperse systems in the technology of building materials and materials]. *Izvestiia Tomskogo politekhnicheskogo universiteta — Proceedings of Tomsk Polytechnic University*, 311(3), 84–88 [in Russian].
- 4 Khavkin, L.M. (1982). *Tekhnologiya silikatnogo kirpicha [Technology of silicate bricks]*. Moscow: Stroizdat [in Russian].
- 5 Isachenko, V.P., Osipova, V.A. & Sukomel, A.S. (1975). *Teploperedacha [Heat Transfer]*. Moscow: Energiia [in Russian].
- 6 Baranova, A.A. (2020). Teploprovodnost i termicheskoe soprotivlenie neavtoklavnogo penobetona na osnove mikroremnezema [Thermal conductivity and thermal correction of non-autoclaved foam concrete based on silica]. *Izvestiia vuzov. Investitsii. Stroitelstvo. Nedvizhimost — News of universities. Investment. Construction. Realty*, 10(3), 370–377 [in Russian].
- 7 Tolstova, Yu.I. (2014). *Osnovy stroitelnoi teplofiziki [Fundamentals of building thermophysics]*. Ekaterinburg: Izdatelstvo Uralskogo universiteta [in Russian].
- 8 Demirboga, R., & Gül, R. (2003). The effects of expanded perlite aggregate, silica fume and fly ash on the thermal conductivity of lightweight concrete. *Cement Concr.*, 33, 723–727.
- 9 Khan, M. (2002). Factors affecting the thermal properties of concrete and applicability of its prediction models. *Building and Environment*, 37, 607–614.
- 10 Kim, K., Jeon, S., Kim, J., & Yang, S. (2003). An experimental study on thermal conductivity of concrete. *Cement Concr. Res.*, 33, 363–371.
- 11 Bulkairova, G., Nussupbekov, B., Bolatbekova, M., Khassenov A., Nussupbekov, U., & Karabekova, D.Zh. (2023) A research of the effect of an underwater electric explosion on the selectivity of destruction of quartz raw materials. *Eastern-European Journal of Enterprise Technologies*, 3(12(123)), 30–37.
- 12 Yutkin, L.A. (1986). *Elektrogidravlicheskii effekt i ego primenenie v promyshlennosti [Electrohydraulic effect and its application in industry]*. Leningrad: Mashinostroenie [in Russian].
- 13 Khassenov, A.K., Stoev, M., Karabekova, D.Zh., Bulkairova, G.A., & Nurbalayeva, D.A. (2021). Electro-pulse method for obtaining raw materials for subsequent flotation enrichment of ore. *Bulletin of the University of Karaganda—Physics*, 1(101), 57–62.

14 Kurets, V.I., Solovyov, M.A., Zhuchkov, A.I., & Barskaya, A.V. (2012). *Elektrorazryvnye tekhnologii obrabotki i razrusheniia materialov [Electrical fracturing technologies for processing and destruction of materials]*. Tomsk: Tomskii politekhnicheskii universitet [in Russian].

15 Khassenov, A.K., Karabekova, D.Zh., Nussupbekov, B.R., Bulkaïrova, G.A., Kudussov, A.S., Alpysova, G.K., & Bolatbekova, M.M. (2023). Investigation of the influences of pulsed electrical discharges on the grinding of quartz raw materials. *Bulletin of the University Of Karaganda–Physics*, 2(110), 93–99.

16 Pustovgar, A.P., Abramova, A.Yu., Eremina, N.E., & Ganiev, S.R. (2019). Issledovanie vozmozhnosti chastichnogo zameshcheniia portlandsementa kvartsevoi mukoi SILVERBOND v sostave tamponazhnykh materialov [Investigation of the possibility of partial substitution of Portland cement with quartz flour SILVERBOND as part of grouting materials]. *Stroitelstvo neftiannykh i gazovykh skvazhin na sushe i na more — Construction of oil and gas wells on land and at sea*, 8, 27–36 [in Russian].

Information about the authors

Khassenov, Ayanbergen (*contact person*) — PhD, Associate professor, Department of Engineering Thermophysics named after Professor Zh.S. Akylbayev, Karaganda Buketov University, e-mail: ayanbergen@mail.ru; ORCID ID: <https://orcid.org/0000-0002-5220-9469>

Bulkaïrova, Gulden — Master in Physics, Department of Engineering Thermophysics named after Professor Zh.S. Akylbayev, Karaganda Buketov University, e-mail: gulden2111@mail.ru; ORCID ID: <https://orcid.org/0000-0001-7390-2214>

Nussupbekov, Bekbolat — Candidate of technical sciences, Professor, Department of Engineering Thermophysics named after Professor Zh.S. Akylbayev Karaganda Buketov University, e-mail: bek_nr1963@mail.ru; ORCID ID: <https://orcid.org/0000-0003-2907-3900>

Schrager, Ernst — Doctor of physical and mathematical sciences, Professor, Faculty of Physics and Technology, National Research Tomsk State University, Tomsk, Russia, e-mail: sher@ftf.tsu.ru

Karabekova, Dana — PhD, Associate professor, Department of Engineering Thermophysics named after Professor Zh.S. Akylbayev Karaganda Buketov University, e-mail: karabekova71@mail.ru; ORCID ID: <https://orcid.org/0000-0001-8776-4414>

Bolatbekova, Madina — Master of natural sciences Department of Radiophysics and Electronics, Karaganda Buketov University, e-mail: r.bolatbekova.madina@gmail.com; ORCID ID: <https://orcid.org/0000-0002-0169-3430>

Zholdasbek, Yerdaulet — Student, Department of Engineering Thermophysics named after Professor Zh.S. Akylbayev, Karaganda Buketov University, e-mail: zoldasbekerdaulet173@gmail.com